Origin of Cenozoic Porphyry Cu Deposits in Southern Tibet

by

Rui Wang

A thesis submitted in partial fulfillment of the requirements for the degree of

Doctor of Philosophy

Department of Earth and Atmospheric Sciences
University of Alberta

Abstract

The Gangdese magmatic belt features extensive Cenozoic magmatic rocks that record geodynamic changes related to the India–Asia collision starting at ~55–50 Ma. Paleocene–Eocene magmas throughout the belt have similar continental arc features. Their intrusive rocks have intermediate $[La/Yb]_N$ and intermediate-to-low Sr/Y ratios, negative Eu anomalies, and consists mainly of pyroxene and plagioclase. These geochemical and mineralogical characteristics suggest that the Paleocene–Eocene magmas were relatively dry and evolved primarily by fractionation of pyroxene and plagioclase. In addition, their magmas were also less oxidized (ΔFMQ -1.2 to +0.8). The relatively low water contents and oxidation state of these magmas may reflect final dehydration of the remnant Neo-Tethyan slab, and with the result that only three small porphyry Cu-Mo deposits associated to this suite.

The Oligo-Miocene igneous rocks show a sharp longitudinal distinction of petrography, magmatic geochemistry, and association with porphyry-type mineralization. The eastern Gangdese group (east of ~89°E) is characterized by mainly intermediate–felsic calc-alkaline plutons related to porphyry Cu-Mo±Au deposits, and minor potassic rocks. Their intrusive igneous rocks have high $[La/Yb]_N$ and Sr/Y ratios, weak or absent Eu anomalies, and amphibole as common phenocrysts. Their magmas were more hydrous and fractionated significant amounts of hornblende and lesser plagioclase prior to upper crustal emplacement. In addition, their magmas were also more oxidized (ΔFMQ+0.8 to +2.9). In contrast, the western group is characterized by potassic volcanic rocks with relatively high Th and K_2O contents, low Sr/Y ratios, and low εNd_i values. There are only one small-sized porphyry Cu deposit to the west of ~89°E. We propose that the sharp longitudinal distinction between magmatism and metallogenic potential in the Oligo-

Miocene Gangdese belt reflects the variable extent of underthrusting of the Indian plate continental lithosphere beneath Tibet. Where subduction-modified Tibetan lithosphere was partially melted by upwelling asthenosphere following slab breakoff in the east, hydrous, oxidized magmas with the result to generate several large porphyry deposits. In contrast, underthrusting of the Indian plate to the west limited the involvement of asthenospheric melts and limited the extent of lithospheric partial melting, with the result that few porphyry deposits are associated with these magmas.

Preface

This thesis is an original work by Rui Wang. Some of the research conducted for this thesis forms part of an international research collaboration. Dr. Jeremy Richards in University of Alberta, as the leader, conducted the collaboration for my doctoral project with Dr. Zeng-qian Hou in Institute of Geology, Chinese Academy of Geological Sciences, Beijing, China.

Chapter 2 was in press as: Wang, R., Richards, J.P., Hou, Z.Q., Yang, Z.M., and DuFrane, S.A., 2014, "Increased magmatic water content–the key to Oligo-Miocene porphyry Cu–Mo ± Au formation in the eastern Gangdese belt, Tibet," *Economic Geology*, in press. Chapter 3 was in press as: Wang, R., Richards, J.P., Hou, Z.Q., Yang, Z.M., Gou, Z.B., and DuFrane, S.A., 2014, "Increasing magmatic oxidation state from Paleocene to Miocene in the eastern Tibetan Gangdese belt: Implication for collision-related porphyry Cu–Mo±Au mineralization," *Economic Geology*, in press. Chapter 4 was published as: Wang, R., Richards, J.P., Hou, Z.Q., and Yang, Z.M., 2014, "Extent of underthrusting of the Indian plate beneath Tibet controlled the distribution of Miocene porphyry Cu–Mo ± Au deposits," *Mineralium Deposita*, v. 49, p. 165–173. DOI 10.1007/s00126-013-0507-y. Chapter 5 was submitted as: Wang, R., Richards, J.P., Zhou, L.M., Hou, Z.Q., Yang, Z.M., Muehlenbachs, K., Stern, R.A., Creaser, R.A., Zhu, J.J., and Li, J.X., 2014, "The role of Indian and Tibetan lithosphere in spatial distribution of Cenozoic magmatism and porphyry Cu-Mo±Au deposits in the Gangdese belt, southern Tibet," *Journal of Petrology*.

The first and corresponding author, Rui Wang, was responsible for the sample collection and preparation, data collection, interpretation, and wrote all the drafts. Jeremy Richards was the supervisory author, and responsible for data interpretation and English editing. Zeng-qian Hou and Zhi-ming Yang were responsible for sample collection and data interpretation. Li-min Zhou was responsible for osmium isotopic data collection and interpretation. Karlis Muehlenbachs, Richard Stern, and Jing-jing Zhu were responsible for oxygen isotopic data collection and interpretation. Robert Creaser and Jin-xiang Li were responsible for strontium and neodymium isotopic data collection and interpretation. Andy DuFrane was responsible for zircon dating process.

Acknowledgement

I would like to express my special appreciation and thanks to my supervisor Prof. Jeremy Richards for his support, advice, incisive and constructive criticism, encouragement, patience, and countless hours of editing of the thesis. Without his help, I would never reach the current point to get the thesis in shape. His advice on both research and my career has been priceless.

A special thank to Prof. Zeng-qian Hou for his guidance and encouragement. I am grateful to his generosity, which helps me to fulfill the fieldwork and analytical work. Sincere thanks to Profs. Tomas Chacko and Martyn Unsworth as my supervisor committees, and Profs. Kevin Ansdell and Robert Creaser as my external examiners. I also want to thank Dr. Zhi-ming Yang, my good friend, for his support in my fieldwork and lab work. Drs. Fang An, Jin-xiang Li, and Jing-jing Zhu are thanked for constructive discussions with me during their visit here. I would also like to thank Zheng-bin Gou, Li-min Zhou, Ke-xian Huang, Deng-hu Du, Yun-fei Liu, Bo Xu, Qiuyun-Li, Huan-chun Qu, and Ciren for help in fieldwork and sample preparation. I thank Dr. Andy DuFrane for help with zircon U-Pb dating with LA-ICPMS, Dr. Li-min Zhou for Re-Os isotope analysis, Dr. Robert Creaser for help with Sr-Nd isotope analysis, Dr. Karlis Muehlenbachs for help with whole-rock, amphibole, and biotite O isotope analysis, Drs. Richard Stern and Anna Oh for help with zircon O isotope and U-Pb analysis with SIMS, Dr. Tomas Chacko and Andrew Locock for help with electron microprobe analyses, and Drs. Ling-hao Zhao and Ming-yue Hu for zircon trace element analysis with LA-HR-ICPMS. We also thank Drs. David Cooke, Thomas Bissig, and Yong-jun Lu for constructive reviews during paper reviewing for journals of Economic Geology and Mineralium Deposita.

This thesis was funded by a Discovery Grant from the Natural Sciences and Engineering Research Council of Canada to Jeremy Richards, the Ministry of Science and Technology of China (973 project 2011CB403100), IGCP/SIDA-600 Project (China), and student research and travel grants from the Society of Economic Geologist Canada Foundation, the Geological Society of America, the Mineralogical Association of Canada Foundation, and the China Institute of the University of Alberta to me. I was also funded by a Chinese Scholarship Council award from Chinese government.

Table of Contents

List of Tables

List of Figures

Chapter 1
Introduction

1.1 Introduction

Porphyry-type ore deposit systems supply world's most Cu and Mo, and significant amounts of Au, Ag, Sn and rare earth elements (Sillitoe, 2010). Porphyry copper deposits are most commonly formed by hydrothermal fluids exsolved from fertile and relatively oxidized subduction-related magmas in arc settings (Sillitoe, 1972, 2010; Burnham, 1979; Hedenquist and Lowenstern, 1994; Richards, 2003, 2011; Cooke et al., 2005). Recently, a number of porphyry-type deposits have been recognized that formed in post-subduction and collisional settings, such as the Qulong porphyry Cu-Mo and Jiama porphyry Cu-Mo-Au deposits in the Gangdese belt, Tibet (Hou et al., 2009, 2011; Yang et al., 2009; Li et al., 2011), the Grasberg Cu-Au deposit in Papua, Indonesia (Pollard et al., 2005; Cloos and Housh, 2008), the porphyry Cu systems in Yunan (Lu et al., 2013), and the Sar Cheshmeh porphyry Cu-Mo deposit in the Kerman porphyry belt, Central Iran (Hezarkhani, 2006; Shafiei et al., 2009; Haschke et al., 2010; Aminzadeh et al., 2011). These deposits are almost indistinguishable from normal arc porphyry deposits in magmatic association, mineralization style, alteration zoning, and metal endowment, but were generated several to tens of millions of years after subduction ceased. Their petrogenesis and tectonic controls are different, and several theories have been put forward to explain the origin of the generative magmas, including partial melting of subduction-modified lithosphere (Guo et al., 2007; Ahmadian et al., 2009; Richards, 2009; Shafiei et al., 2009; Haschke et al., 2010), slab melt-modified mantle (Gao et al., 2010), oceanic slab (Qu et al., 2004, 2007), or newly formed lower crust (Hou et al., 2009, 2011). Geochemical study of igneous rocks associated with such deposits, together with tectonic and structural studies, can be used to constrain metallogenic processes, therefore improve exploration criteria in collisional terrains previously thought to be unprospective.

The India-Asia continent–continent collisional orogen provides a unique opportunity to study the relationship between collisional tectonism, magmatism, and post-subduction porphyry deposits. The India-Asia collision started at ~55–50 Ma (Allègre et al., 1984; Burg and Chen, 1984; Rowley, 1996; de Sigoyer et al., 2000; Meng et al., 2012), and was accompanied by voluminous but largely barren Paleocene–Eocene magmatism in southern Tibet (Wen, 2007; Mo et al., 2008; Chung et al., 2009). These magmatic rocks constitute a major part of the Gangdese magmatic belt, which extends for more than 1600 km E–W. Following this event, a large number

of small-volume calc-alkaline to mildly alkaline granitoids and potassic volcanic lava flows were intruded or erupted in the Gangdese belt between ~30 and 9 Ma, and constitute a 1600 km-long post-collisional magmatic belt (Turner et al., 1996; Miller et al., 1999; Chung et al., 2003, 2005; Ding et al., 2003; Hou et al., 2004; Williams et al., 2004; Gao et al., 2007; Zhao et al., 2009; Zheng et al., 2012a, b; Guo et al., 2013; Wang et al., 2014a, b, c). The Oligo-Miocene igneous rocks in the Gangdese belt show a sharp longitudinal distinction in petrography, magmatic geochemistry, and association with porphyry-type mineralization, with a boundary at ~89°E. The eastern Gangdese group (longitude ~89°–94° E) is characterized mainly by intermediate–felsic calc-alkaline plutons (which are locally associated with porphyry Cu-Mo±Au deposits), and minor potassic volcanic rocks. These magmas are characterized by high Sr/Y and La/Yb ratios (Chung et al., 2003; Hou et al., 2004, 2009; Li et al., 2013; Wang et al., 2014a, b). In contrast, the western Gangdese group (longitude ~80°–89° E) is characterized mainly by potassic volcanic rocks with minor granitoid plutons, which are mostly barren. These magmas have high Th and K_2O contents, and low Sr/Y ratios (Miller et al., 1999; Williams et al., 2004; Chung et al., 2013; Wang et al., 2014a). Many of these igneous rocks were emplaced along north–south-trending normal faults and grabens generated by east–west extension between 19 and 4 Ma (Armijo et al. 1986; Burchfiel et al. 1991; Blisniuk et al. 2001; Williams et al. 2001; Mitsuishi et al. 2012). Most of the granitoids located in the eastern part of the Gangdese belt (between 89°E and 94°E) are associated with porphyry Cu-Mo±Au mineralization (Hou et al. 2011). The largest deposits formed in the eastern Miocene Gagndese belt, and include the giant Qulong porphyry Cu-Mo deposit (16.4 ± 0.5 Ma; 1,420 Mt @ 0.5% Cu; Yang et al. 2009), the giant Jiama porphyry Cu-Mo-Au deposit (14.8 ± 0.33 Ma; 1,054 Mt @ 0.44% Cu; Ying et al., 2014), and several large- to medium-sized porphyry Cu-Mo deposits such as Bangpu, Tangbula, Lakang'e, Chongjiang, Tinggong, and weakly mineralized stocks. In contrast, there are only one small-sized porphyry Cu deposit and few porphyry- or epithermal type mineralization to the west of ~89°E (Zheng et al., 2007). Thus, significant porphyry Cu-Mo±Au mineralization is restricted both in space (east of 89°E) and time (Oligo-Miocene) in the Gangdese belt.

We approach a resolution to these temporal and spatial differences in metallogeny in the India-Asia collisional orogen by synthesizing new and existing geochronological and geochemical data with models of tectonic evolution, and conclude that the controls on magma fertility reflect fundamental changes in tectonomagmatic processes.

1.2 Rationale and objectives

The main objectives of this thesis, which is based on mineralogical, geochemical, and tectonic studies on the Cenozoic magmatism in the Gangdese belt to discuss the tectonomagmatic controls on the formation of porphyry Cu-Mo±Au deposits, southern Tibet, are as follows:

1.2.1 Control of magmatic water content on formation of porphyry Cu-Mo±Au deposits in the Gangdese belt (Chapter 2)

Magmatic water content is a key for the formation of magmatic–hydrothermal deposits. Based on geochemical and mineralogical characteristics, we have shown that the ore-bearing Miocene magmas in the eastern Gangdese belt, Tibet, were more hydrous and fractionated significant amounts of hornblende and lesser plagioclase than earlier Paleogene magmas prior to upper crustal emplacement. These hydrous magmas remobilized metals residual in the deep lithosphere from previous arc magmatism, giving rise to a suite of post-subduction porphyry-type ore deposits.

Published as: Wang, R., Richards, J.P., Hou, Z.Q., Yang, Z.M., and DuFrane, S.A., 2014, Increased magmatic water content–the key to Oligo-Miocene porphyry Cu–Mo ± Au formation in the eastern Gangdese belt, Tibet: Economic Geology, in press.

1.2.2 Control of magmatic redox on formation of porphyry Cu-Mo±Au deposits in the Gangdese belt (Chapter 3)

Magmatic redox state plays an important role in the speciation and solubility of sulfur in silicate melts, which in turn influences the solubility of chalcophile (such as Cu) and siderophile (such as Au) elements. With application of multiple oxygen barometers, we have shown that the high oxidation states of Miocene igneous rocks from the eastern Gangdese belt explain their unique association with large porphyry Cu–Mo deposits in Tibet.

Published as: Wang, R., Richards, J.P., Hou, Z.Q., Yang, Z.M., Gou, Z.B., and DuFrane, S.A., 2014, Increasing magmatic oxidation state from Paleocene to Miocene in the eastern Tibetan

Gangdese belt: Implication for collision-related porphyry Cu–Mo±Au mineralization: Economic Geology, in press.

1.2.3 Tectonomagmatic control on porphyry Cu-Mo±Au deposit distribution in the Gangdese belt (Chapter 4)

By investigating Miocene igneous rocks in 1600 km-long belt, we firstly propose that the sharp longitudinal distinction between magmatism and metallogenic potential in the Miocene Gangdese belt reflects the breakoff of the Greater India slab and the extent of underthrusting by the Indian continental lithosphere at that time. Magmas to the east of ~89°E were derived by partial melting of subduction-modified Tibetan lithosphere (mostly lower crust) triggered by heating of hot asthenospheric melt following slab breakoff. These magmas remobilized metals and volatiles residual in the crustal roots from prior arc magmatism, and generated porphyry Cu-Mo±Au deposits upon emplacement in the upper crust. In contrast, magmas to the west of ~89°E were formed by smaller volume partial melting of Tibetan lithospheric mantle metasomatized by fluids and melts released from the underthrust Indian plate, are less hydrous and reduced, and did not have the capacity to remobilize and transport significant amounts of metals into the upper crust.

Published as: Wang, R., Richards, J.P., Hou, Z.Q., and Yang, Z.M., 2014, Extent of underthrusting of the Indian plate beneath Tibet controlled the distribution of Miocene porphyry Cu–Mo ± Au deposits: Mineralium Deposita, v. 49, p. 165–173. DOI 10.1007/s00126-013-0507-y.

1.2.4 Role of mantle and crust on formation of porphyry Cu-Mo±Au deposits in the Gangdese belt (Chapter 5)

By combining our new data with published lithogeochemical and multiple isotopic (Os-Nd-O) analyses, we show that differential involvement of Indian plate lithosphere, subduction-modified Tibetan lithosphere, and asthenospheric melts leads to the observed spatially and temporally restricted distribution of magmatism and mineralization in the Miocene Gangdese belt

Submitted as: Wang, R., Richards, J.P., Zhou, L.M., Hou, Z.Q., Yang, Z.M., Muehlenbachs, K., Stern, R.A., Creaser, R.A., Zhu, J.J., and Li, J.X., 2014, The role of Indian and Tibetan lithosphere in spatial distribution of Cenozoic magmatism and porphyry Cu-Mo±Au deposits in the Gangdese belt, southern Tibet: Journal of Petrology.

1.3 References

Allégre, C.J., Courtillot, V., Taponnier, P., Hirn, A., Mattauer, M., Coulon, C., Jaeger, J. J., Achache, J., Schärer, U., Marcoux, J., Burg, J. P., Girardeau, J., Armijo, R., Gaiety, C., Göpel, C., Li, T., Xiao, X., Chang, C., Li, G., Lin, B., T, J., Wang, N., Chen, G., Han, T., Wang, X., Den, W., Sheng, H., Gao, Y., Zhou, J., Qiu, H., Bao, P., Wang, S., Wang, B., Zhou, Y., and Xu, R., 1984, Structure and evolution of the Himalayan-Tibet orogenic belt: Nature, v. 307, p.17–22.

Armijo, R., Tapponnier, P., Mercier, J.L., and Han, T.L., 1986, Quaternary extension in southern Tibet: Field observations and tectonic implications: Journal of Geophysics Research, v. 9, p. 13,803–13,872.

Aminzadeh, B., Shahabpour, J., and Maghami, M., 2011, Variation of Rhenium contents in molybdenites from the Sar Cheshmeh porphyry Cu-Mo deposit in Iran: Resource Geology, v. 61, p. 290–295.

Blisniuk, P.M., Hacker, B.R., Glodny, J., Ratschbacher, L., Bi, S.W., Wu, Z.H., McWilliams, M.O., and Calvert, A., 2001, Normal faulting in central Tibet since at least 13.5 Myr ago: Nature, v. 412, p. 628–632.

Burchfiel, B.C., Chen, Z., Royden, L.H., Liu, Y., and Deng, C., 1991, Extensional development of Gabo valley, southern Tibet: Tectonophysics, v. 194, p. 187–193.

Burg, J.P., and Chen, G.M., 1984, Tectonics and structural formation of southern Tibet, China: Nature, v. 11, p. 219–223.

Burnham, C.W., 1979, Magmas and hydrothermal fluids, in Barnes, H.L., ed., Geochemistry of hydrothermal ore deposits, 2nd edition: New York, John Wiley and Sons, p. 71–136.

Chung, S.L., Liu, D., Ji, J.Q., Chu, M.F., Lee, H.Y., Wen, D.J., Lo, C.H., Lee, T.Y., Qian, Q., and Zhang, Q., 2003, Adakites from continental collision zones: melting of thickened lower crust beneath southern Tibet: Geology, v. 31, p. 1021–1024.

Chung, S.L., Liu, D., Ji, J.Q., Chu, M.F., Lee, H.Y., Wen, D.J., Lo, C.H., Lee, T.Y., Qian, Q.,

and Zhang, Q., 2003, Adakites from continental collision zones: melting of thickened lower crust beneath southern Tibet: Geology, v. 31, p. 1021–1024.

Gao, Y.F., Yang, Z.S., Santosh, M., Hou, Z.Q., Wei, R.H., and Tian, S.H., 2010, Adakitic rocks from slab melt-modified mantle sources in the continental collision zone of southern Tibet: Lithos, v. 119, p. 651–663.

Cloos, M., and Housh, T.B., 2008, Collisional delamination: Implications for porphyry-type Cu–Au ore formation in New Guinea: Arizona Geological Society Digest, v. 22, p. 277–293.

Cooke, D.R., Hollings, P., and Walshe, J.L., 2005, Giant porphyry deposits: characteristics, distribution, and tectonic controls: Economic Geology, v. 100, p. 801–818.

Ding, L., Kapp. P., Zhong, D., and Deng, W., 2003, Cenozoic volcanism in Tibet: Evidence for a transition from oceanic to continental subduction: Journal of Petrology, v. 44, p. 1833–1865.

de Sigoyer, J., Chavagnac, V., Blichert-Toft, J., Villa, I.M., Luais, B., Guillot, S., Cosca, M., and Mascle, G., 2000, Dating the Indian continental subduction and collision thickening in the northwest Himalaya: Multichronology of the Tso Morari eclogites: Geology, v. 28, p. 487–490.

Guo, Z.F., Wilson, M., and Liu, J.Q., 2007, Post-collisional adakites in south Tibet: products of partial melting of subduction-modified lower crust: Lithos: v. 96, p. 205–224.

Guo, Z.F., Wilson, M., Zhang, M.L., Cheng, Z.H., and Zhang, L.H., 2013, Post-collisional, K-rich mafic magmatism in south Tibet: constraints on Indian slab-to-wedge transport processes and plateau uplift: Contributions to Mineralogy and Petrolgy, v. 165, p. 1311–1340.

Haschke, M., Ahmadian, J., Murata, M., and McDonald, I., 2010, Copper mineralization prevented by arc-root delamination during Alpine–Himalayan collision in central Iran: Economic Geology, v. 105, p. 855–865.

Hedenquist, J.W., and Lowenstern, J.B., 1994. The role of magmas in the formation of hydrothermal ore deposits: Nature, v. 370, p. 519–527.

Hezarkhani, A., 2006, Hydrothermal evolution of the Sar-Cheshmah porphyry Cu-Mo deposit, Iran: Evidence from fluid inclusions: Journal of Asian Earth Sciences, v. 28, p. 409–422.

Hou, Z.Q., Yang, Z.M., Qu, X.M., Meng, X.J., Li, Z.Q., Beaudoin, G., Rui, Z.Y., Gao, Y.F., and Zaw, K., 2009, The Miocene Gangdese porphyry copper belt generated during post-collisional extension in the Tibetan Orogen: Ore Geology Reviews, v. 36, p. 25–31.

Hou, Z.Q., Zhang, H.R., Pan, X.F., and Yang, Z.M., 2011, Porphyry Cu (-Mo-Au) deposits

related to melting of thickened mafic lower crust: Examples from the eastern Tethyan metallogenic domain: Ore Geology Review, v. 39, p. 21–45.

Li, J.X., Qin, K.Z., Li, G.M., Xiao, B., Chen, L., and Zhao, J.X., 2011, Post-collisional ore-bearing adakitic porphyries from Gangdese porphyry copper belt, southern Tibet: Melting of thickened juvenile arc lower crust: Lithos, v. 126, p. 264–277.

Lu, Y.J., Kerrich, R., Kemp, A.I.S., McCuaig, T.C., Hou, Z.Q., Hart, C.J.R., Bagas, L.,Yang, Z.M., Cliff, J., Belousova, E.A., Jourdan, F., and Evans, N.J., 2013, Intracontinental Eocene-Oligocene porphyry Cu mineral systems of Yunnan, western Yangtze Craton, China: Compositional characteristics, sources, and implications for continental collision metallogeny: Economic Geology, v. 108, p. 1541–1576

Meng, J., Wang, C., Zhao, X., Coe, R., Li, Y.L., and Finn, D., 2012, India-Asia collision was at 24° N and 50 Ma: Paleomagnetic proof from southern Asia: Scientific Reports, 2, 925; doi: 10.1038/srep00925.

Miller, C., Schuster, R., Klotzli, U., Frank, W., and Purtscheller, F., 1999, Post-collisional potassic and ultrapotassic magmatism in SW Tibet: geochemical and Sr–Nd–Pb–O isotopic constraints for mantle source characteristics and petrogenesis: Journal of Petrology, v. 40, p. 1399–1424.

Mitsuishi, M., Wallis, S.R., Aoya, M., Lee, J., and Wang, Y., 2012, E-W extension at 19 Ma in the Kung Co area, S, Tibet: Evidence for contemporaneous E-W and N-S extension in the Himalayan orogen: Earth and Planetary Science Letters, v. 325–326, p. 10–20.

Mo, X.X., Niu, Y.L., Dong, G.C., Zhao, Z.D., Hou, Z.Q., Zhou, S., and Ke, S., 2008, Contribution of syncollisional felsic magmatism to continental crust growth: A case study of the Paleogene Linzizong volcanic succession in southern Tibet: Chemical Geology, v. 250, p. 49–67.

Pollard, P.J., Taylor, R.G., and Peters, L., 2005, Ages of intrusion, alteration, and mineralization at the Grasberg Cu–Au deposit, Papua, Indonesia: Economic Geology, v. 100, p. 1005–1020.

Qu, X., Hou, Z., and Li, Y., 2004, Melt components derived from a subducted slab in late orogenic ore-bearing porphyries in the Gangdese copper belt, southern Tibetan Plateau: Lithos, v. 74, p. 131–148.

Qu, X., Hou, Z., Khin Zaw, and Li, Y., 2007, Characteristics and genesis of Gangdese porphyry copper deposits in the southern Tibetan Plateau: preliminary geochemical and

geochronological results: Ore Geology Reviews, v. 31, p. 205–223.

Richards, J.P., 2003, Tectono-magmatic precursors for porphyry Cu-(Mo-Au) deposit formation: Economic Geology, v. 98, p. 1515−1533.

Richards, J.P., 2009, Postsubduction porphyry Cu–Au and epithermal Au deposits: products of remelting of subduction-modified lithosphere: Geology, v.37, p. 247–250.

Rowley, D.B., 1996, Age of initiation of collision between India and Asia: a review of stratigraphic data: Earth and Planetary Science Letters, v. 145, p. 1–13

Shafiei, B., Haschke, M., and Shahabpour, J., 2009, Recycling of orogenic arc crust triggers porphyry Cu mineralization in Kerman Cenozoic arc rocks, southeastern Iran: Mineralium Deposita, v. 44, 265–283.

Sillitoe, R.H., 1972, A plate tectonic model for the origin of porphyry copper deposits: Economic Geology, v. 67, p. 184−197.

Sillitoe, R.H., 2010, Porphyry copper system: Economic Geology, v. 105, p. 3−41.

Turner, S., Arnaud, N., Liu, J., Rogers, N., Hawkesworth, C., Harris, N., and Kelley, S., 1996, Post-collision, shoshonitic volcanism on the Tibetan Plateau: Implications for convective thinning of the lithosphere and the source of ocean island basalts: Journal of Petrology, v. 37, p. 45–71.

Wang, R., Richards, J.P., Hou, Z.Q., and Yang, Z.M., 2014a, Extent of underthrusting of the Indian plate beneath Tibet controlled the distribution of Miocene porphyry Cu–Mo ± Au deposits: Mineralium Deposita, v. 49, p. 165–173. DOI 10.1007/s00126-013-0507-y.

Wang, R., Richards, J.P., Hou, Z.Q., Yang, Z.M., DuFrane, S.A., 2014b, Increased magmatic water content–the key to Oligo-Miocene porphyry Cu–Mo ± Au formation in the eastern Gangdese belt, Tibet: Economic Geology, in press.

Wang, R., Richards, J.P., Hou, Z.Q., Yang, Z.M., Gou, Z.B., and DuFrane, S.A., 2014c, Increasing magmatic oxidation state from Paleocene to Miocene in the eastern Tibetan Gangdese belt: Implication for collision-related porphyry Cu–Mo±Au mineralization: Economic Geology, in press.

Wen, D.R., 2007, The Gangdese batholith, Southern Tibet: Ages, geochemical characteristics and petrogenesis: Unpublished Ph.D. Thesis, National Taiwan University, 120 p.

Williams, H.M., Turner, S.P., Pearce, J.A., Kelley, S.P., and Harris, N.B.W., 2004, Nature of the source regions for post-collisional, potassic magmatism in southern and northern Tibet from

geochemical variations and inverse trace element modeling: Journal of Petrology, v. 45, p. 555–607.

Yang, Z.M., Hou, Z.Q., White, N.C., Chang, Z.S., Li, Z.Q., and Song, Y.C., 2009, Geology of the post-collisional porphyry copper-molybdenum deposit at Qulong, Tibet: Ore Geology Reviews, v. 36, p. 133–159.

Ying, L.J., Wang, C.S., Tang, J.X., Wang, D.H., Qu, W.J., and Li, C., 2014, Re-Os systematics of sulfides (chalcopyrite, bornite, pyrite and pyrrhotite) from the Jima Cu-Mo deposit of Tibet, China: Journal of Asian Earth Sciences, v. 79, p. 497–506.

Chapter 2
Increased magmatic water content — the key to Oligo-Miocene porphyry Cu-Mo±Au formation in the eastern Gangdese belt, Tibet[1]

2.1 Introduction

The India-Asia continent–continent collisional orogen provides a unique opportunity to study the relationship between collisional tectonism, magmatism, and metallogenesis. The India-Asia collision started at ~55–50 Ma (Allègre et al., 1984; Burg and Chen, 1984; Rowley, 1996; de Sigoyer et al., 2000; Meng et al., 2012), and was accompanied by voluminous but largely barren Paleocene–Eocene magmatism in southern Tibet (Mo et al., 2005; Wen, 2007; Chung et al., 2009). These magmatic rocks constitute part of the Gangdese magmatic belt, which extends for more than 1600 km E–W (Fig. 2-1). Numerous small-volume plugs, dikes, and sills, locally associated with porphyry Cu-Mo±Au deposits, were emplaced during later tectonomagmatic events in the Oligo-Miocene (~30 to 9 Ma; Harrison et al., 2000; Chung et al., 2003; Hou et al., 2004; Guo et al., 2007; Gao et al., 2010; Zheng et al., 2012a,b). This paper seeks to explain the change in fertility of collision-related magmas in the Gangdese belt from the Paleocene–Eocene to the Oligo-Miocene. Two possibilities are considered: firstly, that originally abundant porphyry deposits in Paleocene–Eocene igneous rocks have been eroded away; or secondly that the difference reflects fundamental changes in the style of magmatism, including magma source, geochemistry, and water content.

We approach a resolution to these temporal and spatial differences in metallogeny in the India-Asia collisional orogen by synthesizing new and existing geochronological and geochemical data with models of tectonic evolution, and conclude that the controls on magma fertility reflect fundamental changes in tectonomagmatic processes.

2.2 Geological setting

Tectonic framework

The Himalayan-Tibetan orogen features several micro-continents, flysch complexes, and island arcs, which have been accreted to the southern margin of Asia since the Early Paleozoic

[1] This chapter was published as: Wang, R., Richards, J.P., Hou, Z.Q., Yang, Z.M., and DuFrane, S.A., 2014, Increased magmatic water content–the key to Oligo-Miocene porphyry Cu–Mo ± Au formation in the eastern Gangdese belt, Tibet: Economic Geology, in press.

(Fig. 2-1; Yin and Harrison, 2000, and references therein), culminating with collision between the Indian plate and the Asian accretionary margin along the Indus-Yarlung Zangbo suture in the early Eocene. The Tibetan plateau consists primarily of the Lhasa and Qiangtang terranes, and Songpan-Ganze complex, from south to north, separated from each other by the Bangong-Nujiang and Jinsha sutures (Fig. 2-1). The western Qiangtang terrane is thought to have originated from Gondwana (Metcalfe, 2009), whereas the eastern Qiangtang terrane was derived from the Yangtze craton (Pan et al., 2004). They were accreted to the Lhasa terrane in the Late Jurassic–Early Cretaceous along Bangong-Nujiang suture (Kapp et al., 2005). The Songpan-Ganzi complex is situated at the junction of the North China block, the Eastern Kunlun-Qaidam block, the South China block (including the Yangtze and the Cathaysia blocks), and the Qiangtang block. This complex is like a giant 'suture knot' and comprises huge thicknesses of accretionary complex rocks and volcanic arc rocks (Yin and Harrison, 2000; Enkelmann et al., 2007). There is only one large porphyry Cu-Au deposit located in the Qiangtang terrane (Duobuza porphyry Cu-Au deposit). No large porphyry deposits have been reported from the Songpan-Ganze complex.

The Lhasa terrane is divided into the northern Lhasa subterrane, central Lhasa subterrane, and southern Lhasa subterrane, which are bounded by Shiquan River–Nam Tso Mélange zone and Luobadui–Milashan fault, respectively (Fig. 2; Pan et al., 2004). The central Lhasa subterrane is a microcontinent fragment, which separated from Gondwana in the Late Devonian, and has ancient basement rocks of Proterozoic and Archean ages (Allègre et al., 1984; Dewey et al., 1988, Sengör, 1988; Zhu et al., 2011). Younger (Phanerozoic) crust with positive Hf and Nd isotope compositions was accreted to the margins of the central Lhasa subterrane to form the northern Lhasa and southern Lhasa subterranes (Zhang et al., 2007; Zhu et al., 2011, 2013).

Soft collision: Greater India (the Indian continental margin; Ali and Aitchison, 2005) first collided with the southern Lhasa subterrane at ~55–50 Ma, marking the beginning of the India–Asia collision ("soft collision": van Hinsbergen et al., 2012; Meng et al., 2012). Ridge push from the Indian ocean and slab-pull from the subducting Neo-Tethyan plate caused the Greater Indian plate's lower crust and sub-continental lithospheric mantle to be subducted beneath southern Tibet, while the upper crust was scraped off and accreted to the orogenic margin (Capitanio et al., 2010). The Neo-Tethyan oceanic slab detached from Greater India at ~45 Ma, and is today

observed as a continuous NW–SE- trending high-velocity anomaly at depths between 1100 km and 2300 km beneath India (Van der Voo et al., 1999).

Hard collision: At ~35 Ma, the thicker, more rigid and buoyant Indian craton first contacted and began to underthrust the Asian margin ("hard collision": Replumaz et al., 2010; van Hinsbergen et al., 2012). The Greater India slab detached from the Indian plate diachronously from west (at ~25 ± 5 Ma) to east (at ~10 ± 5 Ma; Van der Voo et al., 1999; Replumaz et al., 2010). The development of Miocene N–S normal faulting in central Tibet marks a change of regional stress from N–S compression to E–W extension, which began at ~19 Ma (Mitsuishi et al., 2012).

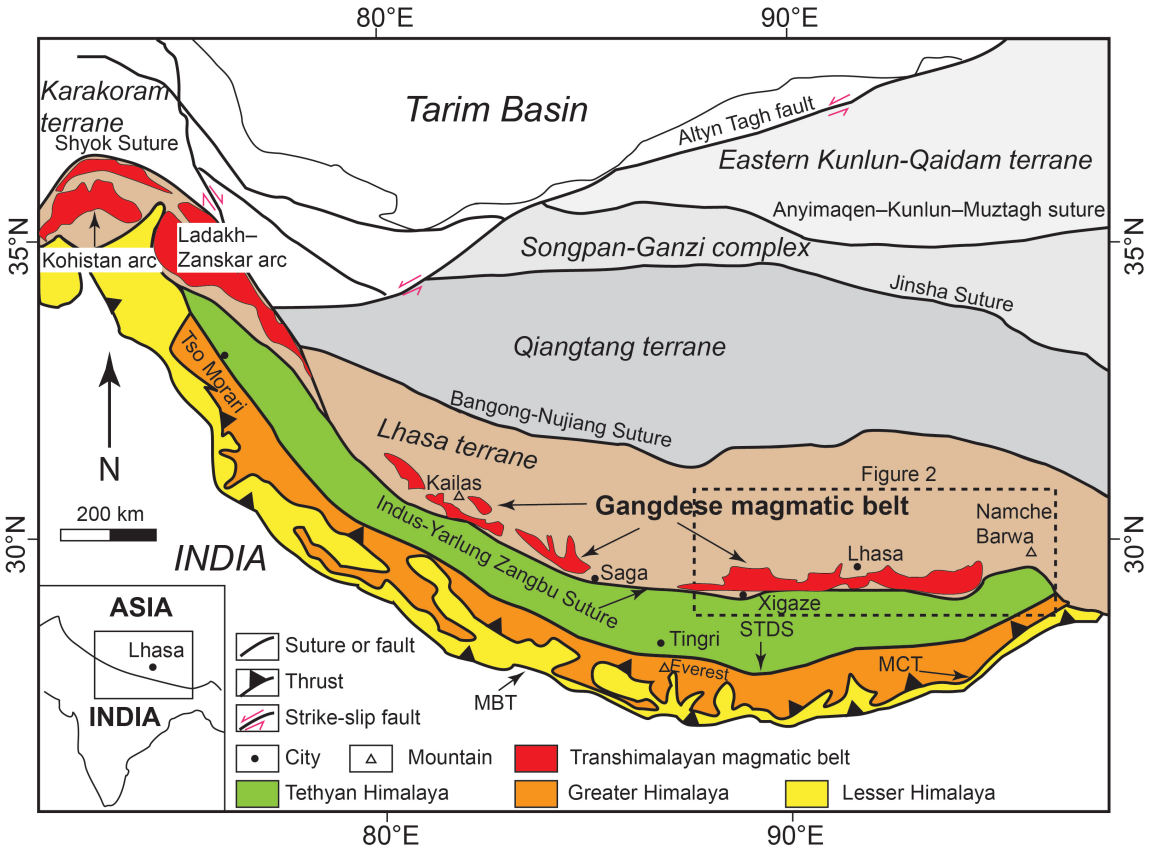

Fig. 2-1. Map indicating major tectonic units and boundaries within the Tibet-Qinghai Plateau (modified from Aitchison et al., 2007; White et al., 2011). Abbreviations: MBT Main Boundary thrust; MCT, Main Central thrust; STDS, South Tibet detachment system.

Mesozoic–Cenozoic Magmatism

Arc magmatism: Northward-directed Neo-Tethyan subduction beneath southern Tibet began in the Late Triassic–Early Jurassic (Chu et al., 2006), and produced voluminous Cretaceous calc-

alkaline magmatism in the Lhasa terrane (Fig. 2-2; Harris et al., 1986; Wen, 2007; Mo et al., 2008). This Andean-style continental subduction was coeval with normal arc magmatism in the main Gangdese belt, and back-arc rifting in the northern magmatic belt (central Lhasa subterrane and northern Lhasa subterrane), characterized by extensive marine transgression strata, normal faulting, and bimodal volcanic rocks (Zhang et al., 2004; Baxter et al., 2009). A series of back-arc basins formed in the Kohistan and Ladakh–Zanskar arc belts of the southern Asian margin (Fig. 2-1; Khan et al., 1996; Treloar et al., 1996; Rolland et al., 2000).

Onset of soft collision: Between ~69 and 53 Ma, the India–Asia convergence rate increased from ~12 cm/yr to ~17 cm/yr, then dropped back to ~10 cm/yr (Lee and Lawyer, 1995). During this time, Gangdese arc magmatism shifted southward from ~30.5°N to ~29.5°N, which suggests rollback of the subducted Neo-Tethyan slab (Kapp et al., 2007). This rollback triggered a magmatic flare-up (Wen, 2007), represented by extensive Paleocene–Eocene I-type intrusive rocks and widespread Linzizong volcanic successions (Fig. 2-2). Intrusive rocks range from gabbro to granite, with diorite and granodiorite being the most common. For example, the Quxu complex (51–47 Ma; Mo et al., 2005; Fig. 2-2) mainly consists of granodiorite, monzogranite, and granite, with subordinate gabbro and pyroxenite (Dong et al., 2006a; Chen et al., 2011). The coeval Linzizong volcanic successions extend in an E–W belt up to 1600 km long, and consist of calc-alkaline andesitic lava flows, tuffs, and breccias, and dacitic to rhyolitic ignimbrites (Coulon et al., 1986; Mo et al., 2005). The sequence reaches a maximum thickness of ~5 km in the Linzhou basin near Lhasa (Pan et al., 2004; Mo et al., 2008) where it is subdivided into the Dianzhong, Nianbo, and Pana Formations (Dong, 2002).

Breakoff of the Neo-Tethyan slab: Slab breakoff generated a series of picritic to basaltic–andesitic rocks that were erupted in the Dazi basin at ~40–38 Ma (Gao et al., 2008). These rocks are characterized by low-K tholeiitic compositions, high MgO (6.3–14.4 wt.%), Cr (131–844 ppm), and Ni (45.2–268 ppm) concentrations, high εNd(t) values (+5.2 to +3.6), and unradiogenic $(^{87}Sr/^{86}Sr)_i$ ratios (0.7043–0.7061).

Hard collision: Hard collision of the Indian craton with the Asian margin at ~35 Ma generated a large number of small-volume calc-alkaline and mildly alkaline granitoid intrusions and potassic and ultrapotassic volcanic rocks that were emplaced or erupted in the Lhasa terrane during the Oligo-Miocene (~30–9 Ma; Chung et al., 2005). Most of the Oligo-Miocene granitoids were emplaced along north–south normal faults and grabens between 19 and 4 Ma (Hou et al.,

2004; Mitsuishi et al., 2012; Zheng et al., 2012a,b). The origin of these granitoids in the eastern Gangdese belt has been the focus of debate in part due to their high Sr/Y and La/Yb ratios, which overlap the range of adakitic rocks. They are also of economic interest because of their common association with porphyry-type deposits. Suggested petrogenetic models have included partial melting of a subducted oceanic slab (Qu et al., 2004, 2007), partial melting of slab melt-modified mantle sources (Gao et al., 2007, 2010), and partial melting of lower crust (Chung et al., 2003; Hou et al., 2004; Guo et al., 2007; Li et al., 2011).

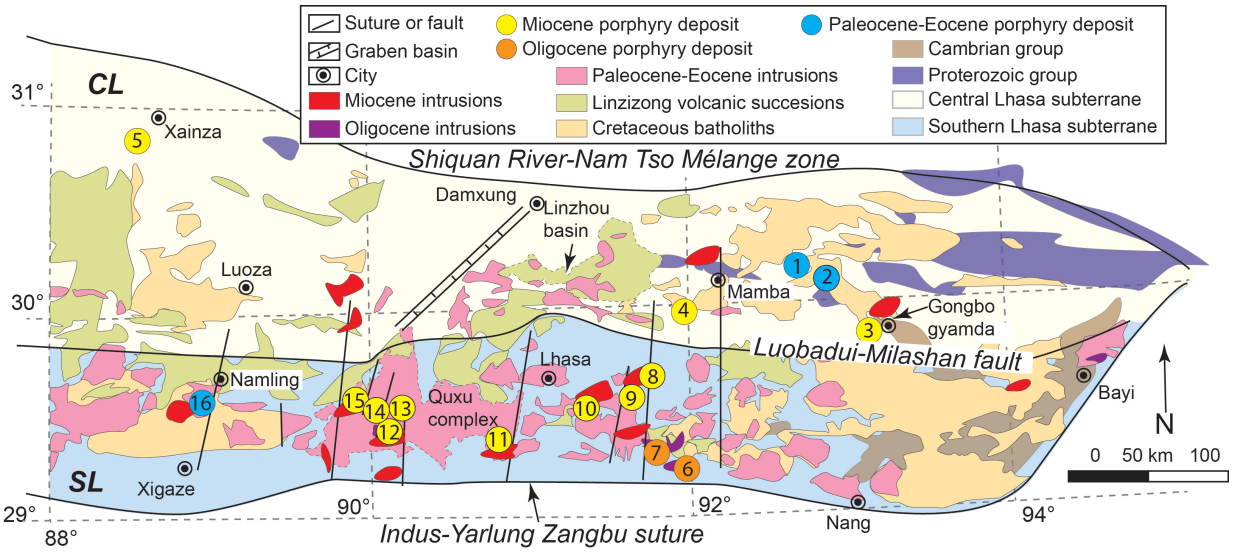

Fig. 2-2. Geology of the eastern Gangdese magmatic belt in the Lhasa terrane (modified from Zhu et al., 2011, 2013). Abbreviations: CL, central Lhasa subterrane; SL, southern Lhasa subterrane. Porphyry deposits (age): 1. Yaguila (Paleocene), 2. Sharang (Eocene), 3. Tangbula (Miocene), 4. Bangpu (Miocene), 5. Lingang (Miocene), 6. Zedang (Oligocene), 7. Nuri (Oligocene), 8. Jiama (Miocene), 9. Qulong (Miocene), 10. Lakang'e (Miocene), 11. Nanmu (Miocene), 12. Gangjiang (Miocene), 13. Chongjiang (Miocene), 14. Tingong (Miocene), 15. Bairong (Miocene), 16. Jiru (Eocene).

Porphyry Cu-Mo±Au deposits in the Gangdese belt

Three episodes of porphyry-type mineralization are associated with collision-related magmatism in the Lhasa terrane (Fig. 2-2), increasing in frequency and size from the Paleocene–Eocene to the Miocene. Only three small deposits are known to have formed in the Paleocene–Eocene: the Yaguila Pb-Zn vein type deposit (62.4 ± 0.6 Ma) with porphyry Mo mineralization (Huang et al., 2012), the Sharang porphyry Mo deposit (52.25 ± 0.31 Ma; 10 Mt @ 0.061% Mo; Zhao et al., 2011a), and the Jiru porphyry Cu deposit (49.2 ± 1.7 Ma; 41.9 Mt @ 0.43 Cu; Zhang

et al., 2008; Zheng et al., 2013). Several deposits formed in the Oligocene, such as the Nuri porphyry and skarn Cu deposit (23.36 ± 0.49 Ma; 79.4 Mt @ 0.73% Cu; Chen et al., 2011, 2012; Zhang et al., 2012) and medium- to small-sized porphyry and skarn Cu-Mo-W deposits such as Mingze, Liebu, Chongmuda, and Kelu. The largest deposits formed in the Miocene, and include the giant Qulong porphyry Cu-Mo deposit (16.4 ± 0.5 Ma; 1,420 Mt @ 0.5% Cu; Yang et al., 2009), the giant Jiama porphyry Cu-Mo-Au deposit (14.8 ± 0.33 Ma; 255.6 Mt @ 1% Cu; personal communication with Jiama mining company), and several large- to medium-sized porphyry Cu-Mo deposits and weakly mineralized stocks (Hou et al., 2011; Fig. 2-2).

All porphyry deposits in the central Lhasa subterrane (e.g., the Sharang, Bangpu, Tangbula, and Jiagang porphyry deposits) are porphyry Mo±Cu type (Mo/Cu >1) associated with significant vein-type Pb-Zn-W mineralization, whereas all the deposits in the southern Lhasa subterrane are porphyry Cu-Mo±Au type (Mo/Cu < 1). This may be because the Mo-rich deposits in the central Lhasa subterrane are associated with high-K felsic plutons, whereas the Cu-rich deposits in the southern Lhasa subterrane are associated with more typical intermediate-composition calc-alkaline plutons.

Preservation of porphyry deposits in the Gangdese belt

Uplift of the Tibetan plateau and consequent erosional loss during the protracted India–Asia collision might explain the scarcity of porphyry deposits in Mesozoic and Paleogene sequences (McInnes et al., 2005). However, while this explanation might apply to the Mesozoic rocks, we discount this possibility in the Paleogene for several reasons.

The Jurassic and Cretaceous magmatic rocks underwent severe exhumation (> 6 km) and deformation (He et al., 2007; Mo et al., 2008). This means that most porphyry deposits of this age have been completely eroded, with only a few such as the Xietongmen porphyry Cu-Au deposit surviving (Tafti et al., 2011).

Various mineralogical and petrologic studies have indicated that many-exposed Paleocene–Eocene granitoids were emplaced at shallow depths, and should therefore preserve porphyry systems if they existed. Of the 16 Paleocene–Eocene intrusive rocks collected for this study, seven of them had porphyritic textures indicative of relatively shallow emplacement (Fig. 2-3A, B; Buddington, 1959; Dilles, 1987). There are also several reports in the literature of shallowly emplaced porphyritic Paleocene–Eocene granitoids from the Nimu (Du et al., 2012), Jiru (Zheng

et al., 2013), Sharang (Zhao et al., 2011a), and Jiagang districts (Ge et al., 2006). The small Jiru porphyry deposit preserves a series of shallow-level alteration zones from K-silicate through quartz–sericite, to an outer propylitic zone (Zheng et al., 2013). The small Sharang porphyry deposit also preserves hydrothermal breccias, and argillic and phyllic alteration (Zhao et al., 2011a). Together, this evidence suggests that erosion has not destroyed evidence of Paleocene–Eocene porphyry deposits, but that they were simply rare and small.

Recently published biotite and K-feldspar $^{40}Ar/^{39}Ar$, apatite fission track, and apatite (U-Th/He) thermochronologic data from the Lhasa terrane indicate that rapid cooling and exhumation occurred from ~85 to 55 Ma. This was followed by a rapid decline in the exhumation rate, from 0.3 mm/yr to 0.01 mm/yr between ~55 and 48 Ma, and <0.05 mm/yr after 45 Ma (Rohrmann et al., 2012). These low uplift rates are consistent with formation of a stable peneplain in Tibet with low catchment-wide erosion rate (Hetzel et al., 2011).

The typical exhumation depth for most of the Eocene igneous rocks in the Lhasa terrane is <2.5 km (van der Beek et al., 2009; Rohrmann et al., 2012), as indicated by widespread exposures of Linzizong volcanic rocks in the Lhasa terrane (65 Ma to 43 Ma), which cover ~30 % of the area of the Gangdese magmatic belt (BGMRXAR, 1993; Mo et al., 2008; Lee et al., 2011). In addition, the lack of detrital zircons of Linzizong volcanic successions age in Himalaya foreland basin strata (DeCelles et al., 2000, 2004) argues against significant exhumation and erosion of the Linzizong volcanic rocks.

We conclude that sufficient exposures of Paleogene volcanic and subvolcanic rocks occur in the Lhasa terrane to reveal porphyry deposits of this age if they existed, but the rare and small examples of such deposits that have been found suggest that such deposits were not formed in abundance at this time. Instead, a reason for their scarcity in the Paleogene must be sought in tectonomagmatic processes.

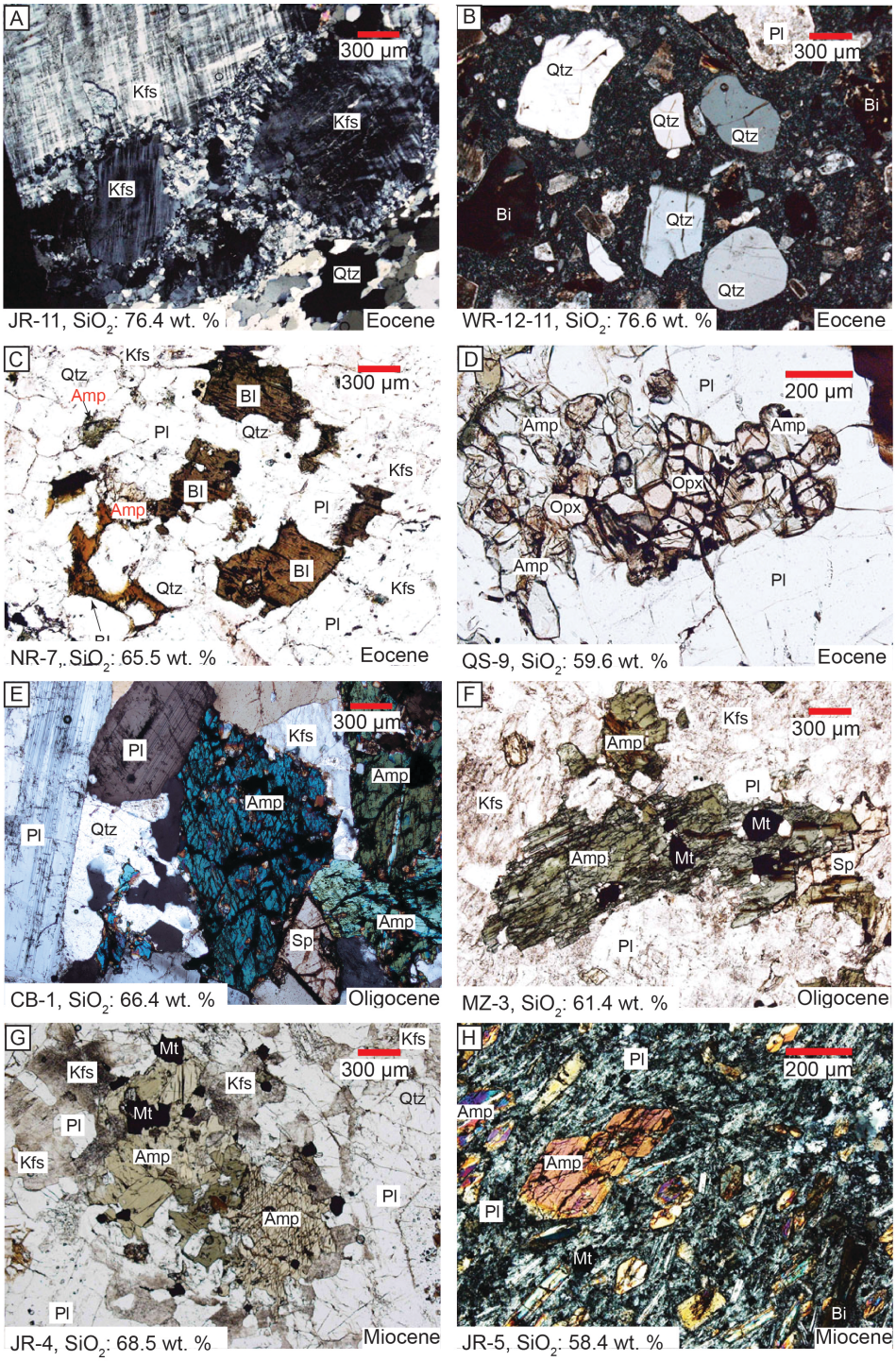

Fig. 2-3. Photomicrographs showing: A. Eocene granite porphyry (JR-11) with K-feldspar phenocryst, and quartz, cross-polarized light; B. Eocene granite porphyry (WR-12-11) with quartz and plagioclase phenocrysts and aphanitic groundmass, biotite is secondary; cross-polarized light; C. Eocene granodiorite (NR-7) with interstitial biotite and amphibole; plane-polarized light; D. Orthopyroxene altered by amphibole in Eocene diorite (QS-9); plane-polarized light; E. Oligocene quartz monzonite (CB-1), with amphibole, plagioclase, K-feldspar, and minor titanite; cross-polarized light; F. Oligocene quartz monzonite (MZ-3), with amphibole, K-

feldspar, plagioclase, and minor titanite; plane-polarized light; G. Miocene granodiorite porphyry (JR-4) with amphibole, K-feldspar, plagioclase, and magnetite; plane-polarized light; H. Miocene monzonite porphyry (JR-5), with abundant amphibole phenocrysts; cross-polarized light. Abbreviations: Amp = Amphibole; Bi = Biotite; Kfs = K-feldspar; Mt = Magnetite; Opx = Orthopyroxene; Pl = Plagioclase; Qtz = Quartz; Ttn = Titanite.

2.3 Sampling strategy

A large amount of lithogeochemical and geochronological data has been published on the Cenozoic igneous rocks in the eastern Gangdese belt (see Fig. 2-4 for sample locations). Because many sample locations in the eastern Gangdese belt are associated with porphyry-type alteration and mineralization, we excluded any samples with >2 wt.% LOI or which have been described as significantly altered. Fieldwork and sampling for this study were designed to complement these published data. Fresh or least-altered samples were collected in the field, and mafic end-members of igneous suites were prioritized in order to evaluate least-evolved compositions.

Paleocene–Eocene igneous rocks: Eleven samples were collected from the Namling, Gurong, Nuri, Zedang Bridge, Kangmaqie, and Riduo districts, and the Kangagang pluton (Fig. 2-4). No lithogeochemical analyses have previously been reported from these districts. Five samples of previously undated diorite porphyry from the Namling district (WR-12-21), Jiru deposit (JR-11), granite porphyry from the Gurong district (WR-12-11), gabbroic diorite from the Kangmaqie pluton (KMQ-12-2), and granodiorite sample from the Riduo district (RD-12-5) were selected for zircon U-Pb dating. The Quxu complex was studied extensively by Dong et al. (2006a, b). We collected five samples with known ages from the same rock unit in order to test its homogeneity.

Oligocene intrusions: Published studies of Oligocene igneous rocks are restricted to the Mingze-Chenba and Bayi districts (Zheng et al., 2012a, b). We collected additional samples of Oligocene rocks from the Qulin and Xueba districts for this study (Fig. 2-4), including one sample of granite from the Xueba district which was dated by zircon U-Pb (XB-12-3). Four samples of Oligocene intrusions with known ages were collected from the Mingze-Zedang area to test the homogeneity of the same rock units.

Miocene intrusions: Nearly all reported Miocene granitoids from the literature are located to the east of 89.5°E. In order to complement this dataset, we collected three samples (JR-2, JR-4, and JR-5) from the Jiru deposit to the west of 89.5°E, and used zircon U-Pb dating to constrain their emplacement ages (JR-2 and JR-5). In addition, one granite sample (WR-12-5) was collected from a pluton (21.3 ± 0.60: Ji et al., 2009) that intruded the Eocene Quxu complex,

where no lithogeochemical analyses had been generated by previous workers.

2.4 Petrography and mineralogy

Paleocene–Eocene sequence

The mafic–intermediate samples collected include gabbroic diorite and diorite. The gabbro has ~55–60 vol.% plagioclase (An = 70–77), 25–30 vol.% pyroxene (dominant augite and minor hypersthene), and minor interstitial biotite and amphibole (< 5 vol.%: Dong et al., 2006b). The intermediate–felsic samples collected include granodiorite, quartz monzonite, and granite, which are mainly composed of clinopyroxene, plagioclase, K-feldspar, and quartz, with minor clinopyroxene, orthopyroxene, amphibole and biotite. Nearly half of the samples from this study have porphyritic textures, with phaneritic or aphanitic groundmass (Fig. 2-3A, B). Amphibole occurs typically as interstitial grains (Fig. 2-3C) or as granular replacements of orthopyroxene (Fig. 2-3D), suggesting late-stage growth from residual melts. Paleocene–Eocene samples reported in the literature (Dong et al., 2006a, b; Wen, 2007) rarely contain hornblende phenocrysts, except for felsic igneous rocks. Together with evidence from our samples, this suggests that early hornblende crystallization did not occur in these magmas, indicating that they were relatively water-poor.

Oligocene sequence

The samples collected for this study include monzodiorite, quartz monzonite, granodiorite, and granite. Amphibole and biotite are common, and occur as phenocrysts or equigranular intergrowths with K-feldspar and plagioclase (Fig. 2-3E, F). Magnetite and titanite are common accessory minerals. Other samples of Oligocene igneous rocks described in the literature mainly consist of granodiorite and quartz monzonite porphyry with amphibole phenocrysts (Zhou et al., 2011; Zheng et al., 2012a, b).

Miocene sequence

The Miocene porphyry samples collected for this study have phenocrysts of plagioclase, K-feldspar, amphibole, and quartz (Fig. 2-3G, H). Other samples reported in the literature are mostly of ore-forming intrusive rocks from the Qulong, Jiama, Chongjiang, Nanmu, Lakang'e, Bairong, and Qiangdui porphyry Cu-Mo±Au deposits (Chung et al., 2003; Hou et al., 2004; Guo

et al., 2007; Yang, 2008; Xu et al, 2010; Li et al., 2011). They occur as shallowly-emplaced, small-volume plugs, dikes, or sills of porphyritic rock that intrude or crosscut earlier intrusive and coeval volcanic rocks. The dominant lithologies are quartz monzonite porphyry and granite porphyry, with subordinate granodiorite and monzonite. They mostly contain phenocrysts of plagioclase, quartz, sanidine, and amphibole (Chung et al., 2005; Hou et al., 2009). In addition to these intrusive rocks, four analyses of volcanic rocks from Maquiang (basaltic andesite, trachyte, and rhyolite) were included in the dataset (Turner et al., 1996).

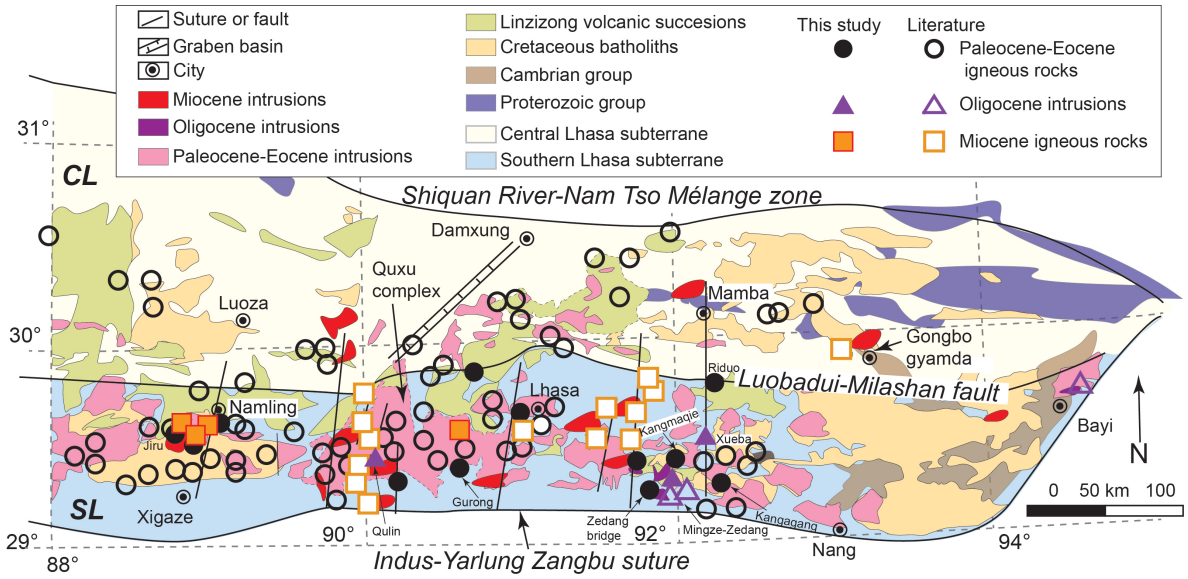

Fig. 2-4. Geology of the eastern Gangdese magmatic belt in the Lhasa terrane (modified from Zhu et al., 2011, 2013), showing locations of samples collected for this study and from the literature (Harrison et al., 2000; Chung et al., 2003; Hou et al., 2004; Chen et al. 2006; Dong et al., 2006a, b; Guo et al., 2007; Wen, 2007; Yang, 2008; Wang et al., 2010; Xia et al., 2010; Xu et al., 2010; Lee et al., 2011; Li et al., 2011; Tafti, 2011; Xiao, 2011; Zhao et al., 2011a, b; Zhu et al., 2011; Ji et al., 2012; Zheng et al., 2012a, b). Abbreviations: CL, central Lhasa subterrane; SL, southern Lhasa subterrane.

2.5 Analytical techniques

Zircon U-Pb dating

Zircons were separated from 2–3 kg samples by heavy-liquid and magnetic methods followed by hand-picking in the Laboratory of the Geological Team of Hebei Province, China. Selected crystals were euhedral, clear, colorless, devoid of mineral and fluid inclusions, and 100–250 μm in diameter, typical of magmatic zircons. The zircons were mounted in epoxy and polished to reveal their interiors.

Cathodoluminescence (CL), backscattered electron (BSE), and secondary electron (SE) images were obtained of the zircon grain mounts prior to analysis, to reveal internal zonations (see Fig. A1 in appendices). U-Pb age determinations were obtained using a multiple collector inductively coupled plasma-mass spectrometry (MC-ICP-MS: Nu Instruments, UK) coupled to a frequency quintupled (λ = 213 nm) Nd:YAG laser ablation system (New Wave Research, USA) at the Radiogenic Isotope Facility, University of Alberta, Canada. Laser ablation pits were approximately 40 μm wide and 15 μm deep. The MC-ICP-MS instrument was fitted with a modified collector block containing twelve Faraday collectors and three ion counting detectors dispersed on the low mass side of the array. The accuracy and precision of the analytical protocols employed during this study are demonstrated through the dating of well-studied, international zircon standards (GJ1 and LH9415). The 2σ reproducibility of the standards was typically one percent for $^{207}Pb/^{206}Pb$ and three percent for $^{206}Pb/^{238}U$. The zircon U-Pb dating results are listed in Table A1 and Figures 2-5, 6.

Lithogeochemcial analysis

Samples for lithogeochemical analysis were prepared by crushing (using corundum plates) and grinding in an agate disk mill at the Hebei Geological Survey Lab., China. The detailed procedures and evaluation of contamination are described by Li et al. (2010). All samples were analyzed by Activation Laboratories (Ancaster, Ontario, Canada) using a combination of methods including instrumental neutron activation analysis and fusion ICP-MS (Actlabs code 4E Research ICP/MS). Accuracy for major elements, as determined by reproducibility of lab standards and duplicates, is typically within 5 relative % (< 3 relative % for SiO_2 and Al_2O_3), and to within 10 relative % for minor and trace elements. The lithogeochemical results are listed in Table 2-2. All of the samples analyzed for this study are relatively fresh, and have low LOI contents (≤ 1.6 wt. %).

Table 2-1 Sample locations, ages, and description from Gangdese belt, Tibet

Sample	Location	Longitude	Latitude	Altitude (m)	Age (Ma)	Rock type (TAS)	Texture	Mineralogy and percentage (vol.% below)
JR-6	Jiru	88°53'18"	29°39'21"	4720	48.68 ± 0.49[1]	Grano-diorite	Equi-granular	~30% Qtz, ~25% Pl, ~15% Kfs, ~10% interstitial Amp, and 5% interstitial Bi
JR-11	Jiru	89°02'52"	29°36'33"	3962	36.33 ± 0.88[2]	Granite	Porphyritic	0.3-1.0 cm Kfs (~50%), ~30% Qtz, and ~10% Pl
WR-12-21	Namling	89°03'43"	29°37'40"	3997	42.67 ± 0.60[2]	Diorite	Porphyritic	0.5–1.0 cm Kfs (~50%), ~15% Pl, 10% Qtz, and interstitial Bi (7%) + Amp (5%) + Ttn (2%)
QS-10	Quxu	90°15'03"	29°20'06"	3689	51–47[3]	Diorite	Equi-granular	~30% Kfs, ~20% Qtz, ~15 % Pl (An = ~30), ~2% Cpx, and ~15% Amp (assemblage, part of them replacing Cpx + Opx)
QS-9	Quxu	91°55'36"	29°53'54"	3589	51–47[3]	Diorite	Equi-granular	~50% Pl (An = 30–46), ~10% Cpx + Opx, ~5% Amp (replacing Cpx), ~10% interstitial Bi, and ~10% Qtz
WR-12-11	Gurong	90°45'57"	29°47'10"	3910	55.18 ± 0.50[2]	Granite	Porphyritic	Phenocrysts: 50% Qtz, 20% Pl, 15% Kfs, ~5% Bi; matrix is composed of fine-grained Qtz, Kfs and Pl
QS-7	Quxu	90°54'17"	29°24'22"	3600	51–47[3]	Quartz monzonite	Porphyritic	Weakly deformed, ~50% Kfs, ~35% Qtz, ~15% Pl, and ~7% interstitial Bi
QS-8	Quxu	90°54'17"	29°24'22"	3600	51–47[3]	Granite	Porphyritic	~50% Kfs, ~35% Qtz, ~15% Pl, interstitial Bi (~7%) and Amp (~3%), and ~3% Ttn
QS-2	Quxu	90°56'58"	29°32'12"	3625	51–47[3]	Diorite	Equi-granular	~50% Pl, ~5% (Cpx + Opx), overgrown and interstitial Amp (~10%), ~10% Qtz, ~5% interstitial Bi, and ~5%Ttn
NR-7	Nuri	91°47'34"	29°19'49"	4683	52[4]	Grano-diorite	Equi-granular	~50% Pl, ~20% Qtz, ~5% Kfs, and 10% interstitial Bi
ZD-1	Zedang Bridge	91°48'54"	29°15'17"	3566	54[4]	Grano-diorite	Equi-granular	~40% Pl, ~25 % Amp (assemblage), ~20% Qtz, and ~10% Kfs
ZD-3	Zedang bridge	91°50'24"	29°15'31"	3561	54[4]	Diorite	Equi-granular	~45% Pl, ~25 % Amp, ~15% Qtz, ~10% Kfs, ~10% Bi, and ~3% Mt with minor ilmenite
KMQ-12-2	Kangma qie	92°01'54"	29°21'29"	3914	50.79 ± 0.45[2]	Gabbroic diorite	Equi-granular	~65% Pl, ~5% Cpx, ~25% with interstitial Amp (replacing Cpx), and 5% Mt with minor Ilm

RD-12-5	Riduo	92°08'45"	29°42'30"	4253	66.30 ± 1.30[2]	Grano-diorite	Equi-granular	~50% Pl, ~20% Qtz, ~15% Kfs, ~5% interstitial Bi, and ~3% Mt
LQ-4	Kanga-gang	92°09'04"	29°17'22"	3559	42.5 ± 1.0[5]	Granite	Porphyritic	~35% Qtz, ~25% Kfs, ~20% Pl, and ~8 % interstitial Bi; phaneritic matrix,
LQ-1	Kangga-gang	92°11'02"	29°15'17"	3566	42.5 ± 1.0[5]	Granite	Porphyritic	~35% Qtz, ~25% Kfs, ~20% Pl, and ~10 % interstitial Bi; phaneritic matrix
WR-12-15	Qulin	90°13'24"	29°24'49"	3700	32.5 ± 0.50[6]	Quartz monzonite	Equi-granular	~30% Kfs, ~25% Pl, ~25% Qtz, ~5% Amp, ~5% Bi, and ~2% Ttn
MZ-2	Mingze	91°51'33"	29°15'15"	3560	30.4 ± 0.30[7]	Monzo-diorite	Equi-granular	~50% Pl, ~35% Amp, and ~5% Bi
MZ-3	Mingze	91°51'33"	29°15'15"	3561	30.4 ± 0.30[7]	Quartz monzonite	Equi-granular	~35% Pl, ~15% Amp, ~15% Kfs, ~15% Qtz, and ~5% Ttn
CB-1	Chenba	91°53'11"	29°15'12"	3650	29.8 ± 0.30[7]	Quartz monzonite	Porphyritic	1.0–2.0 cm Pl (~35%) and Kfs (~20%) phenocrysts, ~20% Qtz, and ~20% Amp
CB-7	Chenba	91°54'51"	29°16'08"	3560	29.8 ± 0.30[7]	Granite	Equi-granular	~40% Pl, ~20% Qtz, ~15% Kfs, ~10% Amp, and ~5% Mt
XB-12-3	Xueba	92°21'32"	29°27'18"	4094	23.41 ± 0.27[2]	Granite	Equi-granular	~40% Pl, ~20% Qtz, ~15% Bi, ~5% Amp, ~5% Cpx (replaced by Amp)
JR-4	Jiru	88°53'18"	29°39'21"	4720	16.0 ± 0.40[8]	Grano-diorite	Porphyritic	Phenocrysts: ~50% Pl, ~40% Amp; phaneritic matrix is composed of Pl, Amp, and Qtz
JR-5	Jiru	88°53'16"	29°39'24"	4697	16.19 ± 0.44[2]	Monzonite	Porphyritic	Phenocrysts: 0.1–0.5 cm Pl (~25%), 0.05–0.1 cm Amp (~60%); aphanitic matrix
JR-2	Jiru	88°54'17"	29°39'45"	4578	14.42 ± 0.31[2]	Quartz monzonite	Porphyritic	Phenocrysts: ~45 % Pl, ~20% Amp, and ~25% Qtz; aphanitic matrix
WR-12-5	Quxu	90°42'46"	29°26'29"	3930	21.3 ± 0.60[6]	Granite	Equi-granular	~40% Pl, ~20% Kfs, ~15% Qtz, ~5% Bi, ~3% Ttn, and ~3% Amp

[1] Age dating is from Zhang et al. (2008); [2] age dating is from this study; [3] age dating is from Mo et al. (2005); [4] age dating is from personal communication with Zheng Yuanchuan; [5] age dating is from Harrison et al. (2000); [6] age dating is from Ji et al. (2009); [7] age dating is from Zheng et al. (2012b); [8] age dating is from Zheng et al. (2013). Total alkali-silica (TAS) after Middlemost (1994). Abbreviations: Amp = Amphibole; Bi = Biotite; Kfs = K-feldspar; Ilm = Ilmenite; Mt = Magnetite; Opx = Orthopyroxene; Pl = Plagioclase; Qtz = Quartz; Ttn = Titanite.

2.6 Zircon U-Pb results

Zircon U-Pb concordia ages and diagrams were generated using Isoplot/Ex (ver. 3.7: Ludwig, 2008). Inverse concordia diagrams (Tera and Wasserburg, 1972) are utilized to evaluate the data, because the error correlation between $^{207}Pb/^{206}Pb$ and $^{238}U/^{206}Pb$ is smaller than between $^{206}Pb/^{238}U$ and $^{207}Pb/^{235}U$ (Corfu et al., 2013). In addition, young zircons (< 200 Ma) normally have high ratios of common to radiogenic lead, which is revealed by correlated arrays to high $^{207}Pb/^{206}Pb$ ratios on a Tera-Wasserburg diagram (Williams, 1998). Inherited zircons with much older ages occur as cores with rims of newly crystallized magmatic zircon. In contrast, antecrystic zircons form slightly earlier than the final crystallization of the magma, and their presence can lead to scatter in age data (Simmons et al., 2013). Cenozoic zircons in this study reveal a complicated history, which might be caused by inherited zircons, antecrystic zircons, the presence of common Pb, Pb loss, and/or a combination of the above.

Paleocene–Eocene sequence

Sample RD-12-5 contained one group of zircons, mostly with low common lead, but which shows an elongated distribution on an age histogram (Fig. 2-5A). This sample yielded an intercept age of 66.30 ± 1.30 Ma (MSWD = 1.8), based on 15/19 zircon crystals (Fig. 2-6A). Four excluded crystals have $^{238}U/^{206}Pb$ ages between ~73 Ma and 69 Ma. These might be antecrysts or xenocrysts because their data plots to the left of the chord defined by the remaining fifteen crystals.

The distribution of individual zircon spot ages (Table A1) and the concordia diagram suggest the potential presence of two populations of zircon in sample WR-12-11 (Fig. 2-5B, 6B). One group intersects the concordia line at 61.22 ± 0.96 (MSWD = 0.24), whereas a younger group intersects concordia at 55.18 ± 0.5 Ma (MSWD = 0.81). The young age with relatively low common lead can best represent the emplacement age of the rock. The older group with ~6 Ma age difference might be xenocrysts.

Sample KMQ-12-2 contained a homogeneous population of zircons, mostly with low common lead contents, and which yielded a concordia intercept age of 50.79 ± 0.45 Ma (MSWD = 0.53; Fig. 2-6C).

Sample WR-12-21 contained one group of zircons, mostly with low common lead, but

which shows a slightly skewed distribution on an age histogram (Fig. 2-5C). The scatter in age data might be caused by an antecryst or inherited crystal, or two young crystals with Pb loss (Fig. 2-6D). Regression of this population (15/18 zircon crystals) yielded an intercept age of 42.67 ± 0.60 Ma (MSWD = 1.5; Fig. 2-6D).

Sample JR-11 contained a homogeneous population of zircons, mostly with low common lead contents, and which yielded an intercept age of 36.33 ± 0.88 Ma (MSWD = 1.07; Fig. 2-6E).

These data are consistent with published radiometric analyses for Paleocene–Eocene igneous rocks, and together define a sequence ranging from 66.30 ± 1.30 Ma to 36.45 ± 0.52 Ma (Dong et al., 2006a, b; Mo et al., 2007, 2008; Ji et al., 2009; 2012; Zhao et al., 2011a, b).

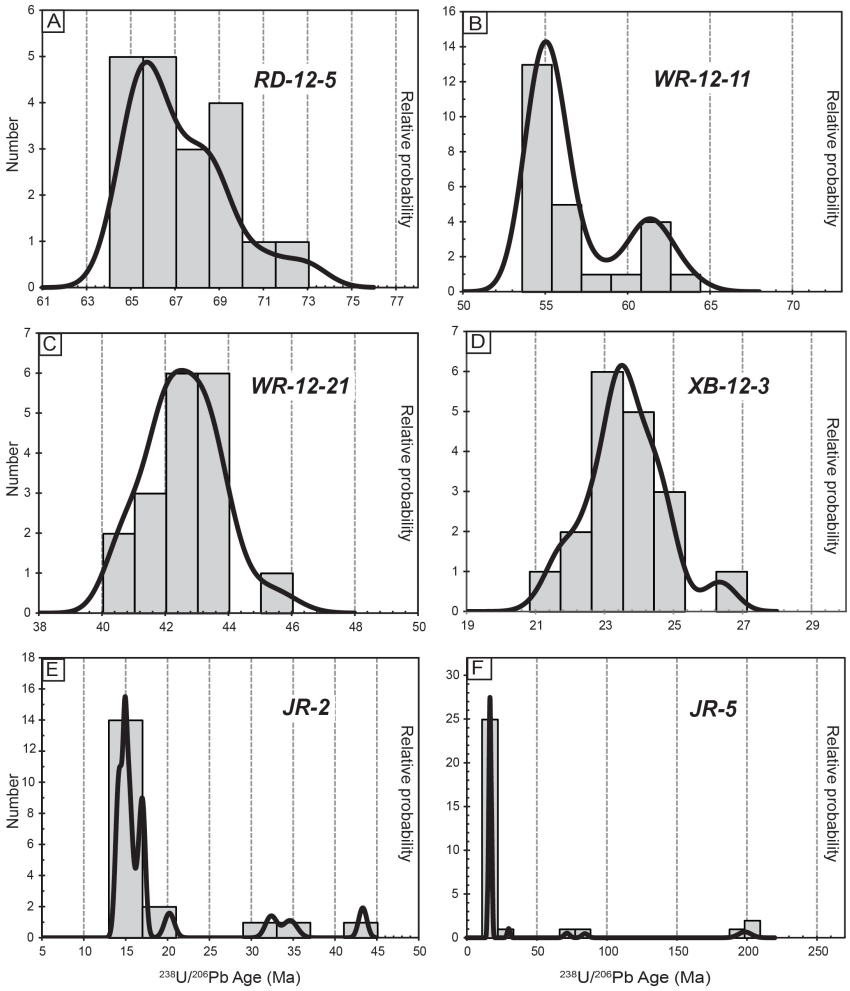

Fig. 2-5. Zircon U-Pb $^{238}U/^{206}Pb$ age histograms and relative probability curves for intrusive samples with complicated ages. A. Sample RD-12-5; B. Sample WR-12-11; C.

Sample WR-12-21; D. Sample XB-12-3; E. Sample JR-2; F. Sample JR-5.

Oligocene sequence

Sample XB-12-3 shows a slightly skewed distribution on an age histogram (Fig. 2-5D), which might be caused by four antecryst or inherited crystals, or one young crystal with Pb loss. Excluding these old and young crystals, this sample yielded an intercept age of 23.41 ± 0.27 Ma (MSWD = 1.7; Fig. 2-6F). Two zircon crystals from this sample have relatively high common lead. The Xueba sample (XB-12-3) age is slightly younger than published Oligocene sequence (~30–26 Ma: Harrison et al., 2000; Zheng et al., 2012a, b).

Miocene sequence

Sample JR-2 has a complicated zircon population (Fig. 2-5E), and some zircon crystals have relatively high common lead. The youngest group intersects concordia at 14.42 ± 0.31 Ma (MSWD = 1.9; Fig. 2-6G). Inherited zircons have $^{238}U/^{206}Pb$ ages of 43, 35, 32, and 20 Ma (Fig. 2-6G; Table A1).

Sample JR-5 also has a complicated zircon population (Fig. 2-5F). The youngest group intersects concordia at 16.19 ± 0.44 Ma (MSWD = 1.9; Fig. 2-6H), but one group of older grains has a concordant $^{238}U/^{206}Pb$ age of 199 Ma (Fig. 2-6H; Table A1).

The ages for these two samples are consistent with published radiometric analyses for Miocene intrusions, and together define a period of Miocene magmatism from ~21 to 9 Ma (Chung et al., 2003; Hou et al., 2004; King et al., 2007; Ji et al., 2009; Li et al., 2011).

2.7 Lithogeochemical Results

Whole-rock geochemical data from this study are illustrated on Figures 2-7, 9 and listed in Table 2-2. These have been supplemented with data (isotopic and geochemical data) from the following sources: Harrison et al. (2000); Chung et al. (2003); Hou et al. (2004); Chen et al. (2006); Dong et al. (2006a, b); Guo et al. (2007); Wen (2007); Yang (2008); Wang et al. (2010); Xia et al. (2010); Xu et al. (2010); Lee et al. (2011); Li et al. (2011); Tafti (2011); Xiao (2011); Zhao et al. (2011a, b); Zhu et al. (2011); Ji et al. (2012); Zheng et al. (2012a, b). Figure 2-4 shows all whole rock sample locations.

Table 2-2 Major and trace element analysis of intrusive rock samples from the Gangdese magmatic belt

Sample	JR-6	JR-11	WR-12-21	QS-10	QS-9	WR-12-11	QS-7	QS-8	QS-2
Weight %									
SiO_2	66.62	76.43	59.29	63.85	59.63	76.56	66.72	71.95	62.73
TiO_2	0.49	0.13	0.76	0.49	0.82	0.13	0.46	0.26	0.56
Al_2O_3	15.16	12.39	19.11	15.69	16.85	12.62	15.14	14.39	16.48
ΣFe_2O_3*	4.68	0.81	4.65	4.47	7.13	1.38	3.05	1.9	4.97
MnO	0.08	0.03	0.09	0.11	0.13	0.06	0.06	0.03	0.1
MgO	1.59	0.13	1.35	1.81	2.43	0.24	1.16	0.65	1.74
CaO	3.53	0.58	3.51	4.26	5.96	1.38	2.84	1.66	4.91
Na_2O	3.4	3.2	4.81	3.56	3.42	3.37	3.64	3.36	4.13
K_2O	3.78	5.21	5.17	3.36	2.69	3.67	4.84	4.7	1.95
P_2O_5	0.18	0.02	0.32	0.15	0.22	0.03	0.2	0.1	0.15
LOI	0.59	0.25	0.50	0.75	0.47	1.52	0.67	0.57	0.66
Total	100.1	99.18	99.54	98.5	99.75	101	98.78	99.57	98.38
ppm									
Sc	8.06	1.75	7.19	11.1	18.1	2.99	5.87	2.96	11.1
V	81	7.0	68	83	159	12	55	27	90
Cr	11.6	bdl	bdl	20.5	bdl	bdl	17.8	12.4	8.5
Co	11.4	0.9	7.5	11.2	16.8	2.4	6.8	3.4	10.7
Ni	7.0	bdl	5.0	8.0	5.0	1.0	9.0	4.0	3.0
Rb	141	213	122	95	90	108	300	201	70
Ba	515	101	1617	464	359	616	767	691	618
Th	28.5	42.1	31.9	12.6	16	11.9	103	86.7	8.42
U	3.5	3.19	4.02	3.13	3.6	1.23	25.9	16.7	2.51
Nb	7.3	11.3	18.7	6.3	5.7	4.1	22.4	12.3	4.6
Ta	0.64	0.5	1.67	0.41	0.46	0.49	2.86	1.84	0.33
La	24.9	37.5	90.9	27.1	21.4	23.7	76.9	63.2	17.6
Ce	47.7	58.4	182	56.2	46	45.1	154	110	34.3
Pb	11	43	33	11	11	18	83	66	7.0
Pr	4.84	4.9	17.4	6.28	5.62	4.27	16.5	10.5	4.09
Sr	453	68	939	496	454	142	522	351	500
Nd	16.4	12.7	57.9	23.6	22.4	14.8	55.7	32.3	15.6
Sm	2.79	1.39	8.04	5.27	5.01	2.47	9.79	4.97	3.22
Zr	180	84	423	159	191	81	255	155	194
Hf	4.4	2.5	9.6	4.1	4.8	2.2	7.1	4.6	4.4
Eu	0.74	0.285	1.9	0.927	1.14	0.375	1.42	0.829	0.987
Gd	2.19	0.8	4.51	4.53	4.53	2.12	6.08	3.0	2.87
Tb	0.34	0.1	0.61	0.75	0.78	0.36	0.79	0.43	0.49
Dy	1.77	0.54	3.19	4.31	4.54	2.17	3.89	2.22	2.81
Y	11	2.0	17	22	23	14	17	11	14
Ho	0.36	0.11	0.62	0.88	0.91	0.44	0.69	0.42	0.57
Er	1.11	0.36	1.66	2.51	2.57	1.32	1.89	1.23	1.63
Tm	0.175	0.058	0.259	0.38	0.375	0.206	0.26	0.191	0.25
Yb	1.22	0.42	1.74	2.46	2.44	1.42	1.61	1.32	1.71
Lu	0.221	0.075	0.266	0.407	0.412	0.235	0.253	0.221	0.302
[La/Yb]N	14.6	64.0	37.5	7.9	6.3	12.0	34.3	34.3	7.4
La/Yb	20.4	89.3	52.2	11.0	8.8	16.7	47.8	47.9	10.3
Sr/Y	41.2	34.0	55.2	22.5	19.7	10.1	30.7	31.9	35.7
Eun/Eu*	0.92	0.83	0.96	0.58	0.73	0.50	0.56	0.66	0.99

Table 2-2 (continued)

Sample	NR-7	ZD-1	ZD-3	KMQ-12-2	RD-12-5	LQ-4	LQ-1	WR-12-15	MZ-2
Weight %									
SiO_2	65.45	65.73	59.52	52.52	69.87	74.76	69.88	68.11	54.83
TiO_2	0.53	0.47	0.68	1.03	0.28	0.16	0.22	0.51	0.68
Al_2O_3	15.52	15.54	17.48	18.00	15.33	13.39	14.77	15.41	14.51
ΣFe_2O_3*	4.37	4.58	6.62	9.89	2.96	1.31	2.5	3.40	6.26
MnO	0.08	0.08	0.11	0.15	0.06	0.04	0.09	0.05	0.10
MgO	2.57	1.89	2.88	3.88	0.79	0.33	0.65	1.15	5.46
CaO	4.06	4.3	6.22	8.03	2.53	1.17	2.68	2.92	8.13
Na_2O	3.48	3.27	3.55	3.34	4.13	3.46	3.95	4.28	3.81
K_2O	3.43	3.00	2.13	1.26	3.00	4.71	3.23	3.49	3.66
P_2O_5	0.23	0.12	0.18	0.27	0.16	0.05	0.09	0.25	0.76
LOI	0.90	0.96	0.65	0.66	0.66	0.43	0.90	0.86	0.95
Total	100.62	99.94	100	99.04	99.79	99.81	98.96	100.4	99.15
ppm									
Sc	9.17	10.3	15	22.8	4.34	2.49	3.33	4.9	16.5
V	102	93	145	234	34	15	29	62	157
Cr	63.8	10.1	17.6	17.3	4.1	bdl	bdl	10.5	183
Co	12.5	10.6	17.6	28	3.5	2	4.7	8.1	21
Ni	34	7	10	15	2	2.0	2.0	12	59
Rb	92	74	54	45	86	240	74	148	205
Ba	563	424	416	289	11	260	678	675	1298
Th	6.62	7.58	2.81	1.51	2.4	35.5	4.41	31.3	16
U	2.15	1.8	0.99	0.52	4.8	7.29	2.2	5.98	210
Nb	4.6	4.2	4.5	2.6	0.54	11.9	5	10.6	14.9
Ta	0.4	0.45	0.32	0.14	21.5	1.46	0.53	1.01	1780
La	23	18.3	15.9	12.1	41.2	23.9	12.7	40.7	92.1
Ce	45.2	34.6	33.4	28.7	9	43.4	25.4	82	178
Pb	13	7	8	bdl	4.11	71	23	51	20
Pr	5.19	3.78	4.11	3.63	381	4	2.78	8.32	72
Sr	893	389	519	639	15.4	178	332	627	11.5
Nd	19.2	13.4	16.4	17.2	2.81	13.2	9.94	29.6	2.49
Sm	3.27	2.63	3.4	4.17	107	2.07	2.19	4.43	7.3
Zr	115	110	189	101	2.8	94	77	198	0.85
Hf	2.9	3	4.6	2.4	0.654	3.3	2.2	4.6	3.99
Eu	0.978	0.674	0.91	1.2	1702	0.342	0.515	0.928	0.67
Gd	2.63	2.23	3.07	4.41	2.33	1.47	1.89	2.28	1.69
Tb	0.38	0.37	0.52	0.64	0.36	0.2	0.31	0.26	0.216
Dy	1.84	2.16	3	3.57	2.12	1.16	1.76	1.28	1.32
Y	8.0	12	16	20	13	6.0	12	7	0.209
Ho	0.34	0.45	0.61	0.68	0.44	0.25	0.38	0.21	4.8
Er	0.95	1.32	1.79	1.93	1.32	0.79	1.18	0.57	0.89
Tm	0.139	0.21	0.267	0.289	0.212	0.128	0.196	0.078	12
Yb	0.95	1.44	1.82	1.87	1.44	0.94	1.46	0.47	41.5
Lu	0.154	0.247	0.309	0.277	0.222	0.172	0.251	0.071	8.19
[La/Yb]N	17.4	9.1	6.3	4.6	20.5	18.2	6.2	62.1	1.6
La/Yb	24.2	12.7	8.7	6.5	28.6	25.4	8.7	86.6	2.2
Sr/Y	111.6	32.4	32.4	32.0	1.2	29.7	27.7	89.6	55.0
Eun/Eu*	1.02	0.85	0.86	0.86	329.56	0.60	0.77	0.89	0.58

Table 2-2 (continued)

Sample	MZ-3	CB-1	CB-7	XB-12-3	JR-4	JR-5	JR-2	WR-12-5
Weight %								
SiO_2	61.42	66.38	71.12	72.79	68.48	58.44	66.12	71.06
TiO_2	0.58	0.45	0.32	0.26	0.37	0.86	0.41	0.24
Al_2O_3	16.12	15.99	14.48	14.35	15.53	16.92	15.96	15.80
ΣFe_2O_3*	4.67	3.33	2.53	1.87	2.35	6.38	2.65	1.65
MnO	0.07	0.05	0.05	0.05	0.02	0.08	0.04	0.04
MgO	2.56	1.6	0.96	0.42	0.8	4.03	1.08	0.50
CaO	4.86	3.94	2.94	1.72	2.27	5.6	2.21	2.41
Na_2O	4.04	4.27	4.19	4.02	4.32	3.92	4.96	4.94
K_2O	4.62	3.68	2.79	3.76	3.4	3.02	3.21	3.05
P_2O_5	0.39	0.22	0.14	0.10	0.11	0.27	0.13	0.09
LOI	0.64	0.54	0.61	0.37	0.8	1.37	2.00	0.31
Total	99.97	100.45	100.13	99.71	98.45	100.89	98.77	100.1
ppm								
Sc	8.9	3.26	3.75	3.54	3.07	9.47	3.91	2.75
V	99	73	45	25	42	150	55	36
Cr	44.8	16.1	7.8	bdl	3.8	91.1	8.6	bdl
Co	11.6	4.9	6.5	4	7.4	16.4	6.5	3
Ni	26	17	7	2	8.0	79	10	3
Rb	205	136	119	180	127	117	106	84
Ba	1430	920	229	465	864	536	727	513
Th	77	36.2	29.9	26.5	10.1	5.05	7.69	8.36
U	13.5	5.44	5.45	4.85	2.53	1.13	2.44	2.66
Nb	19.4	12.6	11.7	12.5	4.8	5.5	3.9	3.7
Ta	1.39	1.2	1.13	1.3	0.5	0.4	0.35	0.17
La	80.6	56.7	41.2	34	20.5	18.9	16	14.3
Ce	161	106	73.2	66.4	40.3	40.2	31.7	27.6
Pb	26	44	20	36	15	17	20	33
Pr	17.4	10.8	7.13	6.37	4.55	5.04	3.69	2.98
Sr	940	859	587	332	754	927	767	735
Nd	58.8	35.5	22.4	21.9	16.2	20	13.9	11.1
Sm	9.18	5.26	3.41	3.33	2.91	4.17	2.5	1.8
Zr	300	177	135	143	113	106	96	87
Hf	7.3	4.3	3.8	3.6	3.2	2.8	2.7	2.8
Eu	1.84	1.16	0.75	0.623	0.646	1	0.667	0.46
Gd	5.88	3.21	2.24	2.08	1.81	3.05	1.83	1.09
Tb	0.74	0.38	0.28	0.29	0.24	0.41	0.22	0.14
Dy	3.6	2	1.29	1.54	1.15	2.05	1.1	0.68
Y	16.0	9.0	6.0	10	5.0	9.0	5.0	4
Ho	0.62	0.33	0.24	0.28	0.19	0.33	0.19	0.13
Er	1.74	0.95	0.7	0.84	0.55	0.9	0.54	0.33
Tm	0.248	0.137	0.103	0.131	0.079	0.119	0.075	0.047
Yb	1.57	0.92	0.75	0.92	0.48	0.7	0.47	0.32
Lu	0.24	0.148	0.134	0.143	0.078	0.115	0.073	0.055
[La/Yb]N	36.8	44.2	39.4	26.5	30.6	19.4	24.4	32.1
La/Yb	51.3	61.6	54.9	37.0	42.7	27.0	34.0	44.7
Sr/Y	58.8	95.4	97.8	33.2	151	103	153	184
Eun/Eu*	0.77	0.86	0.83	0.72	0.86	0.86	0.95	1.0

Eun/Eu* = Eun/0.5*(Smn+Gdn)

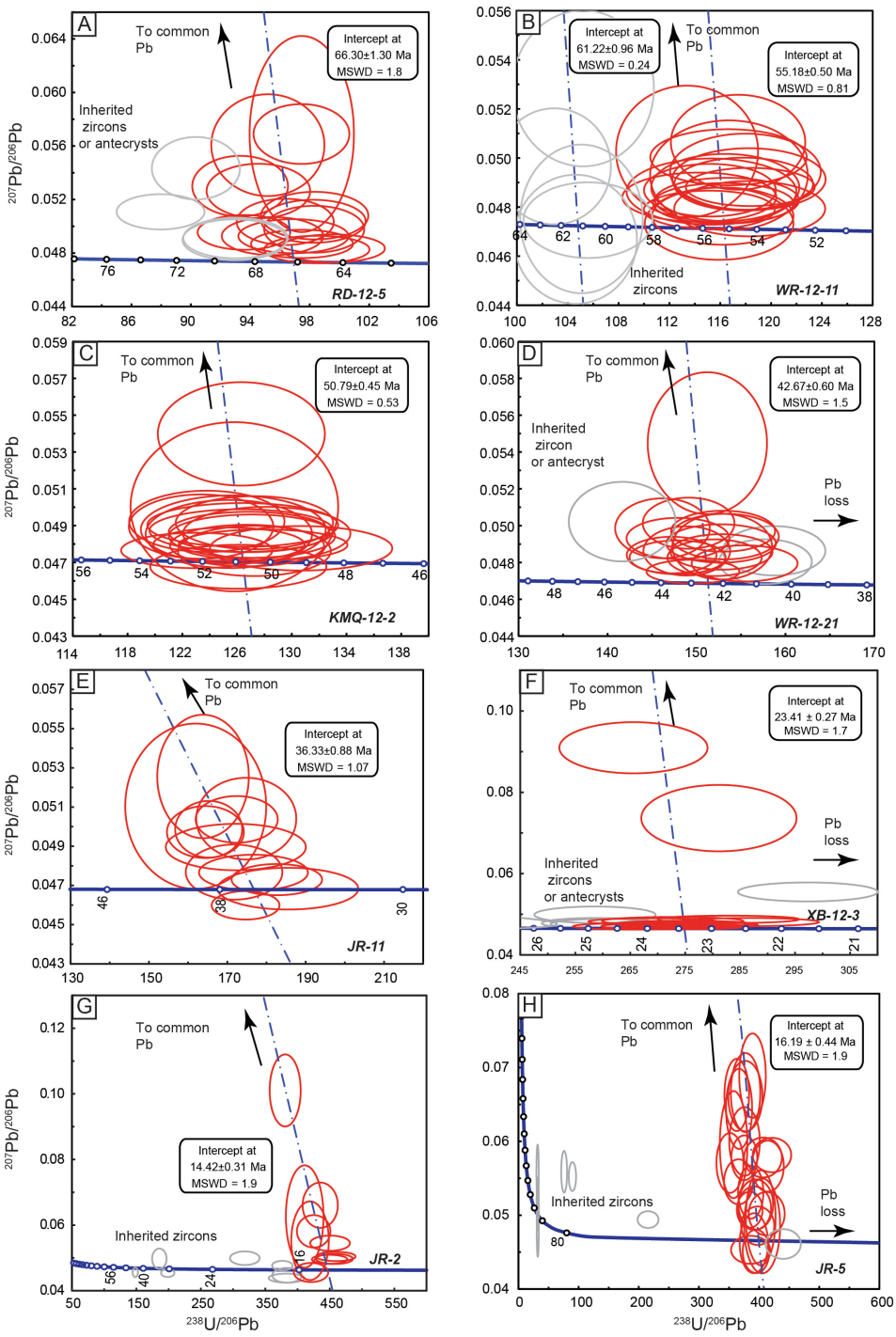

Fig. 2-6. Zircon U-Pb reverse concordia diagrams for intrusive samples. Tera-Wasserburg (1972) concordia diagrams are applied for each sample to demonstrate the presence of inheritance, common Pb and Pb loss. A. Sample RD-12-5; B. Sample WR-12-11, C. Sample KMQ-12-2; D. Sample WR-12-11, E. Sample JR-11; F. XB-12-3, G. Sample JR-2; H. Sample JR-5. Analyses excluded from the age calculation shown in gray (see text for details).

Paleocene–Eocene sequence

The SiO_2 contents of the 16 samples of Paleocene–Eocene intrusive rocks analyzed for this study range from 52.5 wt. % to 76.6 wt. % (Fig. 2-7A). Except for one sample (WR-12-21: Na_2O+K_2O = 10.0 wt. %), the samples are subalkalic and plot in the calc-alkaline to high-K calc-alkaline field (Fig. 2-7). These samples have relatively low Sr/Y (mostly < 40; Fig. 2-8A) and intermediate La/Yb (mostly < 50; Fig. 2-8B) ratios, low Sr contents (mostly < 650 ppm; Fig. 2-8C), and high Y contents (mostly > 10 ppm; Fig. 2-8D). Fifteen samples (except NR-7 with Eu_n/Eu^* =1.02) show negative Eu anomalies (i.e., $Eu_n/Eu^* < 1$), which increase for more fractionated rocks (Fig. 2-8E).

All samples show moderate enrichments of light rare earth elements (LREE) relative to heavy rare earth elements (HREE) on a chondrite-normalized diagram (Fig. 2-9A), with an average $[La/Yb]_N = 18.2 \pm 16.4$ (n = 16). They also show relative depletions in Nb, Ta, P, and Ti, and enrichments in Rb, Ba, Th, U, Pb, and K on a primitive mantle-normalized trace element diagram (Fig. 2-9B).

Our data mostly overlap the ranges of Paleocene–Eocene intrusive rocks from the literature, except for sample JR-11 (age: 36.33 ± 0.88 Ma) with low HREE and MREE, and also show a similar range and pattern to the Linzizong volcanic successions.

Oligocene sequence

Six samples of Oligocene intrusive rocks are intermediate to felsic in composition (SiO_2 = 54.8–72.8 wt.%, Fig. 2-7A), with no mafic rocks comparable to the earlier Paleocene–Eocene suite. These intrusive rocks have relatively high alkali contents (Na_2O+K_2O = 7.0–8.7 wt.%), and two samples plot in the alkaline field (Fig. 2-7A). Most of the samples plot in the high-K calc-alkaline field (Fig. 2-7B). These rocks have high Sr/Y (mostly > 50; Fig. 2-8A) and La/Yb (mostly > 50; Fig. 2-8B) ratios, high Sr contents (up to 1298 ppm; Fig. 2-8C), and intermediate Y contents (6–16 ppm; Fig. 2-8D). All samples have negative Eu anomalies (Eu_n/Eu^* = 0.73–0.89; Fig. 2-8E), and show significant enrichments of LREE over HREE on normalized diagrams ($[La/Yb]_N$ = 26.5–62.1; Fig. 2-9C). These samples show relative enrichment of Rb, Ba, Th, U, and Pb, and depletion of P, Ti, and HREE (Fig. 2-9D).

Our data mostly overlap the ranges of Oligocene intrusive rocks from the literature, but some samples from this study have higher REE concentrations and large ion lithophile elements (LILE) such as Rb and Ba (Fig. 2-9). All our data present negative Eu anomalies, whereas several of samples from the literature have positive Eu anomalies (Fig. 2-8E).

Miocene sequence

The SiO_2 contents of four samples of Miocene intrusive rocks range from 58.4 wt.% to 71.1 wt.%, and they are all calc-alkaline to high-K calc-alkaline in composition (Fig. 2-7). They have high Sr/Y ratios (> 103; Fig. 2-8A), intermediate La/Yb ratios (27.0–44.7, Fig. 2-8B), and high Sr contents (> 700 ppm, Fig. 2-8C). They have lower Y contents (< 10 ppm) than most of the earlier Paleocene–Eocene and Oligocene rocks (Fig. 2-8D). These samples have zero to weakly negative Eu anomalies (Eu_n/Eu^* = 0.86–1.0), and show intermediate enrichment of LREE relative to HREE ($[La/Yb]_N$ = 19.4–32.0; Fig. 2-9E).

Our data mostly overlap the ranges of Miocene intrusive rocks from the literature, but samples from the literature are more high K calc-alkaline and shoshonitic in composition, which might be caused by pervasive alteration nearby porphyry deposits. In addition, samples from the literature extend to be more mafic, and have higher La/Yb and Sr/Y ratios, and Eu anomalies than our data.

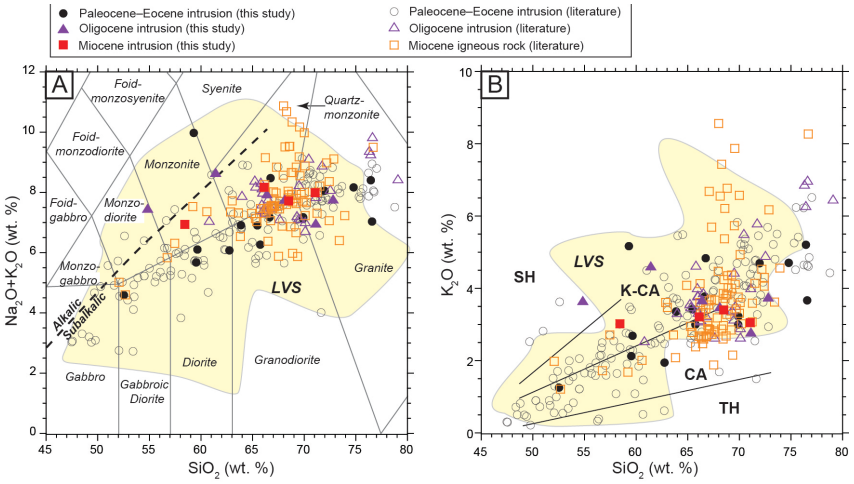

Fig. 2-7. A. Total alkali-silica diagram for Paleocene–Eocene, Oligocene, and Miocene intrusive rock samples from this study (after Middlemost, 1994) compared with data from the literature (for sources of data same with Fig. 2-4). The alkaline/subalkaline boundary

of Ivine and Baragar (1971) is shown. B. SiO_2 vs. total K_2O (after Rickwood, 1989): Abbreviations: CA = Calc-alkaline series; K-CA = High-K calc-alkaline series; LVS = Linzizong volcanic successions; SH = Shoshonite series; TH = Tholeiite series.

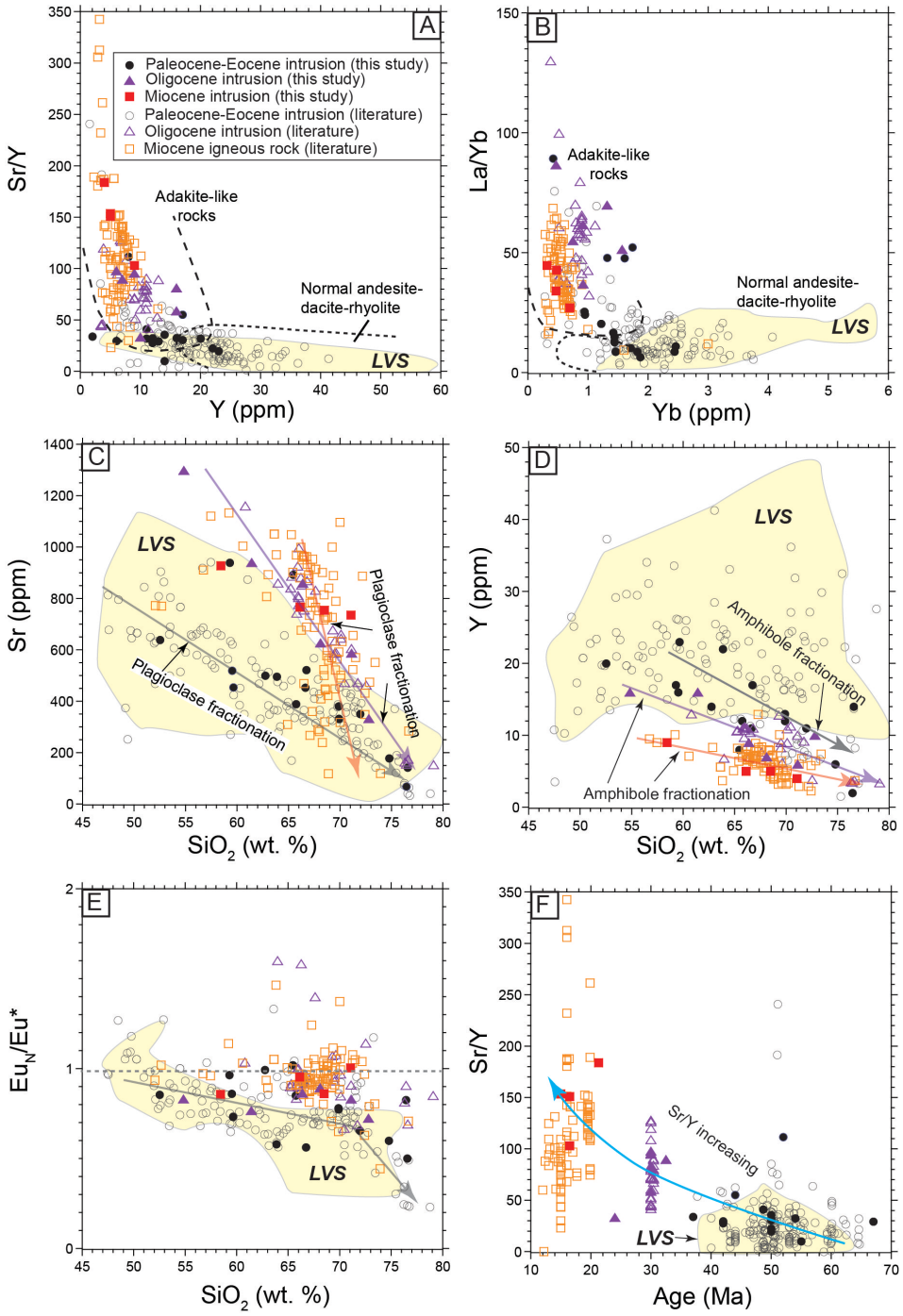

Fig. 2-8. Trace element concentration and ratio plots for Cretaceous, Paleocene–Eocene, Oligocene, and Miocene igneous rocks (for sources of data same with Fig. 2-4) in the Gangdese belt, showing mineral fractionation trends and correlation trends where apparent (see text for details). A. Sr/Y ratios vs. Y; B. La/Yb ratios vs. Yb; C. Sr vs. SiO_2;

D. Y vs. SiO_2; E. Eu_N/Eu^* vs. SiO_2; F. Sr/Y ratios vs. Age; Normalization values from Sun and McDonough (1989). "Adakite-like rock" field from Defant and Drummond (1990). LVS: Linzizong volcanic successions.

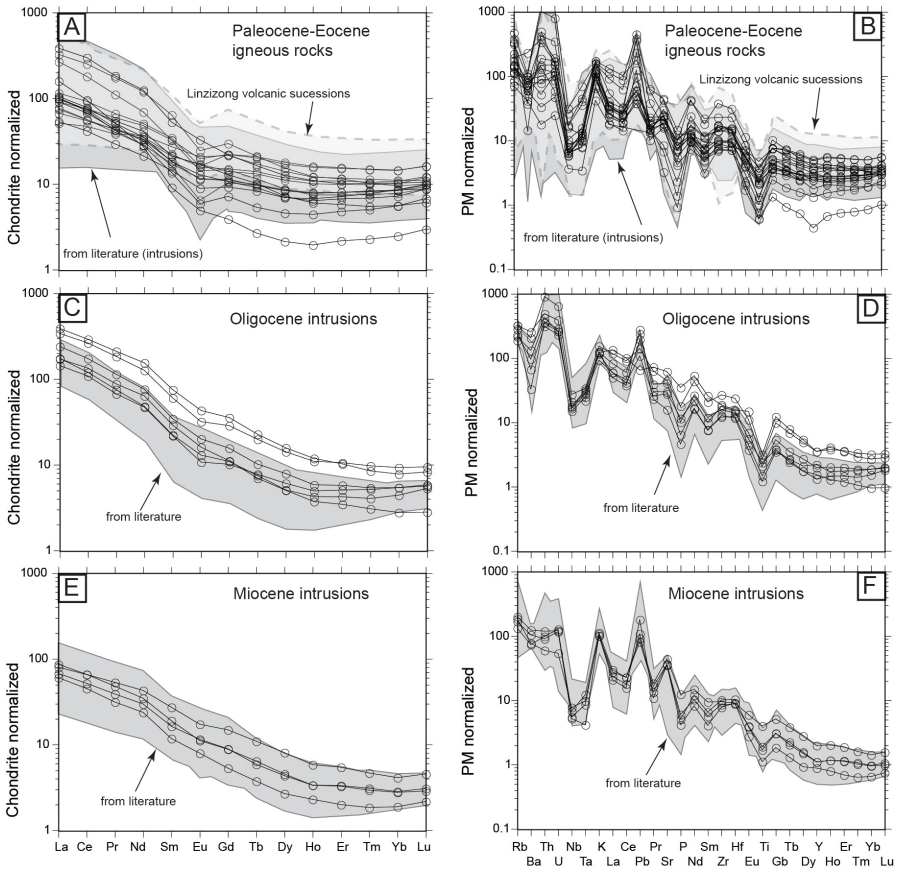

Fig. 2-9. Chondrite- and primitive mantle (PM)-normalized trace element diagrams for samples of igneous rocks (for sources of data same with Fig. 2-4) in the Gangdese belt: A, B. Paleocene–Eocene; C, D. Oligocene; E, F. Miocene. Normalization values of Sun and McDonough (1989).

2.8 Discussion

Changes in trace element contents over time in the Gangdese magmatic belt

This discussion is based on all available whole rock geochemical data. This includes our own data (Figs. 2-7–9; Table 2-2) and those available from the literature (same as above).

Paleocene–Eocene sequence: The Paleocene-Eocene samples have relatively low Sr/Y ratios (mostly < 40; Fig. 2-8A), decreasing Sr concentrations over a wide range of SiO_2 contents from ~47 wt.% to 79 wt.% (Fig. 2-8C), and show increasingly negative Eu

anomalies with SiO_2 (Fig. 2-8E). These characteristics indicate that plagioclase fractionation occurred throughout the evolution of these magmas from mafic to felsic compositions. The Y contents of these rocks (literature data) have an rough increase at ~60 wt.% SiO_2 then decrease at higher silica contents (Fig. 2-8D), which suggests that hornblende (which preferentially partitions Y and middle rare earth elements (MREE); Green and Pearson, 1985; Rollinson, 1993; Davidson et al., 2007; Müntener et al., 2001; Rooney et al., 2011) did not begin to fractionate until relatively evolved compositions were reached. These geochemical features are consistent with the rare occurrence of amphibole phenocrysts in the Paleocene–Eocene sequence, but abundance of plagioclase phenocrysts. In combination, the mineralogy and geochemistry of these Paleocene–Eocene igneous rocks suggest that their magmatic water contents were < 4 wt.% H_2O, the minimum level for hornblende phenocryst crystallization (Naney, 1983; Ridolfi et al., 2010).

Oligocene sequence: No samples of mafic Oligocene rocks were found that could be compared with the Paleocene–Eocene mafic rocks, but the intermediate rocks have much higher Sr (Fig. 2-8C) and variable Eu_n/Eu^* (0.69–1.58; Fig. 2-8E), and lower Y contents (Fig. 2-8D) than Paleocene–Eocene equivalents, and both Sr and Y contents decrease with increasing SiO_2. These observations suggest that little plagioclase fractionation (or restite) occurred early in the evolution of these Oligocene magmas, whereas hornblende was an important early crystallizing phase as indicated by its abundance as phenocrysts in these rocks. The importance of hornblende as a crystallizing phase is reflected in the pronounced listric-shaped REE patterns in the Oligocene rocks, because hornblende preferentially partitions MREE (Fig. 2-9C). These features suggest that the Oligocene intermediate–felsic magmas were relatively hydrous (> 4 wt.% H_2O, thereafter, the magmas with < 4 wt.% H_2O are treated as less hydrous or water-poor), and fractionated abundant early hornblende with plagioclase (e.g., Moore and Carmichael, 1998; Müntener et al., 2001).

Miocene sequence: All of the Miocene intrusions sampled are intermediate to felsic in composition (Fig. 2-7A; > 58.4 wt.% SiO_2), and mafic samples are only found in volcanic rocks reported by Turner et al. (1996). Strontium contents appear to increase initially with silica contents, which might reflect suppressed plagioclase fractionation

(Fig. 2-8C). The decrease of Sr contents after ~65 wt.% SiO_2 suggests later start of plagioclase fractionation. Most of the intermediate composition samples have Eu_n/Eu^* ratios that scatter near 1, but more felsic samples (SiO_2 > 70%) show a trend to lower ratios with SiO_2 (Fig. 2-8E), also indicating late-stage plagioclase fractionation (Weill and Drake, 1973; Frey et al., 1978; Hanson, 1980; Green and Pearson, 1985). The Miocene igneous rocks have even lower Y concentrations (mostly below 10 ppm; Fig. 2-8D) than the Oligocene suite, and pronounced listric-shaped REE patterns (Fig. 2-9E). The common occurrence of hornblende as a phenocryst phase in these rocks combined with a trend of increase of Sr with low SiO_2 and extremely depleted Y contents suggests that fractionation of amphibole occurred earlier and even more extensively than in the Oligocene suite, and indicates that the Miocene magmas were hydrous.

Petrogenesis of soft-collisional Paleocene–Eocene magmas

Neo-Tethyan subduction beneath southern Tibet started in the Late Triassic–Early Jurassic (Chu et al., 2006) and continued until the onset of collision between India and Asia at ~55–50 Ma. Cretaceous magmatic rocks are the main product of this period of subduction. The voluminous Linzizong volcanic successions (~65–43 Ma) and coeval Paleocene-Eocene granitoids are thought to represent a magmatic response to rollback of the Neo-Tethyan slab as this period of subduction came to a close.

The Paleocene–Eocene igneous rocks have calc-alkaline continental arc-like compositions, with enrichments in LILE (Rb, Ba, Th, U, and K), and depletions in HFSE (Nb and Ta). Published data show that most of these Paleogene igneous rocks in the southern Lhasa subterrane have similar Sr-Nd isotope compositions to the Gangdese Cretaceous arc rocks (Fig. 2-10A), suggesting that they are products of Neo-Tethyan subduction.

εNd_i values of these early Paleogene intrusive rocks varies from the central Lhasa subterrane (0 to -9) to the southern Lhasa subterrane (-3 to +10; Fig. 2-10A, B). This is consistent with large exposures of Precambrian basement in the central Lhasa subterrane. These Precambrian strata mainly consist of amphibolite-facies metamorphic rocks. Recent geochronological studies indicate that the protoliths (granite and trondhjemite) are formed between 787 and 748 Ma. This age distribution and Nd model ages (862–1802

Ma) are similar to the High Himalaya basement, and both domains are thought to have formed on the Neo-Proterozoic active margin of Gondwana (Hu et al., 2005). Thus, we use High Himalaya basement ($^{87}Sr/^{86}Sr$ = 0.775, Sr = 31.3 ppm, εNd = -18.3, Nd = 16.8 ppm; Ding et al., 2003) as the proxy of Precambrian basement in the central Lhasa subterrane. A Sr-Nd isotope binary mixing simulation (DePaolo, 1981) between Precambrian basement and depleted mantle ($^{87}Sr/^{86}Sr$ = 0.703, Sr = 20 ppm, εNd = +8, Nd = 1.2 ppm; Taylor and McLennan, 1985) indicates that Paleocene–Eocene magmas to the north of ~30°N (i.e., in the central Lhasa subterrane; εNd_i = 0 to -9) have <20 % contamination with Precambrian basement, whereas contamination is <5% for the high εNd_i (-3 to +10) Paleocene–Eocene magmas from the southern Lhasa subterrane, to the south of ~30°N.

At the end of the Linzizong volcanic episode, picritic to basaltic andesitic lavas of the Dazi Formation (40–38 Ma) were erupted in the Dazi basin. These primitive lavas are interpretated to have been derived from asthenospheric melting triggered by Neo-Tethyan slab break-off (Chung et al., 2005; Gao et al., 2008).

Petrogenesis of hard-collisional Oligo-Miocene magmas

Several models have been proposed for the origin of the Oligo-Miocene granitoids in the Lhasa terrane, including partial melting of the subducted Neo-Tethyan slab (Qu et al., 2004, 2007), and partial melting of thickened and newly formed lower crust (Chung et al., 2003; Hou et al., 2004) or subduction modified lower crust (Guo et al., 2007; Li et al., 2011). Published Sr-Nd isotope compositions of Gangdese Oligo-Miocene igneous rocks overlap those of the cospatial Cretaceous Gangdese arc batholith (Fig. 2-10A), although these intrusions formed ~35 m.y. after the onset of India–Asia collision, and cannot therefore be directly related to subduction. The Greater India slab began to detach at 25 ± 5 Ma until complete break-off at 10 ± 5 Ma (Replumaz et al., 2010).

We propose that detachment is suggested to have triggered upwelling of asthenospheric mantle (Hou et al., 2009), which in turn caused partial melting of previously subduction-modified Tibetan lithosphere. This partial melting zone might be reflected today in a low seismic velocity layer at depths of 100–150 km within the lithosphere (Mechie and Kind, 2013). Being derived from the residues of previous arc

magmatism, the resulting Miocene magmas would have similar geochemical and isotopic compositions to the Cretaceous arc batholiths, despite not being directly related to active subduction. The Sr-Nd isotope compositions of Oligo-Miocene magmas scatter toward the lower crustal garnet-amphibole xenoliths in eastern Tibet (proxy of Tibetan lower crust; Deng et al., 1998), reflecting a certain degree of contamination (< 10%, Fig. 2-10A) upon emplacement. In addition, the scatter of Sr-Nd isotope compositions of Oligo-Miocene magmas might also reflect the contamination with mid-crustal flows (Unsworth et al., 2005; Jamieson et al., 2011; Jamieson and Beaumont, 2013), which have relatively enriched Sr-Nd isotopic compositions ($^{87}Sr/^{86}Sr$ = 0.7071–0.7079, εNd -4 to -6; King et al., 2007).

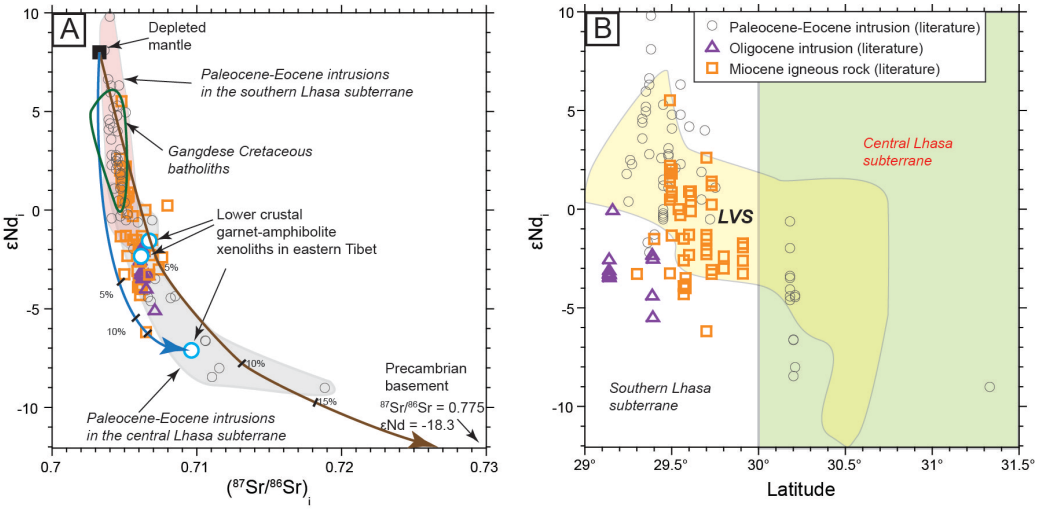

Fig. 2-10. A. εNd_i vs. $(^{87}Sr/^{86}Sr)_i$ diagram for Paleogene igneous rocks (for sources of data same with Fig. 2-4) where the brown line shows mixing (ticks on the curve give percentage of assimilation) between partial melts of depleted mantle ($^{87}Sr/^{86}Sr$ = 0.703, Sr = 20 ppm, εNd = +8, Nd = 1.2 ppm; Taylor and McLennan, 1985) and High Himalaya crystalline basement (proxy for Precambrian basement: $^{87}Sr/^{86}Sr$ = 0.775, Sr = 31.3 ppm, εNd = -18.3, Nd = 16.8 ppm; Ding et al., 2003). The blue line shows mixing between partial melts of depleted mantle and lower crustal garnet-amphibolite xenoliths in Tibet (proxy for Tibetan lower crust; $^{87}Sr/^{86}Sr$ = 0.707, Sr = 593 ppm, εNd = -2.4, Nd = 35.1 ppm; Deng et al., 1998). B. εNd_i vs. latitude, the boundary between central Lhasa subterrane and the southern Lhasa subterrane is about latitude 30°N.

Origin of magmatic water flux from the Paleocene to the Miocene

The mineralogical and geochemical features discussed above indicate that Paleocene–Eocene magmas were relatively water-poor, compared with later post-subduction Oligo-

Miocene magmas. The change of magmatic water contents from the Paleocene–Eocene to the Oligo-Miocene is closely correlated with deep geodynamic process.

The lower water content of the Paleocene–Eocene magmas are thought to reflect the final dehydration of the remnant Neo-Tethyan slab (Fig. 2-11A). In addition, the initiation of Paleocene–Eocene magmatism was triggered by rollback of Neo-Tethyan, which facilitated large-scale partial melting. The generated melts under high temperature are thought to be less hydrous compared to normal arc magmatism. Oligo-Miocene magmas were formed after the main India-Asia collision, and hydrous. We interpret these higher magmatic water contents, in the absence of a direct subduction source, to dehydration melting of previously subduction-modified lithosphere, including hydrous arc cumulates in the lower crust (Kay and Mpodozis, 2001).

Implications for metallogeny

Following Hou et al. (2009) and Richards (2009), we propose that hydrous, relatively oxidized calc-alkaline to mildly alkaline magmas with the potential to form porphyry Cu-Mo±Au deposits were generated during hard-collisional processes in the India–Asia orogen by partial melting of previously subduction-modified and thickened lithosphere. Partial melting remobilized chalcophile (such as Cu) and siderophile metals (such as Mo and Au) left as residues in deep crustal arc cumulate zones and/or metasomatized mantle lithosphere, giving these magmas the potential to form porphyry-type deposits when emplaced into the upper crust (Fig. 2-11B).

The Oligo-Miocene Gangdese porphyries demonstrate that deposits almost indistinguishable from normal arc porphyries can be generated in collisional orogenic belts tens of millions of years after subduction has ceased, by remobilization of fluids and metals previously introduced into the lithosphere by prior subduction events.

The apparently water-poor Paleocene–Eocene magmas were generated during final subduction and dehydration of the remnant Neo-Tethyan oceanic lithosphere, and are not associated with significant mineralization. In contrast, the more hydrous Oligo-Miocene magmas are interpreted to have been derived from partial melting of subduction-modified Tibetan lithosphere in response to post-subduction asthenospheric upwelling, and are associated with several large porphyry Cu-Mo±Au deposits. High magmatic water contents are essential for the formation of magmatic-hydrothermal ore deposits, and we therefore conclude that this increase in magmatic water content from the Paleocene–Eocene to the Oligo-Miocene in the Gangdese belt was essential to the formation of post-subduction porphyry deposits.

2.10 References

Allégre, C.J., Courtillot, V., Taponnier, P., Hirn, A., Mattauer, M., Coulon, C., Jaeger, J. J., Achache, J., Schärer, U., Marcoux, J., Burg, J. P., Girardeau, J., Armijo, R., Gaiety, C., Göpel, C., Li, T., Xiao, X., Chang, C., Li, G., Lin, B., T, J., Wang, N., Chen, G., Han, T., Wang, X., Den, W., Sheng, H., Gao, Y., Zhou, J., Qiu, H., Bao, P., Wang, S., Wang, B., Zhou, Y., and Xu, R., 1984, Structure and evolution of the Himalayan-Tibet orogenic belt: Nature, v. 307, p.17–22.

Aitchison, J.C., Ali, J.R., and Davis, A.M., 2007, When and where did India and Asia collide: Journal of Geophysical Research, v. 112, B5, p. B05423, 10.1029/2006JB004706.

Baxter, A.T., Aitchison, J.C., and Zyabrev, S.V., 2009, Radiolarian age constraints on Mesotethyan ocean evolution, and their implications for development of the Bangong-Nujiang suture, Tibet: Journal of the Geological Society, v.166, p. 689–694.

BGMRXAR (Bureau of Geology Mineral Resources of Xizang Autonomous Region), 1993, Regional Geology of Xizang (Tibet) Autonomous Region: Geological Publishing House, Beijing, 450 p. (in Chinese with English abstract).

Buddington, A.F., 1959, Granite emplacement with special reference to North America: Geological Society of America Bulletin, v. 70, p. 671–747.

Burg, J.P., and Chen, G.M., 1984, Tectonics and structural formation of southern Tibet, China: Nature, v. 11, p. 219–223.

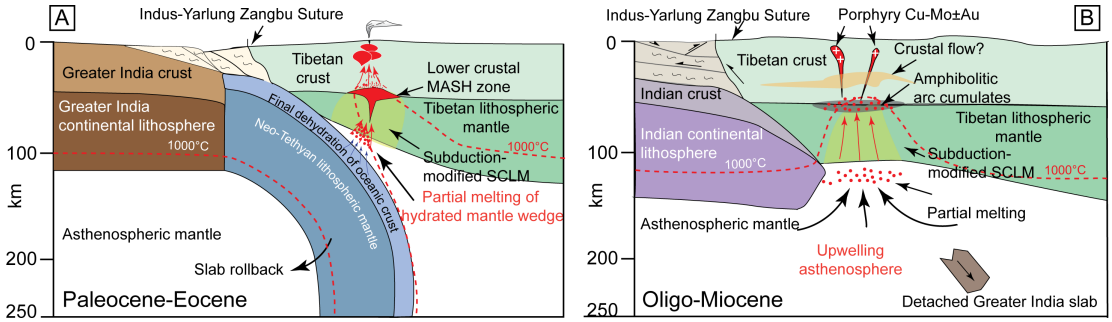

Fig. 2-11. Cartoon cross-sections illustrating the proposed petrogenesis of Cenozoic igneous rocks in the Gangdese belt (approximately to scale). A. Gangdese continental arc: Paleocene-Eocene magmatism was triggered by rollback of Neo-Tethyan slab, and formed by partial melting of hydrated mantle wedge (MASH = melting, assimilation, storage, and homogenization; Hildreth and Moorbath, 1981); B. Miocene magmatism was triggered by Greater India slab breakoff and upwelling of asthenospheric melts, and formed by partial melting of subduction-modified Tibetan lithosphere. Porphyry Cu-Mo±Au deposits formed from these hydrous magmas upon upper crustal emplacement. Thrust systems are inferred from Yin and Harrison (2000). Depths of the Moho, Indian lithosphere–asthenosphere boundary, and Tibetan lithosphere–asthenosphere boundary are estimated from seismic studies (Kumar et al., 2006; Zhao et al., 2010). Crustal flow in middle-crust is inferred from Unsworth et al. (2005), King et al., (2007), and Jamieson et al. (2011).

2.9 Conclusions

Paleocene–Eocene igneous rocks in the Gangdese magmatic belt have intermediate $[La/Yb]_N$ ratios (average = 12.0 ± 8.6, n = 150), intermediate-to-low Sr/Y ratios (mostly <40), and negative Eu anomalies (average = 0.76 ± 0.19, n = 150), which suggest that mineral fractionation of these magmas was dominated by early pyroxene and plagioclase. In contrast, Oligo-Miocene granitoids have higher $[La/Yb]_N$ (average = 32.2 ± 12.0, n = 128) and Sr/Y ratios (mostly >40). Least evolved (intermediate) compositions in the Oligo-Miocene have much higher Sr contents and lower Y contents than equivalent Paleocene–Eocene rocks, suggesting early hornblende fractionation and minor or delayed plagioclase fractionation. Consistent with this interpretation is the fact that amphibole is a common phenocryst phase in the younger granitoids, but is relatively rare and restricted to the groundmass or as late replacements of earlier pyroxene in the Paleocene–Eocene rocks. We interpret these textures and geochemical evidence to indicate that the Oligo-Miocene magmas were more hydrous than the Paleocene–Eocene magmas.

Capitanio, F.A., Morra, G., Goes, S., Weinberg, R.F., and Moresi, L., 2010, India-Asia convergence driven by the subduction of the Greater Indian continent: Nature Geoscience, v. 3, p. 136–139.

Chen, L., Qin, K.Z., Li, G.M., Li, J.X., Xiao, B., Jiang, H.Z., Zhao, J.X., Fan, X., and Jiang, S.Y., 2012, Geological and skarn mineral characteristics of Nuri Cu-W-Mo deposit in southern Gangdese, Tibet: Mineral Deposits, v. 31, p. 417–437 (in Chinese with English abstract).

Chen, L., Qin, K.Z., Li, J.X., Xiao, B., Li, G.M., Zhao, J.X., and Fan, X., 2011, Fluid Inclusion and hydrogen, oxygen, sulfur isotopes of Nuri Cu-W-Mo deposit in the southern Gangdese, Tibet: Resource Geology, v. 62, p. 42–62.

Chen, T., 2006, Geochemistry of the Qushui intrusive of Gangdese in Tibet and its implications for magma mixing: Unpublished Master thesis (in Chinese), China University of Geosciences, Beijing, 59 p.

Chu, M.F., Chung, S.L., Song, B., Liu, D.Y., O'Reilly, S.Y., Pearson, N.J., Ji, J.Q., and Wen, D.J., 2006, Zircon U-Pb and Hf isotope constraints on the Mesozoic tectonics and crustal evolution of southern Tibet: Geology, v. 34, p. 745–748.

Chung, S.L., Chu, M.F., Ji, J.Q., O'Reilly, S.Y., Pearson, N.J., Liu, D.Y., Lee, T.Y., and Lo, C.H., 2009, The nature and timing of crustal thickening in southern Tibet: Geochemical and zircon Hf isotopic constraints from postcollisional adakites: Teconophysics, v. 477, p. 36–48.

Chung, S.L., Chu, M.F., Zhang, Y.Q., Xie, Y.W., Lo, C.H., Lee. T.Y., Lan, C.Y., Li, X.H., Zhang, Q., and Wang, Y.Z., 2005, Tibetan tectonic evolution inferred from spatial and temporal variations in post-collisional magmatism: Earth-Science Reviews, v. 68, p. 173–196.

Chung, S.L., Liu, D., Ji, J.Q., Chu, M.F., Lee, H.Y., Wen, D.J., Lo, C.H., Lee, T.Y., Qian, Q., and Zhang, Q., 2003, Adakites from continental collision zones: melting of thickened lower crust beneath southern Tibet: Geology, v. 31, p. 1021–1024.

Coulon, C., Maluski, H., Bollinger, C., and Wang, S., 1986, Mesozoic and Cenozoic volcanic rocks from central and southern Tibet: $^{39}Ar/^{40}Ar$ dating, petrological characteristics and geodynamical significance: Earth and Planetary Science Letters, v. 79, p. 281–302.

Corfu, 2013, A century of U-Pb geochronology: the long quest towards concordance: GSA bulletin, v. 125, p. 33–47.

Davidson, J., Turner, S., Handley, H., Macpherson, C., and Dosseto, A., 2007, Amphibole "sponge" in arc crust?: Geology, v. 35, p. 787–790.

DePaolo, D., 1981, Trace element and isotopic effects of combined wallrock assimilation and fractionation: Earth and Planetary Science Letters, v. 53, p. 189–202.

DeCelles, P.G., Gehrels, G.E., Najman, Y., Martin, A.J., Carter, A., and Garzanti, E., 2004, Detrital geochronology and geochemistry of Cretaceous–early Miocene strata of Nepal: implications for timing and diachroneity of initial Himalayan orogenesis: Earth and Planetary Science Letters, v. 227, p. 313–330.

DeCelles, P.G., Gehrels, G.E., Quade, J., LaReau, B., Spurlin, M., 2000, Tectonic implication of U–Pb zircon ages of the Himalayan orogenic belt in Nepal: Science, v. 288, p. 497–499.

Deng, W.M., Huang, X., and Zhong, D., 1998, Alkali-rich porphyry and its relation with intraplate deformation of north part of Jinsha River belt in western Yunnan, China: Science in China (Series D), v. 41, p. 297–305.

Defant, M.J., and Drummond, M.S., 1990, Derivation of some modern arc magmas by melting of young subducted lithosphere: Nature, v. 347, p. 662–665.

Dewey, J.F., Shackelton, R.M., Chang, C., and Sun, Y., 1988, The tectonic evolution of the Tibetan Plateau: Philosophical Transactions of the Royal Society London, v. 327, p. 379–413.

de Sigoyer, J., Chavagnac, V., Blichert-Toft, J., Villa, I.M., Luais, B., Guillot, S., Cosca, M., and Mascle, 2000, Dating the Indian continental subduction and collision thickening in the northwest Himalaya: Multichronology of the Tso Morari eclogites: Geology, v. 28, p. 487–490.

Dilles, J.H., 1987, Petrology of the Yerington batholith, Nevada: Evidence for evolution of porphyry copper ore fluids: Economic Geology, v. 82, p. 1750–1789.

Ding, L., Kapp. P., Zhong, D., and Deng, W., 2003, Cenozoic volcanism in Tibet: Evidence for a transition from oceanic to continental subduction: Journal of Petrology, v. 44, p. 1833–1865.

Dong, G.C., Mo, X.X., Zhu, D.C., Wang, L.L., Chen, T., and Li, B., 2006a, Magma

mixing in middle part of Gangdese magma belt: Evidences from granitoid complex: Acta Petrologica Sinica, v.22, p. 835–844 (in Chinese with English abstract).

Dong, G.C., Mo, X.X., Zhao, Z.D., Zhu, D.C., Song, Y.T., and Wang, L., 2006b. Gabbros from southern Gangdese: Implication for mass exchange between mantle and crust: Acta Petrologica Sinica, v. 24, p. 203–210 (in Chinese with English abstract).

Dong, G.C., 2002, Linzizong volcanic rocks and implications for probing India-Eurasia collision process in Linzhou Volcanic Basin, Tibet: Unpublished Ph.D. Thesis (in Chinese), China University of Geosciences, 150 p.

Du, D.H., Yang, Z.M., Li, Q.Y., Liu, Y.F., Ge, S., and Wang, H.Y., 2012, Determination of Eocene porphyritic monzogranite intrusions in Tinggong ore district of Tibet and its geological significance: Mineral Deposits, v. 31, p. 745–757 (in Chinese with English abstract).

Enkelemann, E., Weislogel, A., Ratchbacher, L., Eide, E., Renno, A., and Wooden, J., 2007, How was the Triassic Songpan-Ganzi basin filled? A provenance study: Tectonics, v. 26, TC4007.

Frey, F.A., Chappell, B.W., and Roy, S.D., 1978, Fractionation of rare-earth elements in the Tuolumne Intrusive Series, Sierra Nevada batholith, California: Geology, v. 6, p. 239–242.

Gao, Y.F., Yang, Z.S., Santosh, M., Hou, Z.Q., Wei, R.H., and Tian, S.H., 2010, Adakitic rocks from slab melt-modified mantle sources in the continental collision zone of southern Tibet: Lithos, v. 119, p. 651–663.

Gao, Y.F, Wei, R.H, Hou, Z.Q, Tian, S.H, and Zhao, R.S., 2008, Eocene high-MgO volcanism in southern Tibet: New constraints for mantle source characteristics and deep process: Lithos, v. 105, p. 63–72.

Gao, Y.F., Hou, Z.Q., Kamber, B., Wei, R.H., Meng, X.J., and Zhao, R.S., 2007, Adakite-like porphyries from the southern Tibetan continental collision zones: evidence for slab melt metasomatism: Contributions to Mineralogy and Petrology, v. 153, p. 105–120.

Ge, L.S., Li, H.G., Wang, K.Q., Zou, Y.L., Wang, Z.H., Zhang, X.J., Yuan, S.S., and Xing, J.B., 2006, Geochemical characteristics of the W-Mo-Bi polymetallic deposit in the snow-capped Jaggang mountain, Xainza Country, Tibet: Mineral Deposits, v. 25,

p. 345–348 (in Chinese with English abstract).

Green, T.H., and Pearson, N.J., 1985, Experimental determination of REE partition coefficients between amphibole and basaltic to andesitic liquids at high pressure: Geochimica et Cosmochimica Acta, v. 49, p. v. 1465–1468.

Guo, Z.F., Wilson, M., and Liu, J.Q., 2007, Post-collisional adakites in south Tibet: products of partial melting of subduction-modified lower crust: Lithos: v. 96, p. 205–224.

Harris, N.B.W., Pearce, J.A., and Tindle, A.G., 1986, Geochemical characteristics of collisional-zone magmatism. In: Coward, M.P., Reis, A.C., eds., Collision tectonics: Geological Society, London, Special Publications, v. 19, p. 67–81.

Harrison, T.M., Yin, A., Grove, M., and Lovera, O.M., 2000, The Zedong window: A record of superposed Tertiary convergence in southeastern Tibet, Journal of Geophysical Research: v. 105, p. 19211–19230.

Hanson, G.N., 1980, Rare earth elements in petrogenetic studies of igneous systems: Annual Review of Earth Planetary Sciences, v. 8, p. 371–406.

He, S.D., Kapp, P., DeCelles, P.G., Gehrels, G.E., and Heizler, M., 2007, Cretaceous-Tertiary geology of the Gangdese arc in the Linzhou area, southern Tibet: Tectonophysics, v. 433, p. 15-37.

Hetzel, R., Dunkl, I., Haider, V., Strobl, M., von Eynatten, H., Ding, L., and Frei, D., 2011, Peneplain formation in southern Tibet predates the India-Asia collision and plateau uplift: Geology, v. 39, p.983-986.

Hildreth, W., and Moorbath, S., 1988, Crustal contributions to arc magmatism in the Andes of central Chile: Contributions to Mineralogy and Petrology, v. 98, p. 455–489

Hou, Z.Q., Zhang, H.R., Pan, X.F., and Yang, Z.M., 2011, Porphyry Cu (-Mo-Au) deposits related to melting of thickened mafic lower crust: Examples from the eastern Tethyan metallogenic domain: Ore Geology Review, v. 39, p. 21–45.

Hou, Z.Q., Yang, Z.M., Qu, X.M., Meng, X.J., Li, Z.Q., Beaudoin, G., Rui, Z.Y., Gao, Y.F., and Zaw, K., 2009, The Miocene Gangdese porphyry copper belt generated during post-collisional extension in the Tibetan Orogen: Ore Geology Reviews, v. 36, p. 25–31.

Hou, Z.Q., Gao, Y.F., Qu, X.M., Rui, Z.Y., and Mo, X.X., 2004, Origin of adakitic

intrusives generated during mid-Miocene east-west extension in southern Tibet: Earth and Planetary Science Letters, v. 220, p. 139–155.

Hu, D.G., Wu, Z.H., Jiang, W., Shi, Y.R., Ye, P.S., and Liu, Q.S., 2005, SHRIMP zircon U–Pb age and Nd isotopic study on the Nyainqêntanglha Group in Tibet: Science in China (Series D: Earth Sciences), v. 48, p. 1377–1386.

Huang, K., Zheng, Y., Zhang, S., Li, W., Sun, Q., Li, Q., Liang, W., Fu, Q., and Hou, Z., 2012, LA-ICP-MS zircon U-Pb dating of two types of porphyry in the Yaguila mining area, Tibet: Acta Petrologica et Mineralogica, v. 31, p. 348–360 (in Chinese with English abstract).

Irvine, T.N., and Baragar, W.R.A., 1971, A guide to the chemical classification of the common volcanic rocks: Canadian Journal of Earth Sciences, v. 8, p. 523-548.

Jamieson, R.A., Unsworth, M.J., Harris, N.B,W., Rosenberg, C.L., and Schulmann, 2011, Crustal melting and the flow of mountains: Elements, v. 7, p. 253–260.

Jamieson, R.A., and Beaumont, C., 2013, On the origin of orogens: GSA Bulletin, v. 125, p. 1671–1702.

Ji, W.Q., Wu, F.Y., Chung, S.L., Li, J.X., and Liu, C,Z., 2009, Zircon U-Pb geochronology and Hf isotopic constraints on petrogenesis of the Gangdese batholith, southern Tibet: Chemical Geology, v. 262, p. 229–245.

Ji, W.Q., Wu, F.Y., Liu, C.Z., and Chung, S.L., 2012, Early Eocene crustal thickening in southern Tibet: New age and geochemical constraints from the Gangdese batholith: Journal of Asian Earth Sciences, v. 53, p. 82–95.

Kapp, P., DeCelles, P.G., Leier, A.L., Fabijanic, J.M., He, S., Pullen, A., Gehrels, G.E., and Ding, L., 2007, The Gangdese retroarc thrust belt revealed: GSA Today, v. 17, p. 4–10.

Kapp, P., Yin, A., Harrison, T.M., and Ding, L., 2005, Cretaceous–Tertiary shortening, basin development, and volcanism in central Tibet: Geological Society of America Bulletin, v. 117, p. 865–878, doi: 10.1130/ B25595.1.

Kay, S.M., and Mpodozis, C., 2001, Central Andean ore deposits linked to evolving shallow subduction systems and thickening crust: GSA Today, v. 11, p. 4–9.

Khan, T., Khan, M.A., Jan, M.Q., and Naseem, M., 1996, Back-arc basin assemblages in Kohistan, Northern Pakistan: Geodinamica Acta, v. 9, p. 30–40.

King, J., Harris, N., Argles, T., Parrish, R., Charlier, B., Sherlock, S., and Zhang, H.F., 2007, First field evidence for southward ductile flow of Asian crust beneath southern Tibet: Geology, v. 35, p. 727–730.

Kumar, P., Yuan, X., Kind, R., Ni, J., 2006, Imaging the colliding Indian and Asian lithospheric plates beneath Tibet: Journal of Geophysical Research, v.111, B6: doi: 10.1029/2005JB003930.

Lee, H.Y., Chung, S.L., Ji, J.Q., Qian, Q., Gallet, S., Lo, C.H., Lee, T.Y., and Zhang, Q., 2011, Geochemical and Sr-Nd isotopic constraints on the genesis of the Cenozoic Linzizong volcanic successions, southern Tibet: Journal of Asian Earth Sciences, v. 53, p. 96–114.

Lee, T.Y., and Lawver, L.A., 1995, Cenozoic plate reconstruction of Southeast Asia: Tectonophysics, v. 251, p. 85–138.

Li, J.X., Qin, K.Z., Li, G.M., Xiao, B., Chen, L., and Zhao, J.X., 2011, Post-collsional ore-bearing adakitic porphyries from Gangdese porphyry copper belt, southern Tibet: Melting of thickened juvenile arc lower crust: Lithos, v. 126, p. 264–277.

Li, L.Q., Pan, L.C., and Zhang, G.F., 2010, Non-contamination powdering procedures for geochemical samples: Geological Survey and Research, v. 33, p. 238–240.

Ludwig, 2008, User's manual for Isoplot 3.7: A geochronological toolkit for Microsoft Excel: Berkeley Geochronology Center, Special Publication 4, 76 p.

Mechie, J., and Kind, R., 2013, A model of the crust and mantle structure down to 700 km depth beneath the Lhasa to Golmud transect across the Tibetan plateau as derived from seismological data: Tectonophysics, doi:10.1016/j.tecto.2013.04.030 (in press)

Meng, J., Wang, C., Zhao, X., Coe, R., Li, Y.L., and Finn, D., 2012, India-Asia collision was at 24° N and 50 Ma: Paleomagnetic proof from southern Asia: Scientific Reports, 2, 925; doi: 10.1038/srep00925.

Meng, X., Hou, Z., Gao, Y., Huang, W., Qu, X., and Qu, W., 2003, Re-Os dating for molybdenite from Qulong porphyry copper deposit in Gangdese metallogenic belt, Xizang and its metallogenic significance, v. 49, p. 660–666 (in Chinese with English abstract).

Metcalfe, I., 2009, Late Palaeozoic and Mesozoic tectonic and palaeogeographical evolution of SE Asia, in Buffetaut, E., et al., eds., Late Palaeozoic and Mesozoic

ecosystems in SE Asia: Geological Society of London Special Publication 315, p. 7–23, doi:10.1144/ SP315.2.

McInnes, B.I.A., Evans, N.J., Fu, F.Q., Garwin, S., Belousova, E., Griffin, W.L., Bertens, A., Sukarna, D., Permanadewi, S., Andrew, R.L., and Deckart, K., 2003, Thermal history analysis of selected Chilean, Indonesian and Iranian porphyry Cu-Mo-Au deposits; in Porter, T.M. (Ed.), Super porphyry copper and gold deposits: A global perspective, PGC Publishing, Adelaide, v.1, p. 27–42.

Middlemost, 1994, Naming materials in the magma / igneous rock system: Earth Science Reviews, v. 37, p. 215–224.

Mitsuishi, M., Wallis, S.R., Aoya, M., Lee, J., and Wang, Y., 2012, E-W extension at 19 Ma in the Kung Co area, S, Tibet: Evidence for contemporaneous E-W and N-S extension in the Himalayan orogen: Earth and Planetary Science Letters, v. 325–326, p. 10–20.

Moore, G.M., and Carmichael, I.S.E., 1998, The hydrous phase equilibria (to 3 kbar) of an andesite and basaltic andesite from western Mexico: Constraints on water content and conditions of phenocryst growth: Contributions to Mineralogy and Petrology, v. 130, p. 304–319.

Mo, X.X., Niu, Y.L., Dong, G.C., Zhao, Z.D., Hou, Z.Q., Zhou, S., and Ke, S., 2008, Contribution of syncollisional felsic magmatism to continental crust growth: A case study of the Paleogene Linzizong volcanic succession in southern Tibet: Chemical Geology, v. 250, p. 49–67.

Mo, X.X., Hou, Z.Q., Niu, Y.L., Dong, G.C., Zhao, Z.D. and Yang, Z.M., 2007, Mantle contributions to crustal thickening during continental collision: Evidence from Cenozoic igneous rocks in southern Tibet: Lithos, v. 96, p. 225–242.

Mo, X.X., Dong, G.C., Zhao, Z.D., Guo, T.Y., Wang, L.L., and Chen, T., 2005, Timing of magma mixing in the Gangdise magmatic belt during the India-Asia collision: Zircons SHRIMP U-Pb dating: Acta Geologica Sinica, v. 79, p. 66–76.

Müntener, O., Kelemen, P.B., and Grove, T.L., 2001, The role of H_2O during crystallization of primitive arc magmas under uppermost mantle conditions and genesis of igneous pyroxenites: An experimental study: Contributions to Mineralogy and Petrology, v. 141, p. 643–658.

Naney, M.T., 1983, Phase equilibria of rock-forming ferromagnesian silicates in granitic systems: American Journal of Science, v. 283, p. 993–1033.

Pan, G.T., Ding, J., Yao, D., and Wang, L., 2004, The Guide Book of 1:1,500,000 Geologic map of the Qinghai-Xizang (Tibet) Plateau and adjacent Areas: Chengdu Cartographic Publishing House, 44 p. (in Chinese).

Qu, X., Hou, Z., and Li, Y., 2004, Melt components derived from a subducted slab in late orogenic ore-bearing porphyries in the Gangdese copper belt, southern Tibetan Plateau: Lithos, v. 74, p. 131–148.

Qu, X., Hou, Z., Khin Zaw, and Li, Y., 2007, Characteristics and genesis of Gangdese porphyry copper deposits in the southern Tibetan Plateau: preliminary geochemical and geochronological results: Ore Geology Reviews, v. 31, p. 205–223.

Replumaz, A., Negredo, A.M., Villaseñor, A., and Guillot, S., 2010, Indian continental subduction and slab breakoff during Tertiary collision: Terra Nova, v. 22, p. 290–296.

Ridolfi, F., Renzulli, A., and Puerini, M., 2010, Stability and chemical equilibrium of amphibole in calc-alkaline magmas: An overview, new thermobarometric formulations and application to subduction-related volcanoes: Contributions to Mineralogy and Petrology, v. 160, p. 45–66.

Richards, J.P., 2009, Postsubduction porphyry Cu–Au and epithermal Au deposits: products of remelting of subduction-modified lithosphere. Geology, v.37, p. 247–250.

Rickwood, P.C., 1989, Boundary lines within petrologic diagrams which use oxides of major and minor elements: Lithos, v. 22, p. 247–263.

Rohrmann, A., Kapp, P., Carrapa, B., Reiners, P.W., Guynn, J., Ding, L., and Heizler, M., 2012, Thermochronologic evidence for plateau formation in central Tibet by 45 Ma: Geology, v. 40, p. 187–190.

Rowley, D.B., 1996, Age of initiation of collision between India and Asia: a review of stratigraphic data: Earth and Planetary Science Letters, v. 145, p. 1–13

Rooney, T.O., Franceschi, P., and Hall, C.M., 2011, Water-saturated magmas in the Panama Canal region: A precursor to adakite-like magma generation?: Contributions to Mineralogy and Petrology, v. 161, p. 373–388.

Rolland, Y., and Pêcher, A., and Picard, C., 2000, Middle Cretaceous back-arc formation and arc evolution along the Asian margin: the Shyok Suture Zone in

northern Ladakh (NW Himalaya): Tectonophysics, v. 325, p. 147–173.

Rollinson, H., 1993, Using geochemical data: evaluation, presentation, interpretation: Pearson Education Limited, Harlow, England, 352 p.

Sengör, A.M.C., Altmer, D., Cin, A., Ustaömer, T., and Hsü, K.J., 1988, Origin and assembly of the Tethyside orogenic collage at the expense of Gondwana Land, in Audley-Charles, M.G and Hallam, A., ed., Gondwana and Tethys: Geological Society, London, Special Publications, v. 37, p. 119–181.

Simmons, A.T., Tosdal, R.M., Wooden, J.L., Mattos, B., Concha, O., McCracken, S., and Beale, T., 2013, Punctuated magmatism associated with porphyry Cu-Mo formation in the Paleocene to Eocene of southern Peru: Economic Geology, v. 108, p. 625–639.

Sun, S.S., and McDonough, W.F., 1989, Chemical and isotopic systematics of oceanic basalts: Implications for mantle composition and processes. Geological Society of London Special Publication, v. 42: p. 313–345.

Tafti, R., 2011, Metallogeny, geochronology and tectonic setting of the Gangdese belt, southern Tibet, China: Unpublished Ph.D. thesis, University of British Columbia, Canada, 451 p.

Taylor, S.R., and McLennan, S.M., 1985, The Continental Crust: its Composition and Evolution. Oxford: Blackwell Scientific, 328 p.

Tera, F., and Wasserburg, G.J., 1972, U-Th-Pb systematics in three Apollo 14 basalts and the problem of initial Pb in lunar rocks: Earth and Planetary Science Letters, v. 14, p. 281–304.

Treloar, P.J., Petterson, M.G., Jan, M.Q., and Sullivan, M.A., 1996, A re-evaluation of the stratigraphy and evolution of the Kohistan Arc sequence, Pakistan Himalaya: Implications for magmatic and tectonic arc-building processes: Journal of the Geological Society, v. 153, p. 681–693.

Turner, S., Arnaud, N., Liu, J., Rogers, N., Hawkesworth, C., Harris, N., and Kelley, S., 1996, Post-collision, shoshonitic volcanism on the Tibetan Plateau: Implications for convective thinning of the lithosphere and the source of ocean island basalts: Journal of Petrology, v. 37, p. 45–71.

Unsworth, M.J., Jones, A.G., Wei, W., Marquis, G., Gokarn, S.G., Spratt, J.E., 2005, Crustal rheology of the Himalaya and Southern Tibet inferred from magnetotelluric

data: Nature, v. 438, p. 78–81.

Van der Voo, R., Spakman, W., and Bijwaard, H., 1999, Tethyan subducted slabs under India: Earth and Planetary Sciences Letters, v. 171, p. 7–20.

Van der Beek, P., Melle, J.V., Guillot, S., Pêcher, A., Reiners, P.W., Nicolescu, S., and Latif, M., 2009, Eocene Tibetan plateau remnants preserved in the northwest Himalaya: Nature Geoscience, v. 2, p. 364–368.

van Hinsbergen, D.J.J., Lippert, P.C., Dupont-Nivet, G., McQuarrie, N., Doubrovine, P.V., Spakman, W., and Torsvik, T.H., 2012, Greater India basin hypothesis and a two-stage Cenozoic collision between India and Asia: Proceedings of the National Academy of Science of the United States of America, v. 20, p. 7659–7664.

Wang, B.D., Xu, J.F., Chen, J.L., Zhang, X.G., Wang, L.Q., and Xia, B.B., 2010, Petrogenesis and geochronology of the ore-bearing porphyritic rocks in Tangbula porphyry molybdenum-copper deposit in the eastern segment of the Gangdese metallogenic belt: Acta Petrologica Sinica, 26, v. 26, 1820–1830 (in Chinese with English abstract).

Wen, D.R., 2007, The Gangdese batholith, Southern Tibet: Ages, geochemical characteristics and petrogenesis: Unpublished Ph.D. thesis, National Taiwan University, 120 p.

Weill, D.F., Drake, M.J., 1973, Europium anomaly in plagioclase feldspar: Experiment results and seimiquantitative model: Science, v. 180, p. 1059–1060.

Williams, I.S., 1998, U-Th-Pb geochronology by ion microprobe. In McKibben, M. A., Shanks III, W. C., and Ridley, W. I. (eds.): Applications of micro-analytical techniques to understanding mineralizing processes: Reviews in Economic Geology, v. 7, P. 1–35.

Xia, B.B., Xia, B., Wang, B.D., Li, J.F., Zhang, X.G., and Wang, Y.C., 2010, Formation of the Tangbula porphyry Mo-Cu deposit evidence from SHRIMP Zircon U-Pb dating of Tangbula ore-bearing porphyries: Geotectonic et Metallogenia, v. 34, p. 291–297.

Xiao, B., 2011, Highly oxidized magmatic-hydrothermal ore-forming process at the Qulong giant porphyry Cu-Mo deposit, Gangdese, Tibet: Unpublished Ph.D. thesis (in Chinese), Institute of Geology and Geophysics, Chinese Academy of Sciences, Beijing, 275 p.

Xu, W.C., Zhang, H.F., Guo, L., and Yuan, H.L., 2010, Miocene high Sr/Y magmatism, south Tibet: Product of partial melting of subducted Indian continental crust and its tectonic implication: Lithos, v. 114, p. 293–306.

Yang, Z.M., Hou, Z.Q., White, N.C., Chang, Z.S., Li, Z.Q., and Song, Y.C., 2009, Geology of the post-collisional porphyry copper-molybdenum deposit at Qulong, Tibet: Ore Geology Reviews, v. 36, p. 133–159.

Yang, Z.M., 2008, The Qulong giant porphyry copper deposit in Tibet: Magmatism and mineralization: Unpublished Ph.D. thesis (in Chinese), Institute of Geology Chinese Academy of Geological Sciences, Beijing, 144 p. (in Chinese with English abstract).

Yin, A., and Harrison, T.M., 2000, Geologic evolution of the Himalayan-Tibetan orogen: Annual Review of Earth and Planetary Sciences, v. 28, p. 211–280.

Zhang, G.Y., Zheng, Y.Y., Gong, F.Z., Gao, S.B., Qu, W.J., Pang, Y.C., Shi, Y.R., and Yan, S.Y., 2008, Geochronologic constraints on magmatic intrusions and mineralization of the Jiru porphyry copper deposit, Tibet, associated with continent-continent collisional process: Acta Petrologica Sinica, v. 24, p. 473–479.

Zhang, K.J., Xia, B.D., Wang, G.M., Li, Y.T., and Ye, H.F., 2004, Early Cretaceous stratigraphy, depositional environments, sandstone provenance, and tectonic setting of central Tibet, western China: Geological Society of America Bulletin, v. 116, p. 1202–1222.

Zhang, K, Zhang, Y, Li, B, and Zhong, L, 2007, Nd isotopes of siliciclastic rock from Tibet, western China: constraints on provenance and pre-Cenozoic tectonic evolution: Earth and Planetary Science Letter, v. 256, p. 604–616.

Zhang, S., Zheng, Y., Huang, K., Li, W., Sun, Q., Li, Q., Fu, Q., and Liang, W., 2012, Re-Os dating of molybdenite from Nuri Cu-W-Mo deposit and its geological significance: Mineral deposits, v. 31, p. 337–346 (in Chinese with English abstract).

Zhang, P., Shen, Z., Wang, M., Gan, W.J., Bürgmann, R., Molnar, P., Wang, Q., Niu, Z., Sun, J., Wu, J., Sun, H., and You, X., 2004, Continuous deformation of the Tibetan plateau from global positioning system data: Geology, v. 32, p. 809–812.

Zhao, J.X., Qin, K.Z., Li, G.M., Li, J.X., Xiao, B., and Chen, L., 2011a, Geochemistry and petrogenesis of granitoids at Sharang Eocene porphyry Mo deposit in the main-stage of India-Asia continental collision, northern Gangdese, Tibet: Resource

Geology, v. 62, p. 84–98.

Zhao, J., Yuan, X., Liu, H., Kumar, P., Pei, S., Kind, R., Zhang, Z., Teng, J, Ding, L., Gao, X., Xu, Q., and Wang, W., 2010, The boundary between the Indian and Asian tectonic plates below Tibet: Proceedings of the National Academy of Science of the United States of America, v. 107, p. 11229–11233.

Zhao, Z.D., Zhu, D.C., Dong, G.C., Mo, X.X., DePaolo, D., Jia, L.L., Hu, Z.C., and Yuan, H.L., 2011b, The ~54 Ma gabbro–granite intrusive in southern Dangxung area, Tibet: Petrogenesis and implications: Acta Petrologica Sinica, v. 27, p. 3513–3524.

Zheng, Y.C., Hou, Z.Q., Li, Q.Y., Sun, Q.Z., Liang, W., Fu, Q., Li, W., and Huang, K.X., 2012a, Origin of late Oligocene adakitic intrusives in the southeastern Lhasa terrane: Evidence from in situ zircon U-Pb dating, Hf-O isotopes: Lithos, v. 148, p. 296–311.

Zheng, Y.C., Hou, Z.Q., Li, W., Liang, W., Huang, K.X., Li, Q.Y., Sun, Q.Z., Fu, Q., and Zhang, S., 2012b, Petrogenesis and geological implications of the Oligocene Chongmuda-Mingze adakite-like intrusions and their mafic enclaves, southern Tibet: Journal of Geology, v. 120, p. 647–669.

Zheng, Y.Y., Sun, X., Gao, S.B., Zhao, Z.D., Zhang, G.Y., Wu, S., You, Z.M., and Li, J.D., 2013, Multiple mineralization events at the Jiru porphyry copper deposit, southern Tibet: Implications for Eocene and Miocene magma sources and resource potential: Journal of Asian Earth Sciences, *in press.*

Zhou, L.M., Hou, Z.Q., Zheng, Y.C., and Li, W., 2011, Study on accessory minerals in Yaja granite, northern Tibet: Indicator of the magma source: Acta Petrologica Sinia, 27, p. 2786–2794 (in Chinese with English abstract).

Zhu, D.C., Zhao, Z.D., Niu, Y.L., Mo, X.X., Chung, S.L., Hou, Z.Q., Wang, L.Q., and Wu, F.Y., 2011, The Lhasa terrane: Record of a microcontinent and its histories of drift and growth: Earth and Planetary Science Letters, v. 301, p. 241–255.

Zhu, D.C., Zhao, Z.D., Niu, Y.L., Dilek, Y., Hou, Z.Q., and Mo, X.X., 2013, The origin and pre-Cenozoic evolution of the Tibetan Plateau: Gondwana Research, v. 23, p. 1429–1454.

Chapter 3
Increasing magmatic oxidation state from Paleocene to Miocene in the eastern Gangdese belt, Tibet: Implication for collision-related porphyry Cu-Mo±Au mineralization[1]

3.1 Introduction

Porphyry copper deposits are most commonly formed by hydrothermal fluids exsolved from fertile and relatively oxidized subduction-related magmas in arc settings (Sillitoe, 1972, 2010; Burnham, 1979; Hedenquist and Lowenstern, 1994; Richards, 2003, 2011; Cooke et al., 2005). Recently, a number of porphyry-type deposits have been recognized that formed in post-subduction and collisional settings, such as the Miocene Qulong porphyry Cu-Mo and Jiama porphyry Cu-Mo-Au deposits in the Gangdese belt, Tibet (Hou et al., 2009, 2011; Yang et al., 2009; Li et al., 2011), the Eocene–Oligocene porphyry Cu systems in Yunan (Lu et al., 2013), the Pliocene Grasberg Cu-Au deposit in Papua, Indonesia (Pollard et al., 2005; Cloos and Housh, 2008), and the Miocene Sar Cheshmeh porphyry Cu-Mo deposit in the Kerman porphyry belt, Central Iran (Hezarkhani, 2006; Shafiei et al., 2009; Haschke et al., 2010; Aminzadeh et al., 2011). These deposits are almost indistinguishable from normal arc porphyry deposits in magmatic association, mineralization style, alteration zoning, and metal endowment, but were generated several to tens of millions of years after subduction ceased. Several theories have been put forward to explain the origin of the generative magmas, including partial melting of subduction-modified lithosphere (Guo et al., 2007; Ahmadian et al., 2009; Richards, 2009; Shafiei et al., 2009; Haschke et al., 2010), slab melt-modified mantle (Gao et al., 2010), or newly formed lower crust (Hou et al., 2009, 2011). Melts from subduction-modified lithosphere are thought to be similar in oxidation state, H_2O content, and geochemistry to subduction-related magmas (Richards, 2009, 2011; Haschke et al., 2010; Lee et al., 2012; Wang et al., 2014a, b). However, few studies have attempted to directly constrain the oxidation state (fO_2) of these collision-related magmas.

[1] This chapter was published as: Wang, R., Richards, J.P., Hou, Z.Q., Yang, Z.M., Gou, Z.B., and DuFrane, S.A., 2014, Increasing magmatic oxidation state from Paleocene to Miocene in the eastern Tibetan Gangdese belt: Implication for collision-related porphyry Cu–Mo±Au mineralization: Economic Geology (in press)

Magmatic redox state plays an important role in the speciation and solubility of sulfur in silicate melts, which in turn influences the solubility of chalcophile and siderophile elements (e.g., Hamlyn et al., 1985; Bornhorst and Rose, 1986; Mungall, 2002; Richards, 2003, 2009, 2011; Jugo et al., 2005a, b; Jugo, 2009; Botcharnikov et al., 2011). Recent experiments on basaltic and andesitic glasses by Botcharnikov et al. (2011) indicate that dissolved sulfide activity, and therefore Au solubility in silicate melt reaches a maximum near ΔFMQ+1.0 (where ΔFMQ is measured in log fO_2 units relative to the fayalite–magnetite–quartz oxygen buffer). Limited data available for the solubility of Cu in silicate melts show that it is not as strongly affected by oxidation state as Au, possibly because it dissolves in the melt as oxide rather than sulfide species (Holzheid and Lodders, 2001; Zajacz et al., 2012, 2013). Nevertheless, it can be expected that sulfide saturation under relatively reducing conditions will strip Cu and other chalcophile metals from the melt (Hamlyn et al., 1985; Bornhorst and Rose, 1986; Richards et al., 1991; Spooner, 1993; Richards, 1995; Jugo et al., 2005a, b; Lee et al., 2012), whereas this is less likely to occur in more oxidized melts where sulfur is present mainly in oxide forms (Carroll and Rutherford, 1985; Candela, 1992). Thus, more oxidized melts (above ΔFMQ+1) are likely to be more prospective for the later formation of magmatic-hydrothermal porphyry Cu-Au deposits.

The loss of at least some metal to residual sulfide phases during deep crustal fractionation and crustal interaction (MASH processes of Hildreth and Moorbath, 1988) seems likely (Richards, 2009; Lee et al., 2012), and has been recorded in some instances (e.g., Richards, 2011). Of interest in this paper is the possible remobilization of these sulfide-hosted metals during later, post-subduction or collision-related magmatic processes. We have therefore studied the oxidation state of Cenozoic igneous rocks in the Gangdese belt to understand the control of magmatic oxidation state on collision-related porphyry deposit formation.

3.2 Geological setting of the Gangdese belt

The geological setting of the Gangdese belt has been described by Hou et al. (2009) and Wang et al. (2014a, b). The Gangdese arc is located on the south margin of the Lhasa terrane (Fig. 3-1), and is composed of voluminous calc-alkaline volcanic and intrusive rocks dating from the Jurassic to the Eocene (Harris et al., 1986; Mo et al., 2003, 2008; Dong et al., 2006a, b; Yang et al., 2011). Greater India (the Indian continental margin; Ali and Aitchison, 2005) first collided with the southern Lhasa subterrane at ~55–50 Ma (Allègre et al., 1984; Burg and Chen, 1984;

Rowley, 1996; de Sigoyer et al., 2000; Meng et al., 2012), marking the beginning of the India–Asia "soft collision" (Meng et al., 2012; van Hinsbergen et al., 2012). The Neo-Tethyan oceanic slab detached from Greater India at ~45 Ma (Van der Voo et al., 1999), and the Greater India slab was subsequently underthrust below the Lhasa terrane (Capitanio et al., 2010; Meng et al., 2012). The thicker, more rigid and buoyant Indian craton began to underthrust Asia at ~35 Ma ("hard-collision": Replumaz et al., 2010; van Hinsbergen et al., 2012), followed by breakoff of the Greater India slab at ~25–15 Ma (Van der Voo et al., 1999; Replumaz et al., 2010). A large number of small-volume calc-alkaline to mildly alkaline granitoids and minor volcanic flows were intruded or erupted in the eastern Gangdese belt (~89°E–93°E) between ~30 and 9 Ma (Fig. 3-2; Chung et al., 2003, 2005; Hou et al., 2004; Zhao et al., 2009; Zheng et al., 2012a, b).

Cenozoic porphyry Cu-Mo±Au deposits in Tibet are largely restricted to the Miocene intrusions in the eastern Gangdese belt (Fig. 3-2), and include the giant Qulong porphyry Cu-Mo deposit (1,420 Mt @ 0.5% Cu and 0.03% Mo: Yang et al., 2009), the Jiama porphyry Cu-Mo-Au deposit (1,054 Mt @ 0.44% Cu; Ying et al., 2014), and several medium- to small-sized porphyry Cu-Mo deposits (≤ 1 Mt Cu resource; e.g., Bairong, Chongjiang, Tingong, Nanmu, Gangjiang, and Lakang'e; Hou et al., 2011). Earlier Paleocene-Eocene arc rocks are mostly barren, and only three small porphyry deposits have been discovered there to date: the Sharang porphyry Mo deposit (52.25 ± 0.31 Ma; 10 Mt @ 0.061% Mo; Zhao et al., 2011a, 2014), the Jiru porphyry Cu deposit (49.2 ± 1.7 Ma; 41.9 Mt @ 0.43 Cu; Zheng et al., 2014), and the Yaguila Pb-Zn vein-type deposit (62.4 ± 0.6 Ma) with porphyry Mo mineralization (Huang et al., 2012). Several porphyry and skarn Cu deposits are related to Oligocene granitoids, such as the Nuri porphyry and skarn Cu deposit (23.36 ± 0.49 Ma; 79.4 Mt at 0.73% Cu; Chen et al., 2011, 2012; Zhang et al., 2012), and medium- to small-sized porphyry and Cu-Mo-W skarn deposits such as Mingze, Liebu, and Chongmuda.

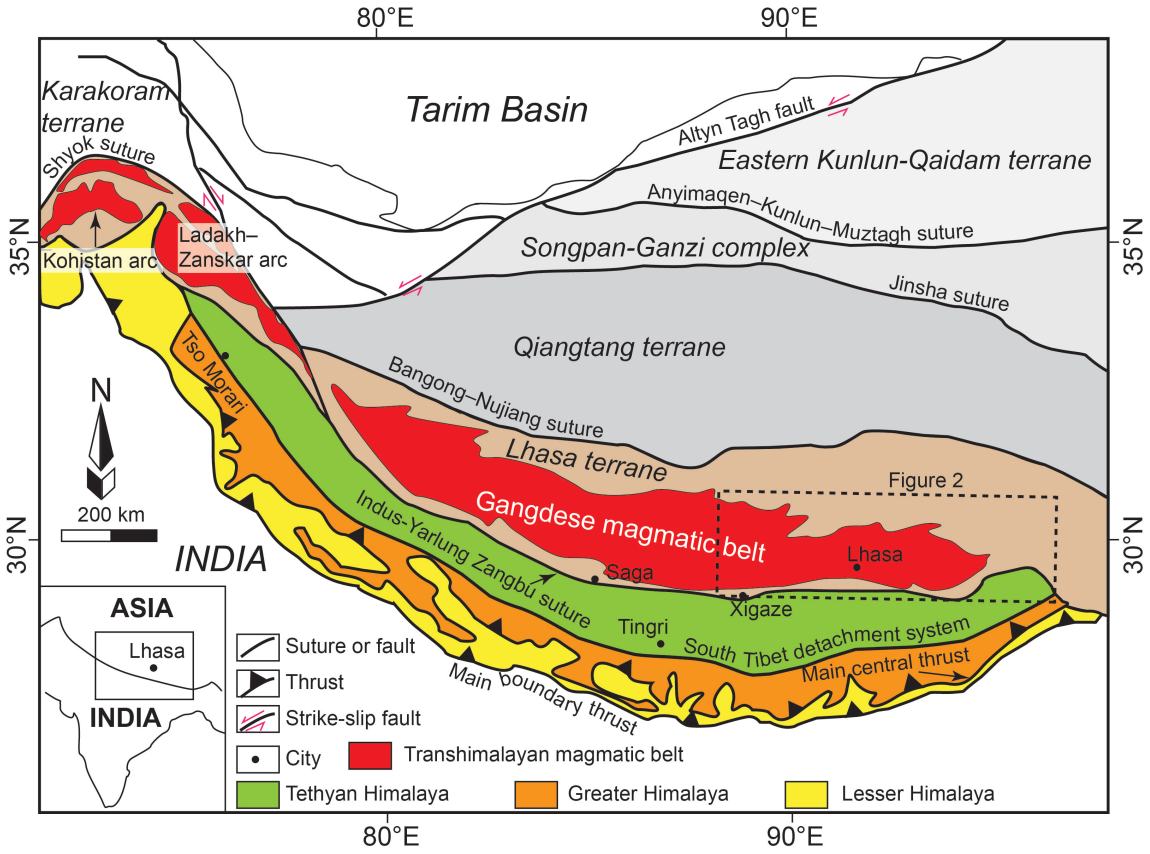

Fig. 3-1. Map indicating major tectonic units, boundaries, and magmatic belts within the Tibet-Qinghai Plateau (modified from Aitchison et al., 2007; White et al., 2011; Wang et al., 2014b).

3.3 Sampling strategy

Cenozoic igneous rocks in the Gangdese belt have been studied extensively by previous researchers (e.g., Hou et al., 2004; Yang, 2008; Li et al., 2011; Yang et al., 2011; Zheng et al., 2014), who mostly focused on variably altered rocks associated with porphyry-type mineralization. Such samples do not reliably preserve a record of original magmatic oxidation state. In order to address this question, we therefore collected new samples of fresh or minimally altered igneous rocks from thirty-five locations along the Gangdese magmatic belt between longitudes 88°E and 93°E (Fig. 3-2). The degree of alteration of these samples was assessed by visual and microscopic inspection, and loss-on-ignition (LOI) values < 2 wt.%. The locations and analytical methods applied to samples collected for this study are listed in Table 3-1.

Table 3-1: Cenozoic igneous rock locations from eastern Gangdese belt, their ages, and applied lithogeochemical and mineralogical analysis.

Sample number	Location	Lithology	Ore affinity	Longitude (E)	Latitude (N)	Altitude (m)	Age (Ma)	Lithogeo-chemistry	FeO	Amp	Mt-Ilm	Zir-con	Py	Pl	Age reference
WR-12-30	Xietong-men	Quartz monzonite	Ore-barren	88°19'11"	29°32'54"	4706	67.7	This study	√				√		Tafti (2011)
JR-2-XS	Jiru	Monzogranite	Ore-fertile	88°53'15"	29°39'21"	4716	48.6	Zheng et al. (2014)		√		1*			Zheng et al. (2014)
WR-12-25	Namling	Monzodiorite	Ore-barren	89°05'47"	29°27'04"	3860	43	This study	√						Wang et al. (2014b)
NM11-01	Nanmu	Quartz monzonite	Ore-barren	89°59'59"	29°20'21"	3780	53	Yang et al. (unpublished data)		√		√			Yang et al. (unpublished data)
QS-10	Quxu	Quartz monzonite	Ore-barren	90°15'03"	29°20'06"	3500	~50	Wang et al. (2014b)		√					Dong (2002)
WR-13-109	Gurong	Andesite	Ore-barren	90°45'30"	29°48'02"	3789	43.2±1.6	Lee et al. (2009)		√	√		√	√	Lee et al. (2009)
WR-13-111	Gurong	Andesite	Ore-barren	90°45'32"	29°48'12"	3789	43.2±1.6	Lee et al. (2009)		√	√			√	Lee et al. (2009)
WR-12-11	Gurong	Granite porphyry	Ore-barren	90°45'57"	29°47'10"	3910	50.18±0.50	Wang et al. (2014b)				√			Wang et al. (2014b)
QS11-05	Quxu	Granodiorite	Ore-barren	90°56'23"	29°30'25"	3615	53	Yang et al. (unpublished data)				√			Yang et al. (unpublished data)
QS-2	Quxu	Diorite	Ore-barren	90°56'58"	29°32'12"	3625	~50	Wang et al. (2014b)		√				√	Dong (2002)
QL-4	Qulong	Andesite	Ore-barren	91°36'40"	29°39'41"	4352	~67	This study							same with QL-5
QL-5	Qulong	Andesite	Ore-barren	91°36'40"	29°39'41"	4352	67.4±1.6	This study							This study
ZD-2	Zedang	Diorite	Ore-barren	91°48'54"	29°15'17"	3566	55.42±0.68	This study		√		√			This study
QS-9	Bangpu	Diorite	Ore-barren	91°55'36"	29°53'54"	3500	~50	Wang et al. (2014b)		√			√	√	Dong (2002)
PN-4	Panan	Andesite	Ore-barren	91°57'58"	29°15'05"	3623	60	This study							BGMRXAR (1993)
PN-5	Panan	Andesite	Ore-barren	91°57'55"	29°15'09"	3574	60	This study							BGMRXAR (1993)
KMQ-12-2	Kangmaqie	Granodiorite	Ore-barren	92°01'54"	29°21'29"	3914	50.79±0.45	Wang et al. (2014b)	√			√			Wang et al. (2014b)
RD-12-5	Riduo	Quartz monzonite	Ore-barren	92°08'45"	29°42'30"	4253	66.3±1.3	Wang et al. (2014b)				√		√	Wang et al. (2014b)
SRD28-04	Sharang	Quartz monzonite	Ore-fertile	92°41'16"	30°11'43"	5215	53	Zhao et al. (2011a)				2*			Zhao et al. (in prep)
0207-7-01	Sharang	Quartz monzonite	Ore-fertile	92°41'16"	30°11'43"	5206	53	Zhao et al. (2011a)				2*			Zhao et al. (in prep)
WR-12-15	Lingang	Quartz monzonite	Ore-barren	90°13'24"	29°24'49"	4000	32.5±0.5	Wang et al. (2014b)							Ji et al. (2009)
MZ-2	Zedang	Monzodiorite	Ore-fertile	91°51'33"	29°15'15"	3560	30.4±0.3	Wang et al.							Zheng et al.

		monzonite						(2014b)						(2012b)
CB-1	Zedang	Quartz monzonite	Ore-fertile	91°53'11"	29°15'12"	3650	27	Wang et al. (2014b)		√				same with CB-3
CB-3	Zedang	Monzodiorite	Ore-fertile	91°53'11"	29°15'12"	3650	27.19±0.29	This study			√			This study
CB-7	Zedang	Granite	Ore-fertile	91°54'51"	29°16'08"	3560	30.3±0.5	Wang et al. (2014b)		√				Zheng et al. (2012)
XB-12-3	Xueba	Granite porphyry	Ore-barren	92°21'32"	29°27'18"	4094	23.41±0.27	Wang et al. (2014b)	√		√		√	Wang et al. (2014b)
PZ11-03	Xigaze	Monzonite	Ore-barren	88°47'52"	29°17'58"	3939	17	Yang et al. (unpublished data)			√			Yang et al. (unpublished data)
JR11-07	Jiru	Quartz monzonite	Ore-fertile	88°53'15"	29°39'21"	4716	15	Yang et al. (unpublished data)			√			Yang et al. (unpublished data)
JR-13	Jiru	Quartz monzonite porphyry	Ore-fertile	88°53'15"	29°39'21"	4716	15	Yang et al. (unpublished data)		√				Yang et al. (unpublished data)
JR-5	Jiru	Monzonite porphyry	Ore-fertile	88°53'16"	29°39'24"	4697	16.19± 0.44	Wang et al. (2014b)		√	√			Wang et al. (2014b)
JR-2	Jiru	Quartz monzonite	Ore-fertile	88°54'17"	29°39'45"	4578	14.42±0.31	Wang et al. (2014b)			√			Wang et al. (2014b)
WR-13-15	Suojin	Dacite	Ore-barren	89°35'04"	29°40'56"	4336	13.9±0.1	Williams (2000)				√	√	Williams (2000)
CJ-4	Chong-jiang	Granite	Ore-fertile	89°58'19"	29°36'50"	4329	12.9±0.3	Hou et al. (2004)		√				Lin et al. (2004)
PG11-03	Pagu	Quartz monzonite	Ore-barren	90°00'48"	29°33'50"	4225	16	Yang et al. (unpublished data)			√			Yang et al. (unpublished data)
PG11-06	Pagu	Granodiorite	Ore-barren	90°00'48"	29°33'28"	4235	13	Yang et al. (unpublished data)			√			Yang et al. (unpublished data)
WR-13-122	Yangying	Andesite	Ore-barren	90°22'38"	29°43'12"	4615	10.73–11.4	Li et al. (1992)				√	√	Zhou et al. (2004)
WR-12-5	Quxu	Granite	Ore-barren	90°42'46"	29°26'29"	3930	21.3±0.6	Wang et al. (2014b)	√					Ji et al. (2009)
QL-10	Qulong	Granodiorite porphyry	Ore-fertile	91°36'51"	29°36'30"	5184	17.6±0.7	Yang (2008)		√				Yang (2008)
JM11-36	Jiama	Granodiorite porphyry	Ore-fertile	91°45'13"	29°41'43"	4650	15	Yang et al. (unpublished data)		√	√			Yang et al. (unpublished data)
BPzk303	Bangpu	Diorite porphyry	Ore-fertile	91°55'38"	29°53'28"	4666	14.07±0.08	Wang et al. (2012)			√		√	Wang et al. (2012)

Abbreviations: Amp = amphibole, FeO = FeO analysis by titration; Ilm = ilmenite; Mt = magnetite; Pl = plagioclase; Py = pyroxene.
1*: Xiang Sun, pers. comm., 2014
2*: Junxing Zhao, pers. comm., 2014

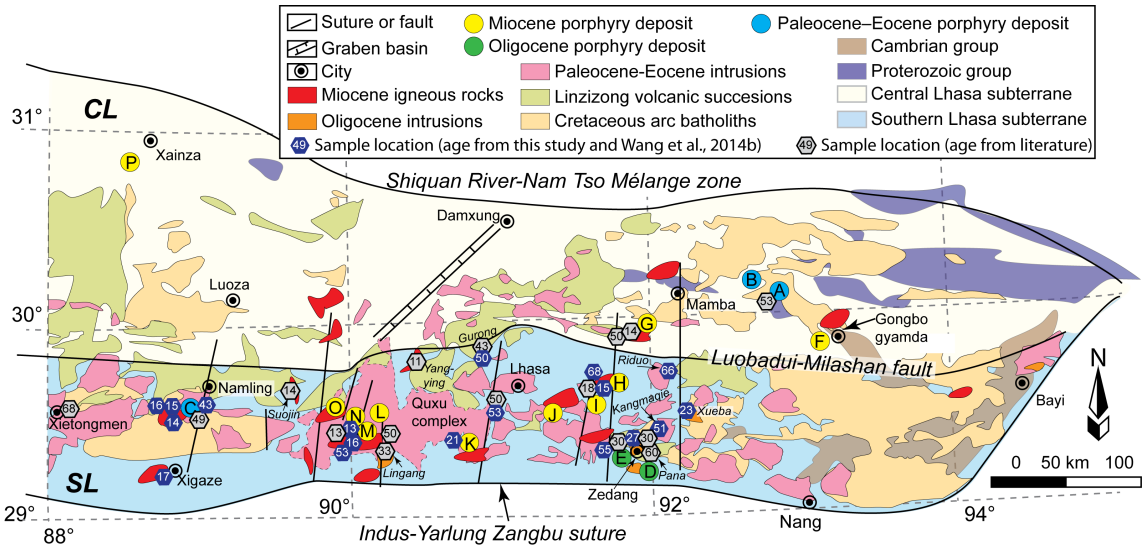

Fig. 3-2. Geology of the eastern Gangdese magmatic belt in the Lhasa terrane, showing the locations of samples described in this paper (modified from Zhu et al., 2011, 2013; Wang et al., 2014b). Abbreviations: CL = central Lhasa subterrane; NL = northern Lhasa subterrane; SL = southern Lhasa subterrane. Porphyry deposits (age): A. Sharang (Eocene), B. Yaguila (Paleocene), C. Jiru (Eocene, also with Miocene porphyry-type Cu-Mo mineralization), D. Zedang (Oligocene), E. Nuri (Oligocene), F. Tangbula (Miocene), G. Bangpu (Miocene), H. Jiama (Miocene), I. Qulong (Miocene), J. Lakang'e (Miocene), K. Nanmu (Miocene), L. Chongjiang (Miocene), M. Gangjiang (Miocene), N. Tingong (Miocene), O. Bairong (Miocene), P. Jiagang (Miocene). Hexagons with numerals mark the locations and ages (in Ma) of samples dated by zircon U-Pb from this study and the literature (see Table 3-1 for data sources). Three samples with new age results are given in Table A2, and eight samples with new lithogeochemical results are given in Table 3-2.

3.4 Petrography

Paleocene–Eocene suite

Twenty samples of Paleocene–Eocene igneous rocks collected from eastern Gangdese belt intrusions and coeval Linzizong volcanic rocks are representative of the lithologies and spatial distribution of such rocks as described and mapped by other authors (e.g., Dong, 2002; Dong et al., 2006a, b; Wen, 2007; Ji et al., 2009; Lee et al., 2009; Mo et al., 2008). Three granitoid samples were collected from ore-forming intrusions in the Eocene Jiru porphyry Cu deposit and Sharang porphyry Mo deposit, and other igneous rock samples were collected from barren intrusions or volcanic flows away from any known mineralization. The mafic–intermediate samples collected include gabbroic diorite, diorite, and andesite. They are mainly composed of clinopyroxene, plagioclase,

subordinate amphibole and orthopyroxene, and accessory minerals such as titanite and magnetite. The intermediate–felsic intrusions include granodiorite, monzodiorite, quartz monzonite porphyry, and granite porphyry, which consist of plagioclase, K-feldspar, and quartz, with minor clinopyroxene, orthopyroxene, amphibole, and biotite (Fig. 3-3A–D).

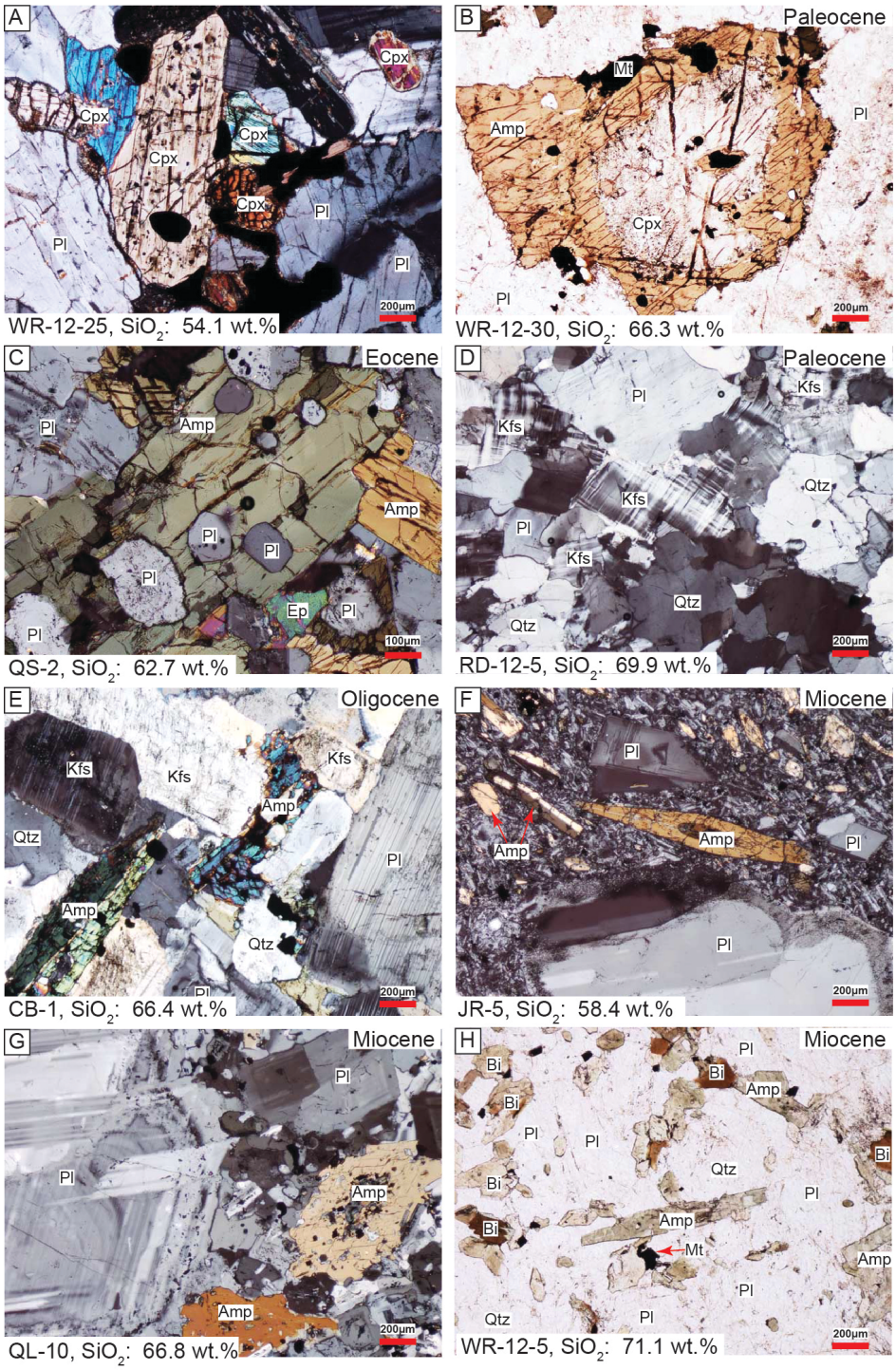

Fig. 3-3. Photomicrographs showing: A. Eocene monzodiorite (WR-12-25) with plagioclase and clinopyroxene; cross-polarized light; B. Paleocene quartz monzonite (WR-12-30) with clinopyroxene replaced by amphibole; cross-polarized light; C. Eocene diorite (QS-2) with plagioclase as inclusions in amphibole; cross-polarized light; D. Paleocene quartz monzonite (RD-12-5) with K-feldspar, plagioclase, and quartz; cross-polarized light; E. Oligocene quartz monzonite (CB-1), with amphibole, plagioclase, and K-feldspar; cross-polarized light; F. Miocene monzonite porphyry (JR-5), with amphibole and plagioclase phenocrysts; cross-polarized light; G. Miocene granodiorite porphyry (QL-10) with amphibole and plagioclase; cross-polarized light; H. Miocene granite (WR-12-5), with amphibole, plagioclase, biotite, and magnetite; plane-polarized light. Abbreviations: Amp = amphibole; Bi = biotite; Cpx = clinopyroxene; Ep = epidote; Kfs = K-feldspar; Mt = magnetite; Pl = plagioclase; Qtz = quartz.

Oligocene suite

Oligocene igneous rocks in the Gangdese belt are sparse, and mainly restricted to 90°E–92.5°E (most intrusions are too small to be visible in Fig. 3-2). Seven samples of granitoid were collected from all five reported locations of Oligocene igneous rocks: five samples were collected from the ore-forming granitoids from porphyry and Cu-Mo-W skarn deposits in the Zedang area, and two samples were collected from the Lingang and Xueba areas away from any known mineralization. The sample suite includes monzodiorite, quartz monzonite porphyry, granite porphyry, and granite. Amphibole is common in this suite, and occurs as phenocrysts or equigranular intergrowths with plagioclase or K-feldspar (Fig. 3-3E). Magnetite, titanite, and zircon are common accessory minerals.

Miocene suite

Miocene igneous rocks in the eastern Gangdese belt occur as shallowly-emplaced, small-volume plugs, dikes, or sills of porphyritic rock, with minor andesitic-andesitic flow, that intruded or covered older Cretaceous–Eocene intrusive and volcanic rocks (Fig. 3-2). The dominant Miocene lithologies are quartz monzonite porphyry, granodiorite, granite porphyry, and minor intermediate–felsic calc-alkaline volcanic rocks. Twelve samples of granitoids were collected from the Bangpu, Chongjiang, Jiama, and Qulong porphyry Cu-Mo±Au deposits, from the Jiru area where Miocene porphyry-type Cu-Mo mineralization has been identified, and from the Xigaze area, Pagu and Quxu areas where no mineralization is known. We collected samples away from known mineralized centers

in order to avoid hydrothermal alteration. The granitoid samples collected for this study have phenocrysts of plagioclase, K-feldspar, amphibole, and quartz (Fig. 3F–H). These granitoids are representative of the lithologies and spatial distribution of such rocks as described and mapped by other authors (e.g. Hou et al., 2004; Yang et al., 2009; Li et al., 2011; Zheng et al., 2014). Coeval volcanic rocks collected from this area are mainly andesite and dacite distal to any known mineralization (the Yangying and Suojin areas: Table 3-1), and contain orthopyroxene, clinopyroxene, amphibole, and plagioclase phenocrysts.

3.5 Analytical techniques

Lithogeochemical analysis

Samples for lithogeochemical analysis were prepared by crushing (using corundum plates) and grinding in an agate disk mill at the Hebei Geological Survey Laboratory, China. The expected contamination of Si and Al by these methods is estimated to be less than 1 relative percent (as assessed from analyses of standards and blanks). All samples were analyzed by Activation Laboratories (Ancaster, Ontario, Canada) using a combination of methods including instrumental neutron activation analysis and fusion ICP-MS (Actlabs code 4E Research ICP/MS). Accuracy for major elements, as determined by reproducibility of standards and duplicates, is typically within five relative percent (< 3 relative % for SiO_2 and Al_2O_3), and to within 10 relative percent for most minor and trace elements. FeO analysis by titration was undertaken for five fresh samples in order to determine whole-rock Fe^{3+}/Fe^{2+} ratios. The accuracy for FeO determination is better than three relative percent.

Electron microprobe analyses

Pyroxene, amphibole, biotite, plagioclase, magnetite, and ilmenite crystals in igneous rocks from the Gangdese belt were analyzed by electron microprobe at the University of Alberta, Canada. Electron microprobe data were acquired on a JEOL 8900 instrument operated at 15 kV accelerating voltage and 15 nA probe current, and with a beam diameter of 1 to 5 μm. A variety of minerals, oxides, and elemental standards were used for calibration, and data reductions were undertaken with the CITZAF routine of J.T.

Armstrong (as implemented by P. Carpenter in the JEOL software). The limits of detection are typically lower than 500 ppm (≤800 ppm for Mn, Fe, Ti, Cr, and Ni; ≤5000 ppm for F), and analytical precision for major elements is better than one relative percent. Amphibole and pyroxene analyses were recalculated to account for Fe^{3+} following the formula of Droop (1987). The ILMAT Excel spreadsheet (Lepage, 2003) was used to recalculate magnetite and ilmenite compositions, and to estimate magmatic temperature and oxidation state. Temperature and fO_2 were also estimated based on the amphibole thermometer and oxygen barometer (Ridolfi et al., 2010), and pressure was estimated using the Al-in-amphibole barometer (Schmidt, 1992). The Probe-AMPH Excel spreadsheet (Tindle and Webb, 1994) was used to recalculate amphibole compositions.

Zircon U-Pb dating

Zircons were separated from 2–3 kg of rock samples by heavy-liquid and magnetic methods followed by hand-picking in the Laboratory of the Geological Team of Hebei Province, China. Selected crystals were typical of magmatic zircons: euhedral, clear, colorless, devoid of mineral and fluid inclusions, and 100–250 μm in diameter. The zircons were mounted in epoxy and polished to reveal their interiors.

Cathodoluminescence (CL), backscattered electron (BSE), and secondary electron (SE) images were obtained of the zircon grain mounts prior to analysis, to reveal internal zonations (see Fig. A1 in appendices). U-Pb age determinations were obtained using a NuPlasma multiple collector inductively coupled plasma mass spectrometer (MC-ICP-MS: Nu Instruments) coupled to a frequency quintupled (λ = 213 nm) Nd:YAG UP-213 laser ablation system (New Wave Research) at the Radiogenic Isotope Facility, University of Alberta, Canada. The laser spot size was 40 μm, with a 4 Hz pulse rate, and a fluence of ~3 J/cm^2. The MC-ICP-MS instrument is fitted with a modified collector block containing twelve Faraday collectors and three ion counting detectors dispersed on the low mass side of the array, allowing simultaneous measurement of U and Pb isotopes. Analytical protocols are modified from Simonetti et al. (2005). We used zircon standard GJ1 (Jackson et al., 2004) and an in-house standard LH9415 (Ashton et al., 1999) to correct for U-Pb laser induced elemental fractionation and instrument bias. The 2σ reproducibility of the standards was typically one percent for $^{207}Pb/^{206}Pb$ and three

percent for $^{206}Pb/^{238}U$. Reported errors are a quadratic combination of (1) the standard error of the analysis and (2) the standard deviation of the standards. Correction for common Pb was done graphically by computing a linear regression through the data and a common $^{207}Pb/^{206}Pb$ value of 0.86, though for most cases the uncorrected $^{206}Pb/^{238}U$ age is within error of the lower intercept age.

Zircon trace element analysis

Zircons were mounted in epoxy with a chip of standard NIST 612 glass. A frequency quintupled Nd-YAG laser (UP 213, New Wave Research) was used to ablate the zircons and standard, and ablated material was carried by He-Ar gas (flow rates of 0.73 L He/min and 0.85 L Ar/min) to a Finnigan MAT ELEMENT II high-resolution inductively coupled plasma mass spectrometer (HR-ICP-MS) at the National Research Center for Geoanalysis, Beijing, China. Laser ablation pits were approximately 40 μm wide and 20 μm deep. Data were acquired for 12 s with the laser off, and 43 s with the laser on, then the system was flushed with He-Ar gas for 15 s with the laser off. Each block of ten zircon analyses was bracketed by analysis of standard glass NIST 612, which was used to correct for mass bias drift during analysis (Pearce et al., 1997). The calibration procedure using internal standards and matrix normalization followed Hu et al. (2008). Calibration was conducted by normalizing count rates for each analyzed element with Si to obtain its concentration, and assuming SiO_2 to be stoichiometric in zircon ($ZrSiO_4$) with a concentration of ca. 32.8 wt.%. Accuracy for most selected elements, as determined by reproducibility of laboratory standards and duplicates, is within 10 relative %, whereas some light rare earth elements (such as La and Pr) have above 10 relative % (depending on concentrations) in accuracy.

In order to avoid mineral and glass inclusions, inherited cores, and fractures, the laser ablation spots in zircon were selected carefully. Apatite inclusions are common in zircon grains and can strongly affect REE contents, so phosphorus was included in the list of elements measured in order to monitor for apatite inclusions.

Table 3-2. Major and trace element analysis of igneous rock samples from the Gangdese magmatic belt

Sample Number	WR-12-30	WR-12-25	QL-4	QL-5	ZD-2	PN-4	PN-5	KMQ-12-2*	CB-3	XB-12-3*	WR-12-5*
Weight %											
SiO_2	66.34	54.07	55.13	56.06	56.73	63.45	53.75	52.52	54.11	72.79	71.06
TiO_2	0.57	0.83	0.74	0.63	0.80	0.73	0.87	1.03	0.91	0.26	0.24
Al_2O_3	15.57	18.54	15.21	14.70	17.10	15.74	19.96	18.00	17.37	14.35	15.80
ΣFe_2O_3*	4.49	8.13	7.63	7.53	7.85	5.52	8.54	9.89	7.00	1.87	1.65
FeO	2.90	5.70	N.A	N.A	N.A	N.A	N.A	6.40	N.A	1.00	0.80
MnO	0.10	0.13	0.18	0.13	0.19	0.09	0.14	0.15	0.14	0.05	0.04
MgO	1.47	4.57	6.95	6.62	3.88	2.19	3.34	3.88	4.30	0.42	0.50
CaO	3.61	8.32	7.85	7.60	6.62	4.38	9.00	8.03	6.15	1.72	2.41
Na_2O	3.84	3.83	2.54	2.38	4.04	3.35	2.81	3.34	4.49	4.02	4.94
K_2O	3.83	1.52	1.51	1.40	1.76	4.06	0.48	1.26	3.20	3.76	3.05
P_2O_5	0.14	0.20	0.11	0.08	0.19	0.19	0.26	0.27	0.82	0.10	0.09
LOI	0.38	0.00	2.40	3.77	1.73	0.77	1.52	0.66	1.14	0.37	0.31
Total	100.30	100.08	100.30	100.90	100.90	100.50	100.70	99.04	99.62	99.71	100.10
ppm											
Sc	10.3	22	26	24.8	20	6.94	14.6	22.8	12.4	3.54	2.75
V	79	242	191	184	178	118	189	234	144	25	36
Cr	8.4	47.8	336	358	46.1	15.5	25.5	17.3	57.9	bdl	bdl
Co	11.1	27	30.1	30.5	21.8	8.5	23.6	28	20.5	4	3
Ni	6	37	113	102	16	13	20	15	43	2	3
Rb	144	30	51	40	63	155	21	45	175	180	84
Ba	541	407	211	277	265	356	111	289	676	465	513
Th	17.8	3.14	5.77	7.24	8.47	22.3	2.95	1.51	66	26.5	8.36
U	2.98	0.74	1.78	2.44	3.22	4.01	0.91	0.52	12.7	4.85	2.66
Nb	7.5	2.3	3.4	3.6	7.1	9.6	3.2	2.6	14.3	12.5	3.7
Ta	0.7	0.15	0.33	0.39	0.98	0.88	0.22	0.14	0.56	1.3	0.17
La	29.3	16.6	14.4	12.5	13	27.9	17.2	12.1	106	34	14.3
Ce	59	33.3	30.2	26	32.4	58.4	36.2	28.7	194	66.4	27.6
Pb	19	bdl	9	bdl	5	8	bdl	bdl	19	36	33
Pr	5.99	3.65	3.69	3.16	4.33	6.74	4.59	3.63	20.8	6.37	2.98
Sr	365	933	315	295	333	465	861	639	661	332	735
Nd	22.7	15.2	14.7	12.6	17.7	24.7	18.5	17.2	74	21.9	11.1
Sm	4.31	3	3.52	2.97	4.08	4.82	4.04	4.17	11.6	3.33	1.8
Zr	211	68	115	109	106	268	94	101	326	143	87
Hf	5.2	1.7	3	3.1	3.6	6.8	2.4	2.4	7.6	3.6	2.8
Eu	0.883	1.1	0.93	0.77	0.862	0.936	1.22	1.2	1.53	0.623	0.46
Gd	3.62	2.82	3.45	2.95	3.9	3.79	3.53	4.41	7.11	2.08	1.09
Tb	0.61	0.44	0.62	0.52	0.66	0.61	0.58	0.64	0.83	0.29	0.14
Dy	3.42	2.32	3.75	3.2	3.9	3.54	3.13	3.57	3.86	1.54	0.68
Y	20	13	19	17	21	18	16	20	17	10	4
Ho	0.68	0.46	0.77	0.67	0.81	0.7	0.6	0.68	0.64	0.28	0.13
Er	2.03	1.29	2.23	1.95	2.41	2.06	1.73	1.93	1.66	0.84	0.33
Tm	0.323	0.192	0.345	0.299	0.389	0.312	0.242	0.289	0.232	0.131	0.047
Yb	2.15	1.24	2.29	1.93	2.75	2.1	1.57	1.87	1.5	0.92	0.32
Lu	0.334	0.189	0.375	0.318	0.454	0.348	0.257	0.277	0.238	0.143	0.055
Sr/Y	18.25	71.77	16.58	17.35	15.86	25.83	53.81	31.95	38.88	33.20	183.75
La/Yb	13.63	13.39	6.29	6.48	4.73	13.29	10.96	6.47	70.67	36.96	44.69

*Data from Wang et al. (2014b) with newly added FeO results (by titration) from this study.
Abbreviations: bdl = below detection limit; N.A. = Non analyzed

3.6 fO_2 meters

Whole-rock Fe^{3+}/Fe^{2+}

The whole-rock Fe^{3+}/Fe^{2+} ratio is an empirical redox indicator (e.g., Brett and Sato, 1984; Rhodes and Vollinger, 2005). However, it can only be used on fresh melt inclusions or igneous rocks devoid of hydrothermal alteration or surficial weathering. Completely unaltered igneous rocks are rare in association with porphyry deposits because of widespread hydrothermal alteration. Consequently, few of the samples collected in this study (or reported in the literature) from within or near porphyry systems in the Gangdese belt are sufficiently fresh for this method to yield reliable indications of original magmatic oxidation state. We report such data where considered reliable.

Amphibole oxygen barometer

Amphibole stability depends on both water content and oxidation state of the magma, as well as other melt compositional variables (e.g., Sisson and Grove, 1993; Grove et al., 2003). Experiments by Scaillet and Evans (1999) and Ridolfi et al. (2008, 2010), combined with oxygen fugacity–amphibole composition regression analyses, show that relative oxygen fugacity (ΔNNO: where NNO is the nickel–nickel oxide buffer) is closely correlated with Mg* (see the definition of Mg* in Ridolfi et al., 2010) of amphibole (R^2 = 0.89). The ΔNNO-Mg* equation (1) is estimated to be accurate to within 0.22 log fO_2 units (1σ; Ridolfi et al., 2010), and is in agreement with the uncertainty expected from experiments (0.2–0.3 log fO_2 units; Scaillet and Evans, 1999; Pichavant et al., 2002).

$$\Delta \mathrm{NNO} = 1.644\mathrm{Mg}^{*} - 4.01 \qquad (1)$$

This oxygen barometer is valid for magmas in the range of 550°–1120°C, <1,200 MPa, and $-1 \leq \Delta\mathrm{NNO} \leq +5$. The method works best for amphibole phenocrysts in volcanic rocks with homogeneous compositions (i.e., unzoned). The advantage of this method is that amphiboles are common in igneous rocks, and fO_2 can be determined from a single mineral phase (i.e., it does not require equilibration with other minerals). In addition,

temperature and pressure can also be retrieved from amphibole analyses (Hollister et al., 1987; Johnson and Rutherford, 1989; Schmidt, 1992; Ridolfi et al., 2010).

Application of this formulation to fO_2 estimates in silicic volcanic rocks in the Panamanian arc, central America (Hidalgo et al., 2011), shows that magmatic oxygen fugacities increase from ΔNNO+1 in high P-T tschermakitic pargasites to ΔNNO+2.5 in shallow-crystallized magnesiohornblendes, in agreement with previous studies (e.g., Carmichael, 1991; Müntener et al., 2001). Similarly, amphiboles from volcanic rocks from the intra-oceanic Kermadec arc in the SW Pacific yielded fO_2 values similar to those calculated from the Fe-Ti two-oxide thermo-oxybarometer (Ghiorso and Evans, 2008; Ridolfi et al., 2010; Barker et al., 2013).

Ilmenite–magnetite oxygen barometer

The ilmenite–magnetite oxygen barometer is used widely to estimate magmatic fO_2 based on the assumed equilibrium between these two Fe-Ti oxides (Buddington and Lindsley, 1964; Andersen and Lindsley, 1985; Bacon and Hirschmann, 1988; Ghiorso and Sack, 1991; Andersen et al., 1993; Audétat and Pettke, 2006; Ghiorso and Evans, 2008; Sauerzapf et al., 2008). However, these minerals are prone to re-equilibration at lower temperatures during slow cooling or due to hydrothermal alteration (Venezky and Rutherford, 1999). Consequently, Fe-Ti oxides rarely retain magmatic compositions in slowly cooled plutonic rocks or in hydrothermally altered rocks (Andersen, 1985; Idrus et al., 2007; Anderson et al., 2008). In addition, ilmenite and magnetite are not always both present in igneous rocks, and where they coexist, they may not have coprecipitated (and therefore may not be an equilibrium mineral assemblage).

We restrict our data to analyses of ilmenite and magnetite from fresh volcanic or subvolcanic rocks where textural equilibrium can be demonstrated (where these minerals occur as intergrowths) or can be assumed (e.g., where both minerals occur in the groundmass, or as microphenocrysts, but not mixtures of the two). The ILMAT spreadsheet of Lepage (2003) was used in this study to calculate temperature and magmatic fO_2 from paired magnetite and ilmenite analyses; this method is based on the empirical approaches given by several authors (Powell and Powell, 1977; Spencer and

Lindsley, 1981; Andersen and Lindsley, 1985). Typical 2σ uncertainties for T and fO_2 are estimated to be ~10–35°C, and 0.1–0.2 log fO_2 units (Spencer and Lindsley, 1981).

Zircon Ce^{4+}/Ce^{3+} and Eu_N/Eu_N ratios*

Zircon is a common accessory mineral in intermediate to felsic intrusive rocks, and is resistant to hydrothermal alteration and surficial weathering. In addition to being used in geochronology and radiogenic isotope tracing, Ce^{4+}/Ce^{3+} ratios in zircon can be used to estimate magmatic oxidation state (Ballard et al., 2002; Trail et al., 2011; Burnham and Berry, 2012). Ce^{4+} preferentially partitions into zircon because it has identical charge and similar ionic size to Zr^{4+}, whereas other light rare earth elements (LREE, including Ce^{3+}) are strongly excluded. Consequently, Ce^{4+}/Ce^{3+} ratios have been used to distinguish relatively oxidized ore-bearing porphyries (Ce^{4+}/Ce^{3+} mostly > 50) from more reduced barren intrusive suites (Ce^{4+}/Ce^{3+} mostly < 50; Ballard et al., 2002; Liang et al., 2006; Muñoz et al., 2012, Wang et al., 2013).

Equation (2) was derived by Ballard et al. (2002) to calculate the Ce^{4+}/Ce^{3+} ratio in zircon based on mineral–melt partitioning of trace elements using a lattice-strain model:

$$Ce^{4+}/Ce^{3+} = \frac{Ce_{melt} - \frac{Ce_{zircon}}{D_{Ce^{3+}}^{zircon/melt}}}{\frac{Ce_{zircon}}{D_{Ce^{4+}}^{zircon/melt}} - Ce_{melt}} \qquad (2)$$

A linear regression of the whole rare earth element (REE) spectrum versus ionic radius is used to derive a value for $D_{Ce^{3+}}^{Zircon/melt}$, and a linear regression of U, Th, Zr, and Hf concentrations versus ionic radius to calculate $D_{Ce^{4+}}^{Zircon/melt}$. Resultant Ce^{4+}/Ce^{3+} ratios have been shown to be directly proportional to magmatic oxidation state in an experimental study by Burnham and Berry (2012). However, it is difficult to quantitatively calculate oxygen fugacities from Ce anomalies in zircon because of difficulties in precisely analyzing La or Pr contents in zircon by laser ablation-ICPMS or ion-microprobe, due to their very low abundances (typically from below 10 ppb to 100 ppb, respectively; Trail et

al., 2011). In addition, the contents of these elements can be affected radically by the presence of small inclusions of apatite, which can be rich in LREE (Ballard et al., 2002).

Eu_N/Eu_N^* ratios (where $Eu_N/Eu_N^* = Eu_N/(Sm_N*Gd_N)^{0.5}$) in zircons also correlate with oxidation state because Eu^{2+} is excluded from zircon relative to Eu^{3+}. Thus, negative Eu anomalies on normalized REE diagrams (which correspond to low Eu_N/Eu_N^* ratios $<< 1$) occur under relatively reducing conditions where most of the Eu is present as Eu^{2+}. REE patterns lacking negative Eu anomalies (i.e., Eu_N/Eu_N^* ratios ≈ 1) are produced under relatively oxidizing conditions where most of the Eu is present as Eu^{3+} (Burnham and Berry, 2012). However, the redox effect on Eu_N/Eu_N^* ratios in zircons is complicated by the effects of plagioclase crystallization, which preferentially partitions Eu^{2+} (relative to Eu^{3+} and other REE). Thus, plagioclase crystallization under relatively reducing conditions will deplete the melt in Eu, and will therefore affect Eu_N/Eu_N^* ratios in zircons. Early plagioclase crystallization occurs in relatively water-poor silicate melts (Moore and Carmichael, 1998), and therefore this effect will be most pronounced in dry, reduced magmas (Baker and Eggler, 1983; Naney, 1983; Rohrlach and Loucks, 2005). On the other hand, hydrous, oxidized magmas (such as those associated with many porphyry deposits) should be relatively unaffected. Consequently, Eu_N/Eu_N^* ratios in zircons from porphyry-related magmas provides an additional but less certain indication of magmatic oxidation state than Ce^{4+}/Ce^{3+} ratios, and should be used with caution.

3.7 Lithogeochemical results

Fresh or least-altered samples were collected for lithogeochemical analyses, and mafic end-members of igneous suites were prioritized in order to evaluate least-evolved compositions. Whole-rock geochemical data from this study and Wang et al. (2014b) are illustrated on Figures 3-4, 5 and listed in Table 3-2. These data have been supplemented with analyses from the following sources: Harrison et al. (2000); Chung et al. (2003); Hou et al. (2004); Chen (2006); Dong et al. (2006a, b); Guo et al. (2007); Wen (2007); Yang (2008); Lee et al. (2009, 2011); Wang et al. (2010); Xia et al. (2010); Xu et al. (2010); Li et al. (2011); Tafti (2011); Xiao (2011); Zhao et al. (2011a, b); Zhu et al. (2011); Ji et al. (2012); Wang et al. (2012); Zheng et al. (2012a, b).

There are no significant differences in major element compositions among Paleocene–

Eocene, Oligocene, and Miocene suites, except that the Oligocene and Miocene suites are slightly alkali-rich (Fig. 3-4A), and rare Oligocene samples have more alkaline compositions. All samples have subduction characteristics, such as relative depletions in Nb and Ta, and enrichments in Rb, Ba, Th, U, K, and Pb on a primitive mantle-normalized trace element diagram (Fig. 3-5B, D, F). Samples from the Paleocene–Eocene suite have relatively low Sr/Y (average = 30.8 ± 16.9, n = 16) ratios, which increase through the Oligocene (average = 70.7 ± 27.0, n = 7) to the Miocene (average = 135 ± 52.8, n = 8; Fig. 3-4B). Samples from the Paleocene–Eocene suite have moderately negative Eu anomalies (Fig. 3-5A), whereas samples from the Oligocene and Miocene suites have weak to absent negative Eu anomalies (Fig. 3-5C, E). In addition, samples from the Oligocene and Miocene suites display listric-shaped REE patterns on a chondrite-normalized diagram (Fig. 3-5C, E).

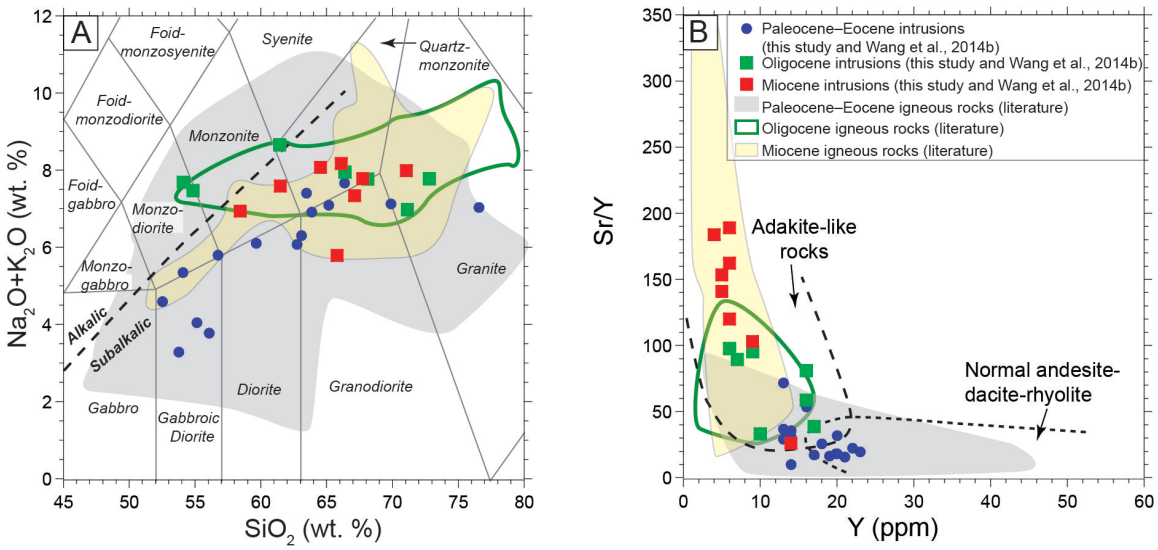

Fig. 3-4. A. Total alkali-silica diagram (after Middlemost, 1994) for Paleocene–Eocene, Oligocene, and Miocene samples of igneous rocks from this study and Wang et al. (2014b) compared with data from the literature (see text and Table 3-1 for data sources). The alkaline/subalkaline boundary of Irvine and Baragar (1971) is shown. B. Sr/Y vs. Y. "Adakite-like rock" field is from Defant and Drummond (1990).

3.8 Mineralogy of Cenozoic igneous rocks from the Gangdese belt

Paleocene–Eocene suite

Both orthopyroxene (enstatite, ferrosilite, and pigeonite) and clinopyroxene (augite and diopside) are present in mafic and intermediate rocks from the Paleocene-Eocene

suite. Plagioclase phenocrysts are ubiquitous in this suite, and the compositions of this mineral range from bytownite (An_{max} = 85) in gabbro to albite (An < 10) in granite. As noted by Wang et al. (2014b), plagioclase in this suite crystallized earlier than amphibole, as illustrated by inclusions of plagioclase in later ophitic amphibole in diorites (Fig. 3-3C) and granodiorites. The amphiboles typically occur as interstitial grains or as granular replacements of orthopyroxene, suggesting late-stage growth from residual melts. These mineralogical characteristics suggest that the Paleocene–Eocene magmas were relatively dry and evolved primarily by fractionation of pyroxene and plagioclase (Wang et al., 2014b). Magnetite is common in this suite, whereas ilmenite is subordinate.

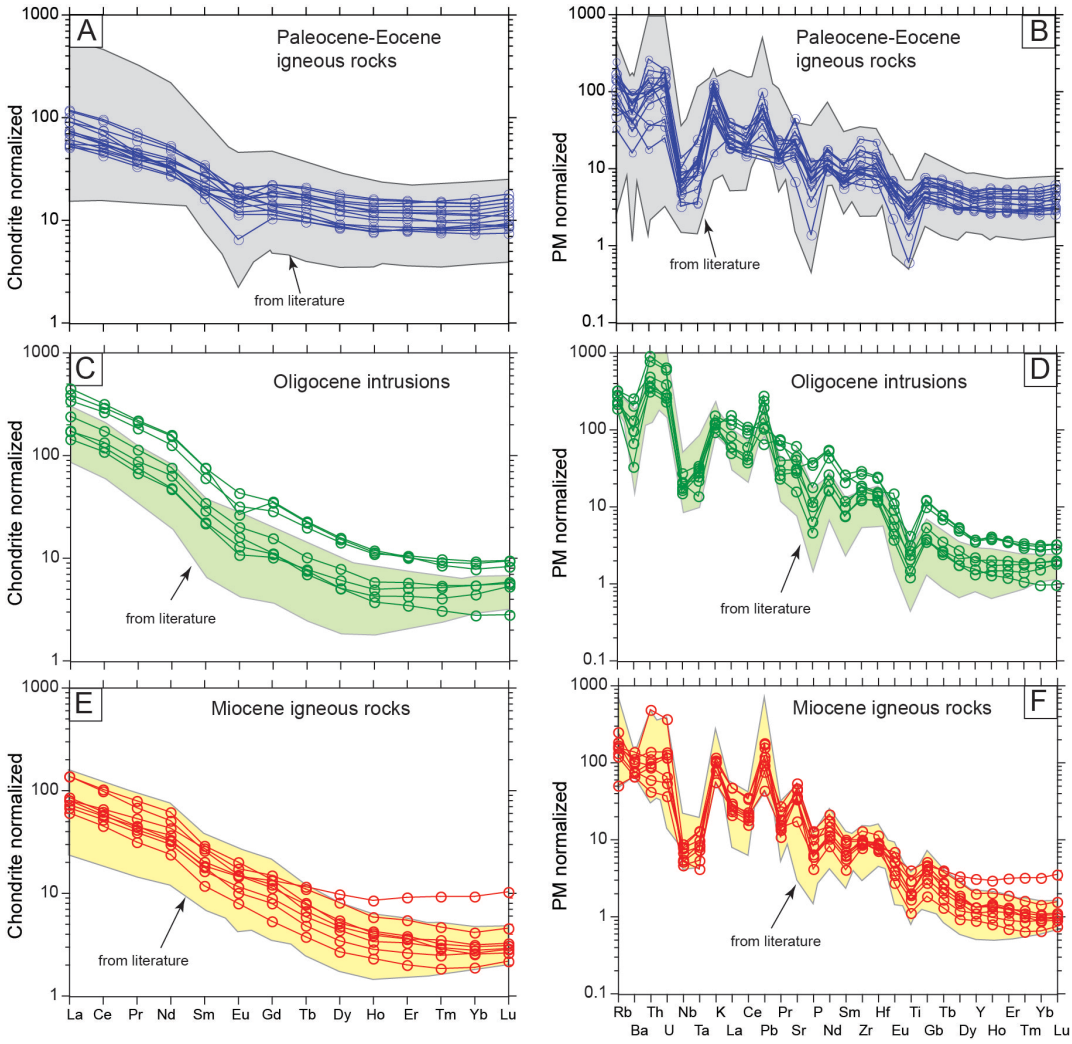

Fig. 3-5. Chondrite- and primitive mantle (PM)-normalized trace element diagrams for Paleocene–Eocene, Oligocene, and Miocene samples of igneous rocks from this study and Wang et al. (2014b) compared with data from the literature (see text and Table 3-1

for data sources): A, B. Paleocene–Eocene igneous rocks; C, D. Oligocene intrusive rocks; E, F. Miocene igneous rocks. Normalization values are from Sun and McDonough (1989).

Oligocene suite

Amphibole is abundant in this suite, and occurs as equigranular intergrowths with plagioclase (Fig. 3-3E). Plagioclase and K-feldspar phenocrysts are ubiquitous in this suite. The compositions of plagioclase range from andesine (An_{max} = 38) in monzodiorite to albite (An < 10) in granite. The Oligocene intermediate–felsic magmas are hydrous (> 4 wt.% H_2O; Wang et al., 2014b), and fractionated abundant early hornblende with plagioclase (e.g., Moore and Carmichael, 1998; Müntener et al., 2001). Magnetite is common in this suite, whereas ilmenite is rare.

Miocene suite

Pyroxenes (augite and diopside) are only present in volcanic rocks. Amphibole phenocrysts are abundant in this suite (Fig. 3-3F–H). The compositions of plagioclases in volcanic rocks rang from labradorite (An_{max} = 56) to albite (An < 10) in andesitic–dacitic sequence. Plagioclase and K-feldspar phenocrysts are common in granitoids (Fig. 3F–H). The compositions of plagioclase in granitoids range from andesine (An_{max} = 47) in granodiorite to albite (An < 10) in granite. The common occurrence of hornblende as a phenocryst phase in these rocks suggests that fractionation of amphibole occurred earlier, and indicates that the Miocene magmas were hydrous (Wang et al., 2014b). Magnetite is common in this suite, whereas ilmenite is rare.

3.9 Zircon U-Pb results

A large number of U-Pb zircon dates exist for Cenozoic rocks from the Gangdese belt, such that the age of most outcrops is well established. However, we have supplemented these data with analyses for three new samples from our suite whose ages were previously unknown. Full analytical data are listed in Table A2.

A sample of andesitic volcanic rock (QL-5) from near the Qulong Cu-Mo deposit mapped as Paleocene contains a homogeneous population of zircons, mostly with relatively low common lead contents. The sample yielded a U-Pb concordia intercept age

of 67.4 ± 1.6 Ma (MSWD = 0.72; Fig. 3-6A; Table A2).

A sample of Paleocene–Eocene diorite (ZD-2) from the Zedang area contains a complicated population of zircons. The scatter in age data appears to be caused by four crystals with Pb loss (Fig. 3-6B). Regression of this population without young crystals (24 of 28 zircon crystals) yielded a concordia intercept age of 55.42 ± 0.68 Ma (MSWD = 1.18; Fig. 3-6B).

One previously undated monzodiorite intrusion from the Zedang area (sample CB-3) contains a homogeneous population of zircons, mostly with low common lead contents. This sample yielded a concordia intercept age of 27.93 ± 0.35 Ma (MSWD = 1.8; Fig. 3-6C).

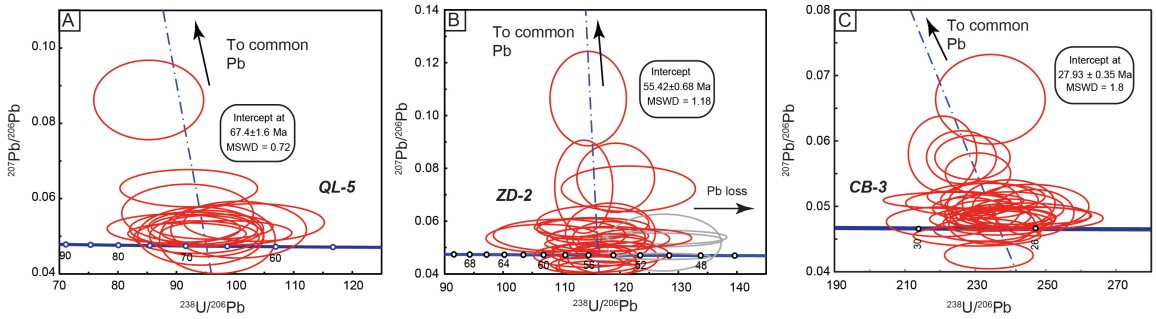

Fig. 3-6. Zircon U-Pb Tera-Wasserburg concordia diagrams for igneous samples. A. Sample QL-5; B. Sample ZD-2, C. Sample CB-3. Error ellipses are plotted at 2σ, analyses excluded from the age calculations are shown in gray (see text for details).

3. 10 Estimates of magmatic oxidation state

Qualitative and quantitative estimates of magmatic oxidation state have been estimated from the compositions of amphiboles, magnetite–ilmenite pairs, zircons, and whole-rock Fe^{3+}/Fe^{2+} ratios for selected fresh samples of Paleocene–Eocene, Oligocene, and Miocene igneous rocks from the eastern Gangdese belt.

Amphiboles

Crystallization pressure and temperature, and magmatic oxidation state were estimated from amphibole compositions using the formulae of Schmidt (1992) and Ridolfi et al. (2010).

Paleocene–Eocene: Amphibole phenocrysts are rare in Paleocene–Eocene igneous rocks. All of the grains analyzed are calcic amphiboles, and are classified as magnesio-hornblende, or rare edenitic hornblende. Calculated crystallization pressures range from 2.2 kbar to 4.5 kbar, temperatures from 768°C to 849°C, and ΔFMQ (relative to the FMQ buffer at 2 kbar) from +1.2 to +2.1 (Fig. 3-7A, B; Table A3). There is a trend of increasing oxidation state from ~ΔFMQ +1.0 in high pressure–temperature amphiboles to ~ΔFMQ+2.0 in more shallowly crystallized amphiboles (Fig. 3-7C, D). In volcanic and subvolcanic rocks, amphibole occurs as granular replacements of orthopyroxene. All of the grains analyzed are calcic amphiboles, and classify as magnesio-hastingsite, edenite, and rare tschermakite. Amphiboles from andesites show higher crystallization pressures (6.4–8.1 kbar) and temperatures (961°–975°C) compared to those from intrusions, but slightly lower ΔFMQ values (+1.2 to +1.7). The average ΔFMQ value defined by amphiboles from the Paleocene–Eocene suite is +1.6 ± 0.2 (n = 40; range = +1.2 to +2.1).

Oligocene: Amphiboles were analyzed from intermediate–felsic intrusions with equigranular textures. All analyzed grains are magnesio-hastingsite, and yield crystallization pressures of 1.4–2.1 kbar and crystallization temperatures of 791°–774°C (Table A3); these pressures and temperatures are consistent with crystallization after magma emplacement in the upper crust. Calculated ΔFMQ values range from +2.5 to +2.8 (average = +2.6 ± 0.1, n = 7; Fig. 3-7A).

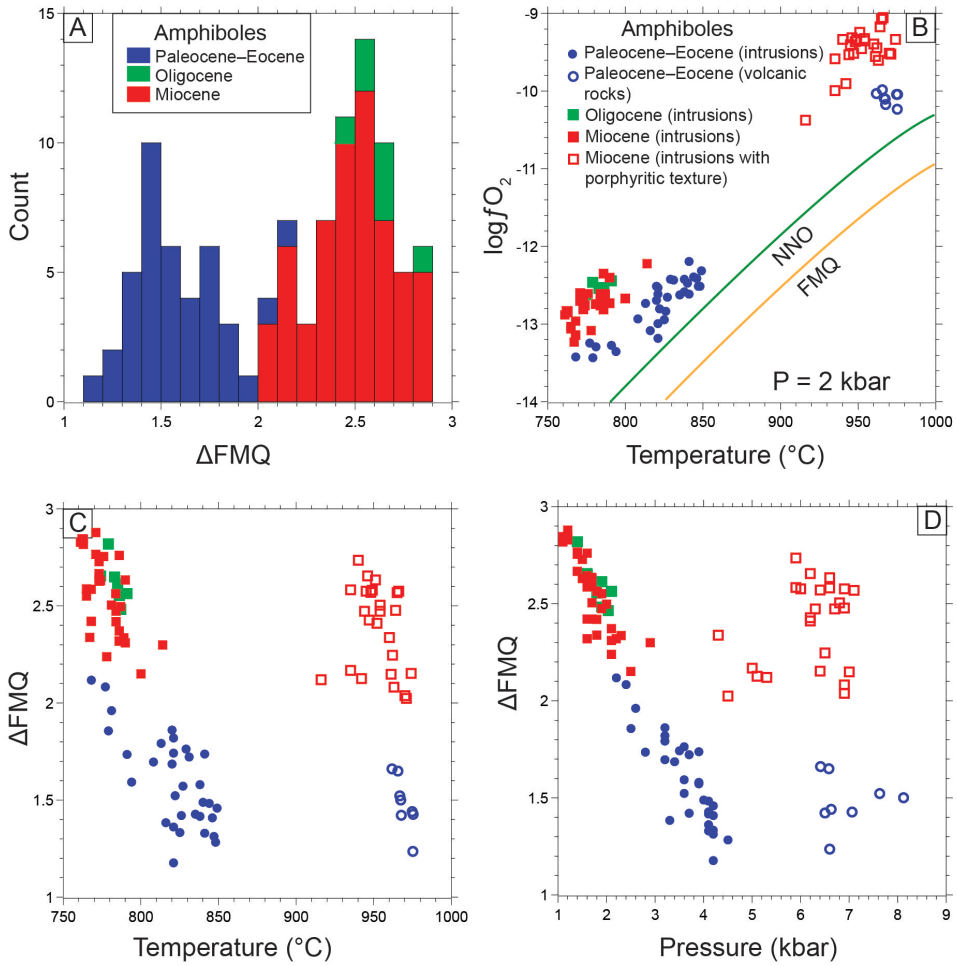

Fig. 3-7. Plots and histogram of oxidation state, temperature, and pressure estimated from amphiboles from Paleocene–Eocene, Oligocene, and Miocene igneous rocks in the Gangdese belt. A. ΔFMQ histogram; B. logfO_2 vs. temperature (at 2 kbar pressure); C. ΔFMQ vs. temperature; D. ΔFMQ vs. pressure. ΔFMQ and temperature were calculated from the spreadsheet of Ridolfi (2010); pressure was calculated using equations of Schmidt (1992). Abbreviations: FMQ = fayalite–magnetite–quartz buffer curve (Heubner, 1971), HM = hematite–magnetite buffer curve (Chou, 1978), NNO = nickel–nickel oxide buffer curve (Heubner and Sato, 1970).

Miocene: Amphiboles analyzed are from intermediate–felsic intrusions, with equigranular or porphyritic textures. All of the grains analyzed are homogeneous, without chemical zonation. They are calcic amphiboles, and classify as magnesio-hornblende, magnesio-hastingsite, and rare tschermakite. They show large variations of crystallization pressure from 1.1 kbar to 7.1 kbar, and also of temperature (761°–974°C; Table A3). Generally, amphiboles in intermediate porphyritic rocks show higher temperatures (915°–974°C) and pressures (4.3–7.1 kbar) compared with amphiboles from felsic

granitoids (temperature: 761°–814°C; pressure: 1.1–2.9 kbar) (Fig. 3-7C–D), which is consistent with expected depths and temperatures of crystallization of phenocrysts in these magmas. ΔFMQ values range from +2.0 to +2.9 (average = 2.5 ± 0.2, n = 58), and are distinctly higher than amphiboles from the Paleocene–Eocene suite (Fig. 3-7A).

Magnetite–Ilmenite

Magmatic oxidation states were also estimated from magnetite-ilmenite mineral pairs using the ILMAT spreadsheet of Lepage (2003).

Paleocene–Eocene: Magnetite is common in this suite, whereas ilmenite is subordinate. In intrusive rocks, ilmenite commonly occurs as small exsolution laths in groundmass magnetite, and these rocks were therefore not suitable for estimation of fO_2. In fresh andesites, however, Fe-Ti oxides commonly occur as microphenocrysts of intergrown ilmenite and magnetite (Fig. 3-8A–C). Five representative magnetite–ilmenite pairs from four andesitic samples yielded calculated temperatures of 625°–781°C, and ΔFMQ values (relative to FMQ buffer at 2 kbar) of -1.2 to +0.8 (average = -0.2 ± 0.8, n = 5; Fig. 3-9).

Oligocene: Magnetite is common in this suite, whereas ilmenite is rare. Both of magnetite and ilmenite occur as inclusions in phenocrysts, or as microphenocrysts. No suitable (equilibrium) magnetite–ilmenite mineral pairs were found in this suite to estimate fO_2.

Miocene: The major Fe-Ti oxide in this suite is magnetite, whereas ilmenite is rare. In intrusive rocks, Fe-Ti oxides commonly occur as inclusions in phenocrysts or as microphenocrysts. Intergrown magnetite–ilmenite mineral pairs are rare in equigranular granitoids, but diorite porphyries preserve several pairs as intergrowths in amphibole phenocrysts (Fig. 3-8D). Two representative pairs yielded calculated temperatures of 920° and 1193°C, and ΔFMQ of +0.8 and +1.3. In fresh dacites, Fe-Ti oxides commonly occur as microphenocrysts, with ilmenite intergrown with magnetite. Four representative magnetite–ilmenite mineral pairs from two dacitic samples yielded calculated temperatures of 630°–708°C, and ΔFMQ of +1.3 to +2.9 (average = +2.2 ± 0.7, n = 4; Fig. 3-9). As in the case of amphiboles, these ΔFMQ values are distinctly higher than those calculated for the Paleocene–Eocene rocks, although the magnetite-ilmenite ΔFMQ

estimates are uniformly lower than the amphibole estimates. Possible reasons for this discordance between the two methods are discussed below.

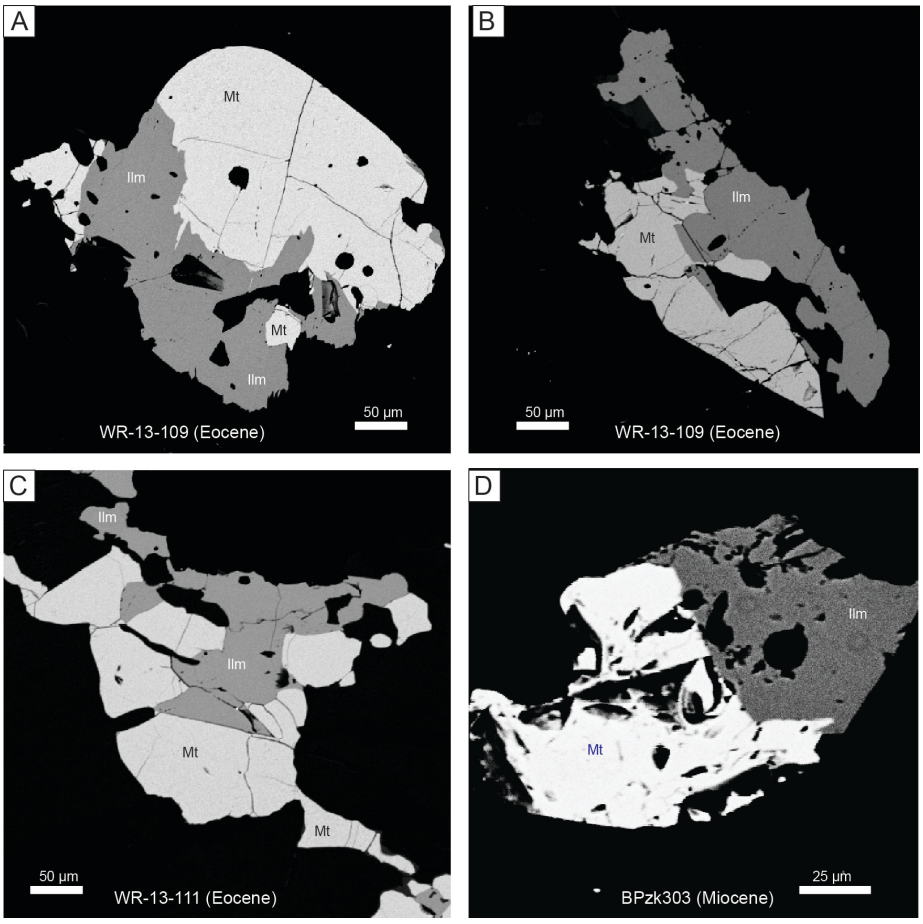

Fig. 3-8. Back-scattered electron images (BSEI) show magnetite and ilmenite as intergrowths in the Paleocene–Eocene suite (A–C), and in the Miocene suite (D). Abbreviations: Ilm = ilmenite, Mt = magnetite.

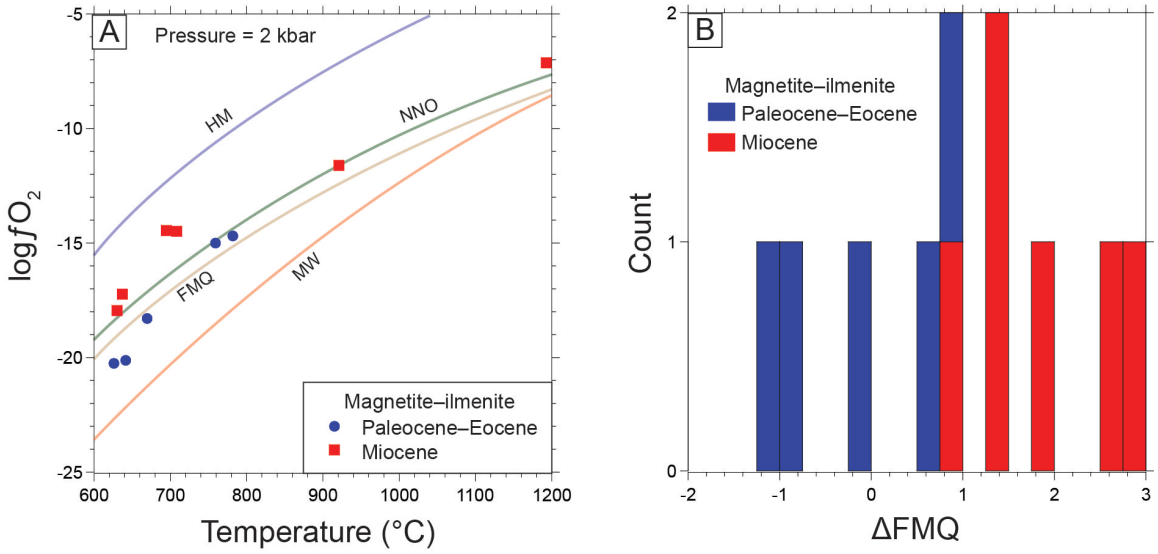

Fig. 3-9. Plots of oxidation state and temperature estimated from magnetite–ilmenite mineral pairs from Paleocene–Eocene and Miocene igneous rocks in the Gangdese belt. A. logfO_2 vs. temperature (at 2 kbar pressure); B. ΔFMQ histogram. ΔFMQ and temperature from magnetite–ilmenite mineral pairs are calculated using ILMAT (Lepage, 2003). Abbreviations: FMQ = fayalite–magnetite–quartz buffer curve (Heubner, 1971), HM = hematite–magnetite buffer curve (Chou, 1978), MW = wüstite–magnetite buffer curve (Eugster and Wones, 1962), NNO = nickel–nickel oxide buffer curve (Heubner and Sato, 1970).

Zircons

Trace element data for zircons from Gangdese Cenozoic igneous rocks are illustrated on Figures 3-10, 11, and reported in Table A4. All zircon samples show positive chondrite-normalized Ce anomalies, small to significant negative Eu anomalies, and enrichments of heavy rare earth elements (HREE; Fig. 3-10A). These trace element patterns and ∑REE abundances of 240 ppm to 3068 ppm are typical of igneous zircons (~250–5000 ppm; Hoskin and Schaltegger, 2003).

Paleocene–Eocene: In general, Paleocene–Eocene zircons from six representative samples have greater enrichments in REE than Oligo-Miocene zircons, except Eu and Ce (Fig. 3-10). Ce^{4+}/Ce^{3+} ratios estimated from the equations of Ballard et al. (2002) are mostly below 50 (6.0–66.8; average = 25.7 ± 18.4, n = 26; Fig. 3-11A), whereas Eu_N/Eu_N* ratios of these zircons are between 0.08 and 0.61, with an average of 0.32 ± 0.14 (n = 26; Fig. 3-11B). Three ore-forming granitoids from the Eocene Sharang porphyry Mo and Jiru porphyry Cu deposits also have low Ce^{4+}/Ce^{3+} and Eu_N/Eu_N* ratios

(Fig. 3-11C). Zircon Ce^{4+}/Ce^{3+} ratios of this suite appear to increase with Eu_N/Eu_N^* ratios (Fig. 3-11C), as expected if larger positive Ce anomalies (reflecting higher Ce^{4+}/Ce^{3+} ratios) and smaller negative Eu anomalies (higher Eu_N/Eu_N^* close to 1) are caused by higher magmatic oxidation state (and vice versa). Temperature values estimated from the equations (Ti-in-zircon geothermometer) of Watson and Harrison (2005) show a large variation from 665°C to 889°C (average: 759 ± 69°C, n = 26, Table A4), with zircon crystallization temperatures broadly decreasing with increasing host-rock silica contents (Fig. 3-11D).

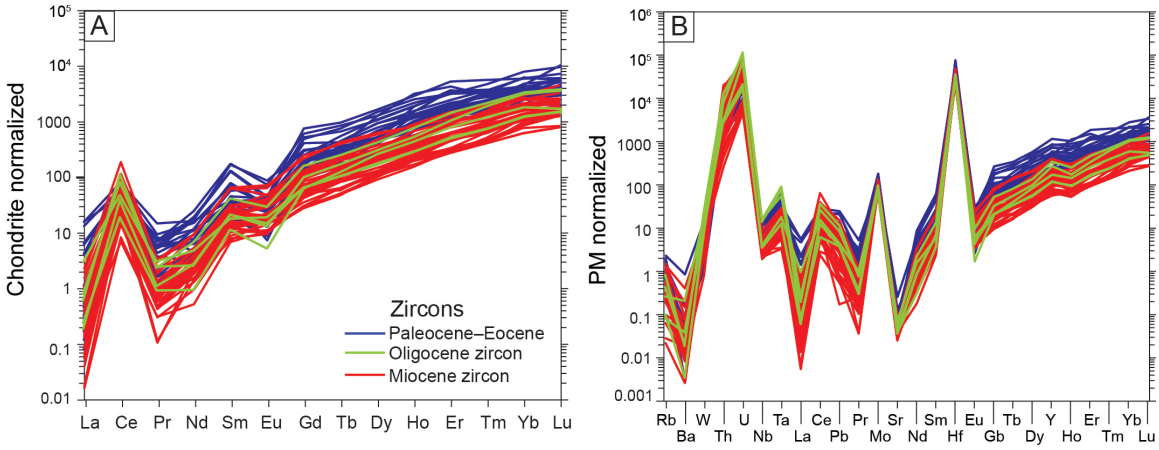

Fig. 3-10. (A) Chondrite-normalized and (B) primitive mantle-normalized trace element diagrams for zircons from Paleocene–Eocene, Oligocene, and Miocene intrusive rocks in the Gangdese belt. Normalization values are from Sun and McDonough (1989).

Oligocene: Oligocene zircons from two representative samples have intermediate trace element contents between those of Paleocene–Eocene and Miocene zircons (Fig. 3-10), intermediate Ce^{4+}/Ce^{3+} ratios (18.6–66.0; average = 50.1 ± 20.5, n = 5; Fig. 3-11A), and weak to moderate negative Eu anomalies (Eu_N/Eu_N^* = 0.19–0.56; average = 0.36 ± 0.14, n = 5; Fig. 3-11B). Temperatures calculated for these zircons range from 640°C to 712°C (average = 675 ± 28°C, n = 5; Fig. 3-11D).

Miocene: Miocene zircons from seven representative samples contain lower abundances of REEs than Paleocene–Oligocene suites except for Eu and Ce (Fig. 3-10). Ce^{4+}/Ce^{3+} ratios are mostly above 50 (32.3 to 141.9; average = 74.3 ± 30.1, n = 33; Fig. 3-11A), and Eu_N/Eu_N^* ratios are mostly above 0.4 (0.36 to 0.87; average = 0.63 ± 0.12, n = 33; Fig. 3-

11B). Both the Ce^{4+}/Ce^{3+} and Eu_N/Eu_N* ratios are higher than in Paleocene–Oligocene suites, suggesting higher magmatic oxidation states in these Miocene magmas (Fig. 3-11C). Temperatures range from 604°C to 782°C (average: 673 ± 40°C, n = 33; Fig. 3-11D). No samples of mafic Miocene rocks were found that could be compared with the Paleocene–Eocene mafic rocks, but the intermediate rocks have lower zircon crystallization temperatures than Paleocene–Eocene equivalents, which may reflect higher magmatic water contents (Wang et al., 2014b) and lower solidus temperatures of these younger magmas (e.g. Hildreth and Moorbath, 1988; Davies and Stevenson, 1992).

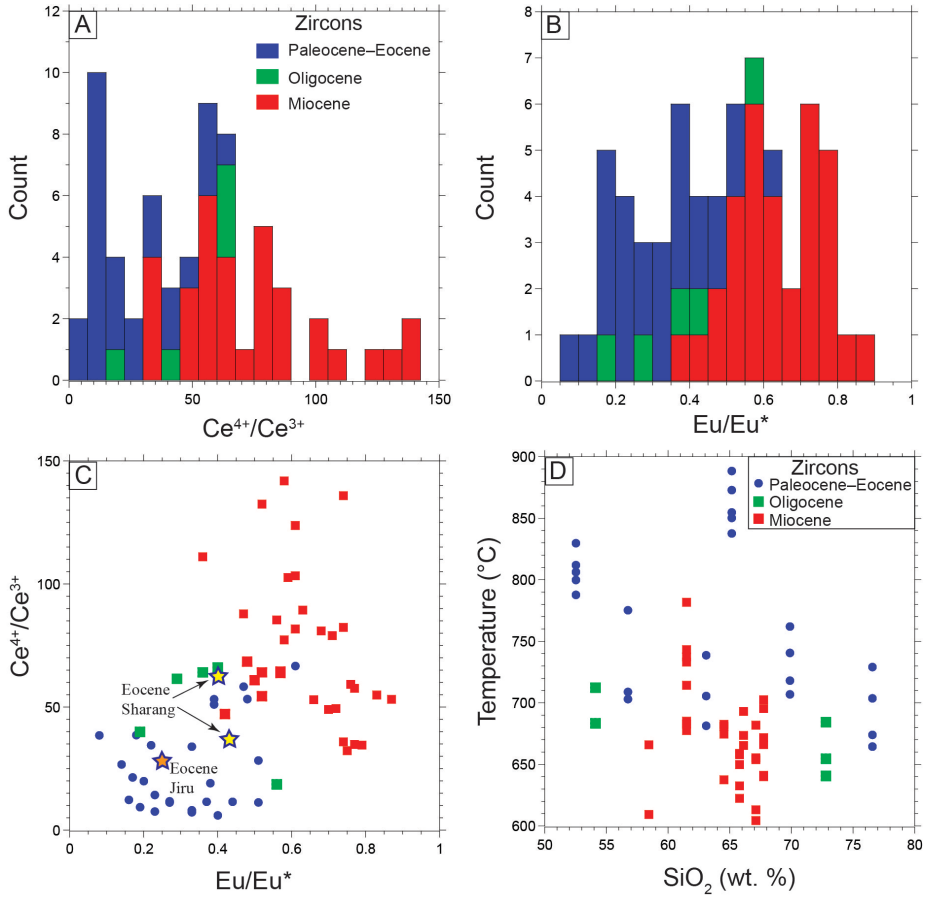

Fig. 3-11. Zircon temperature, trace element ratio plots, and concentration histograms for Paleocene–Eocene, Oligocene, and Miocene zircons from the Gangdese belt. A. Zircon Ce^{4+}/Ce^{3+} ratio histogram; B. Zircon Eu_N/Eu_N* ratio histogram; C. Zircon Ce^{4+}/Ce^{3+} vs. Eu_N/Eu_N^*; D. Temperature vs. host-rock silica. Temperature is calculated from Watson and Harrison (2005), and calculation of zircon Ce^{4+}/Ce^{3+} and Eu_N/Eu_N^* ratios are based on Ballard et al. (2002). In C: Zircon average Ce^{4+}/Ce^{3+} and Eu_N/Eu_N^* ratios of ore-forming intrusions from the Sharang porphyry Mo deposit (personal communication with

Xiang Sun, 2014) and Jiru porphyry Cu deposit (personal communication with Junxing Zhao, 2014) are shown as stars.

Whole-rock Fe^{3+}/Fe^{2+} ratios

Suitable fresh samples for reliable whole-rock Fe^{3+}/Fe^{2+} determination were not abundant. However, the Fe^{3+}/Fe^{2+} ratios of three samples of Paleocene–Eocene intrusive rocks range from 0.28 to 0.39 (average = 0.36 ± 0.06, n = 3; Fig. 3-12A), and plot close to the boundary between "moderately oxidized" and "moderately reduced" magmas, which is close to the FMQ buffer (Fig. 3-12B; Blevin et al., 2004).

In comparison, the whole-rock Fe^{3+}/Fe^{2+} ratios of two samples of fresh Oligocene and Miocene intrusive rocks are 0.68 and 0.86, respectively (Fig. 3-12A). Although these data are sparse, and the Oligo-Miocene rocks have low total Fe contents (meaning that the Fe^{3+}/Fe^{2+} ratios are more sensitive to analytical errors), the results are consistent with higher Fe^{3+}/Fe^{2+} ratios and therefore oxidation states in the Oligo-Miocene rocks compared with the Paleocene–Eocene suite.

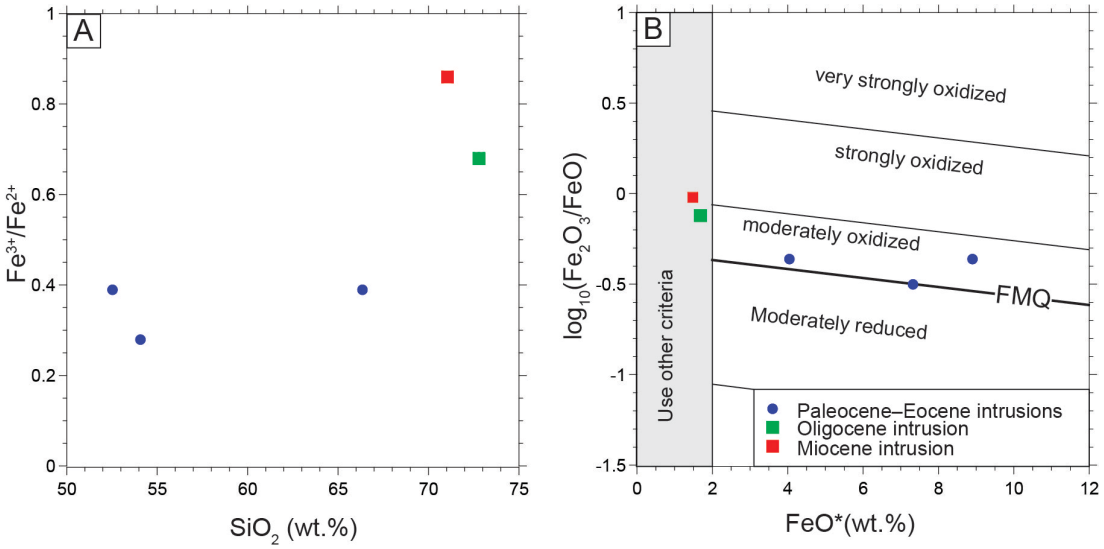

Fig. 3-12. A. Whole-rock Fe^{3+}/Fe^{2+} ratio vs. silica for carefully selected fresh Paleocene–Eocene, Oligocene, and Miocene igneous rocks from the Gangdese belt; B. $\log_{10}(Fe_2O_3/FeO)$ vs. FeO (after Blevin et al., 2004).

3.11 Discussion

Oxidation state of Gangdese Cenozoic magmas

Weakly oxidized Paleocene–Eocene magmas: The oxidation state of Paleocene–Eocene magmas has been investigated using various mineralogical and geochemical parameters. Zircons from this suite have relatively low Ce^{4+}/Ce^{3+} ratios (mostly < 50, average = 25.7 ± 18.4; Fig. 3-11A), and Eu_N/Eu_N* ratios are mostly below 0.4 (average = 0.35 ± 0.19, Fig. 3-11B). Zircon Ce^{4+}/Ce^{3+} (< 50) and Eu_N/Eu_N* ratios (< 0.4) are typical of weakly oxidized or reduced intrusions (e.g., Ballard et al., 2002; Liang et al., 2006; Muñoz et al., 2012; Wang et al., 2013). Three carefully selected samples of fresh Paleocene–Eocene rocks show low–intermediate whole-rock Fe^{3+}/Fe^{2+} ratios between 0.28 and 0.39, which are near the FMQ buffer (Blevin et al., 2004). Magnetite–ilmenite mineral pairs yield ΔFMQ of -0.2 ± 0.8 (Fig. 3-9B). These fO_2 indicators suggest the Paleocene–Eocene magmas were weakly oxidized to moderately reduced, with ΔFMQ < +1.

Amphiboles from the Paleocene–Eocene igneous rocks yielded higher ΔFMQ values (average ΔFMQ = +1.6 ± 0.2, n = 40; Fig. 3-7A) than those calculated from magnetite–ilmenite pairs (-1.2 to +0.8). Similar discrepancies between fO_2 estimates from amphibole compositions and other oxygen barometers have been reported in other studies, especially for intrusive rocks (e.g., Wei and Zhu, 2008; Toummite et al., 2012; Ayati et al., 2013). In order to estimate this discrepancy quantitatively, we calculated fO_2 values for amphiboles from a granodiorite pluton from the Baogutu porphyry Cu-Au deposit Xinjiang Province, China (Wei and Zhu, 2010), where ΔFMQ values have been reported based on magnetite–ilmenite mineral pairs. ΔFMQ values (+1 to +2) defined from amphiboles are systematically higher up to ~1 log unit compared to ΔFMQ (0 to +1) values from magnetite–ilmenite mineral pairs (Wei and Zhu, 2008). This discrepancy may be because the amphibole oxygen barometer of Ridolfi et al. (2010) was calibrated for volcanic rocks, not intrusive rocks. Although the spreadsheet of Ridolfi (2010) indicates that it can be used for amphiboles from intrusive rocks (Filippo Ridolfi, personal communication, 2013), the amphiboles analyzed should have early stage textures and show homogeneous compositions. Amphiboles in the Paleocene–Eocene suite commonly occur as interstitial or ophitic crystals, or as granular replacements of clinopyroxene. Therefore these late-stage amphiboles may not yield values representative of the bulk magmatic oxidation state, but may be recording late-stage increases in fO_2 in residual melts. We consider that amphibole ΔFMQ values are most likely overestimates

of original magmatic fO_2 in the Paleocene–Eocene suite. Based on the various lines of evidence above, we conclude that the fO_2 of Paleocene–Eocene magmas was below ΔFMQ+1.

Moderately oxidized Oligocene magmas: Oligocene intrusions are sparse in the Gangdese belt, and limited data are available to constrain their magmatic oxidation state. However, zircon Ce^{4+}/Ce^{3+} and Eu_N/Eu_N^* ratios are intermediate between Paleocene–Eocene and Miocene values: average Ce^{4+}/Ce^{3+} = 50.1 ± 20.5, n = 5; average Eu_N/Eu_N^* = 0.36 ± 0.14, n = 5 (Fig. 3-11A, B). Amphiboles from this suite record relatively low temperatures and pressures, and relatively high and uniform oxidation states (average ΔFMQ = +2.6 ± 0.1, n = 7; Fig. 3-7A). Notwithstanding the likelihood that calculations of oxidation state from amphibole compositions may overestimate the true value by up to one log unit, we nevertheless suggest the fO_2 range of Oligocene magmas was above ΔFMQ+1.

Oxidized Miocene magmas: Zircons from Miocene magmas have higher Ce^{4+}/Ce^{3+} and Eu_N/Eu_N^* ratios than in the earlier suites: Ce^{4+}/Ce^{3+} = 32.3–141.9, average = 74.3 ± 30.1, n = 33; Eu_N/Eu_N^* = 0.36–0.87; average = 0.63 ± 0.12, n = 33 (Fig. 3-11A, B). These values are similar to those reported from oxidized magmas directly related to porphyry copper deposits in other regions, where zircon Ce^{4+}/Ce^{3+} ratios are above 50, and Eu_N/Eu_N^* ratios are above 0.4 (e.g., Muñoz et al., 2012; Wang et al., 2013). Magnetite–ilmenite mineral pairs record an average ΔFMQ of +1.8 ± 0.8 (n = 6; Fig. 3-9B), whereas early-stage amphiboles record an average ΔFMQ of +2.5 ± 0.2 (n = 58; Fig. 3-7A). Again noting the systematically higher fO_2 estimates from amphibole compositions, we nevertheless suggest that the Miocene magmas were more oxidized than either the Paleocene–Eocene or Oligocene suites, with ΔFMQ > +1.5.

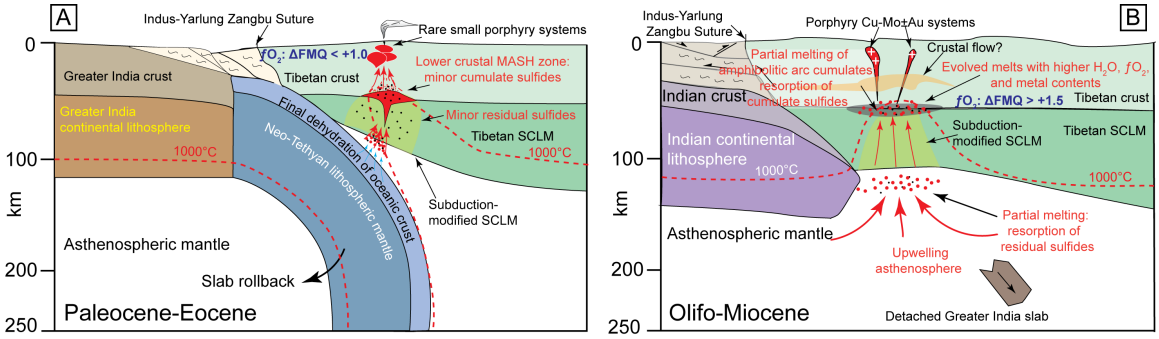

Fig. 3-13. Cartoon cross-sections illustrating the proposed petrogenesis of Cenozoic igneous rocks in the eastern Gangdese belt (modified from Wang et al., 2014b; approximately to scale). A. Paleocene-Eocene magmatism was triggered by rollback of Neo-Tethyan slab, and formed by partial melting of hydrated mantle wedge (MASH = melting, assimilation, storage, and homogenization; Hildreth and Moorbath, 1988). These late-subduction magmas were relatively dry and less oxidized, and generated few porphyry deposits. B. Slab breakoff in the Miocene generated asthenospheric melts that interacted with the previously subduction-modified Tibetan lithosphere to generate more hydrous and oxidized magmas, which were fertile for porphyry formation upon emplacement in the upper crust. Red dots indicate partial melting, and black dots represent sulfides. Blue and red arrows represent fluids and melts, respectively. Thrust systems are inferred from Yin and Harrison (2000). Depths of the Moho, Indian lithosphere–asthenosphere boundary, and Tibetan lithosphere–asthenosphere boundary are estimated from seismic studies (Kumar et al., 2006; Zhao et al., 2010). Crustal flow in middle-crust is inferred from Unsworth et al. (2005), King et al., (2007), and Jamieson et al. (2011). Abbreviation: SCLM = subcontinental lithospheric mantle.

Metallogenic implications of increasing oxidation state during the evolution of Cenozoic magmas in the Gangdese belt

Paleocene–Eocene intrusions and coeval Linzizong volcanic rocks are extensively preserved in the Gangdese belt, but are only known to be associated with three small porphyry deposits. These magmas are thought to be relatively water poor (< 4 wt.%, Wang et al., 2014b), and weakly oxidized (ΔFMQ < +1.0). Their low water content and oxidation state reflect the final dehydration of the remnant Neo-Tethyan slab (Fig. 3-13A). In contrast, Miocene magmatic rocks crop out as small-volume intrusions in the eastern Gangdese belt, and are associated with several large porphyry Cu-Mo±Au deposits, as well as numerous smaller porphyry and skarn deposits. These magmas are thought to have been derived from partial melting of subduction-modified lithosphere, and were relatively water-rich (Wang et al., 2014b) and oxidized (ΔFMQ > +1.5). The

oxidation state of sparse Oligocene magmas was intermediate between these earlier and later suites, or close to the Miocene suite.

Redox state plays an important role in the solubility of Cu and Au in magmas (Holzheid and Lodders, 2001; Botcharnikov et al., 2011; Zajacz et al., 2012, 2013). Under less oxidized conditions (ΔFMQ < +1.0), sulfide saturation will strip Cu and Au from the melt, and leave residual sulfide phases as restite in the mantle or as cumulate minerals in the deep crust during fractionation and crustal interaction (i.e., in the MASH zone of Hildreth and Moorbath, 1988; Richards, 2009, 2011; Lee et al., 2012; Wilkinson, 2013; Chiaradia, 2014). Consequently, the less oxidized Paleocene–Eocene magmas may have left much of their metal load in the mantle or lower crust, leading to sparse upper crustal porphyry-style mineralization (Fig. 3-13A).

Detachment of the Greater India slab at ~25 Ma (Replumaz., 2010) triggered upwelling of asthenospheric melt, which interacted with the subduction-modified Tibetan lithosphere and triggered partial melting (Fig. 3-13B), as suggested by a low-velocity zone in the present Tibetan lithosphere (Hou et al., 2011; Mechie and Kind, 2013). The subsequent Oligo-Miocene magmas overlap with the Sr-Nd isotope compositions of cospatial Cretaceous Gangdese arc batholiths, supporting assimilation of this crustal material (Hou et al., 2004, 2011; Wang et al., 2014b). From ~25 Ma to ~15 Ma in the eastern Gangdese belt, magmas evolved to more silica-rich compositions (Fig. 3-4A), with high Sr/Y ratios, and low Y contents (Fig. 3-4B). These features were interpreted by Wang et al. (2014b) to reflect amphibole fractionation from hydrous magmas. The low crystallization temperatures estimated from Miocene zircons (Fig. 3-11D) also suggest lower solidus temperature in water-rich magmas.

Previous studies suggest that magmatic differentiation by mineral fractionation (accompanied by assimilation of lower crustal materials) will give rise to evolved melts with higher silica and water contents (Hildreth and Moorbath, 1988; Rohrlach and Loucks, 2005; Chiaradia et al., 2012; Loucks, 2013; Wilkinson, 2013), and progressively increasing oxidation states (Gill, 1981; Candela, 1986; Zimmer et al., 2010; Richards et al., 2013). Thus, under more hydrous and oxidizing conditions (ΔFMQ > +1.5) during late-collisional Miocene magmagenesis, residual sulfides from prior arc magmatism in the mantle or deep crust may have been remobilized, releasing Cu, Mo, and Au into the

melts and thus making them available for later magmatic-hydrothermal mineralization upon emplacement in the upper crust (Fig. 3-13B; Richards, 2009, 2011; Lee et al., 2012; Richards and Mumin, 2013; Chiaradia, 2014).

3.12 Conclusions

The Gangdese Paleocene–Eocene magmas were less oxidized, characterized by low Ce^{4+}/Ce^{3+} ratios (mostly < 50, average = 25.7 ± 18.4, n = 26) and Eu_N/Eu_N* ratios (mostly < 0.4, average = 0.35 ± 0.19, n = 26), low–intermediate whole-rock Fe^{3+}/Fe^{2+} ratios (0.28 to 0.39, near the FMQ buffer), and low ΔFMQ values (average = -0.2 ± 0.8, n = 4). These fO_2 indicators suggest the Paleocene–Eocene magmas were weakly oxidized to moderately reduced, with ΔFMQ < +1. Amphibole ΔFMQ values (average = ΔFMQ+1.6 ± 0.2, n = 40) are likely overestimates of original magmatic fO_2 in the Paleocene–Eocene suite, and the suggested fO_2 range was below ΔFMQ+1.

The Oligocene magmas were moderately oxidized. The zircon Ce^{4+}/Ce^{3+} and Eu_N/Eu_N* ratios are intermediate between Paleocene–Eocene and Miocene values: average Ce^{4+}/Ce^{3+} = 50.1 ± 20.5, n = 5; average Eu_N/Eu_N* = 0.36 ± 0.14, n =5. Assuming that amphibole ΔFMQ values (average = ΔFMQ+2.6 ± 0.1, n = 7) were overestimated by up to one log unit, the suggested fO_2 range of Oligocene magmas was above ΔFMQ+1.

The Miocene magmas were oxidized, characterized by higher zircon Ce^{4+}/Ce^{3+} and Eu_N/Eu_N* ratios (Ce^{4+}/Ce^{3+} = 32.3–141.9, average = 74.3 ± 30.1, n = 33; Eu_N/Eu_N* = 0.36–0.87; average = 0.63 ± 0.12, n = 33), and high ΔFMQ values (average = +1.8 ± 0.8, n = 6) estimated from magnetite–ilmenite mineral pairs. Early-stage amphiboles record an average ΔFMQ of +2.5 ± 0.2 (n = 58). Considering systematically higher fO_2 estimates from amphibole compositions, we nevertheless suggest that the Miocene magmas were more oxidized than either the Paleocene–Eocene or Oligocene suites, with ΔFMQ > +1.5.

There was an increase in magmatic oxidation state from the Paleocene to the Miocene. This increase correlates with increased fertility of these magmas, culminating in the formation of large porphyry deposits in the Miocene. The changes of magmatic oxidation state were thought to be related with fundamental changes in the sources of magmas with time throughout the collisional orogen. Detachment of the Greater India slab at ~25 Ma

triggered upwelling of asthenospheric melt, which interacted with the subduction-modified Tibetan lithosphere and triggered partial melting. From ~25 Ma to ~15 Ma in the eastern Gangdese belt, magmas evolved to more silica-rich compositions with high Sr/Y ratios, and low Y contents. These features were interpreted by Wang et al. (2014b) to reflect amphibole fractionation from hydrous magmas. In addition, extensive mineral fractionation in the Miocene also gave rise to evolved hydrous melts with more oxidized contents. We suggest residual sulfides from prior Gangdese arc magmatism may have been remobilized during Miocene magmagenesis in the deep crust under more hydrous and oxidizing conditions (ΔFMQ > +1.5). Cu, Mo, and Au were released into the melts, which generated porphyry Cu-Mo±Au deposits upon emplacement in the upper crust.

3.13 References

Ahmadian, J., Haschke, M., McDonald, I., Regelous, M., RezaGhorbani, M., Emami, M.H., and Murata, M., 2009, High magmatic flux during Alpine–Himalayan collision: Constraints from the Kal-e-Kafi complex, central Iran: Geological Society of American Bulletin, v. 121, p. 857–868.

Aitchison, J.C., Ali, J.R., and Davis, A.M., 2007, When and where did India and Asia collide: Journal of Geophysical Research, v. 112, p. B05423, doi: 10.1029/2006JB004706.

Ali, J.R., and Aitchison, J.C., 2005, Greater India: Earth-Science Reviews, v. 72, p. 169–188.

Allégre, C.J., Courtillot, V., Taponnier, P., Hirn, A., Mattauer, M., Coulon, C., Jaeger, J. J., Achache, J., Schärer, U., Marcoux, J., Burg, J. P., Girardeau, J., Armijo, R., Gaiety, C., Göpel, C., Li, T., Xiao, X., Chang, C., Li, G., Lin, B., T, J., Wang, N., Chen, G., Han, T., Wang, X., Den, W., Sheng, H., Gao, Y., Zhou, J., Qiu, H., Bao, P., Wang, S., Wang, B., Zhou, Y., and Xu, R., 1984, Structure and evolution of the Himalayan-Tibet orogenic belt: Nature, v. 307, p.17–22.

Aminzadeh, B., Shahabpour, J., and Maghami, M., 2011, Variation of Rhenium contents in molybdenites from the Sar Cheshmeh porphyry Cu-Mo deposit in Iran: Resource Geology, v. 61, p. 290–295.

Andersen, D.J., and Lindsley, D.H., 1985, New (and final!) models for the Ti-

magnetite/ilmenite geothermometer and oxygen barometer: Abstract AGU 1985 Spring Meeting Eos Transactions, v. 46, p. 416.

Anderson, J.L., Barth, A., Wooden, J.L., and Mazdab, F., 2008, Thermometers and thermobarometers in granitic systems: Reviews in Mineralogy and Geochemistry, v. 69, p. 121–142.

Andersen, D.J., Lindsley, D.H., and Davidson, P.M., 1993, QUILF: A Pascal program to assess equilibria among Fe-Mg-Mn-Ti oxides, pyroxenes, olivine, and quartz: Computers and Geosciences, v. 19, p. 1333–1350.

Ashton, K.E., Heaman, L.H., Lewry, J.F., Hartlaub, R.P., and Shi, R., 1999, Age and origin of the Jan Lake Complex: a glimpse at the buried Archean craton of the Trans-Hudson Orogen: Canadian Journal of Earth Sciences, v. 36, p. 185–208.

Audétat, A., and Pettke, T., 2006, Evolution of a porphyry-Cu mineralized magma system at Santa Rita, New Mexico (USA): Journal of Petrology, v. 47, p. 2021–2046.

Ayati, F., Yavuz, F., Asadi, H., Richards, J.P., and Jourdan, F., 2013, Petrology and geochemistry of calc-alkaline volcanic and subvolcanic rocks, Dalli porphyry copper-gold deposit, Markazi Province, Iran: International Geology Review, v. 55, p. 158–184.

Bacon, C.R., and Hirschmann, M.M., 1988, Mg/Mn partitioning as a test for equilibrium between coexisting Fe–Ti oxides: American Mineralogist, v. 73, p. 57–61.

Ballard, J.R., Palin, J.M, and Campbell, I.H., 2002, Relative oxidation states of magmas inferred from Ce(IV)/Ce(III) in zircon: Application to porphyry copper deposits of northern Chile: Contributions to Mineralogy Petrology, v. 144, p. 347–364.

Baker, D.R. and Eggler, D.H., 1983, Fractionation paths of Atka (Aleutians) high-alumina basalts: constraints from phase relations: Journal of Volcanology and Geothermal Research, v.18, p. 387–404.

Barker, S.J., Wilson, C.J.N., Baker, J.A., Millet, M.A., Rotella, M.D., Wright, I.C., and Wysoczanski, J.W., 2013, Geochemistry and petrogenesis of silicic magmas in the intra-oceanic Kermadec arc: Journal of Petrology, v. 54, p. 351–391.

BGMRXAR (Bureau of Geology Mineral Resources of Xizang Autonomous Region), 1993, Regional Geology of Xizang (Tibet) Autonomous Region: Geological Publishing House, Beijing, 450 p. (in Chinese with English abstract)

Blevin, P.L., 2004, Redox and compositional parameters for interpreting the granitoid metallogeny of Eastern Australia: Implications for gold-rich ore system: Resource Geology, v. 54, p. 241–252.

Bornhorst, T.J., and Rose, W.I., 1986, Partitioning of gold in young calc-alkaline volcanic rocks from Guatemala: Journal of Geology, v. 94, p. 412–418.

Botcharnikov, R.E., Linnen, R.L., Holtz, W.M., Jugo, P.J., and Berndt, J., 2011, High gold concentrations in sulphide-bearing magma under oxidizing conditions: Nature Geoscience, v. 4, p. 112–115.

Brett, R., and Sato, M., 1984, Intrinsic oxygen fugacity measurements on seven chondrites, a pallasite, and a tektite and the redox state of meteorite parent bodies: Geochimica et Cosmochimica Acta, v. 48, p. 111–120.

Buddington, A.F., and Lindsley, D.H., 1964, Iron–titanium oxide minerals and synthetic equivalents: Journal of Petrology, v. 5, p. 310–357.

Burg, J.P., and Chen, G.M., 1984, Tectonics and structural formation of southern Tibet, China: Nature, v. 11, p. 219–223.

Burnham, C.W., 1979, Magmas and hydrothermal fluids, in Barnes, H.L., ed., Geochemistry of hydrothermal ore deposits, 2nd edition: New York, John Wiley and Sons, p. 71–136.

Burnham, A.D. and Berry, A.J., 2012, An experimental study of trace element partitioning between zircon and melt as a function of oxygen fugacity: Geochimica et Cosmochimica Acta, v. 95, p. 196–212.

Candela, P.A., 1986, The evolution of aqueous vapor from silicate melts: Effect on oxygen fugacity: Geochimica et Cosmochimica Acta, v. 50, p. 1205–1211.

Candela, P.A., 1992, Controls on ore metal ratios in granite-related ore systems: An experimental and computational approach: Transactions of the Royal Society of Edinburgh, Earth Sciences, v. 83, p. 317–326.

Capitanio, F.A., Morra, G., Goes, S., Weinberg, R.F., and Moresi, L., 2010, India-Asia convergence driven by the subduction of the Greater Indian continent: Nature Geoscience, v. 3, p. 136–139.

Carmichael, I.S.E., 1991, The redox states of basic and silicic magmas: a reflection of their source regions?: Contribution to Mineralogy and Petrology, v. 106, p. 129–141.

Carroll, M.R., and Rutherford, M.J., 1985, Sulfide and sulfate saturation in hydrous silicate melts: Journal of Geophysical Research, v. 90, Supplement, p. C601–C612.

Chen, T., 2006, Geochemistry of the Qushui intrusive of Gangdese in Tibet and its implications for magma mixing: Unpublished Master thesis (in Chinese), China University of Geosciences, Beijing, 59 p.

Chen, L., Qin, K.Z., Li, J.X., Xiao, B., Li, G.M., Zhao, J.X., and Fan, X., 2011, Fluid Inclusion and hydrogen, oxygen, sulfur isotopes of Nuri Cu-W-Mo deposit in the southern Gangdese, Tibet: Resource Geology, v. 62, p. 42–62.

Chen, L., Qin, K.Z., Li, G.M., Li, J.X., Xiao, B., Jiang, H.Z., Zhao, J.X., Fan, X., and Jiang, S.Y., 2012, Geological and skarn mineral characteristics of Nuri Cu-W-Mo deposit in southern Gangdese, Tibet: Mineral Deposits, v. 31, p. 417–437. (in Chinese with English abstract)

Chiaradia, M., 2014, Copper enrichment in arc magmas controlled by overriding plate thickness: Nature Geoscience, v. 7, p. 43–46.

Chiaradia, M., Ulianov, A., Kouzmanov, K., and Beate, B., 2012, Why large porphyry Cu deposits like high Sr/Y magmas?: Scientific Reports, v. 2, 685; doi : 10.1038/srep00685.

Chou, I.M., 1978, Calibration of oxygen buffers at elevated P and T using the hydrogen fugacity sensor: American Mineralogist, v. 63, p. 690–703.

Chung, S.L., Liu, D., Ji, J.Q., Chu, M.F., Lee, H.Y., Wen, D.J., Lo, C.H., Lee, T.Y., Qian, Q., and Zhang, Q., 2003, Adakites from continental collision zones: melting of thickened lower crust beneath southern Tibet: Geology, v. 31, p. 1021–1024.

Chung, S.L., Chu, M.F., Zhang, Y.Q., Xie, Y.W., Lo, C.H., Lee. T.Y., Lan, C.Y., Li, X.H., Zhang, Q., and Wang, Y.Z., 2005, Tibetan tectonic evolution inferred from spatial and temporal variations in post-collisional magmatism: Earth-Science Reviews, v. 68, p. 173–196.

Cloos, M., and Housh, T.B., 2008, Collisional delamination: Implications for porphyry-type Cu–Au ore formation in New Guinea: Arizona Geological Society Digest, v. 22, p. 277–293.

Cooke, D.R., Hollings, P., and Walshe, J.L., 2005, Giant porphyry deposits: characteristics, distribution, and tectonic controls: Economic Geology, v. 100, p. 801–

818.

Davies, J.H., and Stevenson, D.J., 1992, Physical model of source region of subduction zone volcanics: Journal of Geophysical Research, v. 97, p. 2037–2070.

Defant, M.J., and Drummond, M.S., 1990, Derivation of some modern arc magmas by melting of young subducted lithosphere: Nature, v. 347, p. 662–665.

de Sigoyer, J., Chavagnac, V., Blichert-Toft, J., Villa, I.M., Luais, B., Guillot, S., Cosca, M., and Mascle, G., 2000, Dating the Indian continental subduction and collision thickening in the northwest Himalaya: Multichronology of the Tso Morari eclogites: Geology, v. 28, p. 487–490.

Dong, G.C., 2002, Linzizong volcanic rocks and implications for probing India-Eurasia collision process in Linzhou Volcanic Basin, Tibet: Unpublished Ph.D. thesis (in Chinese), China University of Geosciences, Beijing, 150 p.

Dong, G.C., Mo, X.X., Zhu, D.C., Wang, L.L., Chen, T., and Li, B., 2006a, Magma mixing in middle part of Gangdese magma belt: Evidences from granitoid complex: Acta Petrologica Sinica, v.22, p. 835–844. (in Chinese with English abstract)

Dong, G.C., Mo, X.X., Zhao, Z.D., Zhu, D.C., Song, Y.T., and Wang, L., 2006b. Gabbros from southern Gangdese: Implication for mass exchange between mantle and crust: Acta Petrologica Sinica, v. 24, p. 203–210. (in Chinese with English abstract)

Droop, G.T.R., 1987. A general equation for estimating Fe^{3+} concentrations in ferromagnesian silicates and oxides from microprobe analyses, using stoichiometric criteria: Mineralogical Magazine, v. 51, p. 431–435.

Eugster, H.P., and Wones, D.R., 1962, Stability relations of the ferroginous biotite, annite: Journal of Petrology, v. 3, p. 82–125.

Gao, Y.F., Yang, Z.S., Santosh, M., Hou, Z.Q., Wei, R.H., and Tian, S.H., 2010, Adakitic rocks from slab melt-modified mantle sources in the continental collision zone of southern Tibet: Lithos, v. 119, p. 651–663.

Ghiorso, M.S., and Sack, R.O., 1991, Fe–Ti oxide geothermometry: thermodynamic formulation and the estimation of intensive variables in silicic magmas. Contribution to Mineralogy and Petrology, v. 108, p. 485–510.

Ghiorso, M.S., and Evans, B.W., 2008, Thermodynamics of rhombohedral oxide solid solutions and a revision of the Fe–Ti two-oxide geothermometer and

oxygenbarometer: American Journal of Science, v. 308, p. 957–1039.

Gill, J.B., 1981, Orogenic andesites and plate tectonics: New York, Springer-Verlag, 390 p.

Grove, T.L., Elkins-Tanton, L.T., Parman, S.W., Müntener, O., and Gaetani, G.A., 2003, Fractional crystallization and mantle melting controls on calc-alkaline differentiation trends: Contribution to Mineralogy and Petrology, v. 145, p. 515–533.

Guo, Z.F., Wilson, M., and Liu, J.Q., 2007, Post-collisional adakites in south Tibet: products of partial melting of subduction-modified lower crust: Lithos: v. 96, p. 205–224.

Hamlyn, P.R., Keays, R.R., Cameron, W.E., Crawford, A.J., and Waldron, H.M., 1985, Precious metals in magnesian low-Ti lavas: Implications for metallogenesis and sulfur saturation in primary magmas: Geochimica et Cosmochimica Acta, v, 49, p. 1797–1811.

Harris, N.B.W., Pearce, J.A., and Tindle, A.G., 1986, Geochemical characteristics of collisional-zone magmatism, in Coward, M.P., Reis, A.C., eds., Collision tectonics: Geological Society, London, Special Publications, v. 19, p. 67–81.

Harrison, T.M., Yin, A., Grove, M., and Lovera, O.M., 2000, The Zedong window: A record of superposed Tertiary convergence in southeastern Tibet: Journal of Geophysical Research, v. 105, p. 19211–19230.

Haschke, M., Ahmadian, J., Murata, M., and McDonald, I., 2010, Copper mineralization prevented by arc-root delamination during Alpine–Himalayan collision in central Iran: Economic Geology, v. 105, p. 855–865.

Hedenquist, J.W., and Lowenstern, J.B., 1994. The role of magmas in the formation of hydrothermal ore deposits: Nature, v. 370, p. 519–527.

Hezarkhani, A., 2006, Hydrothermal evolution of the Sar-Cheshmah porphyry Cu-Mo deposit, Iran: Evidence from fluid inclusions: Journal of Asian Earth Sciences, v. 28, p. 409–422.

Hidalgo, P.J., Vogel, T.A., Rooney, T., Currier, R., and Layer, P.W., 2011, Origin of silicic volcanism in the Panamanian arc: evidence for a two-stage process at El Valle volcano: Contributions to Mineralogy and Petrology, v. 162, p. 1115–1138.

Hildreth, W., and Moorbath, S., 1988, Crustal contributions to arc magmatism in the

Andes of central Chile: Contributions to Mineralogy and Petrology, v. 98, p. 455–489.

Hollister, L.S., Grissom, G.C., Peters, E.K., Stowell, H.H., and Sisson, V.B., 1987, Confirmation of the empirical correlation of Al in hornblende with pressure of solidification of calc-alkaline plutons: American Mineralogist, v. 72, p. 231–239.

Holzheid, A., and Lodders, K., 2001, Solubility of copper in silicate melts as function of oxygen and sulfur fugacities, temperature, and silicate composition: Geochimica et Cosmochimica Acta, v. 65, p. 1933–1951.

Hoskin, P.W.O., and Schaltegger, U., 2003, The composition of zircon and igneous and metamorphic petrogenesis, in Hanchar, J.M., and Hoskin, P.W.O. eds., Zircon: Reviews in Mineralogy and Geochemistry, v. 53, p. 27–62.

Hou, Z.Q., Gao, Y.F., Qu, X.M., Rui, Z.Y., and Mo, X.X., 2004, Origin of adakitic intrusives generated during mid-Miocene east-west extension in southern Tibet: Earth and Planetary Science Letters, v. 220, p. 139–155.

Hou, Z.Q., Yang, Z.M., Qu, X.M., Meng, X.J., Li, Z.Q., Beaudoin, G., Rui, Z.Y., Gao, Y.F., and Zaw, K., 2009, The Miocene Gangdese porphyry copper belt generated during post-collisional extension in the Tibetan Orogen: Ore Geology Reviews, v. 36, p. 25–31.

Hou, Z.Q., Zhang, H.R., Pan, X.F., and Yang, Z.M., 2011, Porphyry Cu (-Mo-Au) deposits related to melting of thickened mafic lower crust: Examples from the eastern Tethyan metallogenic domain: Ore Geology Review, v. 39, p. 21–45.

Hu, M.Y., He, H.L., Zhan, X.C., Fan, X.T., Wang, G., and Jia, Z.R., 2008, Matrix normalization fro in-situ multi-element quantitative of zircon in Laser Ablation-Inductively Coupled Plasma Mass Spectrometry: Chinese Journal of Analytical Chemistry, v. 36, p. 947–983. (in Chinese with English abstract)

Huang, K., Zheng, Y., Zhang, S., Li, W., Sun, Q., Li, Q., Liang, W., Fu, Q., and Hou, Z., 2012, LA-ICP-MS zircon U-Pb dating of two types of porphyry in the Yaguila mining area, Tibet: Acta Petrologica et Mineralogica, v. 31, p. 348–360. (in Chinese with English abstract)

Huebner, J.S., 1971, Buffering techniques for hydrostatic systems at elevated pressure in G. C. Ulmer, ed., Research Techniques for High Pressure and High Temperature: New York, Springer-Verlag, p. 123–177.

Huebner, J.S., and Sato, M., 1970, The oxygen fugacity-temperature relationships of manganese oxide and nickel oxide buffers: American Mineralogist, v. 55, p. 934–952.

Idrus, A., Kolb, J., and Meyer, F.M., 2007, Chemical composition of rock-forming minerals in copper-gold-bearing tonalite porphyries at the Batu Hijau deposit, Sumbawa island, Indonesia: Implications for crystallization conditions and fluorine–chlorine fugacity: Resource Geology, v. 57, p.102–113.

Irvine, T.N., and Baragar, W.R.A., 1971, A guide to the chemical classification of the common volcanic rocks: Canadian Journal of Earth Sciences, v. 8, p. 523-548.

Jackson, S.E., Pearson, N.J., Griffin, W.L., and Belousova, E.A., 2004, The application of laser ablation-inductively coupled plasma-mass spectrometry to in situ U-Pb zircon geochronology: Chemical Geology, v. 211, p. 47–69.

Jamieson, R.A., Unsworth, M.J., Harris, N.B,W., Rosenberg, C.L., and Schulmann, 2011, Crustal melting and the flow of mountains: Elements, v. 7, p. 253–260.

Jamieson, R.A., and Beaumont, C., 2013, On the origin of orogens: GSA Bulletin, v. 125, p. 1671–1702.

Ji, W.Q., Wu, F.Y., Chung, S.L., Li, J.X., and Liu, C.Z., 2009, Zircon U-Pb geochronology and Hf isotopic constraints on petrogenesis of the Gangdese batholith, southern Tibet: Chemical Geology, v. 262, p. 229–245.

Ji, W.Q., Wu, F.Y., Liu, C.Z., and Chung, S.L., 2012, Early Eocene crustal thickening in southern Tibet: New age and geochemical constraints from the Gangdese batholith: Journal of Asian Earth Sciences, v. 53, p. 82–95.

Johnson, M.C., and Rutherford, M.J., 1989, Experimental calibration of the aluminum-in-hornblende geobarometer with application to Long Valley caldera (California) volcanic rocks: Geology, v. 17, p. 837–841.

Jugo, P., 2009, Sulfur content at sufide saturation in oxidized magmas: Geology, v. 37, p. 415–418.

Jugo, P., Luth, R., and Richards, J., 2005a, An experimental study of the sulfur content in basaltic melts saturated with immiscible sulfide or sulfate liquids at 1300 °C and 1.0 GPa: Journal of Petrology, v. 46, p. 783–798.

Jugo, P., Luth, R., and Richards, J., 2005b, Experimental data on the speciation of sulfur as a function of oxygen fugacity in basaltic melts: Geochimica et Cosmochimica Acta,

v. 69, p. 497–503.

King, J., Harris, N., Argles, T., Parrish, R., Charlier, B., Sherlock, S., and Zhang, H.F., 2007, First field evidence for southward ductile flow of Asian crust beneath southern Tibet: Geology, v. 35, p. 727–730.

Kumar, P., Yuan, X., Kind, R., and Ni, J., 2006, Imaging the colliding Indian and Asian lithospheric plates beneath Tibet: Journal of Geophysical Research, v.111, B6: doi: 10.1029/2005JB003930.

Lee, C.T., Luffi, P., Chin, E., Bouchet, R., Dasgupta., Morton, D.M., Roux, V.L., Yin, Q.Z., and Jin, D., 2012, Copper systematics in arc magmas and implications for crust–mantle differentiation: Science, v. 336, p. 64–68.

Lee, H.Y., Chung, S.L., Lo, C.H., Ji, J., Lee, T.Y., Qian, Q., and Zhang, Q., 2009. Eocene Neotethyan slab breakoff in southern Tibet inferred from the Linzizong volcanic record: Tectonophysics, v. 477, p. 20–35.

Lee, H.Y., Chung, S.L., Ji, J.Q., Qian, Q., Gallet, S., Lo, Q.H., Lee, T.Y., and Zhang, Q., 2011, Geochemical and Sr-Nd isotopic constraints on the genesis of the Cenozoic Linzizong volcanic successions, southern Tibet: Journal of Asian Earth Sciences, v. 53, p. 96–114.

Lepage, L.D., 2003, ILMAT: an Excel worksheet for ilmenite–magnetite geothermometry and geobarometry: Computers and Geosciences, v. 29, p. 673–678.

Li, J.X., Qin, K.Z., Li, G.M., Xiao, B., Chen, L., and Zhao, J.X., 2011, Post-collisional ore-bearing adakitic porphyries from Gangdese porphyry copper belt, southern Tibet: Melting of thickened juvenile arc lower crust: Lithos, v. 126, p. 264–277.

Li, J.Z., Zhang, Y.Y., and Luo, H.Y., 1992, A research on petrological characters and genesis of the Cenozoic volcanic rocks in the Yangying village geothermal field, Dangxiong, Tibet, China: Geoscience, v. 6, p. 96–109. (in Chinese with English abstract)

Liang, H.Y., Campbell, I.H., Allen C., Sun, W.D., Liu, C.Q., Yu, H.X., Xie, Y.W., and Zhang, Y.Q., 2006, Zircon Ce^{4+}/Ce^{3+} ratios and ages for Yulong ore-bearing porphyries in eastern Tibet: Mineralium Deposita, v. 41, p. 152–159.

Loucks, R.R., 2013, Distinctive composition and genesis of copper ore-forming arc magmas: Mineralogical Magazine, v. 77, p. 1642.

Lu, Y.J., Kerrich, R., Kemp, A.I.S., McCuaig, T.C., Hou, Z.Q., Hart, C.J.R., Bagas, L.,Yang, Z.M., Cliff, J., Belousova, E.A., Jourdan, F., and Evans, N.J., 2013, Intracontinental Eocene-Oligocene porphyry Cu mineral systems of Yunnan, western Yangtze Craton, China: Compositional characteristics, sources, and implications for continental collision metallogeny: Economic Geology, v. 108, p. 1541–1576

Mechie, J., and Kind, R., 2013, A model of the crust and mantle structure down to 700 km depth beneath the Lhasa to Golmud transect across the Tibetan plateau as derived from seismological data: Tectonophysics, v. 606, p. 187–197.

Meng, J., Wang, C., Zhao, X., Coe, R., Li, Y.L., and Finn, D., 2012, India-Asia collision was at 24° N and 50 Ma: Paleomagnetic proof from southern Asia: Scientific Reports, 2, 925; doi: 10.1038/srep00925.

Middlemost, 1994, Naming materials in the magma / igneous rock system: Earth Science Reviews, v. 37, p. 215–224.

Mo, X.X., Zhao, Z.D., Deng, J.F., Dong, G.C., Zhou, S., Guo, T.Y., Zhang, S.Q., and Wang, L.L., 2003, Response of volcanism to the India–Asian collision: Earth Science Frontiers 10, 135–148. (in Chinese with English abstract)

Mo, X.X., Niu, Y.L., Dong, G.C., Zhao, Z.D., Hou, Z.Q., Zhou, S., and Ke, S., 2008, Contribution of syncollisional felsic magmatism to continental crust growth: A case study of the Paleogene Linzizong volcanic succession in southern Tibet: Chemical Geology, v. 250, p. 49–67.

Moore, G.M., and Carmichael, I.S.E., 1998, The hydrous phase equilibria (to 3 kbar) of an andesite and basaltic andesite from western Mexico: Constraints on water content and conditions of phenocryst growth: Contributions to Mineralogy and Petrology, v. 130, p. 304–319.

Mungall, J.F., 2002, Roasting the mantle: slab melting and the genesis of major Au and Au-rich deposits: Geology, v. 30, p. 915–918.

Müntener, O., Kelemen, P.B., and Grove, T.L., 2001, The role of H_2O during crystallization of primitive arc magmas under uppermost mantle conditions and genesis of igneous pyroxenites: An experimental study: Contributions to Mineralogy and Petrology, v. 141, p. 643–658.

Muñoz, M., Charrier, R., Fanning, C.M., Maksaev, V. and Deckart, K., 2012, Zircon

trace element and O–Hf isotope analyses of mineralized intrusions from El Teniente ore deposit, Chilean Andes: Constraints on the source and magmatic evolution of porphyry Cu–Mo related magmas: Journal of Petrology, v. 53, p. 1091–1122.

Naney, M.T., 1983, Phase equilibria of rock-forming ferromagnesian silicates in granitic systems: American Journal of Science, v. 283, p. 993–1033.

Pearce, N.J.G., Perkins, W.T., Westgate, J.A., Gorton, M.P., Jackson, S.E., Neal, C.R., and Chenery, S.P., 1997, A compilation of new and published major and trace element data for NIST SRM 610 and NIST SRM 612 glass reference materials: Geostandards Newsletter, v. 21, p. 115–144.

Pichavant, M., Martel, C., Bourdier, J.L., and Scaillet, B., 2002, Physical conditions, structure, and dynamics of a zoned magma chamber: Mount Peleè (Martinique, Lesser Antilles Arc): Journal of Geophysical Research, v. 107, B5, 2093. doi:10.1029/2001JB000315.

Pollard, P.J., Taylor, R.G., and Peters, L., 2005, Ages of intrusion, alteration, and mineralization at the Grasberg Cu–Au deposit, Papua, Indonesia: Economic Geology, v. 100, p. 1005–1020.

Powell, R., and Powell, M., 1977, Geothermometry and oxygen barometry using coexisting iron-titanium oxides: a reappraisal: Mineralogical Magazine, v. 41, p. 257–263.

Replumaz, A., Negredo, A.M., Villaseñor, A., and Guillot, S., 2010, Indian continental subduction and slab breakoff during Tertiary collision: Terra Nova, v. 22, p. 290–296.

Rhodes, J.M. and Vollinger, M.J., 2005, Ferric/ferrous ratios in 1984 Mauna Loa lavas: a contribution to understanding the oxidation state of Hawaiian magmas: Contributions to Mineralogy and Petrology, v. 149, 666–674.

Richards, J.P., 1995, Alkalic-type epithermal gold deposits—a review: Mineralogical Association of Canada Short Course Series, v. 23, p. 367–400.

Richards, J.P., 2003, Tectono-magmatic precursors for porphyry Cu-(Mo-Au) deposit formation: Economic Geology, v. 98, p. 1515−1533.

Richards, J.P., 2009, Postsubduction porphyry Cu–Au and epithermal Au deposits: products of remelting of subduction-modified lithosphere: Geology, v.37, p. 247–250.

Richards, J.P., 2011, Magmatic to hydrothermal metal fluxes in convergent and collided

margins: Ore Geology Reviews, v. 40, p. 1–26.

Richards, J.P., and Mumin, H., 2013, Lithospheric fertilization and mineralization by arc magmas: Genetic links and secular differences between porphyry copper ± molybdenum ± gold and magmatic-hydrothermal iron oxide copper-gold deposits: Society of Economic Geologists, Special Publications, v. 17, p. 277–299.

Richards, J.P., McCulloch, M.T., Chappell, B.W., and Kerrich, R., 1991, Sources of metals in the Porgera gold deposit, Papua New Guinea: Evidence from alteration, isotope, and noble metal geochemistry: Geochimica et Cosmochimica Acta, v. 55, p. 565–580.

Richards, J.P., Jourdan, F., Creaser, R.A., Maldonado, G., and DuFrane, A., 2013, Geology, geochemistry, geochronology, and economic potential of Neogene volcanic rocks in the Laguna Pedernal and Salar de Aguas Calientes segments of the Archibarca lineament, northwest Argentina: Journal of Volcanology and geothermal research, v. 258, p. 47–73.

Ridolfi, F., Puerini, M., Renzulli, A., Menna, M., and Toulkeridis, T., 2008, The magmatic feeding system of El Reventador volcano (Sub-Andean zone, Ecuador) constrained by texture, mineralogy and thermobarometry of the 2002 erupted products: Journal of Volcanology and Geothermal Research, v. 176, p. 94–106.

Ridolfi, F., Renzulli, A., and Puerini, M., 2010, Stability and chemical equilibrium of amphibole in calc-alkaline magmas: An overview, new thermobarometric formulations and application to subduction-related volcanoes: Contributions to Mineralogy and Petrology, v. 160, p. 45–66.

Rohrlach, B., and Loucks, R., 2005, Multi-million-year cyclic ramp-up of volatiles in a lower crustal magma reservoir trapped below the Tampakan Cu-Au deposit by Mio-Pliocene crustal compression in the southern Philippinel; in Porter, T.M. (ed.), Super Porphyry Copper & Gold Deposits: A Global Perspective: PGC Publishing, Adelaide, v. 2, p. 369–407.

Rowley, D.B., 1996, Age of initiation of collision between India and Asia: a review of stratigraphic data: Earth and Planetary Science Letters, v. 145, p. 1–13

Sauerzapf, U., Lattard, D., Burchard, M., and Engelmann, R., 2008, The titanomagnetite–ilmenite equilibrium: new experimental data and thermo-oxybarometric application to

the crystallisation of basic to intermediate rocks: Journal of Petrology, v. 49, p. 1161–1185.

Scaillet, B., and Evans, B.W., 1999, The 15 June 1991 eruption of Mount Pinatubo; I, Phase equilibria and pre-eruption P–T–fO_2–fH_2 conditions of the dacite magmas: Journal of Petrology, v. 40, p. 381–411.

Schmidt, M.W., 1992, Amphibole composition in tonalite as a function of pressure; an experimental calibration of the Al-in hornblende barometer: Contribution to Mineralogy and Petrology, v. 110, p. 304–310.

Shafiei, B., Haschke, M., and Shahabpour, J., 2009, Recycling of orogenic arc crust triggers porphyry Cu mineralization in Kerman Cenozoic arc rocks, southeastern Iran: Mineralium Deposita, v. 44, 265–283.

Sillitoe, R.H., 1972, A plate tectonic model for the origin of porphyry copper deposits: Economic Geology, v. 67, p. 184−197.

Sillitoe, R.H., 2010, Porphyry copper system: Economic Geology, v. 105, p. 3−41.

Simonetti, A., Heaman, L.M., Hartlaub, R.P., Creaser, R.A., MacHattie, T.G., and Böhm, C., 2005, U-Pb zircon dating by laser ablation-MC-ICP-MS using a new multiple ion counting Faraday collector array: Journal of Analytical Atomic Spectrometry, v. 20, p. 677–686.

Sisson, T.W., and Grove, T.L., 1993, Temperature and H_2O contents of low-MgO high-alumina basalts: Contribution to Mineralogy and Petrology, v. 113, p. 167–184.

Spencer, K.J., and Lindsley, D.H., 1981, A solution model for coexisting iron-titanium oxides: American Mineralogist, v. 66, p. 1189–1201.

Spooner, E.T.C., 1993, Magmatic sulphide/volatile interaction as a mechanism for producing chalcophile element enriched, Archean Au-quartz, epithermal Au-Ag and Au skarn hydrothermal ore fluids: Ore Geology Reviews, v. 7, p. 359–379.

Sun, S.S., and McDonough, W.F., 1989, Chemical and isotopic systematics of oceanic basalts: Implications for mantle composition and processes: Geological Society of London Special Publication, v. 42: p. 313–345.

Tafti, R., 2011, Metallogeny, geochronology and tectonic setting of the Gangdese belt, southern Tibet, China: Unpublished Ph.D. thesis, University of British Columbia, Canada, 451 p.

Tindle, A.G. and Webb, P.C., 1994, PROBE-AMPH a spreadsheet program to classify microprobe-derived amphibole analyses: Computers and Geosciences, v. 20, p. 1201–1228.

Toummite, A., Ikenne, M., and Beraaouz, E.H., 2012, Geothermobarometry of Askaoun pluton in Ouzellarh-Sirwa promontory (Central Anti-Atlas; Morocco): Open Journal of Geology, v. 2, p. 136–147.

Trail, D., Watson, E.B., and Tailby, N.D., 2011, The oxidation state of Hadean magmas and implications for early Earth's atmosphere: Nature, v. 480, p. 79–82.

Unsworth, M.J., Jones, A.G., Wei, W., Marquis, G., Gokarn, S.G., Spratt, J.E., 2005, Crustal rheology of the Himalaya and Southern Tibet inferred from magnetotelluric data: Nature, v. 438, p. 78–81.

Van der Voo, R., Spakman, W., and Bijwaard, H., 1999, Tethyan subducted slabs under India: Earth and Planetary Sciences Letters, v. 171, p. 7–20.

van Hinsbergen, D.J.J., Lippert, P.C., Dupont-Nivet, G., McQuarrie, N., Doubrovine, P.V., Spakman, W., and Torsvik, T.H., 2012, Greater India basin hypothesis and a two-stage Cenozoic collision between India and Asia: Proceedings of the National Academy of Science of the United States of America, v. 20, p. 7659–7664.

Venezky, D.Y., and Rutherford, M.J., 1999, Petrology and Fe–Ti oxide reequilibration of the 1991 Mount Unzen mixed magma: Journal of Volcanology and Geothermal Research, v. 89, p. 213–230.

Wang, B.D., Xu, J.F., Chen, J.L., Zhang, X.G., Wang, L.Q., and Xia, B.B., 2010, Petrogenesis and geochronology of the ore-bearing porphyritic rocks in Tangbula porphyry molybdenum-copper deposit in the eastern segment of the Gangdese metallogenic belt: Acta Petrologica Sinica, 26, v. 26, 1820–1830. (in Chinese with English abstract)

Wang, F.Y., Liu, S.A., Li, S.G., and He, Y.S., 2013, Contrasting zircon Hf-O isotopes and trace elements between ore-bearing and ore-barren adakitic rocks in central-eastern China: Implications for genetic relation to Cu–Au mineralization: Lithos, v. 156–159, p. 97–111.

Wang, R., Richards, J.P., Hou, Z.Q., and Yang, Z.M., 2014a, Extent of underthrusting of the Indian plate beneath Tibet controlled of Miocene porphyry Cu-Mo±Au deposits:

Mineralium Deposita, v. 49, p. 165–173, DOI: 10.1007/s00126-013-0507-y

Wang, R., Richards, J.P., Hou, Z.Q., Yang, Z.M., and DuFrane, S.A., 2014b, Increased magmatic water content–the key to Oligo-Miocene porphyry Cu-Mo±Au formation in the eastern Gangdese belt, Tibet: Economic Geology, in press.

Wang, Z.H, Liu, Y.L., Liu, H.F., Guo, L.S., Zhang, J.S., and Xu, K.F., 2012, Geochronology and geochemistry of the Bangpu Mo-Cu porphyry ore deposit, Tibet: Ore Geology Review, v. 46, p. 95–105.

Watson, E.B., and Harrison, T.M., 2005, Zircon thermometer reveals minimum melting conditions on earliest Earth: Science, v. 308, p. 841–844.

Wen, D.R., 2007, The Gangdese batholith, Southern Tibet: Ages, geochemical characteristics and petrogenesis: Unpublished Ph.D. Thesis, National Taiwan University, 120 p.

Wei, S.N., and Zhu, Y.F., 2010, Emplacement of the intermediate and acid magmatic rocks in Xinjiang: Constraints from the P-T-fO_2 and geochemistry: Acta Geologica Sinica, v. 84, p. 1017–1029. (in Chinese with English abstract)

White, L.T., Ahmad, T., Ireland, T.R., Lister, G.S., and Forster, M.A., 2011, Deconvolving episodic age spectra from zircons of the Ladakh batholith, northwest Indian Himalaya: Chemical Geology, v. 289, p. 179–196.

Williams, H.M., 2000, Magmatic and tectonic evolution of Southern Tibet and the Himalaya: Ph.D. thesis, The Open University, 329 p.

Wilkinson, J.J., 2013, Triggers for the formation of porphyry ore deposits in magmatic arcs: Nature Geoscience, v. 6, p. 915–925.

Xia, B.B., Xia, B., Wang, B.D., Li, J.F., Zhang, X.G., and Wang, Y.C., 2010, Formation of the Tangbula porphyry Mo-Cu deposit evidence from SHRIMP Zircon U-Pb dating of Tangbula ore-bearing porphyries: Geotectonic et Metallogenia, v. 34, p. 291–297. (in Chinese with English abstract)

Xiao, B., 2011, Highly oxidized magmatic-hydrothermal ore-forming process at the Qulong giant porphyry Cu-Mo deposit, Gangdese, Tibet: Unpublished Ph.D. thesis (in Chinese), Institute of Geology and Geophysics, Chinese Academy of Sciences, Beijing, 275 p.

Xu, W.C., Zhang, H.F., Guo, L., and Yuan, H.L., 2010, Miocene high Sr/Y magmatism,

south Tibet: Product of partial melting of subducted Indian continental crust and its tectonic implication: Lithos, v. 114, p. 293–306.

Yang, Z.M., 2008, The Qulong giant porphyry copper deposit in Tibet: Magmatism and mineralization: Unpublished Ph.D. thesis, Institute of Geology Chinese Academy of Geological Sciences, Beijing, 144 p. (in Chinese with English abstract)

Yang, Z.M., Hou, Z.Q., White, N.C., Chang, Z.S., Li, Z.Q., and Song, Y.C., 2009, Geology of the post-collisional porphyry copper-molybdenum deposit at Qulong, Tibet: Ore Geology Reviews, v. 36, p. 133–159.

Yang, Z.M., Hou, Z.Q., Jiang, Y.F., Zhang, H.R., and Song, Y.C., 2011, Sr-Nd-Pb and zircon Hf isotopic constraints on petrogenesis of the late Jurassic granitic porphyry at Qulong, Tibet: Acta Petrologica Sinica, v. 27, p. 2003–2010. (in Chinese with English abstract)

Yin, A., and Harrison, T.M., 2000, Geologic evolution of the Himalayan-Tibetan orogen: Annual Review of Earth and Planetary Sciences, v. 28, p. 211–280.

Ying, L.J., Wang, C.S., Tang, J.X., Wang, D.H., Qu, W.J., and Li, C., 2014, Re-Os systematics of sulfides (chalcopyrite, bornite, pyrite and pyrrhotite) from the Jima Cu-Mo deposit of Tibet, China: Journal of Asian Earth Sciences, v. 79, p. 497–506.

Zajacz, Z., Candela, P.A., Piccoli, P.M., Wälle, M., and Sanchez-Valle, C., 2012, Gold and copper in volatile saturated mafic to intermediate magmas: Solubilities, partitioning, and implications for ore deposit formation: Geochimica et Cosmochimica Acta, v. 91, p. 140–159.

Zajacz, Z., Candela, P.A., Piccoli, P.M., Sanchez-Valle, C., and Wälle, M., 2013, Solubility and partitioning behavior of Au, Cu, Ag and reduced S in magmas: Geochimica et Cosmochimica Acta, v. 112, p. 288–304.

Zhang, S., Zheng, Y., Huang, K., Li, W., Sun, Q., Li, Q., Fu, Q., and Liang, W., 2012, Re-Os dating of molybdenite from Nuri Cu-W-Mo deposit and its geological significance: Mineral deposits, v. 31, p. 337–346. (in Chinese with English abstract)

Zhao, J., Yuan, X., Liu, H., Kumar, P., Pei, S., Kind, R., Zhang, Z., Teng, J, Ding, L., Gao, X., Xu, Q., and Wang, W., 2010, The boundary between the Indian and Asian tectonic plates below Tibet: Proceedings of the National Academy of Science of the United States of America, v. 107, p. 11229–11233.

Zhao, J.X., Qin, K.Z., Li, G.M., Li, J.X., Xiao, B., and Chen, L., 2011a, Geochemistry and petrogenesis of granitoids at Sharang Eocene porphyry Mo deposit in the main-stage of India-Asia continental collision, northern Gangdese, Tibet: Resource Geology, v. 62, p. 84–98.

Zhao, J.X., Qin, K.Z., Li, G.M., Li, J.X., Xiao, B., Chen, L., Yang, Y.H., Li, C., and Liu, Y.S., 2014, Collision-related genesis of the Sharang porphyry molybdenum deposit, Tibet: Evidence from zircon U-Pb ages, Re-Os ages and Lu-Hf isotopes: Ore Geology Review, v. 56, p. 312–326.

Zhao, Z.D., Mo, X.X., Dilek, Y, Niu, Y.L., DePaolo, D.J., Robinson, P., Zhu, D.C., Sun, C.G., Dong, G.C., Zhou, S., Luo, Z.H., and Hou, Z.Q., 2009, Geochemical and Sr-Nd-Pb-O isotopic compositions of the post-collisional ultrapotassic magmatism in SW Tibet: Petrogenesis and implications for India-continental subduction beneath southern Tibet: Lithos, v. 113, p. 190–212.

Zhao, Z.D., Zhu, D.C., Dong, G.C., Mo, X.X., DePaolo, D., Jia, L.L., Hu, Z.C., and Yuan, H.L., 2011b, The ~54 Ma gabbro–granite intrusive in southern Dangxung area, Tibet: Petrogenesis and implications: Acta Petrologica Sinica, v. 27, p. 3513–3524.

Zheng, Y.C., Hou, Z.Q., Li, Q.Y., Sun, Q.Z., Liang, W., Fu, Q., Li, W., and Huang, K.X., 2012a, Origin of late Oligocene adakitic intrusives in the southeastern Lhasa terrane: Evidence from in situ zircon U-Pb dating, Hf-O isotopes: Lithos, v. 148, p. 296–311.

Zheng, Y.C., Hou, Z.Q., Li, W., Liang, W., Huang, K.X., Li, Q.Y., Sun, Q.Z., Fu, Q., and Zhang, S., 2012b, Petrogenesis and geological implications of the Oligocene Chongmuda-Mingze adakite-like intrusions and their mafic enclaves, southern Tibet: Journal of Geology, v. 120, p. 647–669.

Zheng, Y.Y., Sun, X., Gao, S.B., Zhao, Z.D., Zhang, G.Y., Wu, S., You, Z.M., and Li, J.D., 2014, Multiple mineralization events at the Jiru porphyry copper deposit, southern Tibet: Implications for Eocene and Miocene magma sources and resource potential: Journal of Asian Earth Sciences, v. 79, p. 842–857.

Zhou, S., Mo, X.X., Zhao, Z.D., Qiu, R.Z., Zhang, S.Q., and Guo, T.Y., 2004, ^{40}Ar–^{39}Ar geochronology of Yangying post-collisional volcanic rock south Tibet and its geological significance: Progress in Natural Sciences, v. 12, p. 1411–1488. (in Chinese with English abstract)

Zhu, D.C., Zhao, Z.D., Niu, Y.L., Mo, X.X., Chung, S.L., Hou, Z.Q., Wang, L.Q., and Wu, F.Y., 2011, The Lhasa terrane: Record of a microcontinent and its histories of drift and growth: Earth and Planetary Science Letters, v. 301, p. 241–255.

Zhu, D.C., Zhao, Z.D., Niu, Y.L., Dilek, Y., Hou, Z.Q., and Mo, X.X., 2013, The origin and pre-Cenozoic evolution of the Tibetan Plateau: Gondwana Research, v. 23, p. 1429–1454.

Zimmer, M.M., Plank, T., Hauri, E.H., Yogodzinski, G.M., Stelling, P., Larsen, J., Singer, B., Jicha, B., Mandeville, C., and Nye, C.J., 2010, The role of water in generating the calc-alkaline trend: New volatile data for Aleutian magmas and a new Tholeiitic Index: Journal of Petrology, v. 51, p. 2411–2444.

Chapter 4

Extent of underthrusting of the Indian plate beneath Tibet controlled the distribution of Miocene porphyry Cu–Mo ± Au deposits[1]

4.1 Introduction

The Himalayan-Tibetan orogen formed by collision of India with Asia beginning at ~55–50 Ma (Allègre et al., 1984; Burg and Chen, 1984; Rowley, 1996; de Sigoyer et al., 2000; Meng et al., 2012). Following this event, a large number of small-volume calc-alkaline and mildly alkaline granitoids were mostly emplaced in the eastern Gangdese belt (east of ~89°E) between ~30–10 Ma (Chung et al., 2003, 2009; Hou et al., 2004; Zheng et al., 2012), whereas potassic–ultrapotassic volcanic rocks were mostly erupted in the western Gangdese belt (west of ~89°E) between ~24–8 Ma (Fig. 4-1; Miller et al., 1999; William et al., 2004; Guo et al., 2007, 2013; Zhao et al., 2009). Many of these igneous rocks were emplaced along north–south-trending normal faults and grabens generated by east–west extension between 19 and 4 Ma (Fig. 4-1; Armijo et al., 1986; Burchfiel et al., 1991; Blisniuk et al., 2001; Williams et al., 2001; Mitsuishi et al., 2012). More large and deep rifts (with graben basins) occur in the western Gangdese (Cogen et al., 1998; Tapponnier et al., 2001; Fig. 4-1), might facilitate ascending and eruption of western potassic–ultrapotassic volcanic magmas. Most of the granitoids located in the eastern part of the Gangdese belt (between 89°E and 94°E) have high Sr/Y ratios, and several are associated with giant porphyry Cu-Mo±Au deposits (Hou et al., 2011; Fig. 4-2). The largest deposits formed in the Miocene, and include the giant Qulong porphyry Cu-Mo deposit (16.4 ± 0.5 Ma; 1,420 Mt @ 0.5% Cu; Yang et al., 2009), the giant Jiama porphyry Cu-Mo-Au deposit (14.8 ± 0.33 Ma; 1,054 Mt @ 0.44 % Cu; Ying et al., 2014), and several large- to medium-sized porphyry Cu-Mo deposits such as Bangpu, Tangbula, Lakang'e, Chongjiang, Tinggong, and weakly mineralized stocks. In contrast, there are only one small-sized porphyry Cu deposit and few porphyry- or epithermal type mineralization to the west of ~89°E.

[1] This chapter was published as: Wang, R., Richards, J.P., Hou, Z.Q., and Yang, Z.M., 2014, Extent of underthrusting of the Indian plate beneath Tibet controlled the distribution of Miocene porphyry Cu–Mo ± Au deposits: Mineralium Deposita, v. 49, p. 165–173. DOI 10.1007/s00126-013-0507-y.

The characteristics of these porphyry deposits in Gangdese belt, which were formed in a late-collisional tectonic setting, are similar in many respects to those in arc settings (i.e., mineralization style, alteration zoning, and metal association; Hou et al., 2009). Similar examples of porphyry deposits in arc collisional environments of the world include the Eocene Çöpler porphyry Cu-Au deposit in East Central Anatolia, Turkey (Imer et al., 2012), the late Miocene Sari Gunay porphyry Cu and epithermal Au system in Northwest Iran (Richards et al., 2006), and Miocene Sar Cheshmeh porphyry Cu-Mo deposit in Kerman porphyry belt, Central Iran (Hezarkhani, 2006; Aminzadeh et al., 2011). These deposits are almost indistinguishable from normal arc porphyries can be generated in collisional orogenic belts tens of millions of years after subduction has ceased, by remobilization of fluids and metals previously introduced into the lithosphere by prior subduction events.

We propose that the contrasting styles of late-collisional magmatism and metallogenic potential along the Miocene Gangdese belt reflect different sources of magmatism: fertile magmas in the eastern section of the belt were generated by subduction-modified lower crust melting following breakoff of the Greater India slab, whereas barren magmas to the west of ~89°E were derived from Tibetan lithospheric mantle with input of fluids and melts from underthrust Indian continental lithosphere.

4.2 Geological and tectonic setting

Northward-directed subduction of the Neo-Tethys oceanic lithosphere along the Indus-Yarlung Zangbo suture started in the Late Triassic–Early Jurassic, and produced voluminous calc-alkaline Cretaceous–Eocene granitoids and volcanic rocks in the 1600 km-long Gangdese magmatic belt (Fig. 4-1; Wen, 2007; Chu et al., 2011). Greater India (the Indian continental margin) first contacted the southern margin of Asia (southern Tibet) at ~55–50 Ma, marking the start of the India–Asia collision (van Hinsbergen et al., 2012). During this collisional event, the upper crust of Greater India was scraped off and forms part of the Himalayas, whereas the dense lower crust and sub-continental lithospheric mantle subducted beneath southern Tibet (Capitanio et al., 2010). The Neo-Tethyan oceanic slab detached from Greater India at ~45 Ma (Van der Voo et al., 1999), and a series of picritic to basaltic–andesitic lavas erupted in the Dazi basin between 40–38 Ma, which are thought to be related to this event (Gao et al., 2008). The thicker, more rigid and buoyant Indian craton began to underthrust Asia at ~35 Ma ("hard-collision": Replumaz et

al.,, 2010; van Hinsbergen et al., 2012), followed by breakoff of the dense Greater India slab; this breakoff event started in the west at ~25 ± 5 Ma, and the tear propagated eastward until final detachment beneath eastern Tibet at ~10 ± 5 Ma (Van der Voo et al., 1999; Replumaz et al., 2010). This second slab breakoff event triggered late Oligocene magmatism (29–31 Ma: Ding et al., 2003; Liu et al., 2008) to the north of the western Gangdese belt (south Qiangtang terrane, Fig. 4-1), and Oligo-Miocene magmatism in the eastern Gangdese belt (~30–10 Ma: Hou et al., 2009). Seismic tomographic studies indicate that the Indian continental lithosphere (100 to 200 km thick) extends northward below the Tibetan plateau, and underthrusting was accompanied by NNE–SSW shortening and ESE–WNW extension in the upper plate (Zhang et al., 2004). The extent of underthrusting decreases from west (~33º N, ~87° E) to east (~ 30º N, ~93° E; Kumar et al., 2006; Kind and Yuan 2010; Zhao et al., 2010), and is oblique to the Indus-Yarlung Zangbo suture in eastern Tibet (Fig. 4-1).

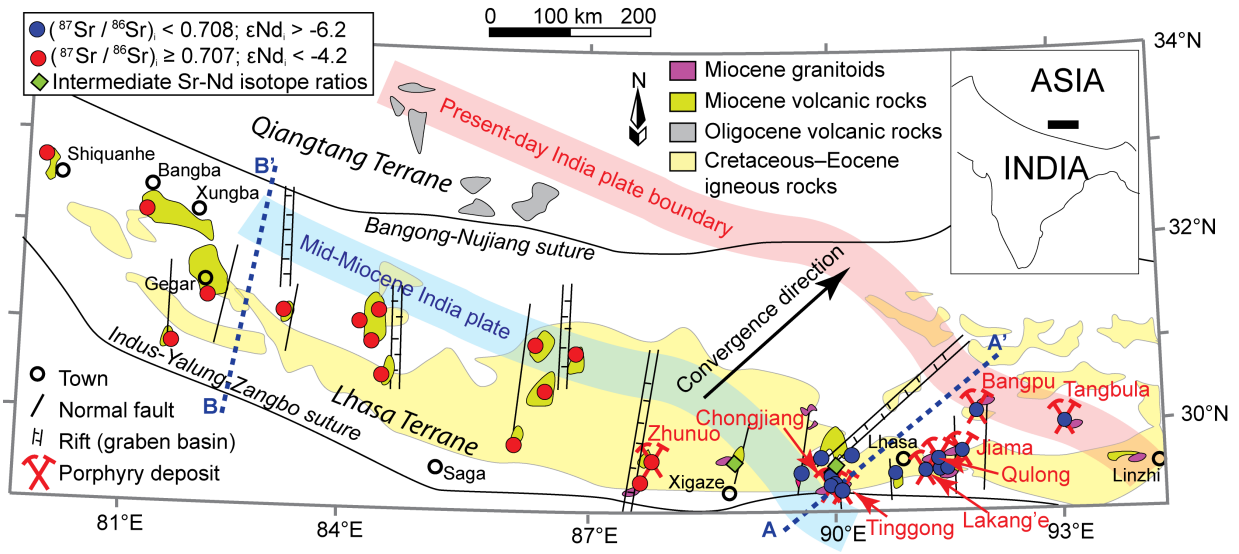

Figure 4-1. Geological setting of the Lhasa terrane, southern Tibet (modified from Wen 2007; Hou et al. 2009; Zhao et al. 2009). The broad pink line represents the present northern limit of the underthrust Indian plate beneath the Tibetan plateau (Kumar et al. 2006; Kind and Yuan 2010; Zhao et al. 2010), whereas the broad blue line is its estimated location in the mid-Miocene; the convergence direction is shown with a black arrow (see text for data sources). The locations of major porphyry Cu-Mo±Au deposits in the Gangdese belt are also shown (labeled in red). Cross-section lines A–A' and B–B' (following seismic profiles of Zhao et al. 2010) are shown in Figure 4-4. The locations of samples with isotopic analyses compiled from the literature are shown as red dots ($(^{87}Sr/^{86}Sr)_i < 0.708$, and $\varepsilon Nd_i > -6.2$), blue dots ($(^{87}Sr/^{86}Sr)_i > 0.707$, and $\varepsilon Nd_i < -4.2$), and green diamonds (with intermediate Sr-Nd isotope ratios); see online appendix in Wang et al., (2014) for sources of data.

4.3 Extent of underthrusting of the Indian lithosphere in the Miocene

In order to understand the potential sources and triggers of magmatism in the Gangdese belt during the Miocene, it is necessary to estimate the northern limit of underthrusting of the Indian continental lithosphere at that time. Based on earthquake vectors, the rate of Quaternary extension in the Himalayas, and other geological parameters, the rate of present day underthrusting (India–Tibet convergence) has been estimated to be between 14 and 20 mm/yr (Feldl and Bilham et al., 2006). Similarly, recent GPS measurements and modeling of plate motions indicate a rate of 17 mm/yr in the Himalayas between ~76°E and 90°E, with a convergence vector directed NE (Banerjee et al., 2008). Thus, assuming a constant convergence rate of 17 mm/yr since the Miocene, the northern limit of underthrusting of the Indian lithosphere at 15 Ma is estimated to be ~255 km SW of the current position, as shown on Figure 4-1. Although there are many uncertainties in this estimate, a location midway between the present position of the plate boundary and its presumed location along the Indus-Yarlung Zangbo suture at the time of hard-collision at ~35 Ma is reasonable. Assuming this location to be broadly correct, it is immediately noticeable from Figure 4-1 that the Miocene plate edge closely matches the boundary between Miocene alkaline volcanism in the western Gangdese belt and calc-alkaline plutonism to the east.

4.4 Samples used for this study

Magmatic compositions are sensitive indicators of geodynamic setting. We have compiled published whole-rock geochemical data for 204 least-altered Miocene volcanic and intrusive rocks from the Gangdese belt of Tibet (see online appendix in Wang et al., 2014) in order to assess spatial differences in composition and petrogenesis along the belt. Because many sample locations in the eastern Gangdese belt are associated with porphyry-type alteration and mineralization, we excluded any samples with >2 wt.% LOI or which were described as significantly altered.

Samples, and their isotopic and geochemical data for this paper are collected from literature: Coulon et al., 1986; Turner et al., 1996; Miller et al., 1999; Williams et al., 2001, 2004; Chung et al., 2003; Ding et al., 2003; Hou et al., 2004; Gao et al., 2007, 2010; Guo et al., 2007; Yang et al., 2009; Zhao et al., 2009; Wang et al., 2010; Xia et al., 2010; Xu et al., 2010; Li et al., 2011.

4.5 Petrology and geochemistry of Miocene igneous rocks

Late-collisional Miocene igneous rocks in the Gangdese belt can be divided into two groups based on Sr-Nd isotope ratios (Fig. 4-2A, Fig. 4-3A). These groupings also broadly correspond to magma types (Fig. 4-2B), the separation between volcanism and plutonism at ~89°E, and the approximate location of the northern boundary of the underthrust Indian plate in the Miocene (Fig. 4-1).

Petrogenesis of low ($^{87}Sr/^{86}Sr)_i$ rocks in the eastern Miocene Gangdese belt

The eastern plutonic suite mainly consists of small (<1 km^2) amphibole-bearing calc-alkaline quartz monzonite porphyry, granite porphyry, granodiorite, and monzonite intrusions, with subordinate amounts of dacitic and rhyolitic volcanic rocks. They are characterized by relatively low and tightly clustered ($^{87}Sr/^{86}Sr)_i$ ratios (0.705 to 0.708, average = 0.7057 ± 0.0008, n = 49; Fig. 4-2C), and positive to weakly negative εNd_i values (+5.5 to -6.1, average = -0.9 ± 2.3, n = 49; Fig. 4-2A, C). They have arc-like geochemical features characterized by enrichments in large-ion lithophile elements (Rb, Ba, Th, U, and K) and depletions in high field strength elements (Nb and Ta). The suite is characterized by high Sr/Y ratios (23 to 342, average = 120 ± 57, n = 86; Fig. 4-2D), low Y and Yb contents (Fig. 4-3B, C), listric-shaped rare earth element (REE) patterns (Fig. 4-3D), and small or absent Eu anomalies (Eu_N/Eu^* = 0.44 to 1.46, average = 0.95 ± 0.13, n = 91; Fig. 4-3E). These features suggest that the magmas evolved by extensive fractionation of amphibole from relatively hydrous and oxidized magmas (Green and Pearson, 1985; Richards, 2011).

The main models for the origin of the Miocene eastern plutons include partial melting of the subducted Neo-Tethyan slab (Qu et al., 2004, 2007), or subduction modified lower crust (Guo et al., 2007; Li et al., 2011). The eastern Gangdese Miocene plutonic rocks have similar compositions and Sr-Nd isotopic ratios to cospatial Cretaceous–Paleocene Gangdese arc batholiths, which were generated in response to Neo-Tethyan subduction (Fig. 4-2C; Wen, 2007). However, the Miocene intrusions formed ~30–45 m.y. after the onset of India–Asia collision, and cannot therefore be directly related to subduction. Breakoff of the dense Greater India slab in the Miocene triggered upwelling of asthenospheric mantle (Hou et al., 2009), which we suggest caused partial melting of previously subduction-modified Tibetan lithosphere (Fig. 4-4A). Being derived from the residues of previous arc magmatism, the resulting Miocene magmas would have

similar geochemical and isotopic compositions to the Cretaceous–Paleocene arc batholiths, despite not being directly related to active subduction. The intermediate–felsic nature (Fig. 4-2B) of most eastern Miocene granitoids suggest their magmas were mostly derived from partial melting of lower crust. In addition, the scatter of Sr-Nd isotope compositions of Oligo-Miocene magmas might also reflect the contamination with mid-crustal flows (Unsworth et al., 2005; Jamieson et al., 2011; Jamieson and Beaumont, 2013), which have relatively enriched Sr-Nd isotopic compositions ($^{87}Sr/^{86}Sr$ = 0.7071–0.7079, εNd -4 to -6; King et al., 2007).

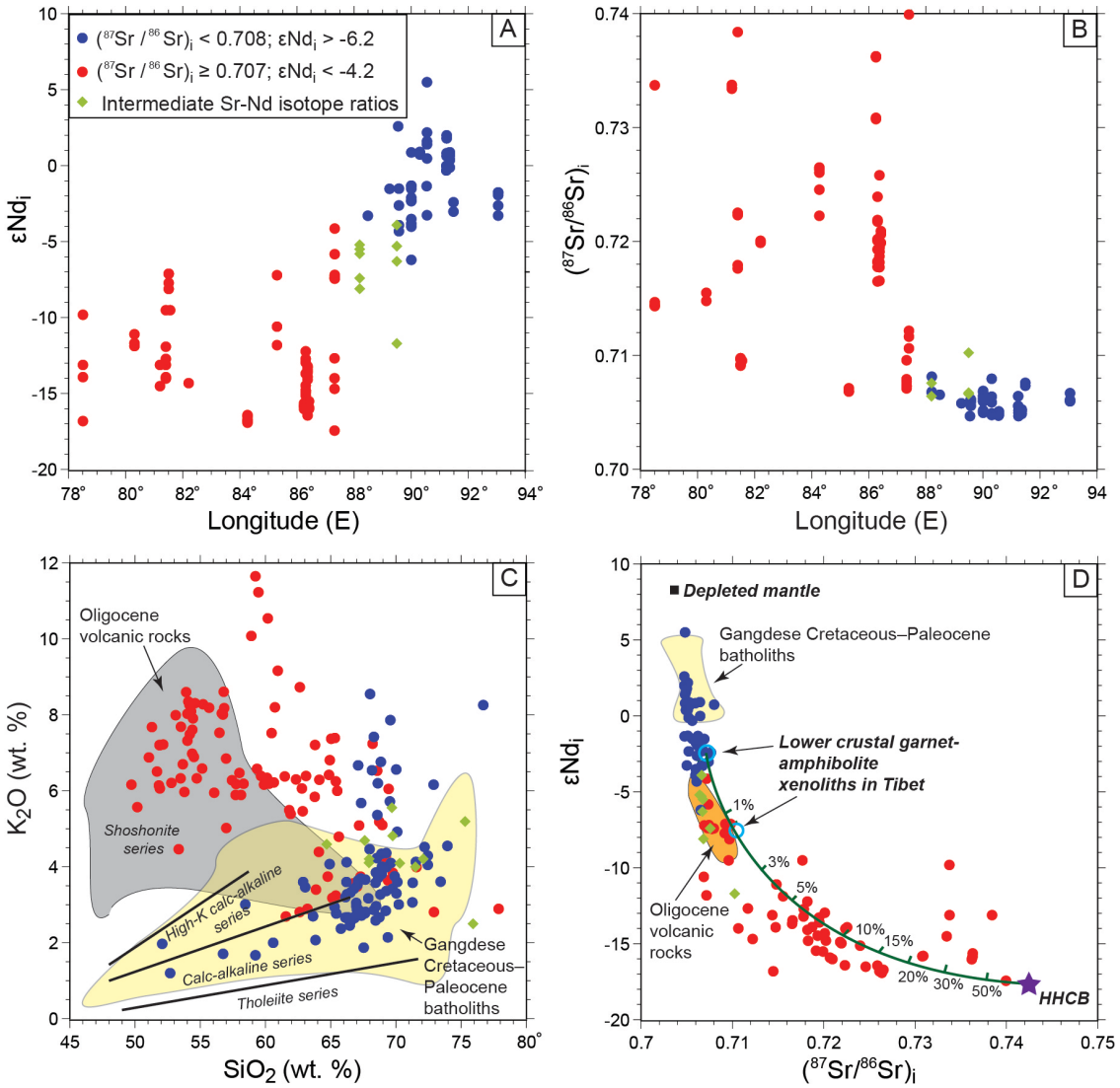

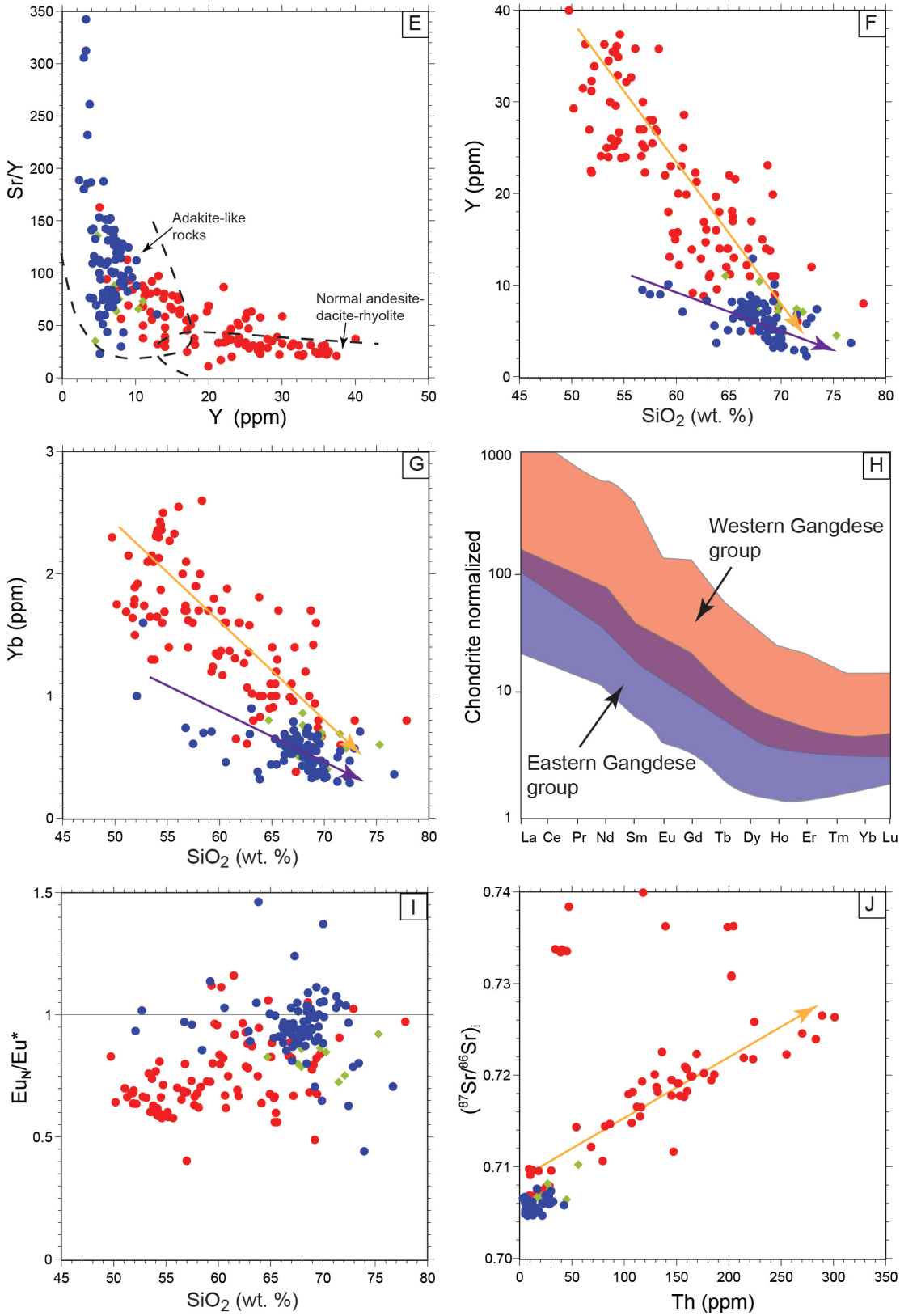

Figure 4-2. Major element, trace element, and Sr-Nd isotope ratio plots for Miocene igneous rocks from the Gangdese belt: A. εNd_i vs. longitude; B. $(^{87}Sr/^{86}Sr)_i$ vs. longitude; C. K_2O vs. SiO_2

(field boundaries from Rickwood 1989); D. εNd_i vs. $(^{87}Sr/^{86}Sr)_i$; E. Sr/Y vs. Y (field boundaries from Defant and Drummond 1993); F. Y vs. SiO_2; G. Yb vs. SiO_2; H. Chondrite-normalized REE patterns (normalization values of Sun and McDonough, 1989); I. Eu_N/Eu^* vs. SiO_2; J. $(^{87}Sr/^{86}Sr)_i$ vs. Th. Correlation trends are shown where apparent. In D, the green line shows mixing between lower crustal garnet-amphibolite xenoliths in Tibet, which are thought to represent Tibetan lithospheric mantle and High Himalayan crystalline basement melts (HHCB: thought to represent the composition of the Indian craton). The Tibetan lithosphere end-member values used in this mixing model are: $(^{87}Sr/^{86}Sr)_i = 0.7065$ and $\varepsilon Nd_i = -2.1$ (Deng et al. 1998); Primitive Mantle values for Sr (21.1 ppm) and Nd (1.354 ppm) (Sun and McDonough 1989) are used because Sr and Nd concentrations in the xenoliths are abnormally high. Values for the High Himalayan crystalline basement melts are: $(^{87}Sr/^{86}Sr)_i = 0.742355$, Sr = 141.28 ppm, $\varepsilon Nd_i = -17.6$, Nd = 45.45 ppm (Inger and Harris 1993; Richards et al. 2005; Guo et al. 2013). Depleted mantle composition from Taylor and McLennan (1985); Oligocene volcanic rock compositions from Ding et al. (2003) and Liu et al. (2008); Gangdese Cretaceous–Paleocene batholith compositions (arc magmas) from Wen (2007).

Petrogenesis of high $(^{87}Sr/^{86}Sr)_i$ rocks in the western Miocene Gangdese belt

West of ~89°E, Miocene volcanic rocks consist of potassic–ultrapotassic trachyandesite–trachyte, and andesite–dacite–rhyolite flows, with minor porphyritic intrusions. Most samples lack amphibole phenocrysts, and some samples have phlogopite and sanidine phenocrysts reflecting their high K-contents (Miller et al., 1999). All samples have high $(^{87}Sr/^{86}Sr)_i$ ratios (0.707 to 0.740, average = 0.7156 ± 0.0089, n = 69; Fig. 4-2C) and low εNd_i values (-4.1 to -17.5, average = -11.7 ± 3.3, n = 67; Fig. 4-2A, C). They have low Sr/Y ratios (11 to 163, average = 62 ± 23, n = 103; Fig. 4-2D), distinct Eu anomalies (Eu_N/Eu^* = 0.4 to 1.2, average = 0.83 ± 0.14, n = 99; Fig. 4-3E), and high contents of REE and other incompatible elements (Fig. 4-3B, C). These characteristics suggest that the western magmas were derived by lower-degree partial melting of Tibetan lithosphere, were less hydrous than the eastern magmas, and that they evolved mainly by fractionation of anhydrous minerals such as plagioclase and pyroxenes (Weill and Drake 1973). Ti-magnetite and ilmenite are common in the groundmass, and coexisting ilmenite–magnetite pairs indicate that magmatic oxygen fugacities were below the FMQ (fayalite–quartz–magnetite) buffer (ΔFMQ = -2.5 to -0.5, temperature = 730–1100°C: Turner et al., 1996; Miller et al., 1999).

Our plate tectonic reconstruction suggests that the Indian craton had underthrust the western Gangdese belt by the Miocene, and therefore a source for these relatively isotopically evolved magmas must be sought in either the Paleozoic–Mesozoic dominated Tibetan lithosphere, or the underthrust Precambrian Indian continental lithosphere (or both). The underthrust Indian

continental lithosphere is thought likely to be a source for these magmas, because their high Rb/Sr ratios (0.5–1.0), old Nd model ages (T_{DM} = 1.16–2.26 Ga), extremely radiogenic Sr isotopic ratios (up to 0.74), and high abundances of incompatible trace elements (Fig. 4-3F; Miller et al., 1999; Williams et al., 2004; Guo et al., 2013) suggest that these magmas originated in part from ancient continental lithosphere. Their Sr-Nd isotopic compositions are similar or close to High Himalayan crystalline basement (Fig. 4-2C; interpreted to represent the composition of the Indian craton: Inger and Harris 1993, Richards et al., 2005, and Guo et al., 2013), and therefore we conclude that the Indian craton may have been a primary source of these magmas. The isotopic and geochemical data scatter towards the composition of Oligocene volcanic rocks in the south Qiangtang terrane, which are known to have been derived from Tibetan lithosphere (Fig. 4-1 and 2B, C; Ding et al., 2003; Liu et al., 2008), suggesting that these lower plate melts may have interacted to with upper plate (Tibetan) lithosphere.

We suggest that underthrusting of the Indian continental lithosphere to depths of >100 km would have caused prograde metamorphism, dehydration, and even partial melting of crustal rocks (Fig. 4-4B). Ascent of these fluids and melts through the overlying thickened and previously subduction-modified Tibetan lithosphere would have caused further melting and interaction, to generate hybrid magmas with widely variable isotopic ratios. The Sr-Nd mixing model (Fig. 4-2C) suggests most of the primitive magmas were enriched by about 3–15% melts released from Indian continental lithosphere.

4.6 Implications for metallogeny

The model outlined above suggests that upwelling, hot asthenospheric melts generated below the eastern Gangdese belt in response to Miocene Greater India slab breakoff caused partial melting of the previously subduction-modified Tibetan lithosphere, mostly amphibolitic cumulate residues at the base of the crust. These deep crustal residues may contain significant metal sulfides left by previous arc magmatism (Lee et al., 2012), because pre- Cretaceous–Eocene arc magmatism in Gangdese belt is significantly barren in mineralization. Following the models of Hou et al., (2009) and Richards (2009), remobilization of chalcophile and siderophile metals (such as Cu, Mo, and Au) left as residues in deep crustal arc cumulate zones (amphibolitic lower crust) and/or metasomatized mantle lithosphere led to the generation of hydrous, fertile magmas capable of forming porphyry Cu-Mo±Au deposits upon upper crustal emplacement.

In contrast, the western Gangdese magmas were derived by partial melting of Tibetan lithospheric mantle metasomatized by fluids and melts released from prograde metamorphism of Indian crustal. These magmas with mafic–intermediate compositions (Fig. 4-2B) stemmed from lithospheric mantle rather than fertile crustal roots (amphibolitic arc cumulates), are under less hydrous and more reduced conditions (ΔFMQ = -2.5 to -0.5), and would have had low metal transportation and ore-forming potential (Botcharnikov et al., 2011; Richards, 2011).

If this geodynamic model is correct, porphyry deposits might also be expected to have formed in the equivalent slab-breakoff tectonic setting to the north of western Gangdese belt in the Oligo-Miocene (at ~25 ± 5 Ma: Replumaz et al., 2010). However, no porphyry or epithermal deposits are known to be related to the Oligocene alkaline volcanic rocks that crop out in this area (Fig. 4-1). The barren nature of these magmas might reflect a lack of previous subduction fertilization of the Tibetan lithosphere to the north of the main Cretaceous–Paleocene Gangdese arc.

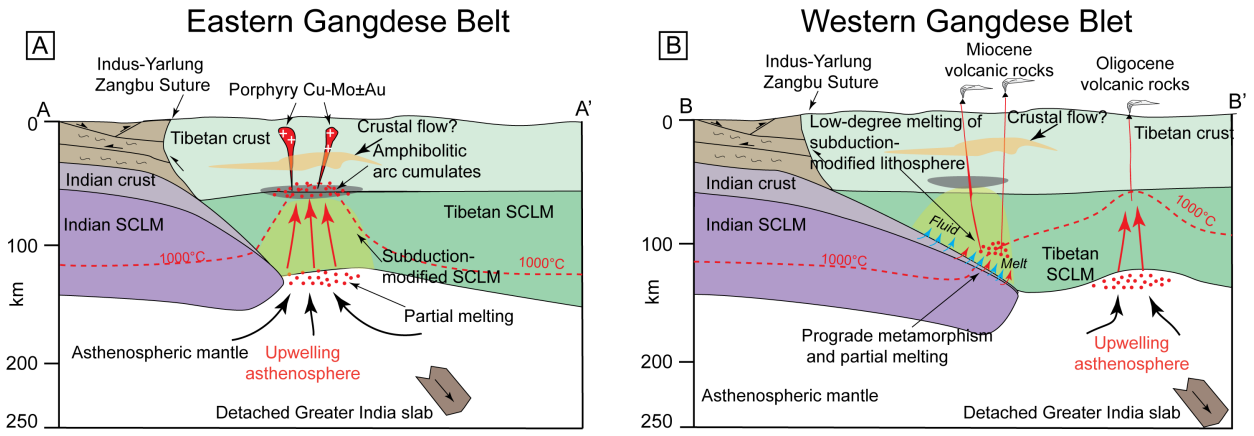

Figure 4-3. Petrogenesis of late-collisional Oligo-Miocene igneous rocks in the Gangdese belt. A: Cross section A–A' in the eastern Gangdese belt showing slab breakoff, upwelling of asthenospheric melts, partial melting of subduction-modified Tibetan lithosphere, and formation of porphyry Cu-Mo±Au deposits upon upper crustal emplacement. B: Cross section B–B' in the western Gangdese belt showing fluids and melts released from underthrust ancient Indian continental lithosphere and interacting with Tibetan lithosphere to produce high $(^{87}Sr/^{86}Sr)_i$ alkaline magmas. Red dots represent partial melting zones. Blue and red arrows represent fluids and melts, respectively. Thrust systems are inferred from Yin and Harrison (2000). Depths of the Moho, Indian lithosphere–asthenosphere boundary, and Tibetan lithosphere–asthenosphere boundary are estimated from seismic studies (Kumar et al. 2006; Zhao et al. 2010). Crustal flow in middle-crust is inferred from Unsworth et al. (2005), King et al., (2007), and Jamieson et al. (2011). Abbreviation: SCLM = sub-continental lithospheric mantle.

4.7 Conclusions

Several giant and large porphyry Cu-Mo±Au deposits were formed in the eastern Gangdese belt of Tibet in the Miocene, tens of millions of years after oceanic lithosphere subduction had ceased. We propose that these deposits were formed from metallogenically fertile magmas generated in response to breakoff of the Greater India slab. Upwelling asthenospheric melts caused partial melting of subduction-modified Tibetan lithosphere, and generated hydrous, oxidized, and metal-enriched melts, which had the potential to form porphyry deposits upon upper crustal emplacement. In contrast, the western Gangdese had been underthrust by the Indian continental lithosphere at this time, and the resulting melts were less hydrous, reduced, and consequently barren.

4. 8 References

Allégre, C.J., Courtillot, V., Taponnier, P., Hirn, A., Mattauer, M., Coulon, C., Jaeger, J. J., Achache, J., Schärer, U., Marcoux, J., Burg, J. P., Girardeau, J., Armijo, R., Gaiety, C., Göpel, C., Li, T., Xiao, X., Chang, C., Li, G., Lin, B., T, J., Wang, N., Chen, G., Han, T., Wang, X., Den, W., Sheng, H., Gao, Y., Zhou, J., Qiu, H., Bao, P., Wang, S., Wang, B., Zhou, Y., and Xu, R., 1984, Structure and evolution of the Himalayan-Tibet orogenic belt: Nature, v. 307, p.17–22.

Aminzadeh, B., Shahabpour, J., and Maghami, M., 2011, Variation of Rhenium contents in molybdenites from the Sar Cheshmeh porphyry Cu-Mo deposits in Iran: Resource Geology, v. 61, p. 290–295.

Armijo, R., Tapponnier, P., Mercier, J.L., and Han, T.L., 1986, Quaternary extension in southern Tibet: Field observations and tectonic implications: Journal of Geophysical Research v, 9, p. 13,803–13,872.

Banerjee, P., Bürgmann., Nagarajan, B., and Apel, 2008, Intraplate deformation of the Indian subcontinent: Geophysical Research Letters, v. 35, L18301, doi: 10.1029/2008GL035468.

Blisniuk, P.M., Hacker, B.R., Glodny, J., Ratschbacher, L., Bi, S.W., Wu, Z.H., McWilliams, M.O., and Calvert, A., 2001, Normal faulting in central Tibet since at least 13.5 Myr ago: Nature, v. 412, p. 628–632.

Botcharnikov, R.E., Linnen, R.L., Wilke, M., Holtz, F., Jugo, P.J., and Berndt, J., 2011, High gold concentrations in sulphide-bearing magma under oxidizing conditions: Naturegeoscience,

v. 4, p. 112–115.

Burchfiel, B.C., Chen, Z., Royden, L.H., Liu, Y., and Deng, C., 1991, Extensional development of Gabo valley, southern Tibet: Tectonophysics, v. 194, p. 187–193.

Burg, J.P., and Chen, G.M., 1984, Tectonics and structural formation of southern Tibet, China: Nature, v. 11, p. 219–223.

Capitanio, F.A., Morra, G., Goes, S., Weinberg, R.F., and Moresi, L., 2010, India-Asia convergence driven by the subduction of the Greater Indian continent: Nature Geoscience, v. 3, p. 136–139.

Chu, M.F., Chung, S.L., O'Reilly, S.Y., Pearson, N.J., Wu, F.Y., Li, X.H., Liu, D.Y., Ji, J.Q., Chu, C.H., and Lee, H.Y., 2011, India's hidden inputs to Tibetan orogeny revealed by Hf isotopes of Transhimalayan zircons and host rocks: Earth and Planetary Science Letters: v. 307, p. 476–486.

Chung, S.L., Chu, M.F., Ji, J.Q., O'Reilly, S.Y., Pearson, N.J., Liu, D.Y., Lee, T.Y., and Lo, C.H., 2009, The nature and timing of crustal thickening in southern Tibet: Geochemical and zircon Hf isotopic constraints from postcollisional adakites: Teconophysics, v. 477, p. 36–48.

Chung, S.L., Chu, M.F., Zhang, Y.Q., Xie, Y.W., Lo, C.H., Lee. T.Y., Lan, C.Y., Li, X.H., Zhang, Q., and Wang, Y.Z., 2005, Tibetan tectonic evolution inferred from spatial and temporal variations in post-collisional magmatism: Earth-Science Reviews, v. 68, p. 173–196.

Cogan, M.J., Nelson, K.D., Kidd, W.S.F., Wu, C.D., and Project INDEPTH Team, 1998, Shallow structure of the Yadong-Gulu rift, southern Tibet, from refraction analysis of Project INDEPTH common midpoint data: Tectonics, v. 17, p. 46–61.

Coulon, C., Maluski, H., Bollinger, C., and Wang, S., 1986, Mesozoic and Cenozoic volcanic rocks from central and southern Tibet: $^{39}Ar/^{40}Ar$ dating, petrological characteristics and geodynamical significance: Earth and Planetary Science Letters, v. 79, p. 281–302.

Deng, W.M., Huang, X., and Zhong, D., 1998, Alkali-rich porphyry and its relation with intraplate deformation of north part of Jinsha River belt in western Yunnan, China: Science of China, Series D, v. 41, p. 297–305.

Defant, M.J., and Drummond, M.S., 1990, Derivation of some modern arc magmas by melting of young subducted lithosphere: Nature, v. 347, p. 662–665.

de Sigoyer, J., Chavagnac, V., Blichert-Toft, J., Villa, I.M., Luais, B., Guillot, S., Cosca, M., and Mascle, 2000, Dating the Indian continental subduction and collision thickening in the

northwest Himalaya: Multichronology of the Tso Morari eclogites: Geology, v. 28, p. 487–490.

Ding, L., Kapp. P., Zhong, D., and Deng, W., 2003, Cenozoic volcanism in Tibet: Evidence for a transition from oceanic to continental subduction: Journal of Petrology, v. 44, p. 1833–1865.

Feldl, N., and Bilham, R., 2006, Great Himalayan earthquakes and the Tibetan plateau: Nature, v. 444, p. 165–170.

Gao, Y.F, Wei, R.H, Hou, Z.Q, Tian, S.H, and Zhao, R.S., 2008, Eocene high-MgO volcanism in southern Tibet: New constraints for mantle source characteristics and deep process: Lithos, v. 105, p. 63–72.

Guo, Z.F., Wilson, M., Zhang, M.L., Cheng, Z.H., and Zhang, L.H., 2013, Post-collisional, K-rich mafic magmatism in south Tibet: constraints on Indian slab-to-wedge transport processes and plateau uplift: Contribution to Mineralogy and Petrolgy, v. 165, p. 1311–1340.

Guo, Z.F., Wilson, M., and Liu, J.Q., 2007, Post-collisional adakites in south Tibet: products of partial melting of subduction-modified lower crust: Lithos: v. 96, p. 205–224.

Green, T.H., and Pearson, N.J., 1985, Experimental determination of REE partition coefficients between amphibole and basaltic to andesitic liquids at high pressure: Geochimica et Cosmochimica Acta, v. 49, p. v. 1465–1468.

Hezarkhani, A., 2006, Hydrothermal evolution of the Sar-Cheshmeh porphyry Cu-Mo deposit, Iran: Evidence from fluid inclusions: Journal of Asian Earth Sciences, v. 28, p. 409–422.

Hou, Z., Gao, Y., Qu, X., Rui, Z., and Mo, X., 2004, Origin of adakitic intrusives generated during mid-Miocene east-west extension in southern Tibet: Earth and Planetary Science Letters, v. 220, p. 139–155.

Hou, Z., Yang, Z., Qu, X., Meng, X., Li, Z., Beaudoin, G., Rui, Z., Gao, Y., and Zaw, K., 2009, The Miocene Gangdese porphyry copper belt generated during post-collisional extension in the Tibetan Orogen: Ore Geology Reviews, v. 36, p. 25–31.

Imer, A., Richards, J.P., and Creaser, R., 2012, Age and tectonomagmatic setting of the Eocene Çöpler–Kabataş magmatic complex and porphyry-epithermal Au deposits, East Central Anatolia, Turkey: Mineralium Deposita, v. 48, p. 557–583.

Inger, S., and Harris, N., 1993, Geochemical constraints on leucogranite magmatism in the Langtang valley, Nepal Himalaya: Journal of Petrology, v. 34, p. 345–368.

Jamieson, R.A., Unsworth, M.J., Harris, N.B,W., Rosenberg, C.L., and Schulmann, 2011, Crustal

melting and the flow of mountains: Elements, v. 7, p. 253–260.

Jamieson, R.A., and Beaumont, C., 2013, On the origin of orogens: GSA Bulletin, v. 125, p. 1671–1702.

Kind, R., and Yuan, X., 2010, Seismic images of the biggest crash on earth: Science, v. 329, p. 1479–1480.

King, J., Harris, N., Argles, T., Parrish, R., Charlier, B., Sherlock, S., and Zhang, H.F., 2007, First field evidence for southward ductile flow of Asian crust beneath southern Tibet: Geology, v. 35, p. 727–730.

Kumar, P., Yuan, X., Kind, R., Ni, J., 2006, Imaging the colliding Indian and Asian lithospheric plates beneath Tibet: Journal of Geophysical Research, v.111, B6: doi: 10.1029/2005JB003930.

Li, J.X., Qin, K.Z., Li, G.M., Xiao, B., Chen, L., and Zhao, J.X., 2011, Post-collsional ore-bearing adakitic porphyries from Gangdese porphyry copper belt, southern Tibet: Melting of thickened juvenile arc lower crust: Lithos, v. 126, p. 264–277.

Liu, S., Hu, R., Feng, X., Zou, H., Li, C., Guo, X., Peng, J., Zhong, H., Qi, L., Qi, Y.Q., and Wang, T., 2008, Cenozoic high Sr/Y volcanic rocks in the Qiangtang terrane, northern Tibet: geochemical and isotopic evidence for the origin of delaminated lower continental melts: Geological Magazine, v. 145, p. 463–474.

Lee, C.A., Luffi, P., Chin, E.J., Bouchet, R., Dasgupta, R., Morton, D.M., Roux, V.L., Yin, Q.Z., and Jin, D., 2012, Copper systematics in arc magmas and implications for crust-mantle differentiation: Science, v. 336, p. 64–68.

Meng, J., Wang, C., Zhao, X., Coe, R., Li, Y.L., and Finn, D., 2012, India-Asia collision was at 24° N and 50 Ma: Paleomagnetic proof from southern Asia: Scientific Reports, 2, 925; doi: 10.1038/srep00925.

Miller, C., Schuster, R., Klotzli, U., Frank, W., and Purtscheller, F., 1999, Post-collisional potassic and ultrapotassic magmatism in SW Tibet: geochemical and Sr–Nd–Pb–O isotopic constraints for mantle source characteristics and petrogenesis: Journal of Petrology, v. 40, p. 1399–1424.

Mitsuishi, M., Wallis, S.R., Aoya, M., Lee, J., and Wang, Y., 2012, E-W extension at 19 Ma in the Kung Co area, S, Tibet: Evidence for contemporaneous E-W and N-S extension in the Himalayan orogen: Earth and Planetary Science Letters, v. 325-326, p. 10–20.

Qu, X., Hou, Z., and Li, Y., 2004, Melt components derived from a subducted slab in late orogenic ore-bearing porphyries in the Gangdese copper belt, southern Tibetan Plateau: Lithos, v. 74, p. 131–148.

Qu, X., Hou, Z., Khin Zaw, and Li, Y., 2007, Characteristics and genesis of Gangdese porphyry copper deposits in the southern Tibetan Plateau: preliminary geochemical and geochronological results: Ore Geology Reviews, v. 31, p. 205–223.

Replumaz, A., Negredo, A.M., Villaseñor, A., and Guillot, S., 2010, Indian continental subduction and slab breakoff during Tertiary collision: Terra Nova, v. 22, p. 290–296.

Richards, J.P., 2011, Magmatic to hydrothermal metal fluxes in convergent and collided margins: Ore Geology Review, v. 40, 1–26

Richards, J.P., 2009. Postsubduction porphyry Cu–Au and epithermal Au deposits: products of remelting of subduction-modified lithosphere: Geology, v.37, p. 247–250.

Richards, J.P., Wikinson, D.M., and Ullrich, T.M., 2006, Geology of the Sari Gunay epithermal gold deposit, Northwest Iran: Economic Geology, v. 101, p. 1455–1496.

Richards, A., Argles, T., Harris, N., Parrish, R., Ahmad, T., Darbyshire, F., Draganits, E., 2005, Himalayan architecture constrained by isotopic tracers from clastic sediments: Earth and Planetary Science Letters, v. 236, p. 773–796.

Rickwood, P.C., 1989, Boundary lines within petrologic diagrams which use oxides of major and minor elements: Lithos, v. 22, p. 247–263.

Rowley, D.B., 1996, Age of initiation of collision between India and Asia: a review of stratigraphic data: Earth and Planetary Science Letters, v. 145, p. 1–13.

Sun, S.S., and McDonough, W.F., 1989, Chemical and isotopic systematics of oceanic basalts: Implications for mantle composition and processes: Geological Society of London Special Publication, v. 42: p. 313–345.

Tapponnier, P., Xu, Z.Q., Roger, F., Meyer, B., Arnaud, N., Wittlinger, G., and Yang, J.S., 2001, Oblique stepwise rise and growth of the Tibet plateau: Science, v. 294, p. 1671–1677.

Turner, S., Arnaud, N., Liu, J., Rogers, N., Hawkesworth, C., Harris, N., and Kelley, S., 1996, Post-collision, shoshonitic volcanism on the Tibetan Plateau: Implications for convective thinning of the lithosphere and the source of ocean island basalts: Journal of Petrology, v. 37, p. 45–71.

Unsworth, M.J., Jones, A.G., Wei, W., Marquis, G., Gokarn, S.G., Spratt, J.E., 2005, Crustal

rheology of the Himalaya and Southern Tibet inferred from magnetotelluric data: Nature, v. 438, p. 78–81.

Van der Voo, R., Spakman, W., Bijwaard, H., 1999, Tethyan subducted slabs under India: Earth and Planetary Sciences Letters, v. 171, p. 7–20.

van Hinsbergen, D.J.J., Lippert, P.C., Dupont-Nivet, G., McQuarrie, N., Doubrovine, P.V., Spakman, W., and Torsvik, T.H., 2012, Greater India basin hypothesis and a two-stage Cenozoic collision between India and Asia: Proceedings of the National Academy of Science of the United States of America, v. 20, p. 7659–7664.

Wang, B.D., Xu, J.F., Chen, J.L., Zhang, X.G., Wang, L.Q., and Xia, B.B., 2010, Petrogenesis and geochronology of the ore-bearing porphyritic rocks in Tangbula porphyry molybdenum-copper deposit in the eastern segment of the Gangdese metallogenic belt: Acta Petrologica Sinica, 26, v. 26, 1820–1830 (in Chinese with English abstract).

Wang, R., Richards, J.P., Hou, Z.Q., and Yang, Z.M., 2014, Extent of underthrusting of the Indian plate beneath Tibet controlled of Miocene porphyry Cu–Cu±Au deposits: Mineralium Deposita, v. 49, p. 165–173, DOI: 10.1007/s00126-013-0507-y

Wen, D.R., 2007, The Gangdese batholith, Southern Tibet: Ages, geochemical characteristics and petrogenesis: Unpublished Ph.D. thesis, National Taiwan University, 120 p.

Weill, D.F., Drake, M.J., 1973, Europium anomaly in plagioclase feldspar: Experiment results and seimiquantitative model: Science, v. 180, p. 1059–1060.

Williams, I.S., 1998, U-Th-Pb geochronology by ion microprobe. In McKibben, M. A., Shanks III, W. C., and Ridley, W. I. (eds.): Applications of micro-analytical techniques to understanding mineralizing processes: Reviews in Economic Geology, v. 7, P. 1–35.

Williams HM, Turner SP, Kelley S, Harris N (2001) Age and composition of dikes in Southern Tibet: new constraints on the timing of east–west extension and its relationship to post-collisional volcanism. Geology 29:339–342

Xiao, B., 2011, Highly oxidized magmatic-hydrothermal ore-forming process at the Qulong giant porphyry Cu-Mo deposit, Gangdese, Tibet: Unpublished Ph.D. thesis (in Chinese), Institute of Geology and Geophysics, Chinese Academy of Sciences, Beijing, 275 p.

Xu, W.C., Zhang, H.F., Guo, L., and Yuan, H.L., 2010, Miocene high Sr/Y magmatism, south Tibet: Product of partial melting of subducted Indian continental crust and its tectonic implication: Lithos, v. 114, p. 293–306.

Yang, Z.M., Hou, Z.Q., White, N.C., Chang, Z.S., Li, Z.Q., and Song, Y.C., 2009, Geology of the post-collisional porphyry copper-molybdenum deposit at Qulong, Tibet: Ore Geology Reviews, v. 36, p. 133–159.

Yin, A., and Harrison, T.M., 2000, Geologic evolution of the Himalayan-Tibetan orogen: Annual Review of Earth and Planetary Sciences, v. 28, p. 211–280.

Zhang, P.Z., Shen, Z., Wang, M., Gan, W.J., Bürgmann, R., Molnar, P., Wang, Q., Niu, Z., Sun, J., Wu, J., Sun, H., and You, X., 2004, Continuous deformation of the Tibetan plateau from global positioning system data: Geology, v. 32, p. 809–812.

Zhao, Z.D., Mo, X.X, Dilek, Y., Niu, Y.L., DePaolo, D.J., Robinson, P., Zhu, D, Sun, C, Dong, G.C., Zhou, S., Luo, Z.H., and Hou, Z.Q., 2009, Geochemical and Sr-Nd-Pb-O isotopic compositions of the post-collisional ultrapotassic magmatism in SW Tibet: Petrogenesis and implications for India-continental subduction beneath southern Tibet: Lithos, v. 113, p. 190–212.

Zhao, J.X., Qin, K.Z., Li, G.M., Li, J.X., Xiao, B., and Chen, L., 2011, Geochemistry and petrogenesis of granitoids at Sharang Eocene porphyry Mo deposit in the main-stage of India-Asia continental collision, northern Gangdese, Tibet: Resource Geology, v. 62, p. 84–98.

Zheng, Y.C., Hou, Z.Q., Li, W., Liang, W., Huang, K.X., Li, Q.Y., Sun, Q.Z., Fu, Q., and Zhang, S., 2012, Petrogenesis and geological implications of the Oligocene Chongmuda-Mingze adakite-like intrusions and their mafic enclaves, southern Tibet: Journal of Geology, v. 120, p. 647–669.

Chapter 5

The role of Indian and Tibetan lithosphere in spatial distribution of Cenozoic magmatism and porphyry Cu-Mo±Au deposits in the Gangdese belt, southern Tibet[1]

5.1 Introduction

The Gangdese magmatic belt is located along the southern margin of the Tibetan plateau, and records a series of magmatic events starting with Late Triassic–Early Jurassic subduction of the Neo-Tethyan ocean (Chu et al., 2006), followed by early collision of Greater India and oceanic slab breakoff in the Eocene ("soft collision" at ~55–50 Ma; Allègre et al., 1984; Van der Voo et al., 1999; de Sigoyer et al., 2000; Gao et al., 2008). "Hard-collision" of the Indian craton with the Asian margin occurred at ~35 Ma (Replumaz et al., 2010; van Hinsbergen et al., 2012), with late-collisional processes in the Oligocene and Miocene. Breakoff of the Greater India slab started in the western part of the belt at ~25 ± 5 Ma, and the tear propagated eastward until final detachment beneath eastern Tibet at ~10 ± 5 Ma (Van der Voo et al., 1999; Replumaz et al., 2010). A large number of small-volume calc-alkaline to high-K alkaline and shoshonitic granitoids and high-K calc-alkaline to shoshonitic lava flows were intruded or erupted in the Gangdese belt between ~30 and 9 Ma, and constitute a 1600 km-long late-collisional magmatic belt (Fig. 5-2; Turner et al., 1996; Miller et al., 1999; Chung et al., 2003, 2005; Ding et al., 2003; Hou et al., 2004, 2009; Williams et al., 2004; Gao et al., 2007; Yang et al., 2009; Zhao et al., 2009; Li et al., 2011; Liu et al., 2011; Zheng et al., 2012; Leng et al., 2013; Guo et al., 2013; Wang et al., 2014a, b, c; Wu et al., 2014; Zheng Y et al., 2014)

The Miocene igneous rocks in the Gangdese belt show a sharp longitudinal distinction in petrography, geochemistry, and association with porphyry-type mineralization, with a boundary at ~89°E. The eastern Gangdese group (longitude ~89°–94° E) is characterized mainly by intermediate–felsic calc-alkaline to high-K calc-

[1] This chapter was submitted as: Wang, R., Richards, J.P., Zhou, L.M., Hou, Z.Q., Yang, Z.M., Muehlenbachs, K., Stern, R.A., Creaser, R.A., Zhu, J.J., and Li, J.X., 2014, The role of Indian and Tibetan lithosphere in spatial distribution of Cenozoic magmatism and porphyry Cu-Mo±Au deposits in the Gangdese belt, southern Tibet: Journal of Petrology.

alkaline plutons (which are locally associated with porphyry Cu-Mo±Au deposits), and minor high-K calc-alkaline to shoshonitic volcanic rocks. These calc-alkaline to high-K calc-alkaline granitoid magmas are characterized by high Sr/Y and $[La/Yb]_N$ ratios (e.g. Chung et al., 2003; Hou et al., 2004, 2009; Li et al., 2011; Wang et al., 2014a, b). In contrast, the western Gangdese group (longitude ~80°–89° E) is characterized mainly by high-K calc alkaline to shoshonitic volcanic rocks and sparse porphyritic plutons that are mostly barren. These alkaline volcanic rocks have high Th and K_2O contents, and low to moderate Sr/Y ratios (Miller et al., 1999; Williams et al., 2004; Guo et al., 2013; Wang et al., 2014a). The cospatial porphyritic plutons with similar mineralogical and geochemical compositions to the western alkaline volcanic rocks are likely their equivalents (e.g. Wang et al., 2012a; Yu et al., 2013).

Previous isotopic studies of Miocene potassic to ultrapotassic volcanic rocks in the western Gangdese belt demonstrate that their compositions are characterized by extremely low εNd_i values (-17.4 to -7.1), but high $(^{87}Sr/^{86}Sr)_i$ and $\delta^{18}O_{VSMOW}$ values (0.7068–0.7399 and +8–+11‰, respectively) (e.g., Miller et al., 1999; Williams et al., 2004; Zhao et al., 2009). These compositions suggest that the Indian lithosphere (with low εNd = -18 to -10, and high $^{87}Sr/^{86}Sr$ = 0.74–0.76 and $\delta^{18}O$ = +10–+14 ‰; France-Lanord et al., 1988; Inger and Harris, 1993) was a likely source. Prior to this study, it was not known whether eastern Gangdese belt Miocene magmatism was also affected by this source, partly because there are few reported occurrences of Miocene potassic to ultrapotassic rocks in this part of the belt. Oligo-Miocene granitoids from the eastern Gangdese belt have been studied for Sr-Nd isotopic compositions, but no Os or O isotopic data have been published. In addition, many of these previously studied intrusive rocks are associated with porphyry-type deposits and have been affected by pervasive hydrothermal alteration, rendering Sr and O isotopic compositions suspect.

In this study, we collected fresh and minimally altered Cenozoic igneous rocks from throughout the 1600 km-long Gangdese magmatic belt, focusing on previously unsampled occurrences of Miocene rocks. By combining our new data with published lithogeochemical and multiple isotopic (Os-Sr-Nd-O) analyses, we show that differential involvement of Indian plate lithosphere, subduction-modified Tibetan lithosphere, and asthenospheric melts explains the observed spatial and temporal distribution of

magmatism, and restriction of porphyry-type mineralization to the eastern Miocene Gangdese belt.

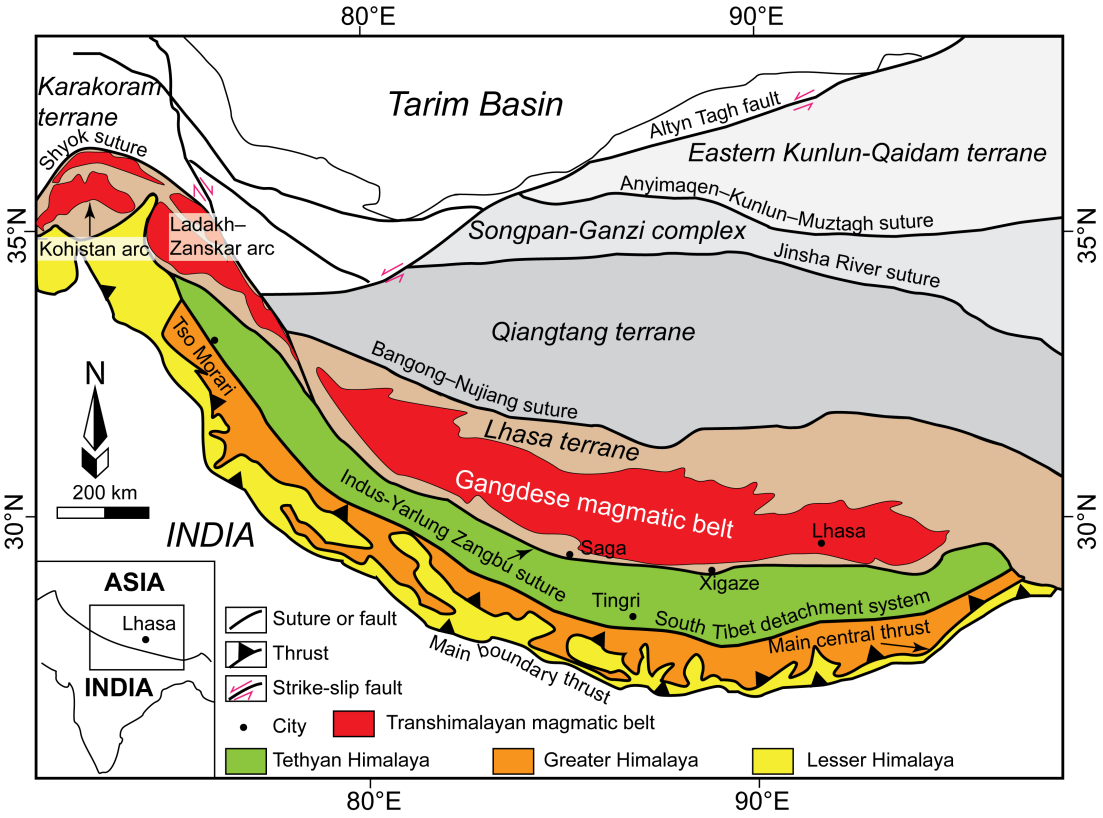

Figure 5-1. Map indicating major tectonic units, boundaries, and magmatic belts within the Tibet–Qinghai Plateau (modified from Aitchison et al., 2007; White et al., 2011; Wang et al., 2014b).

5.2 Tectonic setting

The Himalayan-Tibetan orogen is composed of the Himalayas, Lhasa terrane, Qiangtang terrane, and Songpan-Ganze complex, from south to north, separated from each other by the Indus-Yarlung Zangbu, Bangong-Nujiang, and Jinsha River sutures (Yin and Harrison, 2000; Fig. 5-1). The geological setting of the Lhasa terrane has been described in detail by several authors (e.g., Pan et al., 2004; Mo et al., 2005, 2007, 2008; Wen, 2007; Zhu et al., 2011, 2013; Zhang et al., 2013; Wang et al., 2014b), and is only briefly summarized here. The core of the Lhasa terrane is thought to consist of Archean and Proterozoic crystalline basement that rifted from the Gondwana margin in the Carboniferous–Middle Permian or earlier (Zhu et al., 2010), and was covered by

Paleozoic and Mesozoic metasedimentary and volcanic rocks (Pan et al., 2004; Zhu et al., 2009, 2011). The Lhasa terrane is thought to have collided with the Qiangtang terrane to the north in the Early Cretaceous (Yin and Harrison, 2000; Kapp et al., 2005), and northward subduction of Neo-Tethyan oceanic lithosphere beneath its southern margin began in the Late Triassic or Early Jurassic (Chu et al., 2006). This Andean-style continental subduction produced voluminous Mesozoic–Cenozoic I-type plutons and coeval volcanic rocks, which constitute the 1600 km-long Gangdese magmatic belt (Pan et al., 2004; Mo et al., 2005; Wen, 2007; Zhu et al., 2011; Niu et al., 2013). Whole-rock Nd isotopic and zircon Hf isotopic compositions of crustal xenoliths in Neogene volcanic rocks (mostly $\varepsilon Nd > -5$, $\varepsilon Hf = -5$ to $+20$; Mo et al., 2005, 2007, 2008; Chan et al., 2009; Zhu et al., 2011; Liu et al., 2014) suggest that the crust beneath the Gangdese belt is mostly juvenile.

The India–Asia collision started at ~55–50 Ma when the Greater India plate (Indian continental margin; Ali and Aitchison, 2005) first collided with the Lhasa terrane ("soft collision": Meng et al., 2012; van Hinsbergen et al., 2012). The thicker and more rigid Indian craton (plate) later began to underthrust the Asian margin at ~35 Ma ("hard collision": Replumaz et al., 2010; van Hinsbergen et al., 2012). Following detachment of the Greater India slab in the Oligo-Miocene, the Indian plate continued to underthrust the Lhasa terrane to the present day (Replumaz et al., 2010; van Hinsbergen et al., 2012). Seismic tomographic studies indicate that the Indian continental lithosphere (100 to 200 km thick) extends northward below the Tibetan plateau, but the extent of underthrusting decreases from west (reaching ~33º N at ~87° E, to the north of the Bangong-Nujiang suture) to east (reaching ~ 30º N at ~93° E), with a NE-directed convergence vector (Kumar et al., 2006; Li et al., 2008; Huang et al., 2009; Kind and Yuan, 2010; Zhao et al., 2010; Shokoohi Razi et al., 2014). Orogen-parallel (east–west extension) began at ~19–4 Ma in response to plateau collapse and/or subcontinental mantle lithospheric delamination led to numerous north–south-trending extensional faults and rift basins, which facilitated the ascent of deeply derived magmas (Fig. 5-2; Armijo et al., 1986; Burchfiel et al., 1991; Cogan et al., 1998; Blisniuk et al., 2001; Tapponnier et al., 2001; Copley et al., 2011).

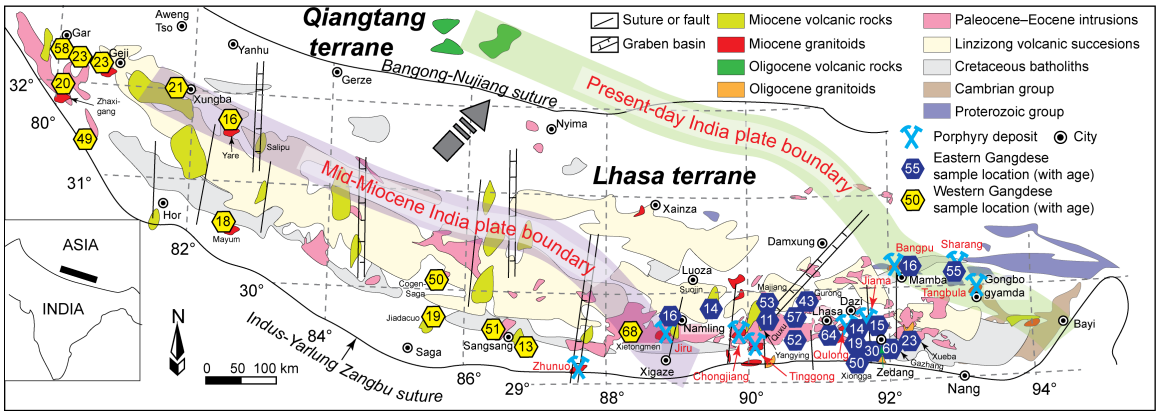

Figure 5-2. Geology of the Gangdese magmatic belt in the Lhasa terrane, showing the locations of samples described in this paper (modified from Zhao et al., 2009; Wang et al., 2014a). The broad green line represents the present northern limit of the underthrust Indian plate beneath the Tibetan plateau, whereas the broad purple line is its estimated location in the mid-Miocene; the convergence direction is shown with a gray arrow (for details see Wang et al., 2014a). Yellow and blue hexagons with numerals mark the locations and ages of samples in the western Gangdese belt and eastern Gangdese belt, respectively (see Table 5-1 for precise locations, and sources of data from the literature). The locations of major porphyry Cu-Mo±Au deposits in the Gangdese belt are also shown.

5.3 Magmatism

Pre-collisional magmatism

North-directed Neo-Tethyan subduction beneath southern Tibet produced voluminous Cretaceous calc-alkaline magmatism in the Lhasa terrane (Harris et al., 1986; Wen, 2007; Mo et al., 2008; Lee et al., 2011). Rollback of the Neo-Tethyan slab at ~69–53 Ma triggered a magmatic flare-up (Kapp et al., 2007; Wen, 2007), represented by extensive Paleocene–Eocene I-type intrusive rocks and widespread Linzizong volcanic successions (Fig. 5-2).

Early collisional magmatism

Neo-Tethyan slab breakoff at ~40–38 Ma generated a series of picritic to basaltic–andesitic rocks that were erupted in the Dazi basin (Gao et al., 2008). These rocks are characterized by high MgO (6.3–14.4 wt.%), Cr (131–844 ppm), and Ni (45.2–268 ppm) contents, high εNd_i values (+5.2 to +3.6), and low $(^{87}Sr/^{86}Sr)_i$ ratios (0.7043–0.7061), and are thought to have been derived by melting of upwelling asthenospheric mantle.

Table 5-1: Cenozoic igneous rock locations from Gangdese belt, their ages, and applied lithogeochemical and isotopic analyses.

Sample number	Location	Lithology	Longitude (E)	Latitude (N)	Altitude (m)	Sr-Nd isotope	Os isotope	$\delta^{18}O$ isotope	Lithogeo-chemistry	Age (Ma)	Age references
WR-13-37	Close Gaer	Basalt	80°02'35"	32°23'03"	4391		This study		This study	58	BGMRXAR (1993)
WR-13-40	Close Gaer	Basalt	80°02'35"	32°23'03"	4391	This study	This study			58	BGMRXAR (1993)
WR-13-42	Geji	Andesite	80°14'55"	32°23'54"	4459			Zircon		51	BGMRXAR (1993)
WR-12-40	Gangre	Monzogranite	80°33'28"	31°27'11"	4717			Biotite		49.3	Unpublished data
WR-13-81	Cogen-Saga	Monzonite	85°24'49"	30°07'46"	5500	This study	This study	Zircon	This study	49.9	Chu et al. (2009)
WR-12-33	Sangsang	Granodiorite	86°19'06"	29°33'17"	5090			Amphibole		50.7	BGMRXAR (1993)
WR-12-30B	Xietong-men	Quartz monzonite	88°19'11"	29°32'54"	4706	This study		Zircon	This study	67.7	Tafti (2011)
WR-13-117	Majiang peak	Trachyandesite	90°07'57"	29°53'53"	5376	This study	This study	Zircon	This study	53	Lee et al. (2009)
WR-13-118	Majiang peak	Dacite	90°07'57"	29°53'53"	5376		This study		This study	53	Lee et al. (2009)
WR-13-2	Quxu	Monzonite	90°43'16"	29°21'20"	3500	Chen (2006)		Zircon	Wen (2007)	51.5	Ji et al. (2009)
WR-12-8	Gurong	Granodiorite	90°43'52"	29°43'52"	3954			Amphibole		56.8	Ji et al. (2009)
WR-13-109	Gurong	Monzodiorite	90°45'30"	29°48'02"	3789	This study			This study	43.2	Lee et al. (2009)
WR-13-113A	Gurong	Gabbroic diorite	90°45'30"	29°48'02"	3789	This study			This study	43.2	Lee et al. (2009)
WR-13-113B	Gurong	Rhyolite	90°45'30"	29°48'02"	3789	This study		Zircon	This study	43.2	Lee et al. (2009)
WR-12-1	Lhasa	Granodiorite	91°10'59"	29°38'06"	3673			Biotite		64.3	Ji et al. (2012)
XG-12-9	Xiongga	Granodiorite	91°36'09"	29°18'34"	3646			Amphibole		50	BGMRXAR (1993)
XG-12-3	Xiongga	Diorite porphyry	91°42'47"	29°16'47"	3661			Amphibole		50	BGMRXAR (1993)
GZ-12-1	Gazhang	Granite	91°53'38"	29°26'27"	4496			Biotite		60.1	Wen (2007)
CB-5	Zedang	Quartz monzonite	91°54'51"	29°16'08"	3650			Zircon	Wang et al. (2014b)	29.8	Wang et al. (2014b)
CMD-17A	Zedang	Quartz monzonite	91°55'04"	29°15'15"	4195	Zheng et al. (2012)	This study		Zheng et al. (2012)	30	Zheng et al. (2012)
CMD-17B	Zedang	Quartz monzonite	91°55'04"	29°15'15"	4195	Zheng et al. (2012)	This study			30	Zheng et al. (2012)
CMD-32A	Zedang	Quartz monzonite	91°53'29"	29°16'03"	4195	Zheng et al. (2012)	This study		Zheng et al. (2012)	30	Zheng et al. (2012)
CMD-32B	Zedang	Quartz monzonite	91°53'29"	29°16'03"	4195	Zheng et al. (2012)	This study			30	Zheng et al. (2012)
CMD-33A	Zedang	Quartz monzonite	91°53'29"	29°16'03"	4195	Zheng et al. (2012)	This study		Zheng et al. (2012)	30	Zheng et al. (2012)
CMD-33B	Zedang	Quartz monzonite	91°53'29"	29°16'03"	4195	Zheng et al.	This study			30	Zheng et al.

											(2014b)
WR-13-36	Gaer	Trachyandesite	80°02'35"	32°23'03"	4391			Zircon		23	Miller et al. (1999)
WR-13-31	Zhaxigang	Quartz monzonite porphyry	80°11'24"	31°51'13"	4615				This study	20	Wang et al. (2012a)
WR-12-52	Gaer	Trachyandesite	80°19'43"	32°22'36"	4496			Phlogopite	Turner et al. (1996)	16	Turner et al. (1996)
WR-13-48	Geji	Quartz monzonite porphyry	80°29'50"	32°21'18"	4684	This study	This study	Zircon	This study	23	Miller et al. (1999)
WR-13-53	Xungba	Trachyandesite	81°52'30"	32°02'36"	4624	This study	This study		This study	21.2	Williams (2000)
10YR07	Yare	Quartz monzonite porphyry	82°19'48"	31°28'48"	4900		This study	Zircon/Yu et al. (2013)	Unpublished data	16	Yu et al. (2013)
WR-13-26	Mayum	Granodiorite porphyry	82°26'33"	30°36'10"	5169	This study			This study	18.4	Hu et al. (2006)
WR-13-84	Jiadacuo	Trachydacite	85°46'00"	29°50'10"	5180	Williams (2000)	This study	Zircon	This study	19	Williams (2000)
WR-13-85	Jiadacuo	Trachyandesite	85°46'00"	29°50'10"	5180	Williams (2000)	This study		This study	19	Williams (2000)
WR-13-18	Sangsang	Trachyandesite	87°01'03"	29°19'15"	4502	This study			Williams (2000)	13	Williams (2000)
JR-5	Jiru	Monzonite porphyry	88°53'16"	29°39'24"	4697	This study	This study	Zircon	Wang et al. (2014b)	16	Wang et al. (2014b)
WR-13-14	Suojin	Trachydacite	89°35'04"	29°40'56"	4336	Williams (2000)		Zircon	Williams (2000)	14	Williams (2000)
WR-13-122	Yangying	Trachyandesite	90°22'38"	29°43'12"	4615	This study	This study	Zircon	This study	11	Zhou et al. (2004)
WR-13-100	Qulong	Monzonite porphyry	91°36'51"	29°36'30"	5184	This study	This study	Zircon	Yang (2008)	14	Yang (2008)
QL02-01	Qulong	Granodiorite porphyry	91°36'51"	29°36'30"	5184	Yang (2008)	This study		Yang (2008)	19	Yang (2008)
QL02-04-2	Qulong	Granodiorite porphyry	91°36'51"	29°36'30"	5184	Yang (2008)	This study	Amphibole	Yang (2008)	19	Yang (2008)
QL02-07	Qulong	Granodiorite porphyry	91°36'51"	29°36'30"	5184	Yang (2008)	This study	Amphibole	Yang (2008)	19	Yang (2008)
QL02-10	Qulong	Granodiorite porphyry	91°36'51"	29°36'30"	5184	Yang (2008)	This study		Yang (2008)	19	Yang (2008)
QL02-13	Qulong	Granodiorite porphyry	91°36'51"	29°36'30"	5184	Yang (2008)	This study		Yang (2008)	19	Yang (2008)
QL02-16	Qulong	Granodiorite porphyry	91°36'51"	29°36'30"	5184	Yang (2008)			Yang (2008)	19	Yang (2008)
QL02-28	Qulong	Granodiorite porphyry	91°36'51"	29°36'30"	5184	Yang (2008)	This study		Yang (2008)	19	Yang (2008)
JM11-34	Jiama	Quartz monzonite porphyry	91°45'13"	29°41'43"	4650		This study	Zircon	Hou et al. (2004)	15	Yang et al. (in prep.)
BP-1	Bangpu	Granite	91°55'38"	29°53'28"	4666	This study		Zircon	Wang et al. (2012b)	16	Wang et al. (2012b)

Table 5-2: Major and trace element analysis of igneous rock samples from the Cenozoic Gangdese magmatic belt

Sample	WR-13-37	WR-13-81	WR-12-30B	WR-13-117	WR-13-118	WR-13-109	WR-13-113A	WR-13-113B	WR-13-53	WR-13-31	WR-13-26	WR-13-48	WR-13-84	WR-13-85	WR-13-122
wt. %															
SiO_2	49.18	57.84	66.01	62.37	64.12	54.33	54.76	74.22	59.39	65.28	66.72	65.58	64.10	62.76	60.42
TiO_2	0.77	1.08	0.57	0.75	0.79	1.14	1.05	0.18	1.22	0.62	0.59	0.82	0.67	0.75	0.78
Al_2O_3	19.13	16.55	15.54	14.86	15.06	17.29	17.90	13.74	12.48	15.89	15.35	14.86	16.22	16.45	15.19
TFe_2O_3	7.84	7.12	4.58	5.56	6.04	11.22	8.80	2.04	4.46	3.71	3.63	3.36	4.06	4.09	5.07
MnO	0.10	0.16	0.10	0.10	0.08	0.32	0.25	0.05	0.08	0.06	0.05	0.06	0.06	0.06	0.13
MgO	3.04	2.95	1.60	1.73	1.73	3.09	3.10	0.27	4.63	1.46	1.82	2.20	2.19	2.24	2.58
CaO	11.08	5.06	3.57	3.25	2.19	3.49	6.04	0.93	4.63	2.62	3.25	2.67	4.41	4.47	4.13
Na_2O	2.70	3.33	3.81	3.71	4.39	5.42	4.14	4.70	1.04	3.77	3.83	3.30	4.14	4.10	3.67
K_2O	0.28	4.81	3.69	3.35	2.63	0.98	1.27	3.95	7.92	5.20	3.41	6.24	3.14	3.06	5.54
P_2O_5	0.14	0.38	0.15	0.22	0.22	0.32	0.44	0.03	1.09	0.24	0.21	0.43	0.22	0.24	0.61
LOI	6.38	0.64	0.30	4.00	3.13	3.10	1.79	0.57	2.07	1.54	1.52	0.78	0.29	1.69	1.43
TOTAL	100.62	99.92	99.91	99.89	100.38	100.70	99.54	100.68	99.00	100.39	100.38	100.67	99.50	99.89	99.55
ppm															
Sc	22.3	14.5	13.4	13.6	16.1	18.6	14	8.3	18.3	9.2	9.0	8.5	7.4	10.2	13.5
V	203.8	157	79.7	73.4	85.1	170	151	5.6	123	70.0	77.6	67.2	75.4	83.7	124
Cr	17.9	28.1	7.2	5.8	8.7	bdl	11.8	4.6	529	8.6	22.8	48.9	518	30.2	66.2
Co	30.8	18.3	10.4	8.9	9.7	11.8	14.9	1.4	20.2	9.4	11.8	9.6	20.9	13.1	20.5
Ni	19.1	18.8	5.5	3.6	5.0	9	10	0.5	112.7	8.7	15.2	31.4	167.4	20.2	41.7
Rb	4.80	213.7	142.0	99.6	79.5	66	88	109	786	242	133	445	121	100	392
Ba	76.8	661	525	818	514	148	311	915	3102	1426	889	2148	752	705	4000
Th	2.00	31.86	17.49	19.82	19.29	4.03	3.55	14.27	206	64.09	12.64	109.0	14.62	9.61	102.3
U	0.47	4.00	2.78	4.22	4.19	2.73	2.56	3.12	25.18	8.68	3.89	14.07	2.87	2.18	14.27
Nb	1.31	14.26	8.43	7.64	7.70	7.7	4.1	7.02	26.81	17.45	7.54	21.06	6.43	4.76	20.17
Ta	0.13	1.29	0.88	0.81	0.79	0.37	0.3	0.78	1.94	2.39	0.99	1.70	0.57	0.41	1.43
La	7.97	61.77	28.77	34.67	38.99	23.9	20.8	31.91	80.70	78.55	33.89	91.08	33.50	28.68	158
Ce	17.14	122.4	52.30	67.08	65.23	50.9	42.1	59.53	204.5	135	63.28	188	58.72	52.49	310
Pb	5.66	14.57	22.49	5.53	5.71	19	19	21.51	63.38	51.86	30.62	104	30.03	25.78	126
Pr	2.54	14.84	6.44	8.46	8.92	6.64	5.36	7.36	31.47	15.05	7.99	23.55	7.74	6.57	35.85
Sr	414	679	316	156	127	180	480	79.5	590	713	691	858	826	868	1529
Nd	11.39	55.41	23.30	32.50	34.57	27.4	22.3	27.23	150.3	50.06	30.68	92.68	29.65	25.23	132.5
Sm	2.88	10.32	4.45	6.38	6.71	6.05	4.63	5.47	33.05	6.90	5.36	15.24	5.21	4.19	20.9
Zr	47.93	332	194	269	266	310	305	215	514	246	139	460	116	140	565
Hf	1.66	9.33	6.04	7.78	7.45	6.1	6.1	6.59	15.72	8.19	4.30	13.51	3.72	4.28	15.12
Eu	0.92	1.85	1.01	1.37	1.47	1.63	1.65	1.13	4.96	1.29	1.23	2.71	1.20	1.12	4.00
Gd	2.90	7.97	4.24	6.00	6.48	5.72	3.89	4.95	17.37	4.19	4.06	8.03	3.69	3.24	12.53
Tb	0.43	1.08	0.63	0.87	0.95	0.92	0.59	0.73	1.61	0.44	0.49	0.84	0.42	0.36	1.31
Dy	2.69	6.05	3.71	5.41	5.54	5.31	3.31	4.41	7.07	2.07	2.53	3.61	2.17	1.70	5.68
Y	13.37	27.28	18.81	26.94	28.77	30	17	22.51	27.26	8.74	11.44	13.66	9.28	6.93	22.56
Ho	0.54	1.10	0.75	1.09	1.10	1.07	0.66	0.88	1.11	0.34	0.46	0.55	0.36	0.28	0.91
Er	1.54	3.14	2.20	3.00	3.14	3.04	1.92	2.60	3.33	1.11	1.24	1.62	0.99	0.78	2.66
Tm	0.24	0.45	0.33	0.46	0.48	0.447	0.277	0.41	0.36	0.13	0.17	0.18	0.13	0.10	0.28
Yb	1.57	3.11	2.35	3.01	3.12	3.04	1.81	2.69	2.54	0.85	1.12	1.11	0.83	0.65	2.01
Lu	0.24	0.45	0.36	0.48	0.47	0.502	0.295	0.43	0.35	0.14	0.17	0.15	0.13	0.09	0.28

Syn-collisional magmatism

"Hard collision" between the Indian craton and the Asian margin at ~35 Ma generated a large number of small-volume calc-alkaline to alkaline intrusions and potassic to ultrapotassic volcanic rocks that were emplaced or erupted in southern Tibet during the Miocene (Ding et al., 2003; Hou et al., 2009; Wang et al., 2014a).

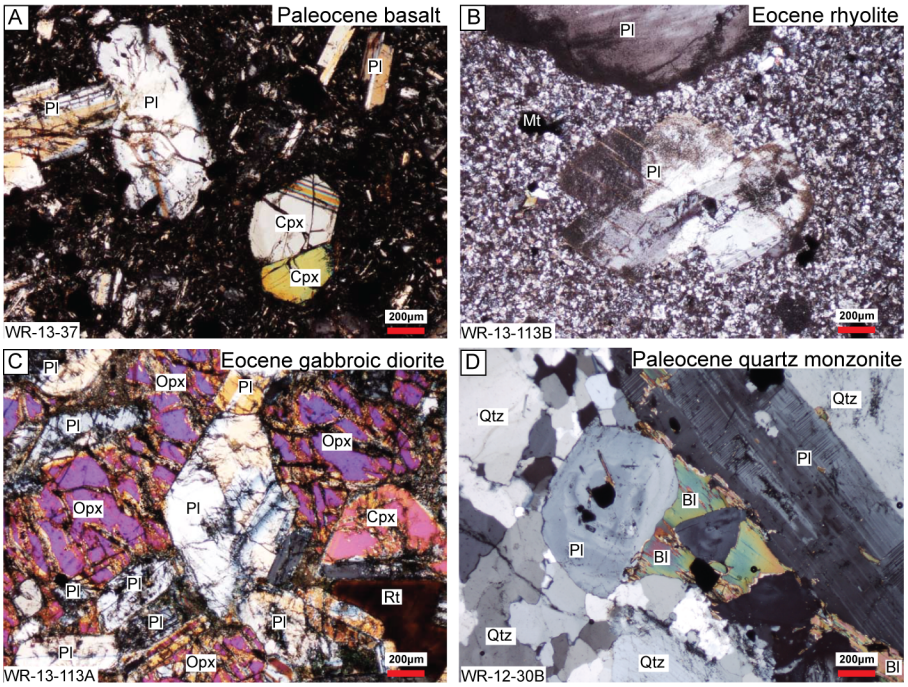

Figure 5-3. Photomicrographs showing: A. Paleocene basalt (sample WR-13-37) with plagioclase and clinopyroxene; cross-polarized light; B. Eocene rhyolite (WR-13-113B) with plagioclase phenocrysts; cross-polarized light; C. Eocene gabbroic diorite (WR-13-113A) with orthopyroxene and plagioclase; cross-polarized light; D. Paleocene quartz monzonite (WR-12-30B) with biotite, plagioclase, and K-feldspar; cross-polarized light. Abbreviations: Bi = Biotite; Cpx = clinopyroxene; Kfs = K-feldspar; Mt = magnetite; Opx = orthopyroxene; Phl = phlogopite; Pl = plagioclase; Rt = rutile.

Granitoid plutons: Oligocene and Miocene granitoid plutons in the eastern Gangdese belt are calc-alkaline to high-K calc-alkaline (monzonites, quartz monzonites, granodiorites, granites; Fig. 5-2). They are associated with several large porphyry Cu-Mo±Au deposits, and have low $(^{87}Sr/^{86}Sr)_i$ ratios (0.7047–0.7076), high εNd_i values (-6.2 to +5.5), and high $[La/Yb]_N$ and Sr/Y ratios (Hou et al., 2004; Li et al., 2011; Wang et al., 2014a, b). Suggested petrogenetic models have included partial melting of a subducted oceanic slab (Qu et al., 2004, 2007), partial melting of slab melt-modified mantle sources (Gao et al.,

2007, 2010), partial melting of thickened lower crust (Chung et al., 2003; Hou et al., 2004), and partial melting of subduction-modified Tibetan lithosphere (Guo et al., 2007; Hou et al., 2009; Li et al., 2011; Zheng et al., 2012; Wang et al., 2014a, b, c).

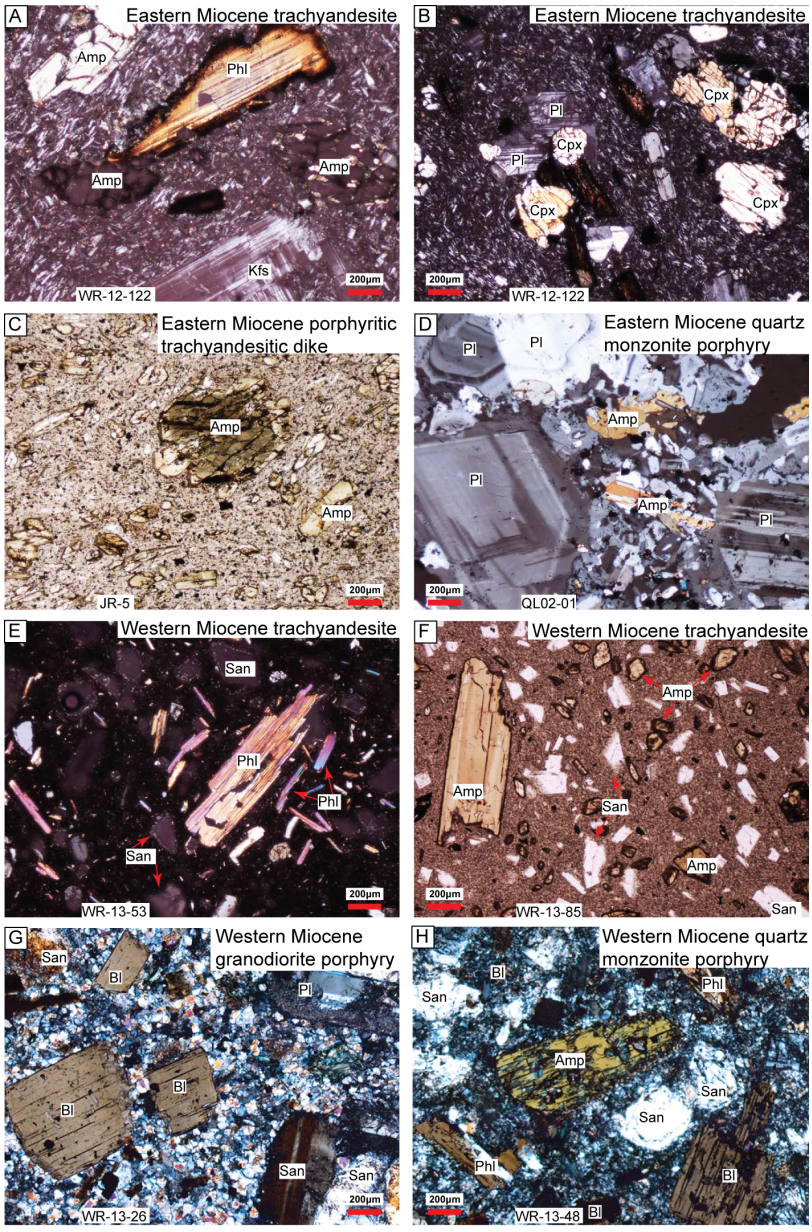

Figure 5-4. Miocene igneous rocks from the eastern (A–D) and western (E–H) Gangdese belt. A, B. Photomicrographs showing: A, B. trachyandesite (WR-13-122) with phlogopite, K-feldspar, and amphibole, and clinopyroxene phenocrysts (cross-polarized light); C. porphyritic trachyandesitic dyke (JR-5) with amphibole phenocrysts (plane-polarized light); D. quartz monzonite porphyry (QL02-01) with amphibole and plagioclase (cross-polarized light); E, F. trachyandesite (WR-13-53 and WR-13-85), G. granodiorite porphyry (WR-13-26), and H. quartz monzonite porphyry (WR-13-48) with

phlogopite, biotite, sanidine, and amphibole phenocrysts (E, G, H: cross-polarized light; F: plane-polarized light); Abbreviations: Amp = amphibole; Bi = biotite; Cpx = clinopyroxene; Kfs = K-feldspar; Phl = phlogopite; Pl = plagioclase; San = sanidine.

In contrast, there are no Oligocene granitoids in the western part of the belt, and few Miocene granitoids have been reported. Those that are known have high-K calc-alkaline to shoshonitic compositions (Zheng et al., 2007; Gao et al., 2010; Wang et al., 2012a; Yu et al., 2013). The western granitoids are mostly barren, and little studied, but granodiorite intrusions in a small Zhunuo porphyry Cu-Mo deposit have moderate $(^{87}Sr/^{86}Sr)_i$ ratios (0.7071–0.7096), and negative εNd_i values (-7.4 to -4.1). Their magmas are interpreted to be derived from slab melt-modified mantle source (Gao et al., 2010).

Alkaline volcanism: Sparse late Oligocene high-K calc-alkaline to shoshonitic volcanic rocks mainly occur in the Qiangtang terrane to the north of the western Gangdese belt, where no coeval granitoids are known (Fig. 5-2). They have basaltic trachyandesitic, tephriphonolitic, trachyandesitic, and trachytic compositions, moderate $(^{87}Sr/^{86}Sr)_i$ ratios (0.7060–0.7092), and negative εNd_i values (-9.2 to -3.8) (Ding et al., 2003; Liu et al., 2008). These alkaline volcanic rocks are thought to be derived from partial melting of enriched lithospheric mantle (Ding et al., 2003; Liu et al., 2008).

In contrast, alkaline volcanic rocks were erupted widely in the Miocene, especially in the western Gangdese belt (Fig. 5-2; minor occurrences also occur in the eastern part of the belt; Miller et al., 1999; Williams et al., 2004; Zhou et al., 2004, 2009; Wang et al., 2014b).

The western Miocene alkaline volcanic rocks have high $(^{87}Sr/^{86}Sr)_i$ ratios (0.7069–0.7399), low εNd_i values (-17.4 to -7.1), and low Sr/Y ratios, quite distinct from the eastern calc-alkaline to high-K calc-alkaline granitoids (Miller et al., 1999; Williams et al., 2004; Guo et al., 2013; Wang et al., 2014a). Petrogenesis of these volcanic rocks is under debate, and their magmas have been interpreted to be derived from the Indian middle-lower crust (Hébert et al., 2014), enriched lithospheric mantle (e.g. Miller et al., 1999; Williams et al., 2004; Zhao et al., 2009), or India plate melt (± fluid)-modified mantle wedge (Guo et al., 2013). Many of these Miocene lavas carry crustal or mantle xenoliths (Chan et al., 2009; Liu C et al., 2011, Liu D et al., 2014). The mineralogy and

geochemistry of peridotite xenoliths from the Salipu area suggest that a hydrous and metasomatized (i.e., phlogopite bearing) lithospheric mantle existed below this part of Gangdese belt at this time (Liu et al., 2011).

Miocene alkaline volcanic rocks are sparse in the eastern Gangdese belt (Yang, 2008; Zhou et al., 2009; Wang et al., 2014b; Fig. 5-2), and little studied.

5.4 Porphyry deposits

Paleocene–Eocene igneous rocks in the Gangdese belt are mostly barren, and only three small porphyry deposits have been discovered to date: the Yaguila Pb-Zn vein-type deposit (62.4 ± 0.6 Ma) with minor associated porphyry Mo mineralization (Huang et al., 2012), the Sharang porphyry Mo deposit (52.25 ± 0.31 Ma; 10 Mt @ 0.061% Mo; Zhao et al., 2011, 2014), and the Jiru porphyry Cu deposit (49.2 ± 1.7 Ma; 41.9 Mt @ 0.43 Cu; Zheng et al., 2014).

In contrast, high-K calc-alkaline plutons in the Oligocene are associated with several porphyry and skarn Cu deposits in the eastern Gangdese belt, including the Nuri porphyry and skarn Cu deposit (23.36 ± 0.49 Ma; 79.4 Mt at 0.73% Cu; Chen et al., 2011, 2012; Zhang et al., 2012), and the smaller Mingze, Liebu, and Chongmuda deposits.

The largest porphyry Cu-Mo±Au deposits occur in association with Miocene calc-alkaline to high-K calc-alkaline intrusive rocks, and are mainly restricted to the eastern Gangdese belt (Fig. 5-2; Hou et al., 2009; Wang et al., 2014b). These include the Qulong porphyry Cu-Mo deposit (16.4 ± 0.5 Ma; 1,420 Mt @ 0.5% Cu; Yang et al., 2009), the Jiama porphyry Cu-Mo-Au deposit (14.8 ± 0.33 Ma; 1,054 Mt @ 0.44 % Cu; Ying et al., 2014), and several small- to medium-sized porphyry Cu-Mo deposits such as Bangpu, Tangbula, Lakang'e, Dabu, Gangjiang, Chongjiang, and Tinggong (as reviewed in Hou et al., 2009).

In the western part of the belt, Miocene high-K calc-alkaline to shoshonitic plutons are associated with only a few, small porphyry and epithermal deposits (e.g., the Zhunuo porphyry Cu-Mo deposit; Zheng et al., 2007). Thus, significant porphyry Cu-Mo±Au mineralization is restricted in space (east of ~89°E), time (Oligo-Miocene), and magmatic association (calc-alkaline to high-K calc-alkaline plutons) in the Gangdese belt. Origin of the collision-related Oligo-Miocene porphyry Cu-Mo±Au deposits in the eastern

Gangdese belt is widely debated. Suggested petrogenetic models of their ore-forming calc-alkaline to high-K calc-alkaline granitoid magmas include partial melting of slab melt-modified mantle source (Gao et al., 2010), partial melting of newly formed lower crust (Hou et al., 2004, 2009; Zheng et al., 2012), partial melting of upwelling asthenosphere (Leng et al., 2013), and partial melting of subduction-modified Tibetan lithosphere (Li et al., 2011; Wang et al., 2014a, b, c; Wu et al., 2014). In addition, the extent of underthrusting of the Indian plate beneath Tibet is thought to play a major control on spatial distribution of Miocene porphyry Cu-Mo±Au deposits in this 1600 km-long Gangdese belt (Fig. 5-2; Wang et al., 2014a).

5.5 Sampling and analysis strategy

Large amounts of lithogeochemical and geochronological data have been published on Cenozoic igneous rocks from the Gangdese belt (as reviewed in Wang et al., 2014a, b, c), but few whole-rock osmium and zircon oxygen isotope data exist. In particular, few such analyses have been reported for Miocene potassic and ultrapotassic volcanic and subvolcanic rocks from the eastern Gangdese belt. For this reason, sampling was focused on the latter lithologies, aiming to complement existing data from other areas (see Table 5-1 for sample locations). Fresh or minimally altered igneous rocks were selected, and mafic end-members of igneous suites were prioritized in order to evaluate least-evolved compositions.

Isotopic compositions of Sr, Nd, and Os in whole-rock samples have been analyzed in order to constrain the contributions of various crustal and mantle sources in their petrogenesis. We have also analyzed oxygen isotopic compositions of igneous amphibole, biotite, phlogopite, and zircon from selected samples to further differentiate crustal versus mantle contributions.

5.6 Petrography and mineralogy

Lithological names used below are based on the TAS classification scheme of Le Maitre (1989) and Middlemost (1994), using whole-rock compositions presented in a later section. The following descriptions are based on a combination of new and published samples and observations.

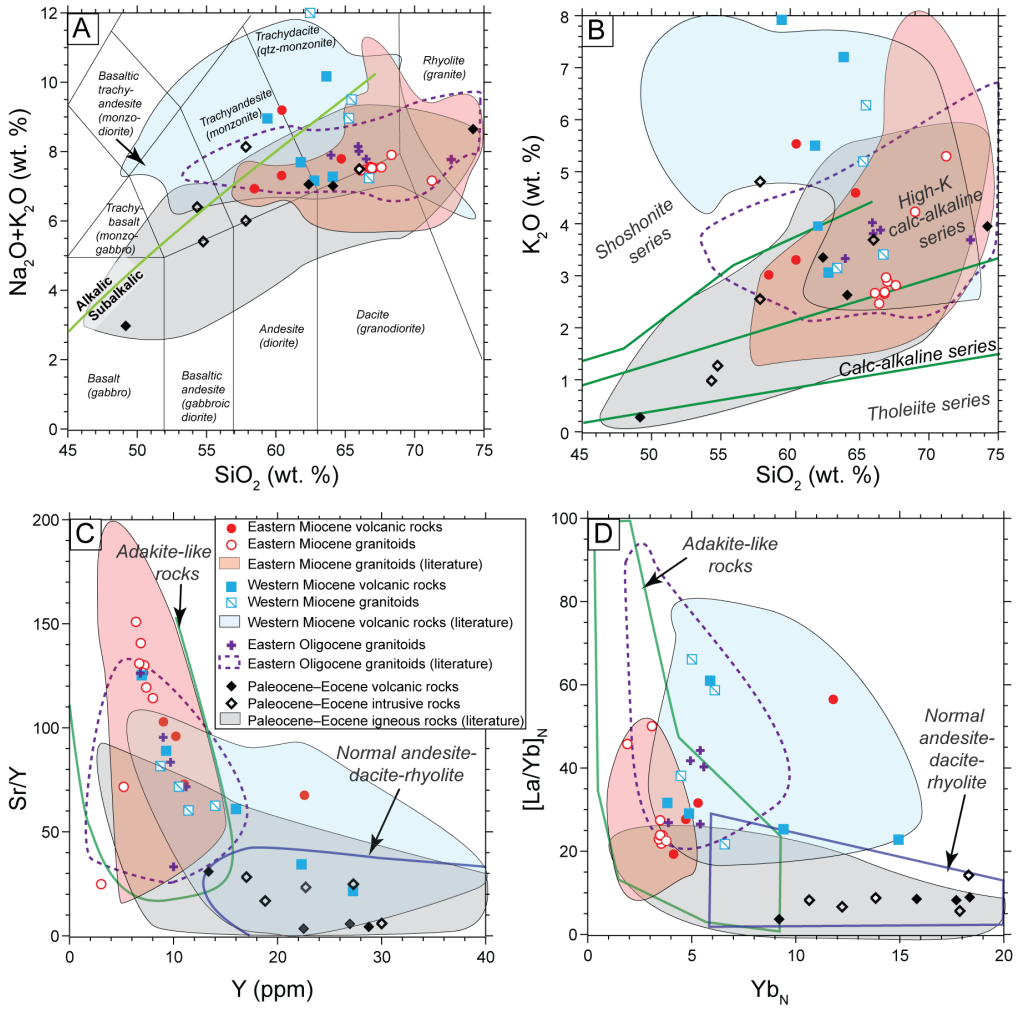

Figure 5-5. A. Total alkali-silica diagram for Paleocene–Eocene, Oligocene, and Miocene igneous rock samples from this study (after Le Maitre, 1989, and Middlemost, 1994). The alkaline/subalkaline boundary of Irvine and Baragar (1971) is shown. B. SiO_2 vs. total K_2O (after Rickwood, 1989). C. Sr/Y vs. Y; "Adakite-like rock" field is from Defant and Drummond (1990). D. $[La/Yb]_N$ vs. Yb_N; "Adakite-like rock" field is from Martin (1999). Typical fields for Paleocene–Eocene, Oligocene, and Miocene igneous rock samples from the literature (see text for data sources) are shown.

Paleocene–Eocene suite

Eighteen samples of igneous rocks were collected from Paleocene–Eocene calc-alkaline to high-K calc-alkaline intrusions (twelve samples) and Linzizong volcanic rocks (six samples) in the Gangdese belt.

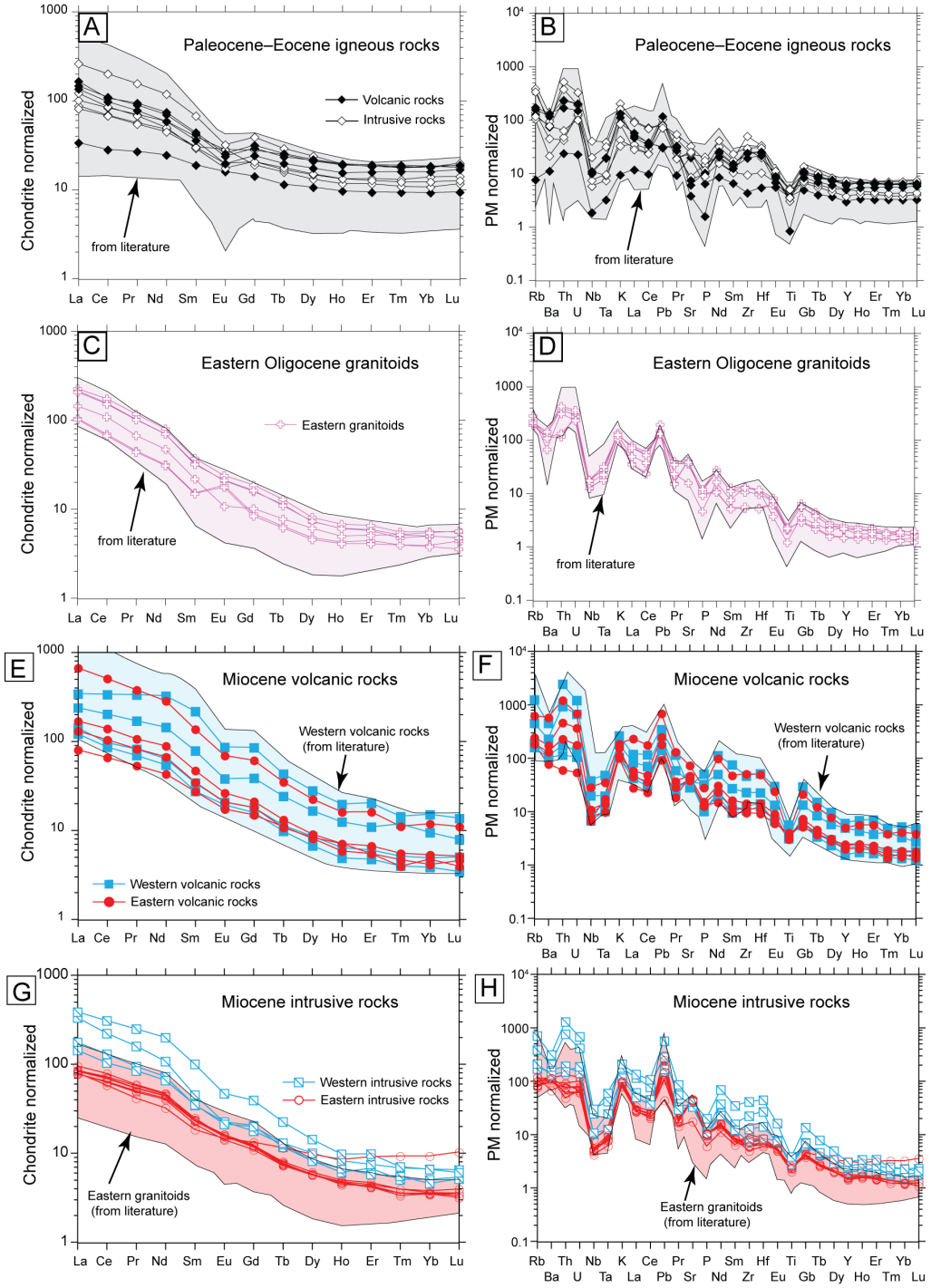

Figure 5-6. Chondrite- and primitive mantle- (PM) normalized trace element diagrams for Paleocene–Eocene, Oligocene, and Miocene samples of igneous rocks from this study (see text and Table 5-1 for data sources): A, B. Paleocene–Eocene igneous rocks; C, D. Oligocene igneous rocks; E, F. Miocene volcanic rocks; G, H. Miocene intrusive rocks. Normalization values are from Sun and McDonough (1989). Typical fields for Paleocene–Eocene, Oligocene, and Miocene igneous rock samples from the literature (see text for data sources) are shown.

The Linzizong volcanic rocks include basalt, basaltic trachyandesite, trachyandesite, andesite, dacite, and rhyolite. The basaltic to trachyandesitic and andesitic lavas are composed of clinopyroxene, plagioclase, and minor amphibole phenocrysts, with accessory minerals such as magnetite, rutile, and titanite set in a hyalopilitic groundmass of plagioclase microlites in glass (Fig. 5-3A). In contrast, the dacites and rhyolites are mainly composed of plagioclase and quartz phenocrysts, set in a glassy or fine-grained quartz-feldspathic groundmass (Fig. 5-3B).

The intrusive rocks include gabbro, gabbroic diorite, monzodiorite, monzonite, quartz monzonite, granodiorite, and granite. The mafic to intermediate intrusions are composed of coarse-grained orthopyroxene, clinopyroxene, plagioclase, and interstitial amphibole (Fig. 5-3C), whereas the felsic intrusions are composed plagioclase, K-feldspar, quartz, and minor interstitial amphibole and biotite (Fig. 5-3D). The samples collected are mostly fresh, and are representative of the lithologies and spatial distribution of such rocks across the region, as determined by our previous work (Wang et al., 2014b, c) and that of others (e.g., Dong, 2002; Chen, 2006; Dong et al., 2006a, b; Wen, 2007; Ji et al., 2009; Lee et al., 2009; Mo et al., 2008). There are no clear petrographic or mineralogical differences in the Paleocene–Eocene suite either spatially or temporally along the Gangdese belt.

Oligocene suite in the eastern Gangdese belt

Oligocene igneous rocks are sparse in the Gangdese belt, and all known occurrences are located in the eastern part of the belt. The main lithologies observed are monzonite, quartz monzonite, and granite porphyry, with minor diorite. The diorites are mainly composed of equigranular coarse-grained amphibole and plagioclase, whereas the quartz monzonite and granite porphyry are mainly composed of amphibole, plagioclase, biotite, quartz, and K-feldspar phenocrysts set in a phaneritic matrix of quartz, plagioclase, and biotite. The nine samples collected from the eastern Gangdese belt for this study are representative of the lithologies and spatial distribution of such rocks as described elsewhere (e.g., Harrison et al., 2000; Zheng et al., 2012; Wang et al., 2014b).

Miocene suite in the eastern Gangdese belt

Miocene igneous rocks in the eastern Gangdese belt occur as shallowly-emplaced calc-alkaline to high-K calc-alkaline granitoid plutons, and minor high-K calc-alkaline to shoshonitic volcanic rocks, that intrude or cover earlier Cretaceous–Eocene intrusive and volcanic rocks (Fig. 5-2).

The collected alkaline volcanic rocks include one trachyandesite, one trachydacite, and two porphyritic trachyandesite dike samples. Trachyandesite and trachydacite lavas consist of clinopyroxene, plagioclase, phlogopite, sanidine, and K-feldspar phenocrysts set in a fine-grained, trachytic groundmass (Fig. 5-4A, B). The porphyritic trachyandesite dike samples have a hyalopilitic texture, and are composed of amphibole and minor plagioclase phenocrysts set in a fine-grained amphibole-feldspathic groundmass (Fig. 5-4C).

Seven samples of granodiorite porphyry (Fig. 5-4D), one sample of quartz monzonite porphyry, and one sample of granite were collected from intrusions associated with the Qulong, Jiama, and Bangpu porphyry deposits, and are common rock types in this part of the belt (e.g., Hou et al., 2004; Yang et al., 2009; Li et al., 2011; Wang et al., 2014b). The quartz monzonite porphyry and granodiorite samples consist of plagioclase, K-feldspar, amphibole, and quartz phenocrysts set in a phaneritic matrix of quartz, plagioclase, and biotite. The granite sample consists of amphibole, plagioclase, K-feldspar, biotite, and quartz with an equigranular texture. All samples were collected well away from the actual porphyry deposits to minimize the effects of hydrothermal alteration.

Miocene suite in the western Gangdese belt

Miocene igneous rocks collected from the western Gangdese belt consist of six high-K calc-alkaline to shoshonitic volcanic rocks (lava flows and pyroclastic deposits), and four high-K calc-alkaline to shoshonitic porphyritic granitoids. The alkaline volcanic rocks are trachyandesitic and trachydacitic, and are mainly composed of phlogopite, sanidine, and amphibole phenocrysts set in an aphanitic or hyalopilitic matrix (Fig. 5-4E, F). These samples are representative of the lithologies and spatial distribution of such rocks as described in the literature (e.g., Miller et al., 1999; Ding et al., 2003; Williams et al., 2004; Zhao et al., 2009; Guo et al., 2013).

Three samples of quartz monzonite porphyry and one sample of granodiorite porphyry

were collected, and consist of amphibole, plagioclase, sanidine, biotite, phlogopite, and quartz phenocrysts set in a fine-grained matrix (Fig. 5-4G, H). These porphyritic granitoids are mineralogically and geochemically similar to the alkaline volcanic rocks, and therefore are equivalents of the alkaline volcanic rocks.

5.7 Analytical techniques

Lithogeochemical analysis

Fresh samples of igneous rock for lithogeochemical analysis were prepared by crushing (using corundum plates) and grinding in an agate disk mill at the Hebei Geological Survey Laboratory, China. The expected contamination of Si and Al by these methods is estimated to be less than one weight percent (as assessed from analyses of standards and blanks). All samples were analyzed at the National Research Center of Geoanalysis, Chinese Academy of Geological Science, in Beijing. Major elements were analyzed by wavelength dispersive X-ray fluorescence spectrometry. Accuracy for major elements, as determined by reproducibility of standards and duplicates, is typically within five relative percent (< 2 relative % for SiO_2 and Al_2O_3). Trace elements were analyzed with a Finnigan MAT inductively coupled plasma mass spectrometer (ICP-MS). Analytical accuracy for most trace elements is better than five relative percent.

Nd-Sr isotope analyses

Finely-ground sample powders (prepared as above) of seven igneous rocks from the Paleocene–Eocene suite, and eight igneous rocks from the Miocene suite were processed and analyzed for Nd-Sr isotopes at the Radiogenic Isotope Facility, University of Alberta.

Rock powders were accurately weighed and spiked with a known amount of mixed ^{150}Nd-^{149}Sm tracer solution, which has been calibrated directly against the Caltech mixed Sm/Nd normal spike described by Wasserburg et al. (1981). Dissolution used 3 ml mixed 24 mol/L HF + 16 mol/L HNO_3 media in sealed PFA Teflon vessels, held at 160°C for 5 days, followed by 3 ml 6 mol/L HCl. Chemical processing blanks are < 500 pg for Sm and Nd, and are insignificant relative to the amounts of Sm or Nd in the samples. Further details can be found in Creaser et al. (1997) and Unterschutz et al. (2002). The isotopic compositions of Sm and Nd were determined in static mode by multi-collector ICP-mass

spectrometry, and detailed procedures are described in Schmidberger et al. (2007). The Geological Survey of Japan Nd isotope standard "Shin Etsu: J-Ndi-1" (Tanaka et al., 2000) was used to monitor Nd isotopic measurements. The long-term average value for this standard obtained in the Radiogenic Isotope Facility is 0.512098 ± 11 [1σ, n = 66, past 6 years]), compared to the recommended value of 0.512107 ± 7 when normalized to $^{146}Nd/^{144}Nd = 0.7219$. This represents an accuracy of ± 0.17 epsilon units.

Rb/Sr analyses were performed using isotope dilution and thermal ionization mass spectrometry (TIMS) using methods described in detail by Creaser et al. (2004). Accurately weighed sample powders were dissolved in HF/HNO_3 as above, together with a known quantity of a mixed ^{87}Rb-^{84}Sr tracer, and Sr and Rb were separated by conventional cation exchange chromatography. The isotopic composition of Rb and Sr were measured using a Micromass Sector 54 instrument using single-filament analysis methods and static Faraday cup detection. The average value of the NIST SRM987 Sr isotope standard measured during the course of the analyses was 0.71027, and all Sr isotope data presented here are adjusted to a value for SRM987 of 0.71025, which is the "accepted value" and is typically used for normalization.

Os isotope analyses

Chemistry and mass spectrometric analyses were performed at the National Research Center of Geoanalysis, Chinese Academy of Geological Science, in Beijing. Four grams of thirty-three finely ground igneous rock powders were spiked with a known amount of mixed ^{185}Re-^{190}Os tracer solution (Du et al., 2004), and put into a clean, dry, chilled Pyrex® borosilicate glass Carius tube. 3 mL of purified 12 mol/L HCl, 5 mL of purified 15 mol/L HNO_3, and 1 mL H_2O_2 (30 %) were added to the tube, and then the tube was sealed. The digestions were performed at about 230 °C for 24–48 hours in an oven. An improved distillation technique was used for the separation of Os, and solvent extraction was used to extract Re (Zhou, 2012; Zhou et al., 2012).

The purified Re and Os were loaded onto platinum filaments, and analyzed by a Thermo Fisher Scientific Triton-plus TIMS (Creaser et al., 1991; Völkening et al., 1991). Re isotope ratios were measured as $^{185}ReO_4^-$ and $^{187}ReO_4^-$ using static-mode Faraday cups. Osmium isotope ratios were measured as $^{186}OsO_3^-$, $^{187}OsO_3^-$, $^{188}OsO_3^-$, $^{189}OsO_3^-$,

$^{190}OsO_3^-$, and $^{192}OsO_3^-$ using multi-Faraday cups. Measured Re and Os ratios were corrected for mass fractionation using $^{185}Re/^{187}Re = 0.59738$ (Gramlich et al., 1973) and for spike and blank contributions using $^{192}Os/^{188}Os = 3.0827$ (Luck and Allègre, 1983). Total procedural blanks for Re and Os are 1.39 and 0.3 ppt, respectively.

Amphibole, phlogopite, and biotite O isotope analysis

Crystals of amphibole, phlogopite, and biotite from fresh igneous rocks were hand separated after coarse crushing, and were then reacted with BrF_5 at 625°C to liberate oxygen (Clayton and Mayeda, 1963). Oxygen was then converted to CO_2 and analyzed for oxygen isotopic ratios on a Finnigan-MAT 252 mass spectrometer in the Stable Isotope Laboratory, University of Alberta. The data are reported in the usual delta notation with respect to Vienna Standard Mean Ocean Water (VSMOW). Analytical reproducibility for $\delta^{18}O$ values was ± 0.1‰ (1 σ).

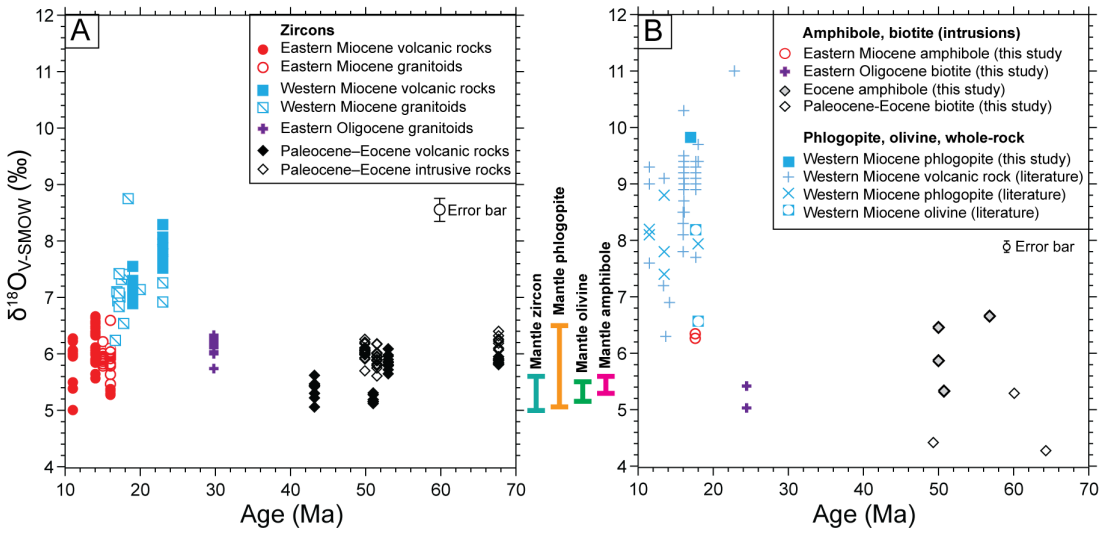

Figure 5-7. Oxygen isotopic compositions versus age for (A) zircon, and (B) amphibole, biotite, clinopyroxene, phlogopite, olivine, and whole-rock for Cenozoic igneous rocks from the Gangdese belt (see text and Table 5-1 for data sources). Mantle phlogopite values: +5.74 ± 0.73 ‰ (Mattey et al., 1994a), mantle olivine values: +5.28 ± 0.18 ‰ (Mattey et al., 1994b), mantle amphibole values: +5.3–5.6 ‰ (Chazot et al., 1997), mantle zircon values: $\delta^{18}O$ = +5.3 ± 0.3 ‰ (Valley et al., 1998).

Zircon O isotope analysis

Zircons were separated from 2–3 kg of crushed rock samples by heavy-liquid and

magnetic methods followed by hand-picking at the Hebei Geological Survey Laboratory, China. Selected crystals were typical of magmatic zircons: euhedral, clear, colorless, devoid of mineral and fluid inclusions, and 75–200 μm in diameter. The zircons were mounted in epoxy and polished to reveal their interiors.

Cathodoluminescence (CL), backscattered electron (BSE), and secondary electron (SE) images were obtained for the zircon grain mounts prior to analysis, to reveal internal zonations. Oxygen isotope analyses were carried out by secondary ion mass spectrometry (SIMS, Cameca 1280) at the Canadian Centre for Isotopic Microanalysis (CCIM), University of Alberta. Pristine zircon core and rim domains (based on CL/BSE/SE images) were targeted for analysis using a 20 keV Cs^+ ion beam with a spot size of ~15 μm diameter. Reported errors are a quadratic combination of the standard error of the analysis and the standard deviation of the reference materials analyzed together with the unknowns, and the uncertainties per analysis are typically ± 0.2 ‰ (2σ). The primary reference material utilized in this study was the CCIM internal zircon S0081 with $\delta^{18}O_{VSMOW}$ = +4.87 ‰. The accuracy of analyses for this study was evaluated from concurrent analyses of secondary reference zircon TEM2 with $\delta^{18}O_{VSMOW}$ = +8.20 ‰ (Black et al., 2004). The mean of 94 analyses was $\delta^{18}O_{VSMOW}$ = +8.27 ‰ (1 σ = 0.13 ‰).

5.8 Geochemical and isotopic results

Whole-rock geochemical data, Sr-Nd-Os isotope data, and mineral (amphibole, biotite, phlogopite, and zircon) O isotope data from this study are listed in Tables 5-2 to 5-6. These data are supplemented with data from the literature as reviewed in Wang et al. (2014a, b, c) in the following discussions.

Whole-rock geochemical data are normalized to volatile-free compositions and plotted on lithological discrimination diagrams in Figure 5-5, and normalized trace element diagrams in Figure 5-6. Mineral oxygen isotopic compositions are plotted in Figure 5-7, and whole-rock Nd and Os isotopic compositions are plotted in Figures 5-8 and 5-9, respectively.

Table 5-3: Zircon O isotope data for the Cenozoic Gangdese magmatic rocks

Sample	Spot Name	$^{18}O/^{16}O$	$\delta^{18}O_{(VSMOW)}$ (‰)	2σ (‰)
WR-13-42	S2811_1@1	0.00201555	5.16	0.22
WR-13-42	S2811_11@1	0.00201547	5.12	0.18
WR-13-42	S2811_15@1	0.00201553	5.15	0.19
WR-13-42	S2811_20@1	0.00201552	5.15	0.19
WR-13-42	S2811_26@1	0.00201584	5.31	0.20
WR-13-42	S2811_26@2	0.00201579	5.28	0.18
WR-13-42	S2811_3@1	0.00201561	5.19	0.19
WR-13-42	S2811_7@1	0.00201547	5.12	0.19
WR-13-81	S2791_1@1	0.00201775	6.26	0.29
WR-13-81	S2791_11@1	0.00201735	6.06	0.26
WR-13-81	S2791_12@1	0.00201663	5.70	0.29
WR-13-81	S2791_12@2	0.00201705	5.91	0.26
WR-13-81	S2791_13@1	0.00201721	5.99	0.26
WR-13-81	S2791_14@1	0.00201742	6.09	0.25
WR-13-81	S2791_15@1	0.00201719	5.98	0.25
WR-13-81	S2791_16@1	0.00201745	6.11	0.24
WR-13-81	S2791_18@1	0.00201760	6.18	0.26
WR-13-81	S2791_19@1	0.00201727	6.02	0.22
WR-13-81	S2791_20@1	0.00201736	6.07	0.25
WR-13-81	S2791_21@1	0.00201764	6.21	0.26
WR-13-81	S2791_4@1	0.00201727	6.02	0.22
WR-13-81	S2791_5@1	0.00201720	5.98	0.24
WR-13-81	S2791_6@1	0.00201731	6.04	0.25
WR-13-81	S2791_7@1	0.00201725	6.01	0.25
WR-13-81	S2791_9@1	0.00201709	5.93	0.25
WR-12-30B	S2796_1@1	0.00201776	6.26	0.25
WR-12-30B	S2796_11@1	0.00201689	5.83	0.25
WR-12-30B	S2796_12@1	0.00201770	6.23	0.25
WR-12-30B	S2796_13@1	0.00201787	6.32	0.23
WR-12-30B	S2796_14@1	0.00201712	5.95	0.26
WR-12-30B	S2796_14@2	0.00201702	5.89	0.23
WR-12-30B	S2796_17@1	0.00201708	5.92	0.25
WR-12-30B	S2796_19@1	0.00201742	6.10	0.26
WR-12-30B	S2796_19@2	0.00201701	5.89	0.27
WR-12-30B	S2796_2@1	0.00201703	5.90	0.24
WR-12-30B	S2796_21@1	0.00201693	5.85	0.24
WR-12-30B	S2796_3@1	0.00201701	5.89	0.26
WR-12-30B	S2796_4@1	0.00201698	5.88	0.24
WR-12-30B	S2796_5@1	0.00201760	6.19	0.24
WR-12-30B	S2796_6@1	0.00201737	6.07	0.26
WR-12-30B	S2796_6@2	0.00201686	5.81	0.25
WR-12-30B	S2796_7@1	0.00201687	5.82	0.24
WR-12-30B	S2796_8@1	0.00201803	6.40	0.22
WR-13-117	S2800_1@2	0.00201684	5.80	0.26
WR-13-117	S2800_11@3	0.00201695	5.86	0.23
WR-13-117	S2800_12@1	0.00201681	5.79	0.23
WR-13-117	S2800_13@3	0.00201703	5.90	0.26
WR-13-117	S2800_14@3	0.00201693	5.85	0.24
WR-13-117	S2800_14@4	0.00201695	5.86	0.24
WR-13-117	S2800_16@1	0.00201740	6.09	0.24
WR-13-117	S2800_21@2	0.00201653	5.65	0.23
WR-13-117	S2800_3@2	0.00201714	5.96	0.23
WR-13-117	S2800_4@2	0.00201718	5.98	0.24
WR-13-117	S2800_5@2	0.00201684	5.81	0.24
WR-13-117	S2800_8@3	0.00201667	5.72	0.23
WR-13-2	S2797_1@1	0.00201723	6.00	0.24
WR-13-2	S2797_11@1	0.00201703	5.90	0.24
WR-13-2	S2797_11@2	0.00201674	5.75	0.23
WR-13-2	S2797_12@2	0.00201715	5.96	0.25
WR-13-2	S2797_18@1	0.00201713	5.95	0.23
WR-13-2	S2797_19@1	0.00201646	5.61	0.27
WR-13-2	S2797_19@2	0.00201680	5.79	0.24
WR-13-2	S2797_20@1	0.00201728	6.02	0.24
WR-13-2	S2797_3@1	0.00201698	5.88	0.23
WR-13-2	S2797_3@2	0.00201688	5.82	0.22
WR-13-2	S2797_4@1	0.00201711	5.94	0.24

WR-13-2	S2797_5@1	0.00201701	5.89	0.30
WR-13-2	S2797_5@2	0.00201759	6.18	0.24
WR-13-2	S2797_9@1	0.00201716	5.96	0.22
WR-13-2	S2797_9@2	0.00201758	6.17	0.23
WR-13-113B	S2808_1@1	0.00201610	5.44	0.19
WR-13-113B	S2808_12@1	0.00201606	5.42	0.20
WR-13-113B	S2808_16@1	0.00201610	5.44	0.19
WR-13-113B	S2808_2@1	0.00201567	5.22	0.19
WR-13-113B	S2808_20@1	0.00201535	5.06	0.19
WR-13-113B	S2808_21@1	0.00201612	5.45	0.18
WR-13-113B	S2808_23@1	0.00201646	5.62	0.20
WR-13-113B	S2808_5@1	0.00201617	5.47	0.18
WR-13-113B	S2808_5@2	0.00201583	5.30	0.18
CB-5	S2861_1@1	0.002017547	6.16	0.18
CB-5	S2861_3@1	0.002017561	6.16	0.15
CB-5	S2861_4@1	0.002017535	6.15	0.14
CB-5	S2861_4@2	0.002017818	6.29	0.18
CB-5	S2861_5@1	0.002017319	6.04	0.18
CB-5	S2861_5@2	0.002017602	6.19	0.15
CB-5	S2861_6@1	0.002017823	6.29	0.21
CB-5	S2861_7@1	0.002016709	5.74	0.22
CB-5	S2861_9@1	0.002017717	6.24	0.18
CB-5	S2861_12@1	0.002017873	6.32	0.16
CB-5	S2861_14@1	0.002017445	6.11	0.16
CB-5	S2861_16@1	0.002017746	6.26	0.20
CB-5	S2861_18@1	0.002017222	6.00	0.15
CB-5	S2861_18@2	0.002017901	6.33	0.23
WR-13-36	S2805_10@1	0.002021831	8.29	0.18
WR-13-36	S2805_10@2	0.002020755	7.76	0.21
WR-13-36	S2805_12@1	0.002021268	8.01	0.21
WR-13-36	S2805_14@1	0.002020733	7.75	0.19
WR-13-36	S2805_2@1	0.002020277	7.52	0.20
WR-13-36	S2805_2@2	0.002020936	7.85	0.21
WR-13-36	S2805_20@1	0.002021391	8.07	0.21
WR-13-36	S2805_20@1	0.00202042	7.59	0.20
WR-13-36	S2805_4@1	0.00202094	7.85	0.19
WR-13-36	S2805_8@1	0.002020811	7.79	0.20
WR-13-84	S2792_10@1	0.00201985	7.30	0.25
WR-13-84	S2792_11@1	0.00201960	7.18	0.26
WR-13-84	S2792_12@1	0.00201907	6.91	0.22
WR-13-84	S2792_12@2	0.00201905	6.91	0.23
WR-13-84	S2792_15@1	0.00201944	7.10	0.24
WR-13-84	S2792_17@1	0.00201985	7.30	0.26
WR-13-84	S2792_18@1	0.00201965	7.20	0.25
WR-13-84	S2792_19@1	0.00201910	6.93	0.26
WR-13-84	S2792_19@3	0.00201938	7.07	0.24
WR-13-84	S2792_2@1	0.00201949	7.13	0.25
WR-13-84	S2792_20@1	0.00202033	7.55	0.26
WR-13-84	S2792_21@1	0.00201961	7.19	0.26
WR-13-84	S2792_21@2	0.00201928	7.02	0.26
WR-13-84	S2792_4@1	0.00201919	6.97	0.27
WR-13-84	S2792_5@1	0.00201933	7.05	0.27
WR-13-84	S2792_6@1	0.00201926	7.01	0.26
WR-13-84	S2792_6@2	0.00201948	7.12	0.24
WR-13-84	S2792_7@1	0.00201925	7.01	0.23
WR-13-84	S2792_9@1	0.00201932	7.04	0.24
WR-13-84	S2792_9@2	0.00201902	6.89	0.29
WR-13-48	S2810_1@1	0.00202088	7.82	0.18
WR-13-48	S2810_12@1	0.00202117	7.96	0.18
WR-13-48	S2810_13@1	0.00201976	7.26	0.19
WR-13-48	S2810_18@1	0.00202135	8.06	0.19
WR-13-48	S2810_21@1	0.00202112	7.94	0.18
WR-13-48	S2810_21@2	0.00201909	6.92	0.18
WR-13-48	S2810_23@1	0.00202137	8.06	0.21
WR-13-48	S2810_3@1	0.00202095	7.85	0.19
WR-13-48	S2810_5@1	0.00202117	7.96	0.19
JR-5	S2803_11@1	0.00201579	5.28	0.19
JR-5	S2803_16@1	0.00201594	5.35	0.20
JR-5	S2803_16@2	0.00201594	5.36	0.19
JR-5	S2803_18@1	0.00201583	5.30	0.18

JR-5	S2803_4@1	0.00201578	5.28	0.21
JR-5	S2803_5@1	0.00201593	5.35	0.18
JR-5	S2803_9@1	0.00201600	5.38	0.19
WR-13-14	S2794_1@1	0.00201832	6.54	0.24
WR-13-14	S2794_10@1	0.00201857	6.67	0.26
WR-13-14	S2794_12@1	0.00201796	6.37	0.25
WR-13-14	S2794_15@1	0.00201804	6.40	0.22
WR-13-14	S2794_16@1	0.00201836	6.56	0.23
WR-13-14	S2794_18@1	0.00201653	5.65	0.24
WR-13-14	S2794_18@2	0.00201636	5.57	0.26
WR-13-14	S2794_19@1	0.00201840	6.58	0.27
WR-13-14	S2794_2@1	0.00201789	6.33	0.24
WR-13-14	S2794_2@2	0.00201821	6.49	0.24
WR-13-14	S2794_3@1	0.00201851	6.64	0.25
WR-13-14	S2794_3@2	0.00201833	6.55	0.23
WR-13-14	S2794_4@1	0.00201816	6.46	0.26
WR-13-14	S2794_7@1	0.00201793	6.35	0.24
WR-13-14	S2794_7@2	0.00201796	6.36	0.23
WR-13-14	S2794_9@1	0.00201728	6.03	0.23
WR-13-122	S2806_1@1	0.00201719	5.98	0.21
WR-13-122	S2806_13@1	0.00201715	5.96	0.20
WR-13-122	S2806_16@1	0.00201720	5.98	0.19
WR-13-122	S2806_2@1	0.00201725	6.01	0.19
WR-13-122	S2806_21@1	0.00201602	5.39	0.21
WR-13-122	S2806_22@1	0.00201779	6.28	0.18
WR-13-122	S2806_23@1	0.00201770	6.23	0.21
WR-13-122	S2806_3@1	0.00201738	6.07	0.19
WR-13-122	S2806_8@1	0.00201525	5.01	0.19
WR-13-122	S2806_8@2	0.00201623	5.50	0.21
WR-13-122	S2806_9@1	0.00201733	6.05	0.20
WR-13-100	S2802_13@1	0.00201703	5.90	0.22
WR-13-100	S2802_14@1	0.00201737	6.07	0.19
WR-13-100	S2802_18@1	0.00201746	6.11	0.19
WR-13-100	S2802_2@1	0.00201699	5.88	0.21
WR-13-100	S2802_2@2	0.00201705	5.91	0.21
WR-13-100	S2802_23@1	0.00201726	6.01	0.20
WR-13-100	S2802_3@1	0.00201702	5.90	0.19
WR-13-100	S2802_4@1	0.00201720	5.99	0.22
WR-13-100	S2802_5@1	0.00201746	6.12	0.21
WR-13-100	S2802_7@1	0.00201693	5.85	0.20
JM11-34	S2804_13@1	0.00201740	6.09	0.22
JM11-34	S2804_17@1	0.00201724	6.01	0.19
JM11-34	S2804_17@2	0.00201725	6.01	0.19
JM11-34	S2804_2@1	0.00201709	5.93	0.19
JM11-34	S2804_2@2	0.00201698	5.87	0.20
JM11-34	S2804_20@1	0.00201681	5.79	0.21
JM11-34	S2804_20@2	0.00201707	5.92	0.19
JM11-34	S2804_22@1	0.00201689	5.83	0.20
JM11-34	S2804_3@1	0.00201712	5.95	0.21
JM11-34	S2804_6@1	0.00201767	6.22	0.20
JM11-34	S2804_6@2	0.00201716	5.96	0.18
JM11-34	S2804_9@1	0.00201703	5.90	0.20
BP-1	S2798_1@1	0.00201720	5.99	0.26
BP-1	S2798_1@2	0.00201707	5.92	0.25
BP-1	S2798_10@1	0.00201707	5.92	0.23
BP-1	S2798_11@1	0.00201718	5.98	0.25
BP-1	S2798_13@1	0.00201740	6.08	0.28
BP-1	S2798_15@1	0.00201729	6.03	0.22
BP-1	S2798_15@2	0.00201746	6.11	0.24
BP-1	S2798_2@1	0.00201726	6.02	0.25
BP-1	S2798_20@1	0.00201617	5.47	0.27
BP-1	S2798_20@2	0.00201714	5.96	0.24
BP-1	S2798_22@1	0.00201650	5.64	0.24
BP-1	S2798_5@2	0.00201680	5.79	0.27
BP-1	S2798_6@1	0.00201744	6.10	0.24
BP-1	S2798_6@2	0.00201731	6.04	0.24
BP-1	S2798_7@1	0.00201690	5.83	0.24
BP-1	S2798_8@1	0.00201731	6.04	0.24
BP-1	S2798_9@1	0.00201844	6.60	0.25

Table 5-4: Amphibole, phlogopite, and biotite O isotope data for the Cenozoic Gangdese magmatic rocks

Sample number	Mineral	$\delta^{18}O_{(VSMOW)}$ (‰)	1σ (‰)
WR-12-8	Amphibole	6.7	0.1
XG-12-9	Amphibole	6.5	0.1
XG-12-3	Amphibole	5.9	0.1
WR-12-33	Amphibole	5.3	0.1
QL10-4-22	Amphibole	6.3	0.1
QL10-4-9	Amphibole	6.4	0.1
WR-12-52	Phlogopite	9.8	0.1
WR-12-1	Biotite	4.3	0.1
WR-12-40	Biotite	4.4	0.1
GZ-12-1	Biotite	5.3	0.1
XB-12-1	Biotite	5.4	0.1
XB-12-7	Biotite	5.0	0.1

Table 5-5: Sr-Nd isotope data for the Cenozoic Gangdese magmatic rocks

Sample number	Age (Ma)	Rb (ppm)	Sr (ppm)	Sm (ppm)	Nd (ppm)	$^{87}Rb/^{86}Sr$	$^{87}Sr/^{86}Sr$	2σ	$(^{87}Sr/^{86}Sr)_i$	$^{147}Sm/^{144}Nd$	$^{143}Nd/^{144}Nd$	2σ	εNd	$(^{143}Nd/^{144}Nd)_i$	$εNd_i$
WR-13-40	58.0	2.2	528.3	3.05	13.58	0.012	0.70515	0.00002	0.70514	0.1357	0.512643	0.000012	0.1	0.51262	0.5
WR-13-81	49.9	208.2	684.7	9.07	49.96	0.880	0.70650	0.00002	0.70588	0.1098	0.512418	0.000009	-4.3	0.51238	-3.7
WR-12-30B	67.8	138.1	306.5	4.37	23.27	1.304	0.70583	0.00002	0.70458	0.1136	0.512657	0.000008	0.4	0.51261	1.1
WR-13-117	53.0	97.3	167.1	5.79	29.83	1.685	0.70862	0.00002	0.70735	0.1173	0.512391	0.000007	-4.8	0.51235	-4.3
WR-13-109	43.2	104.6	311.2	7.28	26.96	0.972	0.70615	0.00002	0.70555	0.1633	0.512619	0.000007	-0.4	0.51257	-0.2
WR-13-113A	43.2	75.9	401.8	4.36	21.01	0.546	0.70565	0.00002	0.70532	0.1253	0.512612	0.000010	-0.5	0.51258	-0.1
WR-13-113B	43.2	97.7	77.2	5.31	27.15	3.663	0.71014	0.00005	0.70789	0.1183	0.512600	0.000005	-0.7	0.51257	-0.3
WR-13-53	21.2	726.2	598.2	28.95	133.84	3.520	0.72732	0.00001	0.72626	0.1308	0.511855	0.000009	-15.3	0.51184	-15.1
WR-13-26	18.0	243.6	297.4	4.88	27.84	2.373	0.71705	0.00002	0.71645	0.1060	0.512222	0.000010	-8.1	0.51222	-7.9
WR-13-48	23.0	240.0	767.9	14.4	88.2	0.905	0.71504	0.00002	0.71474	0.0985	0.512043	0.000005	-11.6	0.51203	-11.3
WR-13-18	14.0	243.6	297.4	10.14	54.25	2.373	0.71705	0.00002	0.71658	0.1131	0.511933	0.000008	-13.8	0.51192	-13.6
JR-5	16.2	103.5	803.8	4.05	19.88	0.372	0.70574	0.00002	0.70566	0.1232	0.512458	0.000010	-3.5	0.51244	-3.4
WR-13-122	11.0	244.8	1110.5	14.12	93.27	0.638	0.71220	0.00002	0.71210	0.0915	0.512150	0.000005	-9.5	0.51214	-9.4
WR-13-100	14.0	145.0	683.0	7.44	41.82	0.614	0.70668	0.00002	0.70656	0.1076	0.512297	0.000008	-6.6	0.51229	-6.5
BP-1	16.0	84.7	126.3	1.76	7.32	1.939	0.70670	0.00002	0.70626	0.1451	0.512588	0.000009	-1.0	0.51257	-0.9

Table 5-6: Osmium isotope data for the Cenozoic Gangdese magmatic rocks

Sample number	Analysis number	Weight (g)	Re (ppt)	2σ	Os (ppt)	2σ	$^{187}Re/^{188}Os$	2σ	$^{187}Os/^{188}Os$	2σ	$(^{187}Os/^{188}Os)_i$
WR-13-37	WR-13-37	4.0	43.0	0.1	7.76	0.05	27.3	0.2	0.2882	0.0024	0.262
WR-13-40	WR-13-40	4.0	285.4	0.9	7.32	0.03	194.8	1.0	0.4139	0.0031	0.226
WR-13-81	WR-13-81	4.0	205.4	0.7	2.53	0.01	423.2	2.8	0.7460	0.0070	0.394
WR-13-117	WR-13-117	4.0	44.0	0.1	0.75	0.01	305.1	2.8	0.7332	0.0085	0.464
WR-13-118	WR-13-118	4.0	52.2	0.2	1.02	0.00	261.3	1.5	0.5949	0.0061	0.364
CMD-17A	CMD-17A	4.0	7.3	0.3	9.02	0.09	3.9	0.2	0.2384	0.0047	0.236
CMD-17B	CMD-17B	4.0	8.4	0.2	6.62	0.11	6.1	0.2	0.3621	0.0099	0.359
CMD-32A	CMD-32A	4.0	8.2	0.2	4.65	0.04	8.5	0.2	0.2693	0.0086	0.265
CMD-32B	CMD-32B	4.0	13.2	0.3	4.38	0.03	14.3	0.3	0.2951	0.0031	0.288
CMD-33A	CMD-33A	4.0	17.8	0.5	5.28	0.05	16.3	0.5	0.2318	0.0111	0.224
CMD-33B	CMD-33B	4.0	11.0	0.3	3.82	0.06	13.8	0.4	0.3394	0.1424	0.332
WR-13-53	WR-13-53	4.0	157.3	0.5	160.5	1.9	4.7	0.1	0.1580	0.0027	0.156
WR-13-84	WR-13-84	4.0	9.6	0.1	2.93	0.01	16.0	0.2	0.1936	0.0015	0.188
WR-13-85	WR-13-85	4.0	34.1	0.1	3.33	0.02	49.7	0.3	0.1977	0.0016	0.182
WR-13-31	WR-13-31	4.0	133.2	0.4	1.02	0.01	723.0	7.0	1.2466	0.0149	1.006
WR-13-26	WR-13-26	4.0	53.2	0.2	1.06	0.01	269.5	1.8	1.0310	0.0085	0.948
10YR07	10YR07	4.0	76.7	0.3	0.89	0.00	442.6	2.3	0.6682	0.0059	0.550
WR-13-48	WR-13-48	4.0	20.6	0.1	2.99	0.02	37.2	0.3	1.0494	0.0097	1.035
WR-13-122	WR-13-123	4.0	54.3	0.4	4.93	0.03	53.5	0.6	0.1844	0.0021	0.175
WR-13-122	WR-13-124A	4.0	42.9	0.2	6.00	0.03	34.7	0.2	0.1656	0.0013	0.159
WR-13-122	WR-13-124B	4.0	39.7	0.3	5.23	0.03	36.7	0.3	0.1602	0.0014	0.153
WR-13-122	WR-13-125	4.0	68.8	0.2	3.87	0.02	86.7	0.6	0.2263	0.0024	0.210
WR-13-100	WR-13-100A	4.0	1348.4	6.0	39.04	0.35	168.4	1.7	0.2157	0.0029	0.176
WR-13-100	WR-13-100B	4.0	660.4	2.6	35.17	0.16	91.3	0.5	0.1997	0.0018	0.178
JR-5	JR-5	4.0	61.9	0.2	3.87	0.02	77.9	0.4	0.2130	0.0031	0.192
JM11-34	JM11-34	4.0	405.5	1.2	5.91	0.02	340.9	1.6	0.3602	0.0047	0.269
QL02-01	QL02-01	4.0	14.9	0.3	0.75	0.03	91.9	5.0	0.8647	0.0521	0.835
QL02-04-2	QL02-04-2	4.0	10.7	0.3	4.03	0.05	12.8	0.4	0.2900	0.0189	0.286
QL02-07	QL02-07	4.0	21.2	0.5	0.90	0.02	108.1	3.2	0.4872	0.0773	0.452
QL02-10	QL02-10	4.0	8.0	0.4	0.99	0.03	36.7	2.2	0.4233	0.0229	0.411
QL02-13	QL02-13	4.0	61.5	0.6	1.07	0.02	284.5	5.2	0.4262	0.0114	0.334
QL02-28	QL02-28A	4.0	8.4	0.2	1.24	0.03	32.7	1.3	0.5063	0.0249	0.496
QL02-28	QL02-28B	4.0	8.4	0.2	3.90	0.04	10.3	0.3	0.5390	0.0367	0.536

5.9 Petrogenesis of Cenozoic igneous rocks in the Gangdese belt

Paleocene–Eocene magmatism

Cospatial and coeval Paleocene–Eocene intrusive and volcanic rocks show a similar compositional range. Five samples of Paleocene–Eocene intrusions have gabbroic dioritic, monzodioritic, monzonitic, and quartz monzonitic compositions, whereas four samples of Linzizong volcanic rocks are basaltic, trachyandesitic, dacitic, and rhyolitic (Fig. 5-5A). They are mostly subalkalic and plot in the calc-alkaline to high-K calc-alkaline fields (Fig. 5-5A, B). Data for other Paleocene–Eocene igneous rocks from the literature show similar but much broader ranges of compositions.

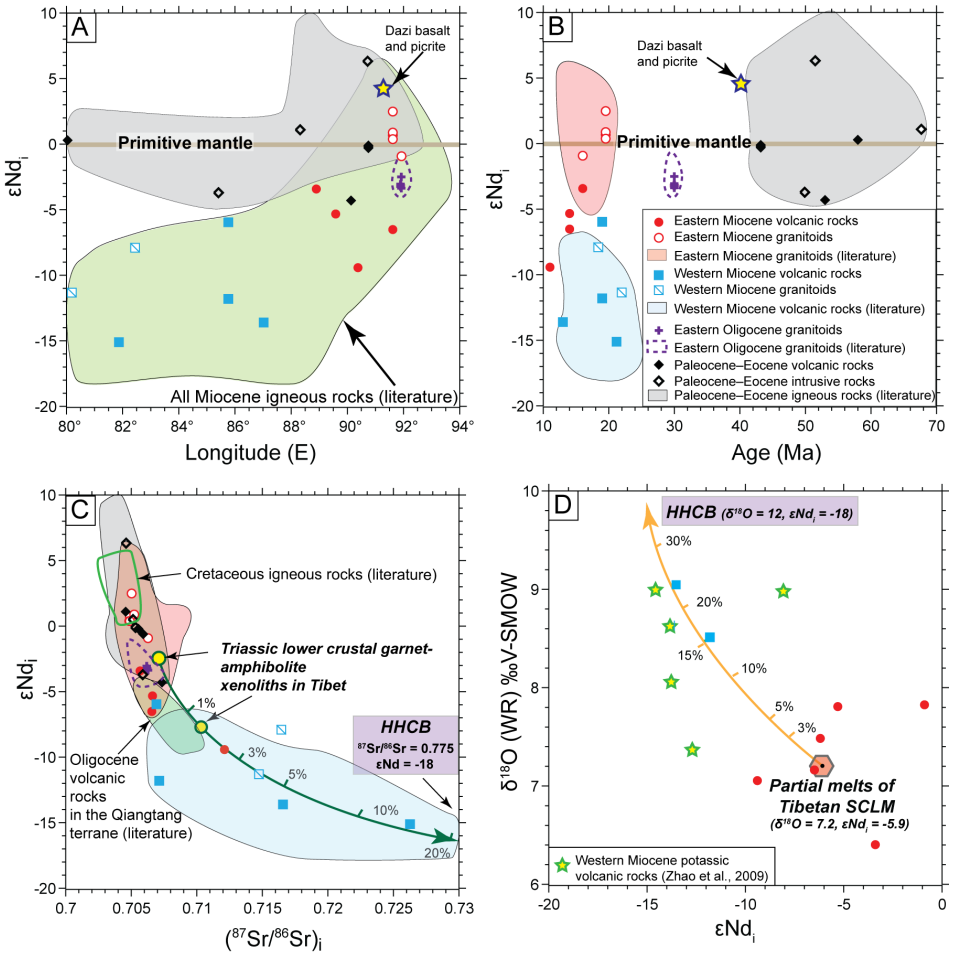

Figure 5-8. A. εNd_i vs. longitude; B. εNd_i vs. age; C. εNd_i vs. $(^{87}Sr/^{86}Sr)_i$; D. Whole-rock $\delta^{18}O$ vs. εNd_i. Values of Dazi basalt and picrite are from Gao et al. (2010). In C, the green line shows mixing between lower crustal garnet-amphibolite xenoliths in Tibet, which are thought to represent Tibetan lithospheric mantle and High Himalayan

crystalline basement melts (HHCB: thought to represent the composition of the Indian craton) (for mixing model details, see Wang et al., 2014a). Qiangtang Oligocene volcanic rock compositions are from Ding et al. (2003) and Liu et al. (2008); Cretaceous igneous rock compositions are from Wen (2007) and Zheng et al. (2014). In D, the orange line shows mixing (ticks on the curve give percentage of assimilation) between melts of HHCB ($\delta^{18}O = 12$, $\varepsilon Nd_i = -18$; France-Lanord et al. 1988; Inger and Harris, 1993) and partial melts of the Tibetan SCLM (represented by average of eastern Miocene alkaline volcanic rocks with mantle Os isotopic ratios: $\delta^{18}O = 7.2$, $\varepsilon Nd_i = -5.9$; magma $\delta^{18}O$ values were obtained from zircon $\delta^{18}O$ values, using $\delta^{18}O$ (Zircon-WR) = $\delta^{18}O$ (Zircon) – $\delta^{18}O$ (WR) ≈ -0.0612 (wt.% SiO_2) + 2.5: Valley et al., 2005). Abbreviations: HHCB = High Himalayan crystalline basement; SCLM = sub-continental lithospheric mantle

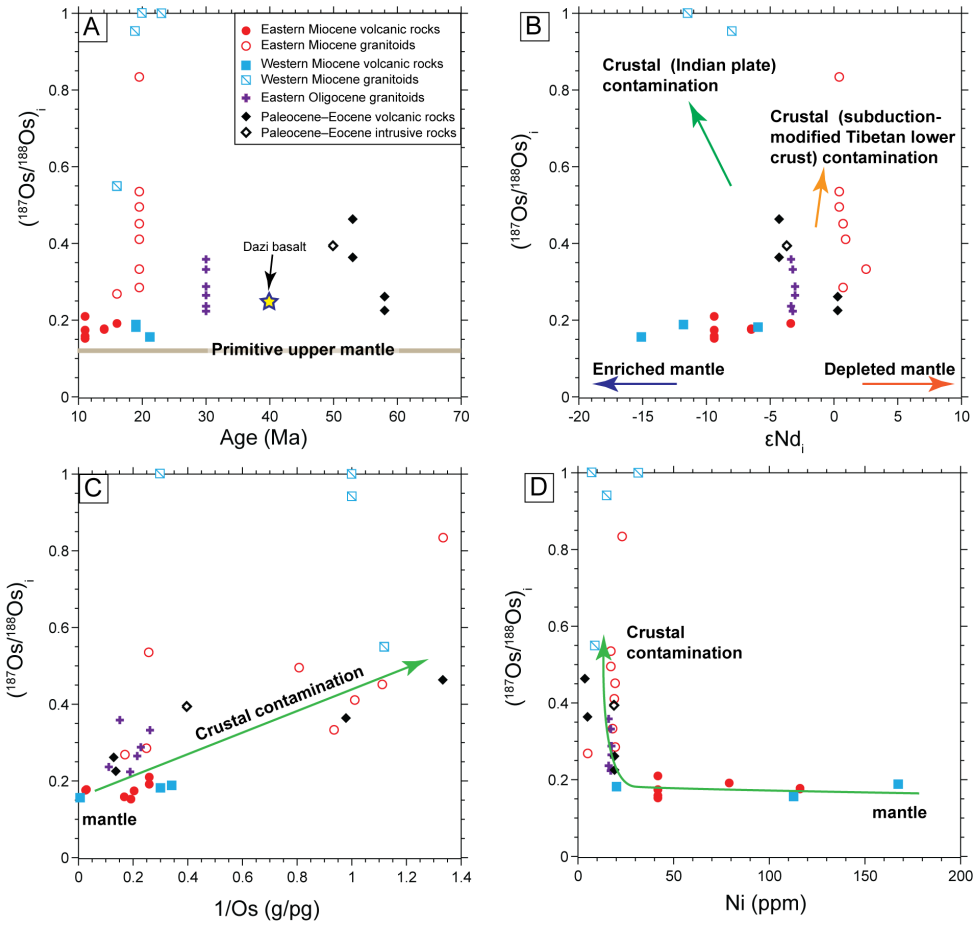

Figure 5-9. A. $(^{187}Os/^{188}Os)_i$ vs. age; B. $(^{187}Os/^{188}Os)_i$ vs. εNd_i; C. $(^{187}Os/^{188}Os)_i$ vs. 1/Os (g/pg); D. $(^{187}Os/^{188}Os)_i$ vs. Ni. Present day primitive upper mantle $^{187}Os/^{188}Os = 0.1296 \pm 0.0008$ (Meisel et al., 2001). Value of Dazi basalt is from Zhou (2012). Apparent trends for crustal contamination are also shown ($^{187}Os/^{188}Os \approx 1–1.5$ for the crust, 0.1100–0.1500 for the mantle: Shirey and Walker, 1998; Widow et al., 1999).

All samples have low Sr/Y and $[La/Yb]_N$ ratios (Fig. 5-5C, D), and show weakly listric normalized rare earth element (REE) patterns with moderate enrichments of light rare earth elements (LREE) relative to middle and heavy rare earth elements (MREE and HREE) ($[La/Yb]_N = 8.7 \pm 3.3$, n = 9, range = 3.7–14.2; Figs. 5D, 6A). They mostly have distinct negative Eu anomalies, indicating fractionation of plagioclase feldspar from relatively dry melts (Wang et al., 2014b). On a primitive mantle-normalized trace element diagram these samples show relative depletions in Nb, Ta, P, and Ti, and enrichments in Th, U, Pb, and K (Fig. 5-6B), typical of arc-related igneous rocks worldwide (Perfit et al., 1980; Pearce, 1982; Arculus and Powell, 1986). Our data fall within the typical ranges of Paleocene–Eocene igneous rocks from the literature, shown as grey fields in Figures 5-5, 6.

Zircon $\delta^{18}O$ values from these rocks show a small range from +5.1 ‰ to +6.4 ‰ (Fig. 5-7A). Two mafic samples with low zircon $\delta^{18}O$ values plot in the mantle range (+5.3 ± 0.3 ‰: Valley et al., 1998), and four intermediate–felsic samples have $\delta^{18}O$ values between +5.6 ‰ and +6.4 ‰ (Fig. 5-7A). These values are similar to values for amphibole and biotite, which range from +5.3 ‰ to +6.7 ‰, and +4.3 ‰ to +5.3 ‰, respectively (Fig. 5-7B). These values are close to the range expected for minerals in equilibrium with mantle-derived magmas, and indicate only minor crustal contamination (Kyser, 1986; Mattey et al., 1994a, b; Chazot et al., 1997; Eiler, 2001).

The $(^{87}Sr/^{86}Sr)_i$, εNd_i, and $(^{187}Os/^{188}Os)_i$ values for these samples range from 0.7046 to 0.7079 (Fig. 5-8C), from -4.3 to +6.3 (Fig. 5-8A, B), and from 0.226 to 0.464 (Fig. 5-9), respectively. Our new Sr-Nd isotopic data mostly overlap the ranges of Paleocene–Eocene igneous rocks from the literature (Fig. 5-8A–C). In addition, Cretaceous Gangdese arc rocks have $(^{87}Sr/^{86}Sr)_i$ compositions ranging from 0.7032 to 0.7048, and εNd_i values from +0.2 to +5.3 (Wen et al., 2007; Zheng et al., 2014), and in combination with our new $(^{187}Os/^{188}Os)_i$ values suggest that these magmas were derived from the mantle in response to Neo-Tethyan subduction, with variable amounts of crustal contamination (Fig. 5-9A–D; Wen, 2007; Wang et al., 2014b).

Eastern Oligocene magmatism

Five samples of granitoid plutons from four locations in the eastern Gangdese belt (none are known to occur in the western part of the belt) have high-K calc-alkaline quartz monzonitic to granitic compositions, similar to the range of published data for these lithologies (Fig. 5-5A, B). They are somewhat more depleted in HREE relative to the Paleocene-Eocene suite ($[La/Yb]_N$ = 35.9 ± 8.5, n = 5, range = 26.5–44.2; Fig. 5-5D), and have pronounced listric-shaped normalized REE patterns that mostly lack significant negative Eu anomalies (some are positive; Fig. 5-6C). These patterns indicate fractionation of hornblende (which preferentially partitions MREE, leading to listric-shaped normalized REE patterns; Green and Pearson, 1985; Rollinson, 1993; Davidson et al., 2007; Müntener et al., 2001; Rooney et al., 2011) and suppression of plagioclase crystallization and fractionation (Naney, 1983; Ridolfi et al., 2010). In combination with the abundance of amphibole phenocrysts in these rocks, these geochemical features suggest that the Oligocene magmas were relatively hydrous (> 4 wt. % H_2O: Wang et al., 2014b).

Zircon $\delta^{18}O$ values of sample CB-5 (+5.7 ‰ and +6.3 ‰; Fig. 5-7A) and biotite (+5.0 ‰ and +5.4 ‰; Fig. 5-7B) are similar to the values from Paleocene–Eocene rocks, as are the $(^{87}Sr/^{86}Sr)_i$, εNd_i, and $(^{187}Os/^{188}Os)_i$ values (0.7062 to 0.7063, -3.4 to -2.5, and 0.224 to 0.359, respectively; Figs. 8 and 9).

Despite the compositional and isotopic similarity to the subduction-related Paleocene–Eocene rocks, the Oligocene rocks are unlikely to have been directly subduction-derived, because they formed ~25 m.y. after the onset of India–Asia collision. We suggest that they were likely derived from partial melting of subduction-modified Tibetan lower crust in a collisional setting (Hou et al., 2009; Wang et al., 2014b).

Miocene alkaline volcanic rocks

Nine samples of potassic to ultrapotassic volcanic rocks from across the Gangdese belt have high-K calc-alkaline to shoshonitic, trachyandesitic to trachydacitic compositions (Fig. 5-5A, B). They have high Sr/Y (average = 74.6 ± 33.0, range = 21.6–125.3, n = 9; Fig. 5-5C) and $[La/Yb]_N$ ratios (average = 33.9 ± 14.7, range = 19.4–61.0; Figs. 5D, 6E), with steeper normalized REE patterns from high LREE to low HREE compared with the Paleocene–Eocene and Oligocene rocks. These compositions are similar to those reported

in the literature for alkaline volcanic rocks from the western Gangdese belt (no published data are available for comparison from the eastern part of the belt; Figs. 5 and 6).

Although there is little difference between the chemical compositions of these alkaline rocks from east to west, they do show distinct isotopic compositions. Zircon and amphibole $\delta^{18}O$ values for eastern samples range from +5.0 ‰ to +6.7 ‰ (similar to the Paleocene–Eocene and Oligocene rocks), whereas zircons from the western suite have higher values (+6.9 to +8.3 ‰; Fig. 5-7A), and whole rocks and phlogopite extend this range to +11.0 ‰ (Fig. 5-7B).

Strontium, neodymium, and osmium isotopic compositions are also distinct both from the earlier igneous rocks, and by longitude. The eastern volcanic rocks have higher $(^{87}Sr/^{86}Sr)_i$ values (0.7057 to 0.7121), and lower εNd_i (-3.4 to -9.4) and $(^{187}Os/^{188}Os)_i$ values (0.156 to 0.210) compared with the older suites, while the western suite has even higher $(^{87}Sr/^{86}Sr)_i$ (0.7069 to 0.7263) and lower εNd_i values (-6.0 to -15.1), and similar $(^{187}Os/^{188}Os)_i$ ratios (0.156 to 0.182) (Figs. 7–9).

These Sr, Nd, and O isotopic data all suggest a significant crustal involvement in the petrogenesis of these alkaline magmas, particularly for the western suite, but the low Os isotopic compositions also indicate a mantle source. We thus consider that these magmas were likely derived by melting of Tibetan SCLM, with contamination by crustal melts. However, the extremely high Sr-O and low Nd isotopic compositions of the western suite extend well beyond the range of compositions thought to represent Tibetan crust in the Gangdese belt ($^{87}Sr/^{86}Sr < 0.71$ and $\varepsilon Nd > -10$; as reviewed in Zhao et al., 2009), but they are similar to the compositions of High Himalayan crystalline basement, which is commonly used as a proxy for the Indian plate lithosphere ($^{87}Sr/^{86}Sr = 0.74$ to 0.76), $\delta^{18}O$ = +10–+14 ‰, εNd = -18 to -10; France-Lanord et al., 1988; Zhao et al., 2009). We therefore propose that the western alkaline volcanic rocks include a component of melt from the underthrust Indian lithosphere

Miocene granitoid plutons

Thirteen samples of granitoid plutons from across the Gangdese belt have calc-alkaline to high-K calc-alkaline (rare shoshonitic), quartz monzonitic, granodioritic, and granitic compositions (Fig. 5-5A, B). They have high Sr/Y (average = 98.8 ± 38.9, range

= 23.9–151.0, n = 13) and $[La/Yb]_N$ ratios (average = 34.4 ± 15.6, range = 21.7–66.1, n =13) (Fig. 5-5C, D). The eastern granitoids have pronounced listric-shaped normalized REE patterns, similar to the Oligocene suite, whereas the western granitoids have steep normalized REE patterns from high LREE to low HREE (Fig. 5-6G), similar to the western alkaline volcanic rocks (Fig. 5-6E).

As for the alkaline volcanic rocks, zircon and amphibole $\delta^{18}O$ values for granitoid samples from the eastern Gangdese belt (+5.5 ‰ to +6.6 %) are similar to values from the older Paleocene–Eocene and Oligocene rocks, but the western granitoids (like the western alkaline volcanic rocks) extend to higher values (up to +8.8 ‰; Fig. 5-7).

Strontium, neodymium, and osmium isotopic ratios for the eastern granitoids are also similar to the older suites, but the western granitoids have higher $(^{87}Sr/^{86}Sr)_i$ ratios (0.7147 to 0.7165; Fig. 5-8C) and lower εNd_i values (-7.9 to -11.3; Fig. 5-8), comparable to the coeval western alkaline volcanic rocks. However, $(^{187}Os/^{188}Os)_i$ values are much higher than any of the other lithologies (0.550 to 1.035; Fig. 5-9).

We interpret these data to indicate that the eastern Miocene granitoids, like the cospatial Oligocene granitoids, were derived by partial melting of subduction-modified Tibetan lithosphere (Guo et al., 2007; Li et al., 2011; Wang et al., 2014b). In contrast, the isotopic compositions of the western granitoids suggest a similar source to the coeval and cospatial alkaline volcanic rocks, but with a higher degree of crustal contamination upon emplacement (as reflected in their crustal Os isotopic values; Fig. 5-9).

5.10 Implications for geodynamic change and metallogeny

Our new geochemical and isotopic data for Cenozoic igneous rocks from the Tibetan Gangdese belt are interpreted to reflect the diachronous transition from subduction-related to collisional magmatism, and finally to underthrusting of the Indian lithosphere.

Paleocene–Eocene intermediate-composition intrusive and volcanic rocks are calc-alkaline to high-K calc-alkaline, and have similar geochemical and isotopic compositions to normal subduction-related magmatism. They are thought to have formed during the final stages of subduction of Neo-Tethyan lithosphere, and incipient collision between the Greater Indian plate and the accretionary Eurasian margin (i.e., the Lhasa terrane of southern Tibet). These early Paleogene rocks are associated with few porphyry-type

deposits, possibly because the magmas appear to have been relatively water-poor and reduced, reflecting terminal dehydration of the subducting Neo-Tethyan slab (Wang et al., 2014b).

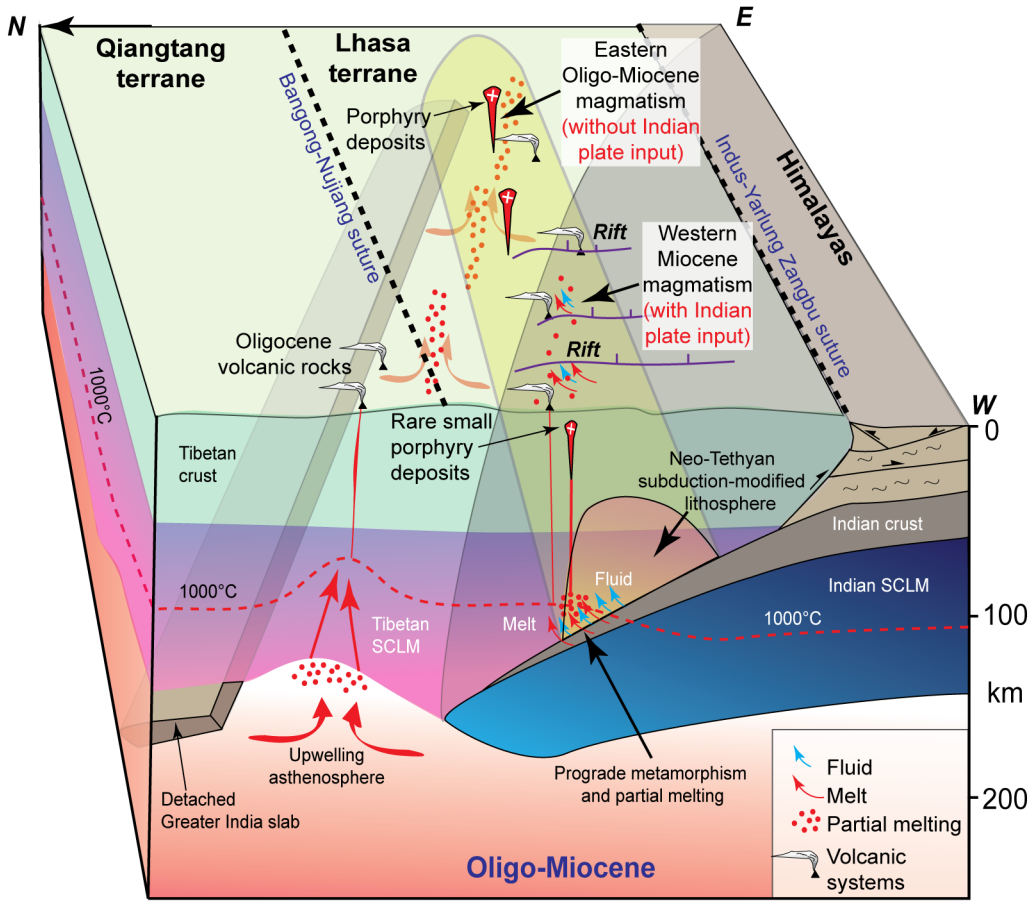

Figure 5-10. Petrogenesis of late-collisional Oligo-Miocene igneous rocks in southern Tibet. The breakoff of Greater India slab started in the west at ~25 ± 5 Ma, and the tear propagated eastward until final detachment beneath eastern Tibet at ~10 ± 5 Ma (Van der Voo et al., 1999; Replumaz et al., 2010). This breakoff event triggered upwelling of asthenospheric melts and partial melting of the Tibetan SCLM, and produced a suite of Oligo-Miocene magmatism from west to east. The following underthrusting Indian lithosphere extended more in the western Gangdese belt. Prograde metamorphism Indian lithosphere released melts ± fluids into the Tibetan SCLM, and triggered its partial melting, then derived alkaline magmas ascended through rift zones. In contrast, the eastern Gangdese belt was not fully underthrust by Indian lithosphere in the Miocene. Upwelling of asthenospheric melts interacted with subduction-modified Tibetan lithosphere, and produced continental arc-like magmas and porphyry deposit systems. Thrust systems are inferred from Yin and Harrison (2000). Depths of the Moho, Indian lithosphere–asthenosphere boundary, and Tibetan lithosphere–asthenosphere boundary

are estimated from seismic studies (Kumar et al., 2006; Zhao et al., 2010; Shokoohi Razi et al., 2014). Abbreviations: SCLM = sub-continental lithospheric mantle.

Oligocene magmatism was restricted to eastern Gangdese belt with high-K calc-alkaline granitoids, and to Qiangtang terrane with high-K calc-alkaline to shoshonitic volcanic rocks. The granitoids mostly occur as small plutons, and are compositionally similar to the earlier Paleocene–Eocene suite, but show greater fractionation of REE, higher Sr/Y and $[La/Yb]_N$ ratios, and mostly lack significant Eu anomalies. These compositions have been interpreted by Wang et al. (2014b) to reflect increasing water content in these Oligocene magmas. The rocks are isotopically similar to the Paleocene–Eocene suite, and were likely derived by partial melting of previously subduction-modified Tibetan lithosphere (Wang et al., 2014b). A few small porphyry deposits are associated with these Oligocene granitoid intrusions. The sparse alkaline volcanic rocks are barren, have moderate $(^{87}Sr/^{86}Sr)_i$ ratios (0.7060–0.7092) and negative εNd_i values (-9.2 to -3.8; Ding et al., 2003; Liu et al., 2008), and only erupted in the Qiangtang terrane (to the north of western Gangdese), which is lack of previous subduction fertilization of this part of the Tibetan lithosphere to the north of the main Cretaceous–Paleocene Gangdese arc. We suggest the alkaline volcanic magmas were derived by partial melting of enriched Tibetan SCLM during early breakoff of Greater India slab started in the western Tibet at ~25 ± 5 Ma (Fig. 5-10; Van der Voo et al., 1999; Replumaz et al., 2010).

A significant geochemical and isotopic change is observed in Miocene magmatism, which was characterized predominantly by calc-alkaline to high-K calc-alkaline plutonism in the eastern part of the Gangdese belt (east of ~89°E) and alkaline volcanism to the west (although minor high-K calc-alkaline to shoshonitic plutonism occurs in the west, and minor alkaline volcanism in the east).

The eastern calc-alkaline to high-K calc-alkaline granitoids are broadly compositionally similar to the Paleocene–Eocene and Oligocene suites, but show higher Sr/Y ratios, and are interpreted to be even more hydrous and oxidized than the earlier suites (Wang et al., 2014b, c). Isotopic compositions are also similar, but extend to higher $(^{187}Os/^{188}Os)_i$ values, which are interpreted to reflect a greater involvement of crustal melts in these relatively felsic (granodioritic to granitic) rocks, mixed into magmas derived from subduction-modified Tibetan lower crust. Their high water contents and

oxidation states have been identified as a major factor in their association with several large porphyry Cu-Mo±Au deposits in the eastern Gangdese belt (Wang et al., 2014a, b, c).

The small number of granitoid plutons that occur in the western part of the Gangdese belt (west of ~89°E) are compositionally similar to their eastern counterparts, but they are slightly more potassic, and have significantly elevated $\delta^{18}O$, $(^{87}Sr/^{86}Sr)_i$, and $(^{187}Os/^{188}Os)_i$ ratios, and lower εNd_i values. These isotopic values are interpreted to reflect a significant crustal involvement in these magmas, but more specifically, the very low εNd_i values may indicate the involvement of partial melts from the underthrust Indian crust, because such low values are not known from any potential crustal sources in the Tibetan lithosphere. Few porphyry-type deposits are known to be associated with these sparse western Miocene granitoids.

High-K calc-alkaline to shoshonitic volcanism is widespread in the western Gangdese belt, but of limited extent in the east. The few eastern volcanic rocks sampled are isotopically similar to their coeval eastern granitoids, but show slightly higher $(^{87}Sr/^{86}Sr)_i$ and lower εNd_i and $\delta^{18}O$ values. In contrast, the western alkaline volcanic rocks show the highest $(^{87}Sr/^{86}Sr)_i$ and lowest εNd_i and $\delta^{18}O$ values, and are interpreted to reflect the involvement of partial melts from the underthrust Indian lithosphere (Fig. 5-10).

Miocene porphyry-type deposits are rare in the western Gangdese belt, and we interpret the evidence for Indian plate underthrusting to indicate that this process has limited the melting of subduction-modified Tibetan lower crust, and thereby limited the generation of fertile magmas. In contrast, in the eastern part of the belt below which underthrusting had not extended in the Miocene, upwelling asthenosphere (in response to slab breakoff; Fig. 5-10) caused partial melting of these fertile lower crustal sources, and gave rise to a suite of calc-alkaline to high-K calc-alkaline granitoids with high potential to form magmatic-hydrothermal porphyry deposits.

Under more hydrous and oxidizing conditions ($\Delta FMQ > +1.5$; Wang et al., 2014c), residual sulfides from prior arc magmatism left in the mantle or deep crust may have been remobilized, releasing metals into the melts and thus making them available for formation of post-subduction porphyry systems (Chiaradia et al., 2009; Richards, 2009;

Tomkins et al., 2009; Lee et al., 2012; Richards and Mumin, 2013; Chiaradia, 2014; Wang et al., 2014c).

5.11 Conclusions

New lithogeochemical and Os-Sr-Nd-O isotopic data for Cenozoic igneous rocks collected from the 1600 km-long Gangdese magmatic belt reflect variable involvement of Indian plate lithosphere, subduction-modified Tibetan lithosphere, and asthenospheric mantle during the India–Asia collision, leading to different types of magmatism and association with porphyry Cu-Mo±Au deposits along the belt. Paleocene–Eocene magmas throughout the Gangdese belt are typical of continental arc magmas, and likely formed in the final stages of Neo-Tethyan subduction, prior to slab breakoff at ~40–38 Ma. Later Oligo-Miocene magmas show a sharp longitudinal distinction of geochemical and isotopic compositions, and association with porphyry-type mineralization. Oligo-Miocene granitoids in the eastern Gangdese belt are calc-alkaline to high-K calc-alkaline in compositions, and are characterized by similar $(^{87}Sr/^{86}Sr)_i$, εNd_i and zircon $\delta^{18}O$ values to the earlier Paleocene–Eocene igneous rocks. They were most likely derived from partial melting of subduction-modified Tibetan lithosphere (mostly lower crust). These late-collisional magmas are hydrous and oxidized, and were able to remobilize Cu, Mo, and Au from deep crustal residues of prior arc magmatism, leading to a unique association with several large porphyry Cu-Mo±Au deposits in eastern Tibet.

In contrast, Miocene high-K calc-alkaline to shoshonitic granitoids in western Tibet are characterized by crust-like $(^{187}Os/^{188}Os)_i$, high $(^{87}Sr/^{86}Sr)_i$, low εNd_i and high zircon $\delta^{18}O$ values, suggesting that these magmas involved a large component of melts ± fluids from the underthrust Indian plate, and experienced high degrees of crustal contamination during emplacement. These magmas are relatively reduced and infertile, and are only associated with one known small porphyry Cu-Mo deposit.

High-K calc-alkaline to shoshonitic volcanic rocks in the western Gangdese belt have extremely low εNd_i values (-7.1 to -17.4), crust-like zircon $\delta^{18}O$ values (+6.2–+8.8 ‰), but low, mantle-like $(^{187}Os/^{188}Os)_i$ ratios. We suggest that these magmas were derived from partial melting of the Tibetan SCLM but included ~3–25 % melts ± fluids from the underthrust Indian plate. Sparse high-K calc-alkaline to shoshonitic volcanic rocks in the

eastern Gangdese belt are characterized by moderate εNd_i values (-9.4 to -3.4), and mantle-like $(^{187}Os/^{188}Os)_i$ (0.154–0.210) and zircon $\delta^{18}O$ values (+5.0–+6.7 ‰). These magmas are thought to have been derived largely from partial melting of enriched Tibetan SCLM, and show no evidence of an Indian plate source, suggesting that underthrusting had not extended this far east by the Miocene.

5.12 References

Aitchison, J.C., Ali, J.R., and Davis, A.M., 2007, When and where did India and Asia collide: Journal of Geophysical Research, v. 112, p. B05423, doi: 10.1029/2006JB004706.

Ali, J.R., and Aitchison, J.C., 2005, Greater India: Earth-Science Reviews, v. 72, p. 169–188.

Allégre, C.J., Courtillot, V., Taponnier, P., Hirn, A., Mattauer, M., Coulon, C., Jaeger, J. J., Achache, J., Schärer, U., Marcoux, J., Burg, J. P., Girardeau, J., Armijo, R., Gaiety, C., Göpel, C., Li, T., Xiao, X., Chang, C., Li, G., Lin, B., T, J., Wang, N., Chen, G., Han, T., Wang, X., Den, W., Sheng, H., Gao, Y., Zhou, J., Qiu, H., Bao, P., Wang, S., Wang, B., Zhou, Y., and Xu, R., 1984, Structure and evolution of the Himalayan-Tibet orogenic belt: Nature, v. 307, p. 17–22.

Arculus, R., and Powell, R., 1986, Source component imixing in the regions of arc magma generation: Journal of Geophysical Research, v. 91, p. 5913–5926.

Armijo, R., Tapponnier, P., Mercier, J.L., and Han, T.L., 1986, Quaternary extension in southern Tibet: Field observations and tectonic implications: Journal of Geophysics Research, v. 9, p. 13,803–13,872.

BGMRXAR (Bureau of Geology Mineral Resources of Xizang Autonomous Region), 1993, Regional Geology of Xizang (Tibet) Autonomous Region: Geological Publishing House, Beijing, 450 p. (in Chinese with English abstract).

Black, L.P., Kamo, S.L., Allen, C.M., Davis, D., Aleinikoff, J.N., Valley, J.W., Mundil, R., Campbell, I.H., Korsch, R.J., Williams, I.S., and Foudoulis, C., 2004, Improved $^{206}Pb/^{238}U$ microprobe geochronology by the monitoring of a trace-element-related matrix effect; SHRIMP, ID-TIMS, ELA-ICP-MS and oxygen isotope documentation for a series of zircon standards: Chemical Geology, v. 205, p. 115–140.

Blisniuk, P.M., Hacker, B.R., Glodny, J., Ratschbacher, L., Bi, S.W., Wu, Z.H., McWilliams, M.O., and Calvert, A., 2001, Normal faulting in central Tibet since at least 13.5 Myr ago: Nature, v. 412, p. 628–632.

Burchfiel, B.C., Chen, Z., Royden, L.H., Liu, Y., and Deng, C., 1991, Extensional development of Gabo valley, southern Tibet: Tectonophysics, v. 194, p. 187–193.

Chan, G.H.N., Waters, D.J., Searle, M.P., Aitchison, J.C., Horstwood, M.S.A., Crowley, Q., Lo, C.H., and Chan, J.S.L., 2009, Probing the basement of southern Tibet: evidence from crustal entrained in a Miocene ultrapotassic dyke: Journal of the Geological society, London, v. 166, p. 45–52.

Chazot, G., Lowry, D., Menzies, M., and Mattey, D., 1997, Oxygen isotope compositions of hydrous and water-poor mantle peridotite: Geochimica et Cosmochimica Acta, v. 61, p. 161–169.

Chen, T., 2006, Geochemistry of the Qushui intrusive of Gangdese in Tibet and its implications for magma mixing: Unpublished Master thesis (in Chinese), China University of Geosciences, Beijing, 59 p.

Chen, L., Qin, K.Z., Li, J.X., Xiao, B., Li, G.M., Zhao, J.X., and Fan, X., 2011, Fluid Inclusion and hydrogen, oxygen, sulfur isotopes of Nuri Cu-W-Mo deposit in the southern Gangdese, Tibet: Resource Geology, v. 62, p. 42–62.

Chen, L., Qin, K.Z., Li, G.M., Li, J.X., Xiao, B., Jiang, H.Z., Zhao, J.X., Fan, X., and Jiang, S.Y., 2012, Geological and skarn mineral characteristics of Nuri Cu-W-Mo deposit in southern Gangdese, Tibet: Mineral Deposits, v. 31, p. 417–437. (in Chinese with English abstract)

Chiaradia, M., Merino, D., and Spikings, R., 2009, Rapid transition to long-lived deep crustal magmatic maturation and the formation of giant porphyry-related mineralization (Yanacocha, Peru): Earth and Planetary Science Letters, v. 288, p. 505–515.

Chiaradia, M., 2014, Copper enrichment in arc magmas controlled by overriding plate thickness: Nature Geoscience, v. 7, p. 43–46.

Chu, M.F., Chung, S.L., Song, B., Liu, D.Y., O'Reilly, S.Y., Pearson, N.J., Ji, J.Q., and Wen, D.J., 2006, Zircon U-Pb and Hf isotope constraints on the Mesozoic tectonics and crustal evolution of southern Tibet: Geology, v. 34, p. 745–748.

Chu, M.F., Wang, K.L., Griffin, W.L., Chung, S.L., O'Reilly, S.Y., Pearson, N.J., and Iizuka, Y., 2009, Apatite compositions: Tracing petrogenetic process in Transhimalayan granitoids: Journal of Petrology, v. 50, p. 1829–1855.

Chung, S.L., Chu, M.F., Zhang, Y.Q., Xie, Y.W., Lo, C.H., Lee. T.Y., Lan, C.Y., Li, X.H., Zhang, Q., and Wang, Y.Z., 2005, Tibetan tectonic evolution inferred from spatial and temporal variations in post-collisional magmatism: Earth-Science Reviews, v. 68, p. 173–196.

Clayton, R.N., and Mayeda, T.K., 1963, The use of bromine penta-fluoride in the extraction of oxygen from oxide and silicates for isotope analysis: Geochimica et Cosmochimica Acta, v. 27, p. 43–52.

Cogan, M.J., Nelson, K.D., Kidd, W.S.F., Wu, C.D., and Project INDEPTH Team, 1998, Shallow structure of the Yadong-Gulu rift, southern Tibet, from refraction analysis of Project INDEPTH common midpoint data: Tectonics, v. 17, p. 46–61.

Copley, A., Avouac, J.P., and Wernicke, B.P., 2012, Evidence for mechanical coupling and strong Indian lower crust beneath southern Tibet: Nature, v. 472, p. 79–81.

Creaser, R.A., Papanastassiou, D.A., and Wasserburg, G.J., 1991, Negative thermal ion mass spectrometry of osmium, rhenium and iridium: Geochimica Cosmochimica Acta, v. 55, p. 397– 404.

Creaser, R.A., Erdmer, P., Stevens, R.A., and Grant, S.L., 1997, Tectonic affinity of Nisutlin and Anvil assemblage strata from the Teslin tectonic zone, northern Canadian Cordillera: Constraints from neodymium isotope and geochemical evidence: Tectonics, v. 16, p. 107–121.

Creaser, R.A., Grutter, H., Carlson, J. and Crawford, B., 2004, Macrocrystal phlogopite Rb–Sr dates for the Ekati property kimberlites, Slave Province, Canada: evidence for multiple intrusive episodes in the Paleocene and Eocene: Lithos, v. 76, p. 399–414.

de Sigoyer, J., Chavagnac, V., Blichert-Toft, J., Villa, I.M., Luais, B., Guillot, S., Cosca, M., and Mascle, 2000, Dating the Indian continental subduction and collision thickening in the northwest Himalaya: Multichronology of the Tso Morari eclogites: Geology, v. 28, p. 487–490.

Deng, W.M., Huang, X., and Zhong, D., 1998, Alkali-rich porphyry and its relation with intraplate deformation of north part of Jinsha River belt in western Yunnan, China:

Science in China Series D, 41: 297–305. (in Chinese with English abstract)

Defant, M.J., and Drummond, M.S., 1990, Derivation of some modern arc magmas by melting of young subducted lithosphere: Nature, v. 347, p. 662–665.

Dickin, A.P., 2005, Radiogenic isotope geology (2nd edition): Cambridge University Press, 492 p.

Ding, L., Kapp. P., Zhong, D., and Deng, W., 2003, Cenozoic volcanism in Tibet: Evidence for a transition from oceanic to continental subduction: Journal of Petrology, v. 44, p. 1833–1865.

Dong, G.C., 2002, Linzizong volcanic rocks and implications for probing India-Eurasia collision process in Linzhou Volcanic Basin, Tibet: Unpublished Ph.D. Thesis, China University of Geosciences, Beijing, 150 p. (in Chinese with English abstract)

Dong, G.C., Mo, X.X., Zhu, D.C., Wang, L.L., Chen, T., and Li, B., 2006a, Magma mixing in middle part of Gangdese magma belt: Evidences from granitoid complex: Acta Petrologica Sinica, v.22, p. 835–844. (in Chinese with English abstract)

Dong, G.C., Mo, X.X., Zhao, Z.D., Zhu, D.C., Song, Y.T., and Wang, L., 2006b. Gabbros from southern Gangdese: Implication for mass exchange between mantle and crust: Acta Petrologica Sinica, v. 24, p. 203–210. (in Chinese with English abstract)

Du, A.D., Wu, S.Q., Sun, D.Z., Wang, S.X, Qu, W.J., Markey, R., Stein, H., Morgan, J., and Malinovskiy, D., 2004, Preparation and certification of Re-Os dating reference materials: molybdenite HLP and JDC: Geostandard and Geoanalytical Research, v. 28, p. 41–52.

England, P., and Houseman, G., 1989, Extension during active convergence, with application to the Tibetan Plateau, Journal of Geophysics Research, v. 94, p.17561–17579.

Eiler, J.M., 2001, Oxygen isotope variations of basaltic lavas and upper mantle rocks, in Valley, J.W., Cole, D.R., eds., Stable isotope geochemistry, Reviews in Mineralogy and Geochemistry, v. 43, p. 319–364.

France-Lanord, C., Sheppard, S.M.F., and Le Fort, P., 1988, Hydrogen and oxygen isotope variations in the High Himalaya peraluminous Manaslu leucogranite: Evidence for heterogeneous sedimentary source: Geochemica et Cosmochimica Acta: v. 52, p. 513–526.

Gao, Y.F, Wei, R.H, Hou, Z.Q, Tian, S.H, and Zhao, R.S., 2008, Eocene high-MgO volcanism in southern Tibet: New constraints for mantle source characteristics and deep process: Lithos, v. 105, p. 63–72.

Goldstein, S.L., O'Nions, R.K., and Hamilton, P.J., 1984, A Sm-Nd isotopic study of atmospheric dusts and particulates from major river systems: Earth and Planetary Science Letters, v. 70, p. 221–236.

Gramlich, J.W., Murphy, T.J., Garner, E.L., and Shields, W.R., 1973, Absolute isotopic abundance ratio and atomic weight of a reference sample of rhenium: Journal of Research of National Bureau of Standards, v. 77A, p. 691–698.

Guo, Z.F., Wilson, M., Zhang, M.L., Cheng, Z.H., and Zhang, L.H., 2013, Post-collisional, K-rich mafic magmatism in south Tibet: constraints on Indian slab-to-wedge transport processes and plateau uplift: Contributions to Mineralogy and Petrolgy, v. 165, p. 1311–1340.

Harris, N.B.W., Pearce, J.A., and Tindle, A.G., 1986, Geochemical characteristics of collisional-zone magmatism, in Coward, M.P., Reis, A.C., eds., Collision tectonics: Geological Society, London, Special Publications, v. 19, p. 67–81.

Hébert, R., Guilmette, C., Dostal, J., Bezard, R., Lesage, G., Bédard, É., and Wang, C.S., 2014, Miocene post-collisional shoshonites and their crustal xenoliths, Yarlung Zangbo Suture Zone southern Tibet: Geodynamic implications: Gondwana Research, v. 25, p. 1263–1271.

Hou, Z.Q., Gao, Y.F., Qu, X.M., Rui, Z.Y., and Mo, X.X., 2004, Origin of adakitic intrusives generated during mid-Miocene east-west extension in southern Tibet: Earth and Planetary Science Letters, v. 220, p. 139–155.

Hou, Z.Q., Yang, Z.M., Qu, X.M., Meng, X.J., Li, Z.Q., Beaudoin, G., Rui, Z.Y., Gao, Y.F., and Zaw, K., 2009, The Miocene Gangdese porphyry copper belt generated during post-collisional extension in the Tibetan Orogen: Ore Geology Reviews, v. 36, p. 25–31.

Hu, P., Nie, F.J., Jiang, S.H., Liu, Y., and Zhang, W.Y., 2006, Zircon SHRIMP U-Pb age of Songtuoga intrusion in Mayum gold deposit district, Xizang (Tibet) and its geological significances: Gelogical Review, v. 52, p. 276–282 (in Chinese with English abstract).

Huang, G.C., Wu, F.T., Roecker, S.W., and Sheehan, A.F., 2009, Lithospheric structure of the central Himalaya from 3-D tomographic imaging: Tectonophysics, v. 475, p. 524–543.

Huang, K., Zheng, Y., Zhang, S., Li, W., Sun, Q., Li, Q., Liang, W., Fu, Q., and Hou, Z., 2012, LA-ICP-MS zircon U-Pb dating of two types of porphyry in the Yaguila mining area, Tibet: Acta Petrologica et Mineralogica, v. 31, p. 348–360. (in Chinese with English abstract)

Inger, S., and Harris, N., 1993, Geochemical constraints on leucogranite magmatism in the Langtang valley, Nepal Himalaya: Journal of Petrology, v. 34, p. 345–368.

Irvine, T.N., and Baragar, W.R.A., 1971, A guide to the chemical classification of the common volcanic rocks: Canadian Journal of Earth Sciences, v. 8, p. 523–548.

Ji, W.Q., Wu, F.Y., Chung, S.L., Li, J.X., and Liu, C, Z., 2009, Zircon U-Pb geochronology and Hf isotopic constraints on petrogenesis of the Gangdese batholith, southern Tibet: Chemical Geology, v. 262, p. 229–245.

Kapp, P., Yin, A., Harrison, T.M., and Ding, L., 2005, Cretaceous–Tertiary shorting, basin development, and volcanism in central Tibet: GSA Bulletin, v. 117, p. 865–878.

Kapp, P., DeCelles, P.G., Leier, A.L., Fabijanic, J.M., He, S., Pullen, A., Gehrels, G.E., and Ding, L., 2007, The Gangdese retroarc thrust belt revealed: GSA Today, v. 17, p. 4–10.

Kyser, T. K., 1986, Stable isotope variations in the mantle: Mineralogical Society of America, Reviews in Mineralogy, v. 16, p. 141–164.

Kumar, P., Yuan, X., Kind, R., and Ni, J., 2006, Imaging the colliding Indian and Asian lithospheric plates beneath Tibet: Journal of Geophysical Research, v. 111, B6: doi 10.1029/2005JB003930.

Kind, R., and Yuan, X., 2010, Seismic images of the biggest crash on earth: Science, v. 329, p. 1479–1480.

Lee, H.Y., Chung, S.L., Lo, C.H., Ji, J., Lee, T.Y., Qian, Q., and Zhang, Q., 2009, Eocene Neotethyan slab breakoff in southern Tibet inferred from the Linzizong volcanic record: Tectonophysics, v. 477, p. 20–35.

Le Maitre, R.W., ed., 1989, A classification of igneous rocks and glossary of terms: Oxford, Blackwell Scientific Publications, 193 p.

Li, C., van der Hilst, R.D., Meltzer, A.S., and Engdahl, E.R., 2008, Subduction of the Indian lithophere beneath the Tibetan plateau and Burma: Earth and Planetary Science Letters, v. 274, p. 157–168.

Li, J.X., Qin, K.Z., Li, G.M., Xiao, B., Chen, L., and Zhao, J.X., 2011, Post-collisional ore-bearing adakitic porphyries from Gangdese porphyry copper belt, southern Tibet: Melting of thickened juvenile arc lower crust: Lithos, v. 126, p. 264–277.

Liang, X.F., Sandvol, E., Chen, Y.J., Hearn, T., Ni, J., Klemperer, S., Shen, Y., and Tilmann, F., 2012, A complex Tibetan upper mantle: A fragemented Indian slab and no south-verging subduction of Eurasian lithosphere: Earth and Planetary Sciences Letters, v. 333–334, p. 101–111.

Liu, C.Z., Wu, F.Y., Chung, S.L., and Zhao, Z.D., 2012, Fragments of hot and metasomatized mantle lithosphere in Middle Miocene ultrapotassic lavas, southern Tibet: Geology, v. 39, p. 923–926.

Liu, D., Zhao, Z.D., Zhu, D.C., Niu, Y.L., and Harrison, T.M., 2014, Zircon xenocrysts in Tibetan ultrapotassic magmas: Imaging the deep crust through time: Geology, v. 42, p. 43–46.

Liu, S., Hu, R.Z., Feng, C.X., Zou, H.B., Li, C., Chi, G.X., Peng, J.T., Zhong, H., Qi, L., Qi, Y.Q., and Wang, T., 2008, Cenozoic high Sr/Y volcanic rocks in the Qiangtang terrane, northern Tibet: geochemical and isotopic evidence for the origin of delaminated lower continental melts: Geological Magazine, v. 145, p. 463–474.

Luck, J.M., and Allègre, C.J., 1983, ^{187}Re–^{187}Os systematics in meteorites and Cosmochemical consequence: Nature, v. 302, p. 130–132.

Martin, H., Adakitic magmas: modern analogues of Archaean granitoids: Lithos, v. 46, p. 411–429.

Mattey, D.P., Lowry, D., Macpherson, C.G., and Chazot, G., 1994a, Oxygen isotope compositions of mantle minerals by laser fluorination analysis: homogeneity in peridotite, heterogeneity in eclogites: Mineralogical Magazine, v. 58A, p. 573–574.

Mattey, D., Lowry, D., and Macpherson, C., 1994b, Oxygen isotope composition of mantle peridotite: Earth and Planetary Science Letters, v. 128, p. 231–241.

Meisel, T., Walker, R.J., Irving, A.J., and Lorand, J.P., 2001, Osmium isotopic compositions of mantle xenoliths: A global perspective: Geochimica et Cosmochimica

Acta, v. 65, p. 1311–1323.

Miller, C., Schuster, R., Klotzli, U., Mair, V., Frank, W., and Purtscheller, F., 1999, Post-collisional potassic and ultrapotassic magmatism in SW Tibet: geochemical Sr–Nd–Pb–O isotopic constraints for mantle source characteristics and petrogenesis: Journal of Petrology, v. 40, p. 1399–1424.

Mo, X.X., Dong, G.C., Zhao, Z.D., Guo, T.Y., Wang, L.L., and Chen, T., 2005, Timing of magma mixing in the Gangdise magmatic belt during the India-Asia collision: Zircons SHRIMP U-Pb dating: Acta Geologica Sinica, v. 79, p. 66–76.

Mo, X.X., Hou, Z.Q., Niu, Y.L., Dong, G.C., Zhao, Z.D. and Yang, Z.M., 2007, Mantle contributions to crustal thickening during continental collision: Evidence from Cenozoic igneous rocks in southern Tibet: Lithos, v. 96, p. 225–242.

Mo, X.X., Niu, Y.L., Dong, G.C., Zhao, Z.D., Hou, Z.Q., Zhou, S., and Ke, S., 2008, Contribution of syncollisional felsic magmatism to continental crust growth: A case study of the Paleogene Linzizong volcanic succession in southern Tibet: Chemical Geology, v. 250, p. 49–67.

Pan, G.T., Ding, J., Yao, D., and Wang, L., 2004, The Guide Book of 1:1,500,000 Geologic map of the Qinghai-Xizang (Tibet) Plateau and adjacent Areas: Chengdu Cartographic Publishing House, 44 p. (in Chinese)

Pearce, J.A., 1982, Trace element characteristics of lavas from destructive plate boundaries, in Thorp, R.S., eds., Andesites: Orogenic Andesites and Related Rocks, John Wiley and Sons, New York, 724 p.

Perfit, M.R., Gust, D.A., Bence, A.E., Arculus, R.J., and Taylor, S.R., 1984, Chemical characteristics of island arc basalts: implication for mantle sources: Chemical Geology, v. 30, p. 227–256.

Replumaz, A., Negredo, A.M., Villaseñor, A., and Guillot, S., 2010, Indian continental subduction and slab breakoff during Tertiary collision: Terra Nova, v. 22, p. 290–296.

Royden, L.H., Burchfiel, B.C., King, R.W., Wang, E., Chen, Z.L., Shen, F., and Liu, Y.P., 1997, Surface Deformation and lower crustal flow in eastern Tibet: Science, v. 276, p. 788–790.

Rickwood, P.C., 1989, Boundary lines within petrologic diagrams which use oxides of major and minor elements: Lithos, v. 22, p. 247–263.

Schmidberger, S.S., Heaman, L.M., Simonetti, A., Creaser, C.A., and Whiteford, S., 2007, Lu-Hf, in-situ Sr and Pb isotope and trace element systematics for mantle eclogites from the Diavik diamond mine: Evidence for Paleoproterozoic subduction beneath the Slave craton, Canada: Earth and Planetary Science Letters, v. 254, p. 55–68.

Shokoohi Razi, A., Levin, V., Roecker, S.W., and Huang G.D., 2014, Crustal and uppermost mantle structure beneath western Tibet using seismic traveltime tomography: Geochemistry, Geophysics, Geosystems, DOI 10.1002/2013GC005143

Shirey, S.B., and Walker, R.J., 1998, The Re-Os isotope system in cosmochemistry and high temperature geochemistry: Annual Reviews of Earth and Planetary Sciences: v. 26, p. 423–500.

Stern, R.A., and Ickert, R.B., 2010, Zircon oxygen isotopes by SIMS: Performance evaluation of the Canadian IMS1280: Geochimica et Cosmochimica Acta, v. 74, A993.

Sun, S.S., and McDonough, W.F., 1989, Chemical and isotopic systematics of oceanic basalts: Implications for mantle composition and processes: Geological Society of London Special Publication, v. 42: p. 313–345.

Tafti, R., 2011, Metallogeny, geochronology and tectonic setting of the Gangdese belt, southern Tibet, China: Unpublished Ph.D. thesis, University of British Columbia, Canada, 451 p.

Tanaka, T., Togashi, S., Kamioka, H., Amakawa, H., Kagami, H., Hamamoto, T., Yuhara, M., Orihashi, Y., Yoneda, S., Shimizu, H., Kunimaru, T., Takahashi, K., Yanagi, T., Nakano, T., Fujimaki, H., Shinjo, R., Asahara, Y., Tanimizu, M., and Dragusanu, C., 2000, JNdi-1; a neodymium isotopic reference in consistency with LaJolla neodymium: Chemical Geology, v. 168, p. 279–281.

Tapponnier, P., Xu, Z.Q., Roger, F., Meyer, B., Arnaud, N., Wittlinger, G., and Yang, J.S., 2001, Oblique stepwise rise and growth of the Tibet plateau: Science, v. 294, p. 1671–1677.

Tomkins, A.G., Weinberg, R.F., and McFarlane, C.R.M., 2009, Preferential magma extraction from K- and metal-enriched source regions in the crust: Mineralium Deposita, v. 44, p. 171–181.

Turner, S., Arnaud, N., Liu, J., Rogers, N., Hawkesworth, C., Harris, N. and Kelley, S., 1996, Post-collision, shoshonitic volcanism on the Tibetan Plateau: implications for convective thinning of the lithosphere and the source of ocean island basalts: Journal of Petrology, v. 37, p. 45–71.

Unterschutz, J.L.E., Creaser, R.A., Erdmer, P., Thompson R.I., and Daughtry, K.L., 2002, North American margin origin of Quesnel terrane strata in the southern Canadian Cordillera: Inferences from geochemical and Nd isotopic characteristics of Triassic metasedimentary rocks: Geological Society of America Bulletin, v. 114, p. 462–475.

van Hinsbergen, D.J.J., Lippert, P.C., Dupont-Nivet, G., McQuarrie, N., Doubrovine, P.V., Spakman, W., and Torsvik, T.H., 2012, Greater India basin hypothesis and a two-stage Cenozoic collision between India and Asia: Proceedings of the National Academy of Science of the United States of America, v. 20, p. 7659–7664.

Valley, J.W., Kinny, P.D., Schulze, D.J., Spicuzza, M.J., 1998, Zircon megacrysts from kimberlite: oxygen isotope variability among mantle melts: Contributions to Mineralogy and Petrology, v. 133, p. 1–11.

Valley, J.W., Lackey, J.S., Cavosie, A.J., Clechenko, C.C., Spicuzza, M.J., Basei, M.A.S., Bindeman, I.N., Ferreira, V.P., Sial, A.N., King, E.M., Peck, W.H., Sinha, A.K., and Wei, C.S., 2005, 4.4 billion years of crustal maturation: oxygen isotope ratios of magmatic zircon: Contributions to Mineralogy and Petrology, v. 150, p. 561–580.

Völkening, J., Walczyk, T., and Heumann, K.G., 1991, Osmium isotope ratio determinations by negative thermal ion mass spectrometry: International Journal of Mass Spectrometry and Ion Processes, v. 105, p. 147–159.

Wang, R., Richards, J.P., Hou, Z.Q., and Yang, Z.M., 2014a, Extent of underthrusting of the Indian plate beneath Tibet controlled the distribution of Miocene porphyry Cu–Mo ± Au deposits: Mineralium Deposita, v. 49, p. 165–173. DOI 10.1007/s00126-013-0507-y.

Wang, R., Richards, J.P., Hou, Z.Q., Yang, Z.M., DuFrane, S.A., 2014b, Increased magmatic water content–the key to Oligo-Miocene porphyry Cu–Mo ± Au formation in the eastern Gangdese belt, Tibet: Economic Geology, in press.

Wang, R., Richards, J.P., Hou, Z.Q., Yang, Z.M., Gou, Z.B., and DuFrane, S.A., 2014c, Increasing magmatic oxidation state from Paleocene to Miocene in the eastern Tibetan Gangdese belt: Implication for collision-related porphyry Cu–Mo±Au mineralization: Economic Geology, in press.

Wang, S.F., Wang, C., Phillips, R.J., Murphy, M.A., Fang, X.M., and Yue, Y.H., 2012a, Displacement along the Karakoram fault, NW Himalaya, estimated from LA-ICP-MS U-Pb dating of offset geologic markers: Earth and Planetary Sciences Letters, v. 337–338, p. 156–163.

Wang, Z.H, Liu, Y.L., Liu, H.F., Guo, L.S., Zhang, J.S., and Xu, K.F., 2012b, Geochronology and geochemistry of the Bangpu Mo-Cu porphyry ore deposit, Tibet: Ore Geology Review, v. 46, p. 95–105.

Wasserburg, G.J., Jacobsen, S.B., DePaolo, D.J., McCulloch, M.T., and Wen, T., 1981, Precise determination of Sm/Nd ratio, Sm, Nd isotopic abundances in standard solutions: Geochimica et Cosmochimica Acta, v. 45, p. 2311–2323.

Wen, D.R., 2007, The Gangdese batholith, Southern Tibet: Ages, geochemical characteristics and petrogenesis: Unpublished Ph.D. thesis, National Taiwan University, 120 p.

White, L.T., Ahmad, T., Ireland, T.R., Lister, G.S., and Forster, M.A., 2011, Deconvolving episodic age spectra from zircons of the Ladakh batholith, northwest Indian Himalaya: Chemical Geology, v. 289, p. 179–196.

Williams, H.M., 2000, Magmatic and tectonic evolution of Southern Tibet and the Himalaya: Ph.D. thesis, The Open University, 329 p.

Williams, H.M., Turner, S.P., Pearce, J.A., Kelley, S.P., and Harris, N.B.W., 2004, Nature of the source regions for post-collisional, potassic magmatism in southern and northern Tibet from geochemical variations and inverse trace element modeling: Journal of Petrology, v. 45, p. 555–607.

Widow, E., Hoernle, K.A., Shirey, S.B., and Schmincke, H.U., Os isotope systematics in the Canary Islands and Madeira: Lithospheric contamination and mantle plume signatures: Journal of Petrology, v. 40, p. 279–296.

Wu, S., Zheng, Y.Y., Sun, X., Liu, S.A., Geng, R.R., You, Z.M., Ouyang, H.T., Lei, D., and Zhao, Z.Y., 2014, Origin of the Miocene porphyries and their mafic microgranular

enclaves from Dabu porphyry Cu-Mo deposit, southern Tibet: implications for magma mixing/mingling and mineralization: International Geology Review: v, 56, p. 571–595.

Yang, Z.M., 2008, The Qulong giant porphyry copper deposit in Tibet: Magmatism and mineralization: Unpublished Ph.D. thesis, Institute of Geology Chinese Academy of Geological Sciences, Beijing, 144 p. (in Chinese with English abstract).

Yang, Z.M., Hou, Z.Q., White, N.C., Chang, Z.S., Li, Z.Q., and Song, Y.C., 2009, Geology of the post-collisional porphyry copper-molybdenum deposit at Qulong, Tibet: Ore Geology Reviews, v. 36, p. 133–159.

Yin, A., and Harrison, T.M., 2000, Geologic evolution of the Himalayan-Tibetan orogen: Annual Review of Earth and Planetary Sciences, v. 28, p. 211–280.

Ying, L.J., Wang, C.S., Tang, J.X., Wang, D.H., Qu, W.J., and Li, C., 2014, Re-Os systematics of sulfides (chalcopyrite, bornite, pyrite and pyrrhotite) from the Jima Cu-Mo deposit of Tibet, China: Journal of Asian Earth Sciences, v. 79, p. 497–506.

Yu, F., Hou, Z.F., Zhao, Z.D., Zheng, Y.C., Li, Q.Y., and Duan, L.F., 2013, Geochemistry and origin of Yare complex in western Tibet: constraints from Zircon U-Pb and Hf-O isotopes: 2013's National Symposium on Petrology and Geodynamics Abstract, p. 521–522.

Zhang, S., Zheng, Y., Huang, K., Li, W., Sun, Q., Li, Q., Fu, Q., and Liang, W., 2012, Re-Os dating of molybdenite from Nuri Cu-W-Mo deposit and its geological significance: Mineral deposits, v. 31, p. 337–346. (in Chinese with English abstract)

Zhang, Z.M., Dong, X., Santosh, M., and Zhao, G.C., 2013, Metmorphism and tectonic evolution of the Lhasa terrane, Central Tibet: Gondwana Research, v. 25, p. 170–189.

Zhao, J., Yuan, X., Liu, H., Kumar, P., Pei, S., Kind, R., Zhang, Z., Teng, J, Ding, L., Gao, X., Xu, Q., and Wang, W., 2010, The boundary between the Indian and Asian tectonic plates below Tibet: Proceedings of the National Academy of Science of the United States of America, v. 107, p. 11229–11233.

Zhao, J.X., Qin, K.Z., Li, G.M., Li, J.X., Xiao, B., and Chen, L., 2011, Geochemistry and petrogenesis of granitoids at Sharang Eocene porphyry Mo deposit in the main-stage of India-Asia continental collision, northern Gangdese, Tibet: Resource Geology, v. 62, p. 84–98.

Zhao, J.X., Qin, K.Z., Li, G.M., Li, J.X., Xiao, B., Chen, L., Yang, Y.H., Li, C., and Liu, Y.S., 2014, Collision-related genesis of the Sharang porphyry molybdenum deposit, Tibet: Evidence from zircon U-Pb ages, Re-Os ages and Lu-Hf isotopes: Ore Geology Review, v. 56, p. 312–326.

Zhao, Z.D., Mo, X.X., Dilek, Y, Niu, Y.L., DePaolo, D.J., Robinson, P., Zhu, D.C., Sun, C.G., Dong, G.C., Zhou, S., Luo, Z.H., and Hou, Z.Q., 2009, Geochemical and Sr-Nd-Pb-O isotopic compositions of the post-collisional ultrapotassic magmatism in SW Tibet: Petrogenesis and implications for India-continental subduction beneath southern Tibet: Lithos, v. 113, p. 190–212.

Zheng, Y.C., Hou, Z.Q., Li, W., Liang, W., Huang, K.X., Li, Q.Y., Sun, Q.Z., Fu, Q., and Zhang, S., 2012, Petrogenesis and geological implications of the Oligocene Chongmuda-Mingze adakite-like intrusions and their mafic enclaves, southern Tibet: Journal of Geology, v. 120, p. 647–669.

Zheng, Y.C., Hou, Z.Q., Gong, Y.L., Liang, W., Sun, Q.Z., Zhang, S., Fu, Q., Huang, K.Q., Li, Q.X., and Li, W., 2014, Petrogenesis of Cretaceous adakite-like intrusions of the Gangdese plutonic belt, southern Tibet: implications for mid-ocean ridge subduction and crustal growth: Lithos, doi: 10.1016/j.lithos.2013.12.013

Zheng, Y.Y., Duo, J., Cheng, S.B., Gao, S.B., and Dai, F.H., 2007, Progress in porphyry copper exploration from the Gangdise belt, Tibet, China: Frontier of Earth Science in China, v. 1, p. 226–232.

Zheng, Y.Y., Sun, X., Gao, S.B., Zhao, Z.D., Zhang, G.Y., Wu, S., You, Z.M., and Li, J.D., 2014, Multiple mineralization events at the Jiru porphyry copper deposit, southern Tibet: Implications for Eocene and Miocene magma sources and resource potential: Journal of Asian Earth Sciences, v. 79, p. 842–857.

Zhou, L.M., 2012, Research of Re-Os isotope system in intermediate–acidic rocks and the application in Tibetan plateau: Chinese Academy of Geological Science, Ph.D. thesis, 111 p. (in Chinese with English abstract)

Zhou, L.M., Gao, B.Y., Wang, L.B., Li. C., Qu, W.J., Hou, Z.Q., and Du, A.D., 2012, Improvements on the separation method of Osmium by direct distillation in Carius Tube: Rock and Mineral Analysis, v. 31, p. 413–418 (in Chinese with English abstract).

Zhou, S., Mo, X.X., Zhao, Z.D., Qiu, R.Z., Zhang, S.Q., and Guo, T.Y., 2004, ^{40}Ar–^{39}Ar geochronology of Yangying post-collisional volcanic rock south Tibet and its geological significance: Progress in Natural Sciences, v. 12, p. 1411–1488.

Zhou, S., Mo, X.X., Zhao, Z.D., Qiu, R.Z., Niu, Y.L., Guo, T.Y., and Zhang, S.G., 2009, $^{40}Ar/_{39}Ar$ geochronology of post-collisional volcanism in the middle Gangdese belt, southern Tibet: Journal of Asian Earth Sciences, v. 37, p. 246–258.

Zhu, D.C., Mo, X.X., Niu, Y.L., Zhao, Z.D., Wang, L.Q., Liu, Y.S., and Wu, F.Y., 2009, Geochemical investigation of Early Cretaceous igneous rocks along an east-west traverse throughout the central Lhasa Terrane, Tibet: Chemical Geology, v. 268, p. 298–312.

Zhu, D.C., Mo, X.X., Zhao, Z.D., Niu, Y.L., Wang, L.Q., Chu, Q.H., Pan, G.T., Xu, J.F., and Zhou, C.Y., 2010, Presence of Permian extension- and arc-type magmatism in southern Tibet: Petrogeographic implications: Geological Society of America Bulletin, v. 122, p. 979–993.

Zhu, D.C., Zhao, Z.D., Niu, Y.L., Mo, X.X., Chung, S.L., Hou, Z.Q., Wang, L.Q., and Wu, F.Y., 2011, The Lhasa terrane: Record of a microcontinent and its histories of drift and growth: Earth and Planetary Science Letters, v. 301, p. 241–255.

Zhu, D.C., Zhao, Z.D., Niu, Y.L., Dilek, Y., Hou, Z.Q. and Mo, X.X., 2013, The origin and pre-Cenozoic evolution of the Tibetan Plateau: Gondwana Research, v. 23, p. 1429–1454.

Chapter 6
Conclusions

6.1 Conclusion

Significant porphyry Cu-Mo±Au mineralization is restricted both in space (east of 89°E) and time (Oligo-Miocene) in the Gangdese belt, south Tibet. There are two major conclusions from this study: (1) there was an increase in magmatic oxidation state and water content from the Paleocene to the Miocene in the eastern Gangdese belt (to the east ~89°E); (2) the extent of underthrusting of the Indian plate beneath Tibet controlled the distribution of Miocene porphyry Cu-Mo±Au deposits in the 1600 km long Gangdese magmatic belt.

Paleocene–Eocene igneous rocks in the eastern Gangdese magmatic belt have intermediate $[La/Yb]_N$ ratios (average = 12.0 ± 8.6, n = 150), intermediate-to-low Sr/Y ratios (mostly <40), and negative Eu anomalies (average = 0.76 ± 0.19, n = 150), which suggest that mineral fractionation of these magmas was dominated by early pyroxene and plagioclase. These magmas were also less oxidized, characterized by low Ce^{4+}/Ce^{3+} ratios (mostly < 50, average = 25.7 ± 18.4, n = 26) and Eu_N/Eu_N* ratios (mostly < 0.4, average = 0.35 ± 0.19, n = 26), low to intermediate whole-rock Fe^{3+}/Fe^{2+} ratios (0.28 to 0.39, near the FMQ buffer), and low ΔFMQ values (average = -0.2 ± 0.8, n = 4). These fO_2 indicators suggest that the Paleocene–Eocene magmas were weakly oxidized to moderately reduced, with ΔFMQ < +1. Amphibole ΔFMQ values (average = ΔFMQ+1.6 ± 0.2, n = 40) are likely overestimates of original magmatic fO_2 in the Paleocene–Eocene suite, and the suggested fO_2 range was below ΔFMQ+1. Paleocene–Eocene magmas throughout the Gangdese belt show continental arc characteristics similar to earlier Cretaceous arc magmas. They formed in the final stages of Neo-Tethyan subduction prior to slab breakoff at ~40–38 Ma.

In contrast, Oligo-Miocene granitoids in the eastern Gangdese belt have higher $[La/Yb]_N$ (average = 32.2 ± 12.0, n = 128) and Sr/Y ratios (mostly >40). Least evolved (intermediate compositions) rocks in the Oligo-Miocene have much higher Sr contents and lower Y contents than equivalent Paleocene–Eocene rocks, suggesting early hornblende fractionation and minor or delayed plagioclase fractionation. Consistent with this interpretation is the fact that amphibole is a common phenocryst phase in the younger granitoids, but is relatively rare and restricted to the groundmass or as late replacements of earlier pyroxene in the Paleocene–Eocene rocks. We interpret these textures and geochemical evidence to indicate that the Oligo-Miocene magmas

were more hydrous than the Paleocene–Eocene magmas. The Oligocene magmas were also somewhat more oxidized. The zircon Ce^{4+}/Ce^{3+} and Eu_N/Eu_N* ratios are intermediate between Paleocene–Eocene and Miocene values: average Ce^{4+}/Ce^{3+} = 50.1 ± 20.5, n = 5; average Eu_N/Eu_N* = 0.36 ± 0.14, n = 5. Assuming that amphibole ΔFMQ values (average = ΔFMQ+2.6 ± 0.1, n = 7) were overestimated by up to one log unit, the suggested fO_2 of Oligocene magmas was above ΔFMQ+1.

In comparison, the Miocene magmas were significantly more oxidized, with higher zircon Ce^{4+}/Ce^{3+} and Eu_N/Eu_N* ratios (Ce^{4+}/Ce^{3+} = 32.3–141.9, average = 74.3 ± 30.1, n = 33; Eu_N/Eu_N* = 0.36–0.87; average = 0.63 ± 0.12, n = 33), and high ΔFMQ values (average = +1.8 ± 0.8, n = 6) estimated from magnetite–ilmenite mineral pairs. Early-stage amphiboles record an average ΔFMQ of +2.5 ± 0.2 (n = 58). Considering systematically higher fO_2 estimates (up to one log unit) from amphibole compositions, we nevertheless suggest that the Miocene magmas were more oxidized than either the Paleocene–Eocene or Oligocene suites, with ΔFMQ > +1.5.

Thus, we conclude that there was an increase in magmatic oxidation state and water content from the Paleocene to the Miocene in the eastern Gangdese belt. This increase correlates with increased fertility of these magmas, culminating in the formation of large porphyry deposits in the Miocene. The changes of magmatic oxidation state are thought to be related to fundamental changes in the sources of magmas with time throughout the collisional orogen. Detachment of the Greater India slab at ~25 Ma triggered upwelling of asthenospheric melt, which interacted with the subduction-modified Tibetan lithosphere and triggered partial melting. From ~25 Ma to ~15 Ma in the eastern Gangdese belt, magmas evolved to more silica-rich compositions with high Sr/Y ratios, and low Y contents. These features are interpreted to reflect amphibole fractionation from hydrous magmas. In addition, extensive mineral fractionation in the Miocene also gave rise to evolved hydrous melts with high oxidation state. Such magmatic characteristics are favorable for the subsequent formation of magmatic–hydrothermal porphyry Cu-Mo±Au deposits. We suggest that residual sulfides from prior Gangdese arc magmatism may have been remobilized during Miocene magmagenesis in the deep crust under these more hydrous and oxidizing conditions (ΔFMQ > +1.5). Cu, Mo, and Au were released into the melts, which generated porphyry Cu-Mo±Au deposits upon emplacement in the upper crust.

Mineralogical, lithogeochemical and Os-Nd-O isotope data for Cenozoic igneous rocks collected from the 1600 km-long Gangdese magmatic belt reflect variable involvement of Indian

plate lithosphere, subduction-modified Tibetan lithosphere, and asthenospheric mantle during magmagenesis. These variations are reflected in the differing metallogenic potential of these igneous rocks. Following Oligo-Miocene magmas show a sharp longitudinal distinction of geochemical and isotopic compositions, and association with porphyry-type mineralization. Oligo-Miocene granitoids in the eastern Gangdese belt are calc-alkaline to high-K calc-alkaline in compositions, and characterized by similar εNd_i and zircon $\delta^{18}O$ values to the earlier Paleocene–Eocene igneous rocks. They were most likely derived from partial melting of subduction-modified Tibetan lithosphere (mostly lower crust). Therefore, they have unique association with several large porphyry Cu-Mo±Au deposits in southern Tibet. In contrast, western Miocene alkaline granitoids are characterized by low εNd_i and high zircon $\delta^{18}O$ values, suggesting involvement of Indian lithosphere, but limited partial melting of subduction-modified Tibetan lithosphere. The magmas are reduced and barren, and only one small porphyry Cu-Mo deposit is known to be associated with this western suite. Sparse alkaline volcanic rocks in the eastern Gangdese belt are characterized by moderate εNd_i values (-9.4 to -3.4), low $(^{187}Os/^{188}Os)_i$ ratios (0.154–0.210), and low zircon $\delta^{18}O$ values (5.0–6.7 ‰), which indicate that these magmas were derived from partial melting of the Tibetan SCLM. In contrast, potassic volcanic rocks in the western Gangdese belt have extremely low εNd_i values (-17.5 to -6.0) and higher crustal-like zircon $\delta^{18}O$ values (6.2–8.8 ‰), suggesting that these magmas were derived from partial melting of the Tibetan SCLM but included ~3–25 % melts ± fluids from the underthrust Indian plate.

6.2 Future research

My completed studies were mostly based on indirect geochemical and mineralogical methods. In addition to magmatic water content and oxidation state, the concentrations of other components like S, Cl, alkalis and the ore metals themselves are also critical for the formation of porphyry Cu deposits. Studies on these components will be able to reconstruct the evolution of the concentrations of key ore-forming components in Gangdese systems before and during the ore-forming events, thereby providing important insights into petrogenetic processes ultimately leading to ore generation.

Appendices

Table A1: U-Pb laser-ablation multicollector inductively coupled plasma–mass spectrometer (LA-MC-ICP-MS) analytical data for intrusive rock samples from the Gangdese belt

Sample name	^{206}Pb (cps)	^{204}Pb (cps)	^{207}Pb/^{206}Pb	2 σ	^{207}Pb/^{235}U	2 σ	^{206}Pb/^{238}U	2 σ	^{207}Pb*/ ^{206}Pb* age (Ma)	2 σ	^{207}Pb*/ ^{235}U age (Ma)	2 σ	^{206}Pb*/ ^{238}U age (Ma)	2 σ
JR-11														
JR11-1	182646	233	0.04896	0.00097	0.03921	0.00342	0.00581	0.00049	146	46	39	3	37	3
JR11-2	38763	220	0.05256	0.00257	0.04424	0.00337	0.00610	0.00036	310	108	44	3	39	2
JR11-3	22903	199	0.05041	0.00170	0.03975	0.00273	0.00572	0.00034	214	76	40	3	37	2
JR11-4	61508	199	0.04987	0.00118	0.04161	0.00202	0.00605	0.00026	189	54	41	2	39	2
JR11-5	37445	167	0.04768	0.00115	0.03828	0.00243	0.00582	0.00034	84	56	38	2	37	2
JR11-6	120511	177	0.04730	0.00065	0.03570	0.00191	0.00547	0.00028	64	32	36	2	35	2
JR11-7	31330	166	0.04540	0.00128	0.03491	0.00193	0.00558	0.00026	-34	67	35	2	36	2
JR11-8	71777	158	0.05037	0.00097	0.04028	0.00215	0.00580	0.00029	212	44	40	2	37	2
JR11-9	52930	170	0.04447	0.00090	0.03574	0.00217	0.00583	0.00033	-85	49	36	2	37	2
JR11-10	35136	137	0.04287	0.00126	0.03256	0.00163	0.00551	0.00022	-175	72	33	2	35	1
JR11-11	75005	173	0.04972	0.00108	0.04170	0.00223	0.00608	0.00030	182	50	41	2	39	2
JR11-12	64335	129	0.04684	0.00087	0.03482	0.00283	0.00539	0.00043	41	44	35	3	35	3
JR11-13	12720	113	0.04148	0.00202	0.03715	0.00271	0.00650	0.00035	-258	119	37	3	42	2
JR11-14	29501	104	0.04458	0.00140	0.03190	0.00543	0.00519	0.00087	-79	75	32	5	33	6
JR11-15	68068	95	0.04766	0.00074	0.03719	0.00246	0.00566	0.00036	82	37	37	2	36	2
JR11-16	12743	81	0.02943	0.00299	0.02534	0.00277	0.00625	0.00025	-1219	292	25	3	40	2
JR11-17	40277	77	0.04093	0.00115	0.03321	0.00136	0.00588	0.00018	-292	70	33	1	38	1
JR11-18	129622	64	0.04599	0.00059	0.03630	0.00154	0.00572	0.00023	-3	31	36	2	37	1
JR11-19	22472	47	0.03660	0.00216	0.02882	0.00256	0.00571	0.00038	-586	153	29	3	37	2
JR11-20	15032	54	0.04301	0.00742	0.03821	0.00683	0.00644	0.00030	-167	382	38	7	41	2
JR11-21	35878	97	0.05104	0.00345	0.04346	0.00492	0.00617	0.00056	243	149	43	5	40	4
JR11-23	18439	40	0.03754	0.00293	0.03421	0.00330	0.00661	0.00038	-518	197	34	3	42	2
JR11-24	57155	56	0.04471	0.00099	0.03572	0.00187	0.00579	0.00028	-71	53	36	2	37	2
JR11-25	70592	26	0.04359	0.00092	0.03326	0.00142	0.00553	0.00021	-134	51	33	1	36	1
JR11-27	11680	26	0.01935	0.00561	0.01654	0.00488	0.00620	0.00033	-2785	1019	17	5	40	2
JR11-28	46762	19	0.04205	0.00159	0.03218	0.00172	0.00555	0.00021	-223	93	32	2	36	1
JR11-29	14480	25	0.02368	0.00461	0.01993	0.00397	0.00610	0.00026	-1955	612	20	4	39	2
JR11-30	46208	29	0.03859	0.00131	0.02991	0.00151	0.00562	0.00021	-445	87	30	1	36	1
WR-12-21														
WR1221-21	23585	258	0.04863	0.00109	0.04225	0.00157	0.00630	0.00019	130	52	42	2	40	1
WR1221-20	55307	297	0.04804	0.00100	0.04199	0.00143	0.00634	0.00017	101	48	42	1	41	1
WR1221-18	37293	273	0.04795	0.00080	0.04254	0.00151	0.00643	0.00020	97	39	42	1	41	1
WR1221-14	34419	259	0.04941	0.00101	0.04447	0.00170	0.00653	0.00021	167	47	44	2	42	1
WR1221-11	30304	278	0.04970	0.00091	0.04479	0.00162	0.00654	0.00020	181	42	44	2	42	1
WR1221-17	56190	294	0.04886	0.00146	0.04406	0.00186	0.00654	0.00020	141	69	44	2	42	1
WR1221-08	37063	269	0.04857	0.00079	0.04383	0.00152	0.00654	0.00020	127	38	44	1	42	1
WR1221-12	30399	250	0.04903	0.00085	0.04425	0.00165	0.00655	0.00022	149	40	44	2	42	1
WR1221-01	61314	316	0.04826	0.00081	0.04377	0.00145	0.00658	0.00019	112	39	43	1	42	1
WR1221-13	26071	292	0.05448	0.00315	0.04967	0.00339	0.00661	0.00024	391	125	49	3	42	2
WR1221-02	157403	280	0.04750	0.00053	0.04378	0.00134	0.00668	0.00019	74	26	44	1	43	1
WR1221-04	25307	304	0.05014	0.00113	0.04636	0.00168	0.00671	0.00019	201	52	46	2	43	1

WR1221-16	73101	280	0.04863	0.00109	0.04503	0.00157	0.00672	0.00018	130	52	45	2	43	1
WR1221-10	29573	279	0.04931	0.00091	0.04596	0.00170	0.00676	0.00022	162	43	46	2	43	1
WR1221-07	49750	286	0.04828	0.00075	0.04502	0.00151	0.00676	0.00020	113	36	45	1	43	1
WR1221-05	32967	290	0.04840	0.00081	0.04534	0.00148	0.00679	0.00019	119	39	45	1	44	1
WR1221-06	32507	310	0.04986	0.00133	0.04703	0.00188	0.00684	0.00020	188	61	47	2	44	1
WR1221-19	17494	284	0.05022	0.00176	0.04889	0.00241	0.00706	0.00024	205	80	48	2	45	2
WR-12-11														
WR1211-19	163075	491	0.04882	0.00063	0.05687	0.00212	0.00845	0.00030	139	30	56	2	54	2
WR1211-12	53270	458	0.04794	0.00092	0.05586	0.00253	0.00845	0.00035	96	45	55	2	54	2
WR1211-18	62306	486	0.04914	0.00103	0.05729	0.00267	0.00846	0.00035	154	48	57	3	54	2
WR1211-08	63946	484	0.04944	0.00127	0.05778	0.00280	0.00848	0.00035	169	59	57	3	54	2
WR1211-25	82240	481	0.04893	0.00088	0.05726	0.00240	0.00849	0.00032	145	42	57	2	54	2
WR1211-16	43634	514	0.05064	0.00158	0.05948	0.00287	0.00852	0.00031	225	71	59	3	55	2
WR1211-06	25061	477	0.04930	0.00183	0.05825	0.00333	0.00857	0.00037	162	84	57	3	55	2
WR1211-03	44148	483	0.05003	0.00093	0.05913	0.00278	0.00857	0.00037	196	43	58	3	55	2
WR1211-10	104950	446	0.04828	0.00075	0.05712	0.00243	0.00858	0.00034	113	36	56	2	55	2
WR1211-04	48372	459	0.04880	0.00112	0.05781	0.00271	0.00859	0.00035	138	53	57	3	55	2
WR1211-11	134680	473	0.04815	0.00068	0.05711	0.00236	0.00860	0.00033	107	33	56	2	55	2
WR1211-02	27510	479	0.04763	0.00095	0.05652	0.00248	0.00861	0.00034	81	47	56	2	55	2
WR1211-14	26014	497	0.04732	0.00120	0.05630	0.00273	0.00863	0.00036	66	59	56	3	55	2
WR1211-01	30709	466	0.04863	0.00110	0.05815	0.00305	0.00867	0.00041	130	52	57	3	56	3
WR1211-22	50267	488	0.04869	0.00088	0.05828	0.00239	0.00868	0.00032	133	42	58	2	56	2
WR1211-23	299511	497	0.04789	0.00064	0.05735	0.00223	0.00869	0.00032	94	31	57	2	56	2
WR1211-09	52527	456	0.04840	0.00082	0.05836	0.00271	0.00874	0.00038	119	39	58	3	56	2
WR1211-13	29848	511	0.05027	0.00219	0.06112	0.00363	0.00882	0.00036	207	98	60	3	57	2
WR1211-17	30427	519	0.05269	0.00151	0.06625	0.00320	0.00912	0.00036	315	64	65	3	59	2
WR1211-21	15885	477	0.04747	0.00126	0.06198	0.00294	0.00947	0.00037	73	62	61	3	61	2
WR1211-15	19126	517	0.05284	0.00260	0.06925	0.00453	0.00951	0.00041	322	108	68	4	61	3
WR1211-05	16237	474	0.04752	0.00247	0.06235	0.00400	0.00952	0.00036	75	119	61	4	61	2
WR1211-07	11761	448	0.04669	0.00215	0.06154	0.00366	0.00956	0.00036	33	107	61	3	61	2
WR1211-24	14108	497	0.04966	0.00193	0.06652	0.00350	0.00971	0.00034	179	88	65	3	62	2
WR1211-20	19653	525	0.07659	0.00561	0.10429	0.00875	0.00988	0.00040	1110	140	101	8	63	3
KMQ-12-2														
KMQ1202-01	43241	436	0.04916	0.00118	0.05326	0.00234	0.00786	0.00029	155	55	53	2	50	2
KMQ1202-02	55155	435	0.04795	0.00069	0.05170	0.00217	0.00782	0.00031	97	34	51	2	50	2
KMQ1202-03	26900	455	0.04677	0.00097	0.05114	0.00238	0.00793	0.00033	37	49	51	2	51	2
KMQ1202-04	39395	492	0.04904	0.00097	0.05349	0.00263	0.00791	0.00036	150	46	53	3	51	2
KMQ1202-05	27680	511	0.04895	0.00143	0.05471	0.00249	0.00811	0.00028	145	67	54	2	52	2
KMQ1202-06	32229	500	0.04879	0.00152	0.05351	0.00288	0.00795	0.00035	138	71	53	3	51	2
KMQ1202-07	64079	497	0.04798	0.00075	0.05276	0.00207	0.00797	0.00029	98	36	52	2	51	2
KMQ1202-08	37277	521	0.04843	0.00096	0.05254	0.00230	0.00787	0.00031	120	46	52	2	51	2
KMQ1202-09	32181	517	0.05398	0.00230	0.05893	0.00342	0.00792	0.00031	370	93	58	3	51	2
KMQ1202-10	58106	518	0.04765	0.00079	0.05339	0.00215	0.00813	0.00030	82	39	53	2	52	2
KMQ1202-11	39313	514	0.04923	0.00136	0.05484	0.00255	0.00808	0.00030	159	63	54	2	52	2
KMQ1202-13	41885	501	0.04855	0.00151	0.05338	0.00269	0.00797	0.00032	126	72	53	3	51	2
KMQ1202-14	35471	450	0.05003	0.00375	0.05483	0.00492	0.00795	0.00039	196	166	54	5	51	3
KMQ1202-15	48600	486	0.04857	0.00118	0.05225	0.00240	0.00780	0.00030	127	56	52	2	50	2
KMQ1202-16	26524	467	0.04762	0.00111	0.05160	0.00221	0.00786	0.00028	81	55	51	2	50	2
KMQ1202-17	49995	483	0.04873	0.00095	0.05319	0.00253	0.00792	0.00034	135	45	53	2	51	2
KMQ1202-19	48345	520	0.04792	0.00092	0.05214	0.00214	0.00789	0.00029	95	45	52	2	51	2
KMQ1202-20	31135	497	0.04777	0.00099	0.05040	0.00234	0.00765	0.00032	88	48	50	2	49	2

KMQ1202-21	60243	502	0.04866	0.00090	0.05288	0.00222	0.00788	0.00030	131	43	52	2	51	2
RD-12-5														
RD1205-12	85890	746	0.04835	0.00085	0.06697	0.00226	0.01004	0.00029	117	41	66	2	64	2
RD1205-21	60599	682	0.04827	0.00084	0.06759	0.00231	0.01016	0.00030	113	40	66	2	65	2
RD1205-06	61724	773	0.05080	0.00145	0.07123	0.00295	0.01017	0.00031	232	65	70	3	65	2
RD1205-14	99532	755	0.04978	0.00143	0.06983	0.00280	0.01017	0.00028	185	66	69	3	65	2
RD1205-18	52344	711	0.05038	0.00131	0.07070	0.00276	0.01018	0.00030	213	59	69	3	65	2
RD1205-05	49416	738	0.04869	0.00086	0.06887	0.00233	0.01026	0.00030	133	41	68	2	66	2
RD1205-19	29292	735	0.05690	0.00598	0.08049	0.00879	0.01026	0.00030	488	217	79	8	66	2
RD1205-08	53100	768	0.05690	0.00183	0.08051	0.00338	0.01026	0.00028	488	69	79	3	66	2
RD1205-07	60580	761	0.04927	0.00104	0.07010	0.00264	0.01032	0.00032	160	49	69	3	66	2
RD1205-17	37653	735	0.05033	0.00141	0.07203	0.00284	0.01038	0.00029	210	64	71	3	67	2
RD1205-04	39043	757	0.04927	0.00116	0.07114	0.00267	0.01047	0.00031	161	54	70	3	67	2
RD1205-01	41213	886	0.05606	0.00311	0.08122	0.00522	0.01051	0.00034	455	118	79	5	67	2
RD1205-09	32601	788	0.05264	0.00166	0.07677	0.00335	0.01058	0.00032	313	70	75	3	68	2
RD1205-02	70219	866	0.04955	0.00106	0.07302	0.00253	0.01069	0.00029	174	49	72	2	69	2
RD1205-13	29219	749	0.05301	0.00185	0.07832	0.00351	0.01072	0.00030	329	77	77	3	69	2
RD1205-15	29684	689	0.04913	0.00124	0.07284	0.00290	0.01075	0.00033	154	58	71	3	69	2
RD1205-20	27912	683	0.04899	0.00125	0.07268	0.00291	0.01076	0.00033	148	59	71	3	69	2
RD1205-03	30155	824	0.05434	0.00191	0.08294	0.00366	0.01107	0.00030	385	77	81	3	71	2
RD1205-10	19481	720	0.05109	0.00108	0.08008	0.00277	0.01137	0.00031	245	48	78	3	73	2
RD1205-22	474839	692	0.10423	0.00115	3.19295	0.11227	0.22218	0.00742	1701	20	1455	27	1293	39
XB-12-03														
XB1203-03	230206	554	0.05600	0.00131	0.02586	0.00142	0.00335	0.00017	452	51	26	1	22	1
XB1203-01	100496	360	0.04806	0.00063	0.02246	0.00091	0.00339	0.00013	102	30	23	1	22	1
XB1203-07	62537	440	0.04808	0.00082	0.02315	0.00094	0.00349	0.00013	103	40	23	1	22	1
XB1203-08	79299	423	0.04876	0.00074	0.02376	0.00096	0.00353	0.00013	136	35	24	1	23	1
XB1203-02	89755	601	0.07365	0.00667	0.03612	0.00359	0.00356	0.00015	1032	173	36	4	23	1
XB1203-16	116841	480	0.04750	0.00055	0.02372	0.00089	0.00362	0.00013	74	27	24	1	23	1
XB1203-24	139523	515	0.04734	0.00063	0.02368	0.00094	0.00363	0.00014	67	31	24	1	23	1
XB1203-14	162112	500	0.04700	0.00056	0.02357	0.00085	0.00364	0.00012	49	28	24	1	23	1
XB1203-09	114577	450	0.04768	0.00061	0.02392	0.00091	0.00364	0.00013	84	30	24	1	23	1
XB1203-10	40583	474	0.04832	0.00083	0.02443	0.00103	0.00367	0.00014	115	40	25	1	24	1
XB1203-22	103114	476	0.04705	0.00059	0.02389	0.00090	0.00368	0.00013	52	29	24	1	24	1
XB1203-21	98392	503	0.04820	0.00067	0.02469	0.00095	0.00372	0.00013	109	32	25	1	24	1
XB1203-23	109753	503	0.04702	0.00064	0.02441	0.00089	0.00376	0.00013	50	32	24	1	24	1
XB1203-25	190959	1130	0.09096	0.00514	0.04722	0.00331	0.00377	0.00016	1446	104	47	3	24	1
XB1203-17	177625	506	0.04733	0.00057	0.02488	0.00096	0.00381	0.00014	66	28	25	1	25	1
XB1203-19	48133	511	0.04795	0.00094	0.02533	0.00105	0.00383	0.00014	97	46	25	1	25	1
XB1203-05	12575	427	0.04994	0.00151	0.02667	0.00126	0.00387	0.00014	192	69	27	1	25	1
XB1203-20	48408	501	0.04766	0.00084	0.02692	0.00108	0.00410	0.00015	83	41	27	1	26	1
XB1203-15	28425	507	0.05022	0.00139	0.04109	0.00215	0.00593	0.00026	205	63	41	2	38	2
XB1203-06	82765	440	0.05156	0.00072	0.16307	0.00848	0.02294	0.00115	266	32	153	7	146	7
JR-5														
JR5-35	40465	202	0.04610	0.00164	0.01445	0.00094	0.00227	0.00012	3	84	15	1	15	1
JR5-14	21359	331	0.05815	0.00190	0.01903	0.00133	0.00237	0.00015	535	70	19	1	15	1
JR5-2	23509	194	0.05665	0.00282	0.01885	0.00136	0.00241	0.00013	478	107	19	1	16	1
JR5-21	40069	171	0.05020	0.00240	0.01677	0.00128	0.00242	0.00014	204	107	17	1	16	1
JR5-12	20981	332	0.05782	0.00221	0.01961	0.00145	0.00246	0.00016	523	82	20	1	16	1
JR5-25	15115	249	0.04855	0.00525	0.01653	0.00205	0.00247	0.00015	126	236	17	2	16	1
JR5-26	13663	239	0.04966	0.00525	0.01700	0.00199	0.00248	0.00012	179	230	17	2	16	1

JR5-24	15736	200	0.04858	0.00213	0.01684	0.00121	0.00251	0.00014	127	100	17	1	16	1
JR5-5	16916	175	0.04511	0.00240	0.01575	0.00111	0.00253	0.00012	-50	125	16	1	16	1
JR5-29	22208	277	0.05145	0.00278	0.01798	0.00145	0.00253	0.00015	261	119	18	1	16	1
JR5-19	36751	153	0.05095	0.00240	0.01792	0.00134	0.00255	0.00015	239	105	18	1	16	1
JR5-4	13579	173	0.04621	0.00331	0.01629	0.00142	0.00256	0.00013	9	164	16	1	16	1
JR5-15	11009	293	0.06890	0.00467	0.02442	0.00200	0.00257	0.00012	896	134	24	2	17	1
JR5-31	11254	259	0.05312	0.00293	0.01897	0.00134	0.00259	0.00011	334	121	19	1	17	1
JR5-3	19677	170	0.04532	0.00154	0.01619	0.00124	0.00259	0.00018	-39	81	16	1	17	1
JR5-28	13457	282	0.05075	0.00199	0.01820	0.00109	0.00260	0.00012	229	88	18	1	17	1
JR5-7	8247	238	0.06661	0.00437	0.02433	0.00205	0.00265	0.00014	825	131	24	2	17	1
JR5-10	16454	242	0.06613	0.00390	0.02418	0.00206	0.00265	0.00016	810	119	24	2	17	1
JR5-9	11708	214	0.05999	0.00380	0.02202	0.00185	0.00266	0.00015	603	132	22	2	17	1
JR5-18	14482	130	0.05778	0.00247	0.02122	0.00135	0.00266	0.00012	521	91	21	1	17	1
JR5-17	11111	133	0.06441	0.00444	0.02422	0.00204	0.00273	0.00013	755	139	24	2	18	1
JR5-1	10992	182	0.05452	0.00249	0.02055	0.00145	0.00273	0.00015	393	99	21	1	18	1
JR5-13	11887	315	0.06628	0.00400	0.02519	0.00191	0.00276	0.00013	815	121	25	2	18	1
JR5-22	16808	185	0.05956	0.00593	0.02297	0.00258	0.00280	0.00015	588	202	23	3	18	1
JR5-20	19545	200	0.05708	0.00331	0.02239	0.00175	0.00284	0.00015	495	123	22	2	18	1
JR5-11	140346	330	0.04941	0.00093	0.03163	0.00217	0.00464	0.00031	167	43	32	2	30	2
JR5-16	25351	94	0.05523	0.00160	0.08492	0.00530	0.01115	0.00062	422	63	83	5	71	4
JR5-16B	17203	112	0.05588	0.00231	0.10151	0.00676	0.01317	0.00069	448	89	98	6	84	4
JR5-27	8881	249	0.04900	0.00379	0.21055	0.01895	0.03116	0.00143	148	172	194	16	198	9
JR5-27B	8973	280	0.05152	0.00294	0.22219	0.01616	0.03128	0.00141	264	126	204	13	199	9
JR5-23	16788	220	0.05584	0.00305	0.24187	0.01791	0.03142	0.00157	446	117	220	15	199	10
JR-2														
JR2-1	7976	112	0.03639	0.00485	0.01162	0.00158	0.00232	0.00006	-601	329	12	2	15	0
JR2-2	74070	110	0.04559	0.00119	0.04238	0.00147	0.00674	0.00015	-24	62	42	1	43	1
JR2-3	3988	79	-0.01272	-0.01238	-0.00388	-0.00378	0.00221	0.00008			-4	-4	14	1
JR2-4	3706	106	-0.02106	-0.02017	-0.00609	-0.00584	0.00210	0.00009			-6	-6	14	1
JR2-5.0	640	74	-0.65964	-0.31377	-0.12025	-0.06038	0.00132	0.00021			-130	-72	9	1
JR2-5	1203	76	-0.27836	-0.08303	-0.06695	-0.02065	0.00174	0.00014			-70	-23	11	1
JR2-6	1945	98	-0.10630	-0.02597	-0.02888	-0.00719	0.00197	0.00010			-30	-8	13	1
JR2-7	108432	52	0.04543	0.00103	0.03153	0.00152	0.00503	0.00021	-33	54	32	1	32	1
JR2-8	3549	56	-0.02664	-0.01735	-0.00806	-0.00526	0.00219	0.00010			-8	-5	14	1
JR2-9	132137	39	0.04384	0.00112	0.01578	0.00102	0.00261	0.00015	-120	62	16	1	17	1
JR2-9B	81999	32	0.04470	0.00183	0.01606	0.00103	0.00261	0.00013	-72	97	16	1	17	1
JR2-9C	168954	53	0.04766	0.00118	0.01745	0.00074	0.00266	0.00009	82	58	18	1	17	1
JR2-10	5479	97	0.05810	0.00404	0.01885	0.00161	0.00235	0.00012	534	145	19	2	15	1
JR2-11	4317	141	0.06263	0.01274	0.02101	0.00444	0.00243	0.00014	696	383	21	4	16	1
JR2-12	42550	162	0.04971	0.00127	0.01499	0.00086	0.00219	0.00011	181	58	15	1	14	1
JR2-12B	16175	214	0.10104	0.00897	0.03658	0.00376	0.00263	0.00014	1643	156	36	4	17	1
JR2-13	22532	148	0.04992	0.00170	0.02163	0.00148	0.00314	0.00019	191	77	22	1	20	1
JR2-14B	38496	149	0.04976	0.00252	0.03696	0.00262	0.00539	0.00027	184	114	37	3	35	2
JR2-15	29187	154	0.05044	0.00115	0.01514	0.00090	0.00218	0.00012	215	52	15	1	14	1
JR2-16	125677	413	0.06607	0.00564	0.02093	0.00209	0.00230	0.00012	808	169	21	2	15	1
JR2-17	33485	168	0.04957	0.00112	0.01520	0.00083	0.00222	0.00011	175	52	15	1	14	1
JR2-17B	31354	173	0.05449	0.00190	0.01668	0.00110	0.00222	0.00012	391	76	17	1	14	1
JR2-18	3367	153	0.05525	0.00980	0.01817	0.00338	0.00238	0.00014	422	354	18	3	15	1
JR2-19	18238	156	0.04556	0.00238	0.01492	0.00110	0.00238	0.00012	-26	122	15	1	15	1
JR2-19B	4806	149	0.03232	0.01009	0.01059	0.00341	0.00238	0.00019	-935	733	11	3	15	1

Table A2 U-Pb laser-ablation multi-collector inductively coupled plasma–mass spectrometer (LA-MC-ICP-MS) analytical data for Cenozoic Gangdese igneous rocks.

Sample name	^{206}Pb (cps)	^{204}Pb (cps)	^{207}Pb/^{206}Pb	2 σ	^{207}Pb/^{235}U	2 σ	^{206}Pb/^{238}U	2 σ	^{207}Pb*/^{206}Pb* age (Ma)	2 σ	^{207}Pb*/^{235}U age (Ma)	2 σ	^{206}Pb*/^{238}U age (Ma)	2 σ
QL-5														
QL5-1	9928	176	0.04812	0.00386	0.06985	0.00815	0.01053	0.00089	105	179	69	8	68	6
QL5-1B	12012	174	0.04824	0.00234	0.07246	0.00741	0.01089	0.00098	111	111	71	7	70	6
QL5-2	8372	177	0.05828	0.00404	0.08726	0.01091	0.01086	0.00113	540	145	85	10	70	7
QL5-3	8506	184	0.04626	0.00353	0.06827	0.00824	0.01070	0.00100	11	174	67	8	69	6
QL5-4	5410	160	0.03581	0.00627	0.05244	0.01041	0.01062	0.00099	-645	424	52	10	68	6
QL5-4B	5033	182	0.03172	0.00743	0.04510	0.01122	0.01031	0.00086	-991	585	45	11	66	5
QL5-5	6157	199	0.03272	0.00614	0.04484	0.00941	0.00994	0.00093	-900	474	45	9	64	6
QL5-6	12495	213	0.04137	0.00271	0.05937	0.00652	0.01041	0.00092	-265	159	59	6	67	6
QL5-7	19059	206	0.04933	0.00265	0.06900	0.00736	0.01014	0.00093	163	121	68	7	65	6
QL5-8	12774	207	0.04886	0.00316	0.07524	0.00919	0.01117	0.00116	141	145	74	9	72	7
QL5-8B	5413	195	0.04860	0.00628	0.07294	0.01191	0.01088	0.00109	129	279	71	11	70	7
QL5-9	6490	232	0.07986	0.00862	0.12914	0.01814	0.01173	0.00105	1193	199	123	16	75	7
QL5-10	6713	173	0.04429	0.00407	0.05915	0.00781	0.00969	0.00092	-94	211	58	7	62	6
QL5-11	9233	170	0.03609	0.00370	0.05355	0.00752	0.01076	0.00103	-624	259	53	7	69	7
QL5-12	12055	170	0.03684	0.00445	0.05339	0.00784	0.01051	0.00088	-569	299	53	8	67	6
ZD-2														
ZD2-1	15665	171	0.05763	0.00300	0.06897	0.00601	0.00868	0.00061	516	110	68	6	56	4
ZD2-2	17275	180	0.05136	0.00245	0.06086	0.00489	0.00859	0.00056	257	106	60	5	55	4
ZD2-3	11011	176	0.05941	0.00513	0.07100	0.00779	0.00867	0.00059	582	177	70	7	56	4
ZD2-4	14356	190	0.05439	0.00256	0.06437	0.00486	0.00858	0.00051	387	103	63	5	55	3
ZD2-5	12876	217	0.05693	0.00327	0.06864	0.00575	0.00875	0.00053	489	122	67	5	56	3
ZD2-6	20899	192	0.05389	0.00212	0.05803	0.00444	0.00781	0.00051	366	86	57	4	50	3
ZD2-7	9522	179	0.05331	0.00376	0.06227	0.00631	0.00847	0.00062	342	152	61	6	54	4
ZD2-8	20180	193	0.05289	0.00212	0.05760	0.00469	0.00790	0.00056	324	89	57	4	51	4
ZD2-9	5513	210	0.07226	0.00704	0.08204	0.01020	0.00823	0.00064	993	186	80	10	53	4
ZD2-10	7475	211	0.05467	0.00492	0.06873	0.00848	0.00912	0.00077	399	190	67	8	59	5
ZD2-11	6014	128	0.05188	0.00880	0.05611	0.01015	0.00784	0.00049	280	348	55	10	50	3
ZD2-12	10656	132	0.04692	0.00357	0.05667	0.00564	0.00876	0.00056	45	173	56	5	56	4
ZD2-13	9685	109	0.04774	0.00372	0.05569	0.00583	0.00846	0.00059	86	175	55	6	54	4
ZD2-14	8726	102	0.05357	0.00511	0.06253	0.00655	0.00847	0.00036	353	202	62	6	54	2
ZD2-15	17250	113	0.05266	0.00206	0.06119	0.00342	0.00843	0.00034	314	86	60	3	54	2
ZD2-16	4789	128	0.10642	0.01460	0.12808	0.01856	0.00873	0.00041	1739	232	122	17	56	3
ZD2-17	3462	126	0.07645	0.01069	0.08837	0.01299	0.00838	0.00038	1107	257	86	12	54	2
ZD2-19	10948	106	0.05366	0.00275	0.05970	0.00449	0.00807	0.00044	357	112	59	4	52	3
ZD2-20	5603	125	0.05550	0.00925	0.06466	0.01131	0.00845	0.00045	433	334	64	11	54	3
ZD2-21	13699	161	0.05349	0.00432	0.06894	0.00763	0.00935	0.00071	349	173	68	7	60	5
ZD2-23	11958	149	0.04862	0.00226	0.05958	0.00329	0.00889	0.00026	130	106	59	3	57	2
ZD2-24	8552	129	0.04617	0.00513	0.05359	0.00660	0.00842	0.00045	6	248	53	6	54	3
ZD2-26	12095	137	0.04356	0.00242	0.05192	0.00400	0.00864	0.00046	-135	132	51	4	55	3
ZD2-28	6674	163	0.07304	0.01440	0.08850	0.01773	0.00879	0.00031	1015	355	86	16	56	2

ZD2-29	15966	161	0.04221	0.00220	0.05013	0.00361	0.00861	0.00043	-214	126	50	3	55	3
ZD2-30	17417	181	0.04402	0.00299	0.05353	0.00457	0.00882	0.00046	-109	159	53	4	57	3
ZD2-30B	37618	172	0.04664	0.00094	0.05048	0.00281	0.00785	0.00041	31	47	50	3	50	3
ZD2-31	5045	193	0.04366	0.00559	0.05173	0.00706	0.00859	0.00040	-130	290	51	7	55	3
CB-3														
CB3-1	45315	80	0.04860	0.00156	0.02751	0.00197	0.00411	0.00026	129	74	28	2	26	2
CB3-1B	33797	61	0.04819	0.00137	0.02685	0.00184	0.00404	0.00025	109	66	27	2	26	2
CB3-2	61731	80	0.04805	0.00150	0.02820	0.00196	0.00426	0.00026	102	72	28	2	27	2
CB3-2B	13232	74	0.04252	0.00168	0.02507	0.00148	0.00428	0.00019	-196	96	25	1	28	1
CB3-3	59289	65	0.05052	0.00144	0.03092	0.00190	0.00444	0.00024	219	65	31	2	29	2
CB3-4	18435	56	0.05040	0.00298	0.02901	0.00215	0.00418	0.00019	214	131	29	2	27	1
CB3-5	45369	84	0.04825	0.00126	0.02805	0.00169	0.00422	0.00023	112	61	28	2	27	1
CB3-6	38153	61	0.05090	0.00220	0.02999	0.00195	0.00427	0.00021	236	97	30	2	27	1
CB3-7	36683	70	0.04972	0.00203	0.02859	0.00190	0.00417	0.00022	182	93	29	2	27	1
CB3-8	20072	90	0.04867	0.00182	0.02873	0.00164	0.00428	0.00018	132	86	29	2	28	1
CB3-9	15060	50	0.04890	0.00181	0.02809	0.00153	0.00417	0.00017	143	85	28	2	27	1
CB3-10	15169	62	0.05005	0.00311	0.02966	0.00215	0.00430	0.00016	197	138	30	2	28	1
CB3-10A	104259	109	0.04902	0.00289	0.02739	0.00191	0.00405	0.00015	149	133	27	2	26	1
CB3-11	61753	40	0.05803	0.00471	0.03626	0.00322	0.00453	0.00016	531	169	36	3	29	1
CB3-12	73133	36	0.05752	0.00330	0.03508	0.00237	0.00442	0.00016	511	121	35	2	28	1
CB3-13	16194	30	0.05019	0.00129	0.02996	0.00127	0.00433	0.00015	204	58	30	1	28	1
CB3-13A	14172	50	0.04971	0.00135	0.03009	0.00135	0.00439	0.00016	181	62	30	1	28	1
CB3-14	45300	40	0.05507	0.00253	0.03290	0.00186	0.00433	0.00014	415	99	33	2	28	1
CB3-15	42707	24	0.05747	0.00275	0.03457	0.00211	0.00436	0.00017	510	102	35	2	28	1
CB3-16	30980	39	0.04705	0.00203	0.02706	0.00146	0.00417	0.00014	52	100	27	1	27	1
CB3-17	30383	73	0.04639	0.00139	0.02754	0.00159	0.00431	0.00021	18	71	28	2	28	1
CB3-17A	43119	57	0.04721	0.00246	0.02773	0.00187	0.00426	0.00018	60	120	28	2	27	1
CB3-18	25877	112	0.04763	0.00185	0.02980	0.00208	0.00454	0.00026	81	90	30	2	29	2
CB3-19	53199	72	0.04857	0.00112	0.02740	0.00182	0.00409	0.00026	127	53	27	2	26	2
CB3-20	60784	73	0.06637	0.00559	0.03906	0.00391	0.00427	0.00023	818	167	39	4	27	1
CB3-21	20406	50	0.04828	0.00120	0.02781	0.00146	0.00418	0.00019	113	58	28	1	27	1
CB3-22	56083	77	0.05092	0.00101	0.03137	0.00237	0.00447	0.00033	237	45	31	2	29	2
CB3-23	51400	65	0.05151	0.00165	0.03047	0.00203	0.00429	0.00025	264	72	30	2	28	2
CB3-24	56854	65	0.05090	0.00178	0.02996	0.00180	0.00427	0.00021	236	79	30	2	27	1
CB3-25	46897	80	0.04747	0.00151	0.02768	0.00173	0.00423	0.00023	73	74	28	2	27	1
CB3-25B	24956	81	0.04549	0.00127	0.02721	0.00191	0.00434	0.00028	-29	66	27	2	28	2
CB3-26	15144	77	0.05000	0.00275	0.02805	0.00218	0.00407	0.00022	195	123	28	2	26	1

Table A3 Electron microprobe analysis results of amphibole, ilmenite, magnetite, pyroxene, and plagioclase: amphibole.

Sample number	NM11-01	NM11-01	NM11-01	NM11-01	NM11-01	NM11-01	NM11-01	NM11-01	NM11-01	QS-10	QS-10	QS-10	QS-10	QS-10	QS-10
Weight %															
SiO_2	45.02	45.12	45.15	44.89	44.34	45.10	45.14	45.07	45.70	44.60	45.29	45.00	44.72	46.15	45.55
TiO_2	1.48	1.41	1.49	1.65	1.53	1.41	1.61	1.64	1.26	1.32	1.39	1.50	1.43	1.44	1.34
Al_2O_3	8.61	8.57	8.73	8.42	8.61	9.03	8.64	8.75	8.33	8.49	8.01	8.22	8.34	8.06	7.97
FeO	16.39	16.24	16.18	16.12	16.30	16.88	17.07	16.87	16.71	16.53	15.94	15.97	15.83	15.35	16.51
MnO	0.65	0.66	0.66	0.62	0.61	0.73	0.70	0.68	0.72	0.74	0.67	0.66	0.69	0.65	0.77
MgO	11.57	11.33	11.54	11.61	11.45	11.03	11.17	11.26	11.50	11.05	12.07	11.82	12.09	12.48	11.44
CaO	11.56	11.45	11.54	11.22	11.45	11.84	11.52	11.59	11.59	11.37	11.30	11.47	11.19	11.54	11.46
Na_2O	1.44	1.45	1.60	1.54	1.47	1.34	1.46	1.51	1.23	1.36	1.54	1.52	1.56	1.49	1.43
K_2O	1.15	1.19	1.17	1.17	1.17	1.11	1.15	1.21	1.06	0.95	0.94	0.87	0.92	0.90	0.89
F	0.29	0.24	0.27	0.29	0.28	0.24	0.28	0.24	0.22	0.00	0.00	0.00	0.00	0.00	0.00
Cl	0.12	0.13	0.09	0.13	0.15	0.08	0.13	0.13	0.10	0.00	0.00	0.00	0.00	0.00	0.00
Total	98.28	97.79	98.42	97.65	97.35	98.78	98.87	98.95	98.41	96.47	97.14	97.13	96.78	98.07	97.36
No. of oxygens	23	23	23	23	23	23	23	23	23	23	23	23	23	23	23
Si	6.67	6.72	6.68	6.68	6.64	6.66	6.66	6.65	6.74	6.70	6.72	6.70	6.65	6.76	6.77
Al^{iv}	1.33	1.28	1.32	1.32	1.36	1.34	1.34	1.35	1.26	1.30	1.28	1.30	1.35	1.24	1.23
Al^{vi}	0.17	0.22	0.20	0.16	0.16	0.24	0.17	0.17	0.18	0.20	0.12	0.14	0.11	0.15	0.17
Ti	0.16	0.16	0.17	0.18	0.17	0.16	0.18	0.18	0.14	0.15	0.15	0.17	0.16	0.16	0.15
Cr	0.00	0.00	0.00	0.00	0.00	0.00	0.00	0.00	0.00	0.00	0.00	0.00	0.00	0.00	0.00
Fe^{3+}	0.54	0.45	0.44	0.55	0.54	0.45	0.53	0.49	0.59	0.56	0.65	0.57	0.74	0.55	0.54
Fe^{2+}	1.49	1.57	1.56	1.45	1.50	1.64	1.58	1.60	1.47	1.52	1.33	1.42	1.23	1.33	1.52
Mn	0.08	0.08	0.08	0.08	0.08	0.09	0.09	0.09	0.09	0.09	0.08	0.08	0.09	0.08	0.10
Mg	2.55	2.51	2.55	2.58	2.55	2.43	2.46	2.48	2.53	2.47	2.67	2.62	2.68	2.73	2.53
Ca	1.83	1.83	1.83	1.79	1.84	1.87	1.82	1.83	1.83	1.83	1.80	1.83	1.78	1.81	1.82
Na	0.41	0.42	0.46	0.44	0.43	0.38	0.42	0.43	0.35	0.40	0.44	0.44	0.45	0.42	0.41
K	0.22	0.23	0.22	0.22	0.22	0.21	0.22	0.23	0.20	0.18	0.18	0.17	0.17	0.17	0.17
F	0.13	0.11	0.13	0.14	0.13	0.11	0.13	0.11	0.10	0.00	0.00	0.00	0.00	0.00	0.00
Cl	0.03	0.03	0.02	0.03	0.04	0.02	0.03	0.03	0.02	0.00	0.00	0.00	0.00	0.00	0.00
OH*	1.84	1.86	1.85	1.83	1.83	1.87	1.84	1.86	1.87	2.00	2.02	2.01	2.02	2.05	2.02
Total	17.46	17.47	17.51	17.46	17.49	17.47	17.46	17.49	17.38	17.41	17.42	17.43	17.41	17.40	17.40
P (kbars)	4.1	4.1	4.2	4.0	4.2	4.5	4.1	4.2	3.9	4.1	3.7	3.9	3.9	3.6	3.6
ΔNNO	0.55	0.47	0.47	0.55	0.53	0.34	0.39	0.38	0.62	0.48	0.78	0.64	0.80	0.82	0.58
$\log fO_2$	-12.39	-12.58	-12.41	-12.47	-12.31	-12.51	-12.61	-12.51	-12.65	-12.62	-12.43	-12.42	-12.19	-12.42	-12.80
ΔFMQ	1.79	1.86	1.82	1.69	1.39	1.42	1.70	1.36	1.59	1.18	1.33	1.43	1.72	1.58	1.74
T (°C)	844	838	846	840	849	848	841	847	827	835	831	838	841	829	822

Table A3-amphibole (Conti.)

Sample number	WR-13-109	WR-13-109	WR-13-109	WR-13-109	WR-13-111	WR-13-111	WR-13-111	WR-13-111	QS-2	QS-2	QS-2	QS-2	QS-2	QS-2	QS-2
Weight %															
SiO_2	41.68	41.91	42.14	41.98	41.87	41.68	41.54	41.43	45.97	45.04	44.93	45.37	45.20	44.91	46.08
TiO_2	3.44	3.46	3.29	3.29	3.46	3.41	3.44	3.48	1.04	0.98	1.10	1.02	1.33	1.32	1.07
Al_2O_3	11.65	11.81	11.61	11.81	11.67	11.66	11.47	11.44	7.48	7.33	7.33	7.66	7.45	7.91	7.39
FeO	11.98	12.10	12.03	11.97	12.38	11.77	12.13	11.70	16.33	16.41	16.34	16.92	17.08	16.61	16.14
MnO	0.17	0.18	0.19	0.19	0.25	0.17	0.16	0.21	0.64	0.67	0.68	0.72	0.70	0.68	0.70
MgO	13.99	14.00	14.31	14.26	13.88	13.76	14.13	14.09	11.96	11.96	11.92	11.57	10.96	11.04	11.70
CaO	11.10	11.15	11.07	11.03	11.14	11.11	11.18	11.24	11.83	11.78	11.70	11.83	11.83	11.84	11.95
Na_2O	2.52	2.53	2.54	2.54	2.74	3.27	3.03	2.89	1.18	1.19	1.23	1.22	1.26	1.10	1.04
K_2O	0.39	0.38	0.40	0.38	0.38	0.38	0.39	0.39	0.82	0.85	0.85	0.81	0.84	0.92	0.80
F	0.00	0.00	0.10	0.05	0.68	1.54	0.91	0.95	0.00	0.00	0.00	0.00	0.00	0.00	0.00
Cl	0.01	0.04	0.02	0.01	0.03	0.02	0.03	0.02	0.00	0.00	0.00	0.00	0.00	0.00	0.00
Total	97.01	97.64	97.70	97.56	98.51	98.77	98.50	97.85	97.28	96.26	96.19	97.17	96.72	96.35	96.90
No. of oxygens	23	23	23	23	23	23	23	23	23	23	23	23	23	23	23
Si	6.78	7.04	6.10	6.08	6.08	6.12	6.23	6.50	6.82	6.77	6.76	6.77	6.82	6.78	6.88
Al^{iv}	1.22	0.96	1.90	1.92	1.92	1.88	1.77	1.50	1.18	1.23	1.24	1.23	1.18	1.22	1.12
Al^{vi}	1.02	1.37	0.08	0.09	0.08	0.14	0.25	0.62	0.13	0.06	0.06	0.11	0.14	0.18	0.18
Ti	0.42	0.44	0.36	0.36	0.38	0.38	0.39	0.41	0.12	0.11	0.12	0.11	0.15	0.15	0.12
Cr	0.00	0.00	0.00	0.00	0.00	0.00	0.00	0.00	0.00	0.00	0.00	0.00	0.00	0.00	0.00
Fe^{3+}	1.63	1.70	0.89	0.90	0.77	0.48	1.52	1.54	0.56	0.65	0.64	0.60	0.39	0.41	0.44
Fe^{2+}	0.00	0.00	0.56	0.54	0.74	0.96	0.00	0.00	1.47	1.42	1.42	1.51	1.77	1.69	1.58
Mn	0.02	0.03	0.02	0.02	0.03	0.02	0.02	0.03	0.08	0.09	0.09	0.09	0.09	0.09	0.09
Mg	3.39	3.50	3.09	3.08	3.01	3.01	3.16	3.30	2.65	2.68	2.67	2.57	2.46	2.48	2.60
Ca	1.94	2.01	1.72	1.71	1.73	1.75	1.80	1.89	1.88	1.90	1.89	1.89	1.91	1.91	1.91
Na	0.80	0.82	0.71	0.71	0.77	0.93	0.88	0.88	0.34	0.35	0.36	0.35	0.37	0.32	0.30
K	0.08	0.08	0.07	0.07	0.07	0.07	0.07	0.08	0.16	0.16	0.16	0.15	0.16	0.18	0.15
F	0.00	0.00	0.05	0.02	0.31	0.72	0.43	0.47	0.00	0.00	0.00	0.00	0.00	0.00	0.00
Cl	0.00	0.01	0.00	0.00	0.01	0.01	0.01	0.00	0.00	0.00	0.00	0.00	0.00	0.00	0.00
OH*	2.00	1.99	1.95	1.97	1.68	1.28	1.56	1.52	2.02	2.00	1.99	2.01	1.99	1.99	2.01
Total	19.30	19.96	17.50	17.50	17.58	17.75	18.09	18.74	17.38	17.41	17.41	17.40	17.44	17.41	17.36
P (kbars)	7.6	8.1	6.4	6.6	6.5	6.6	6.6	7.1	3.2	3.2	3.2	3.4	3.3	3.7	3.2
ΔNNO	0.63	0.60	0.77	0.75	0.53	0.35	0.56	0.54	0.84	0.92	0.88	0.74	0.44	0.48	0.74
$\log fO_2$	-10.09	-10.10	-10.03	-9.98	-10.17	-10.23	-10.04	-10.04	-12.73	-12.51	-12.53	-12.69	-13.08	-12.83	-12.93
ΔFMQ	1.76	1.52	2.08	1.86	2.12	1.74	1.74	1.96	1.48	1.42	1.41	1.49	1.46	1.28	1.33
T (°C)	967	967	962	966	968	975	975	975	813	820	821	820	816	826	808

Table A3-amphibole (Conti.)

Sample number	ZD-2	ZD-2	ZD-2	ZD-2	ZD-2	ZD-2	QS-9	QS-9	QS-9	QS-9	MZ-3	MZ-3	MZ-3	MZ-3	MZ-3
Weight %															
SiO_2	47.69	47.90	48.37	46.48	47.23	47.90	44.38	44.49	44.03	43.90	48.85	48.34	48.37	48.20	48.53
TiO_2	1.49	1.37	1.35	1.85	1.64	1.38	1.13	0.85	1.15	1.26	0.90	1.15	1.10	1.21	1.16
Al_2O_3	6.56	6.74	6.37	7.98	7.06	6.97	8.56	7.81	8.49	8.61	5.68	5.91	5.67	5.94	5.98
FeO	15.24	15.82	14.78	15.36	16.15	16.13	19.76	20.02	20.12	20.01	13.33	13.21	13.05	13.10	12.82
MnO	0.61	0.61	0.55	0.58	0.62	0.72	0.53	0.63	0.49	0.46	0.27	0.36	0.35	0.35	0.40
MgO	12.86	12.33	13.03	12.59	12.16	12.49	10.06	9.92	9.54	9.95	14.73	14.66	14.87	14.57	14.87
CaO	11.07	11.47	11.08	11.05	11.21	11.08	11.03	10.53	11.23	10.89	11.82	11.73	11.82	11.61	11.59
Na_2O	1.19	1.17	1.28	1.69	1.41	1.27	1.26	0.97	1.18	1.29	1.27	1.37	1.31	1.56	1.41
K_2O	0.54	0.61	0.52	0.62	0.61	0.61	1.00	0.81	1.00	0.97	0.61	0.65	0.63	0.62	0.63
F	0.00	0.00	0.00	0.00	0.00	0.00	0.00	0.00	0.00	0.00	0.00	0.00	0.00	0.00	0.00
Cl	0.00	0.00	0.00	0.00	0.00	0.00	0.00	0.00	0.00	0.00	0.00	0.00	0.00	0.00	0.00
Total	97.25	98.13	97.33	98.21	98.09	98.56	97.73	96.07	97.27	97.44	97.52	97.42	97.19	97.17	97.39
No. of oxygens	23	23	23	23	23	23	23	23	23	23	23	23	23	23	23
Si	6.97	7.00	7.05	6.76	6.90	6.93	6.61	6.69	6.63	6.56	7.09	7.03	7.05	7.03	7.04
Al^{iv}	1.03	1.00	0.95	1.24	1.10	1.07	1.39	1.31	1.37	1.44	0.91	0.97	0.95	0.97	0.96
Al^{vi}	0.10	0.16	0.15	0.13	0.12	0.12	0.11	0.08	0.13	0.08	0.06	0.04	0.02	0.06	0.06
Ti	0.16	0.15	0.15	0.20	0.18	0.15	0.13	0.10	0.13	0.14	0.10	0.13	0.12	0.13	0.13
Cr	0.00	0.00	0.00	0.00	0.00	0.00	0.00	0.00	0.00	0.00	0.00	0.00	0.00	0.00	0.00
Fe^{3+}	0.70	0.51	0.58	0.67	0.59	0.75	0.95	1.20	0.82	1.02	0.50	0.51	0.52	0.46	0.54
Fe^{2+}	1.16	1.42	1.22	1.20	1.38	1.20	1.51	1.32	1.71	1.48	1.12	1.10	1.07	1.14	1.01
Mn	0.08	0.08	0.07	0.07	0.08	0.09	0.07	0.08	0.06	0.06	0.03	0.04	0.04	0.04	0.05
Mg	2.80	2.68	2.83	2.73	2.65	2.69	2.23	2.23	2.14	2.22	3.19	3.18	3.23	3.17	3.21
Ca	1.73	1.79	1.73	1.72	1.76	1.72	1.76	1.70	1.81	1.74	1.84	1.83	1.84	1.82	1.80
Na	0.34	0.33	0.36	0.48	0.40	0.36	0.36	0.28	0.34	0.37	0.36	0.39	0.37	0.44	0.40
K	0.10	0.11	0.10	0.12	0.11	0.11	0.19	0.16	0.19	0.19	0.11	0.12	0.12	0.12	0.12
F	0.00	0.00	0.00	0.00	0.00	0.00	0.00	0.00	0.00	0.00	0.00	0.00	0.00	0.00	0.00
Cl	0.00	0.00	0.00	0.00	0.00	0.00	0.00	0.00	0.00	0.00	0.00	0.00	0.00	0.00	0.00
OH*	2.05	2.05	2.06	2.06	2.05	2.07	2.01	1.99	1.99	2.01	2.07	2.06	2.06	2.05	2.07
Total	17.17	17.24	17.19	17.31	17.27	17.19	17.31	17.14	17.35	17.30	17.31	17.33	17.33	17.37	17.31
P (kbars)	2.4	2.5	2.2	3.5	2.8	2.6	4.1	3.6	4.2	4.2	1.6	1.8	1.6	1.9	1.9
ΔNNO	1.11	0.88	1.14	0.80	0.77	0.99	0.40	0.62	0.22	0.38	1.69	1.60	1.69	1.53	1.65
$\log fO_2$	-13.24	-13.43	-13.42	-12.61	-13.27	-13.29	-12.99	-13.35	-13.18	-12.94	-12.74	-12.58	-12.54	-12.62	-12.53
ΔFMQ	1.31	1.57	1.42	1.24	1.44	1.43	1.52	1.50	1.66	1.65	2.56	2.82	2.65	2.56	2.65
T (°C)	777	779	768	821	791	781	821	794	821	825	774	786	783	787	785

Table A3-amphibole (Conti.)

Sample number	CB-1	CB-7	JR-5	JR-5	JR-5	JR-5	JR-5	JR-13	JR-13	JR-13	JR-13	JR-13	JR-13	JR-13	JR-13
Weight %															
SiO_2	48.36	48.89	44.50	44.68	44.52	44.25	43.87	43.87	42.99	44.18	44.68	43.33	43.41	42.83	42.82
TiO_2	1.14	1.08	2.38	1.81	1.89	2.04	1.84	1.80	1.95	1.87	1.86	2.05	2.00	2.19	2.00
Al_2O_3	6.26	5.49	10.31	11.28	12.12	11.62	11.26	11.51	12.51	11.73	11.59	11.84	11.35	12.29	12.48
FeO	12.81	13.03	11.33	8.45	8.30	9.41	9.47	8.79	10.84	8.30	7.43	9.60	9.23	10.06	9.63
MnO	0.46	0.71	0.16	0.14	0.07	0.11	0.10	0.09	0.09	0.10	0.08	0.11	0.14	0.05	0.07
MgO	14.78	15.11	15.21	17.08	16.88	16.31	16.44	16.05	15.03	16.56	17.02	15.79	16.10	15.20	15.45
CaO	11.56	11.38	11.06	10.97	10.73	11.00	11.01	11.05	10.93	10.95	11.02	11.38	11.03	11.28	11.32
Na_2O	1.49	1.39	2.56	2.66	2.75	2.75	2.69	2.42	2.59	2.56	2.58	2.65	2.72	2.68	2.65
K_2O	0.61	0.54	0.51	0.60	0.65	0.62	0.59	0.73	0.70	0.71	0.77	0.66	0.68	0.72	0.72
F	0.00	0.00	0.00	0.00	0.00	0.00	0.00	0.23	0.21	0.20	0.21	0.20	0.18	0.21	0.20
Cl	0.00	0.00	0.00	0.00	0.00	0.00	0.00	0.02	0.01	0.01	0.00	0.00	0.00	0.02	0.03
Total	97.55	97.62	98.16	97.74	98.07	98.16	97.31	96.56	97.85	97.17	97.24	97.61	96.84	97.52	97.38
No. of oxygens	23	23	23	23	23	23	23	23	23	23	23	23	23	23	23
Si	7.01	7.05	6.38	6.31	6.26	6.27	6.26	6.33	6.16	6.30	6.36	6.22	6.26	6.18	6.30
Al^{iv}	0.99	0.93	1.62	1.69	1.74	1.73	1.74	1.67	1.84	1.70	1.64	1.78	1.74	1.82	1.70
Al^{vi}	0.07	0.00	0.12	0.19	0.27	0.21	0.16	0.28	0.27	0.27	0.30	0.23	0.19	0.27	0.27
Ti	0.12	0.12	0.26	0.19	0.20	0.22	0.20	0.20	0.21	0.20	0.20	0.22	0.22	0.24	0.20
Cr	0.00	0.00	0.00	0.00	0.00	0.00	0.00	0.00	0.00	0.00	0.00	0.00	0.00	0.00	0.00
Fe^{3+}	0.55	0.74	0.79	0.95	0.96	0.88	0.96	0.77	0.95	0.84	0.74	0.74	0.82	0.70	0.84
Fe^{2+}	1.00	0.83	0.56	0.05	0.02	0.24	0.17	0.29	0.35	0.15	0.15	0.41	0.29	0.51	0.15
Mn	0.06	0.09	0.02	0.02	0.01	0.01	0.01	0.01	0.01	0.01	0.01	0.01	0.02	0.01	0.01
Mg	3.19	3.25	3.25	3.60	3.54	3.44	3.50	3.45	3.21	3.52	3.61	3.38	3.46	3.27	3.52
Ca	1.79	1.76	1.70	1.66	1.62	1.67	1.68	1.71	1.68	1.67	1.68	1.75	1.70	1.74	1.67
Na	0.42	0.39	0.71	0.73	0.75	0.76	0.74	0.68	0.72	0.71	0.71	0.74	0.76	0.75	0.71
K	0.11	0.10	0.09	0.11	0.12	0.11	0.11	0.13	0.13	0.13	0.14	0.12	0.12	0.13	0.13
F	0.00	0.00	0.00	0.00	0.00	0.00	0.00	0.11	0.10	0.09	0.09	0.09	0.08	0.09	0.09
Cl	0.00	0.00	0.00	0.00	0.00	0.00	0.00	0.00	0.00	0.00	0.00	0.00	0.00	0.01	0.01
OH*	2.07	2.08	2.09	2.12	2.13	2.12	2.10	1.89	1.90	1.91	1.91	1.91	1.92	1.90	1.90
Total	17.33	17.25	17.50	17.50	17.48	17.54	17.54	17.52	17.52	17.51	17.53	17.61	17.59	17.63	17.51
P (kbars)	2.1	1.4	5.3	5.9	6.6	6.2	6.0	6.3	7.0	6.4	6.2	6.5	6.2	6.9	6.4
ΔNNO	1.61	1.86	1.22	1.84	1.72	1.53	1.68	1.57	1.23	1.66	1.75	1.35	1.52	1.13	1.24
$\log fO_2$	-12.44	-12.46	-10.37	-9.33	-9.24	-9.51	-9.40	-9.53	-9.55	-9.36	-9.31	-9.44	-9.45	-9.51	-9.33
ΔFMQ	2.48	2.61	2.12	2.74	2.64	2.43	2.58	2.47	2.66	2.25	2.41	2.15	2.57	2.04	2.15
T (°C)	791	779	916	940	951	947	945	944	961	948	946	962	952	970	974

Table A3-amphibole (Conti.)

Sample number	JR-13	JR-13	JR-13	JR-13	JR-13	JR-13	JR-13	JR-13	JR-13	JR-13	JR-13	JR-13	CJ-4	QL-10	QL-10
Weight %															
SiO_2	43.93	42.85	43.82	44.06	43.32	43.49	43.91	43.49	44.13	43.81	44.53	43.39	47.36	48.97	49.87
TiO_2	2.10	2.25	2.06	2.04	2.32	1.84	1.83	1.87	1.81	1.94	1.96	1.96	1.31	0.91	0.83
Al_2O_3	11.40	12.41	11.88	12.44	12.34	12.41	12.20	12.63	11.98	12.51	11.09	12.18	7.24	5.43	5.15
FeO	10.56	10.02	8.44	9.15	10.09	8.31	8.47	7.78	8.08	8.48	8.84	9.70	12.73	12.23	12.29
MnO	0.16	0.09	0.10	0.08	0.11	0.06	0.08	0.08	0.08	0.07	0.12	0.11	0.49	0.36	0.40
MgO	15.17	15.15	16.21	15.08	15.32	16.57	16.31	16.51	16.52	16.43	16.56	15.95	14.15	15.14	15.35
CaO	10.96	11.30	11.35	10.62	11.06	10.80	10.70	10.51	10.71	10.91	10.97	10.59	11.56	11.60	11.81
Na_2O	2.47	2.57	2.59	2.43	2.61	2.71	2.70	2.73	2.63	2.67	2.51	2.56	1.40	1.38	1.26
K_2O	0.62	0.72	0.69	0.70	0.71	0.77	0.76	0.78	0.74	0.79	0.70	0.78	0.78	0.75	0.70
F	0.21	0.20	0.21	0.24	0.17	0.19	0.19	0.20	0.16	0.19	0.27	0.18	0.40	0.65	0.63
Cl	0.00	0.02	0.01	0.01	0.01	0.00	0.03	0.01	0.01	0.00	0.01	0.02	0.04	0.04	0.05
Total	97.57	97.58	97.36	96.86	98.05	97.15	97.17	96.59	96.84	97.80	97.56	97.41	97.46	97.46	98.33
No. of oxygens	23	23	23	23	23	23	23	23	23	23	23	23	23	23	23
Si	6.58	6.60	6.65	7.07	6.19	6.20	6.26	6.22	6.30	6.21	6.34	6.19	6.92	7.14	7.20
Al^{iv}	1.42	1.40	1.35	0.93	1.81	1.80	1.74	1.78	1.70	1.79	1.66	1.81	1.08	0.86	0.80
Al^{vi}	0.27	0.19	0.19	0.76	0.27	0.28	0.32	0.34	0.32	0.30	0.21	0.23	0.16	0.07	0.07
Ti	0.17	0.16	0.14	0.16	0.25	0.20	0.20	0.20	0.19	0.21	0.21	0.21	0.14	0.10	0.09
Cr	0.00	0.00	0.00	0.00	0.00	0.00	0.00	0.00	0.00	0.00	0.00	0.00	0.00	0.00	0.00
Fe^{3+}	0.50	0.57	0.61	0.00	0.80	0.93	0.87	0.92	0.86	0.88	0.86	1.08	0.48	0.43	0.41
Fe^{2+}	1.38	1.42	1.42	1.45	0.40	0.06	0.14	0.01	0.11	0.13	0.19	0.08	1.08	1.06	1.07
Mn	0.04	0.04	0.04	0.04	0.01	0.01	0.01	0.01	0.01	0.01	0.01	0.01	0.06	0.04	0.05
Mg	2.65	2.62	2.60	2.53	3.26	3.52	3.47	3.52	3.52	3.47	3.52	3.39	3.08	3.29	3.30
Ca	1.81	1.82	1.82	1.52	1.69	1.65	1.64	1.61	1.64	1.66	1.67	1.62	1.81	1.81	1.83
Na	0.53	0.51	0.46	0.44	0.72	0.75	0.75	0.76	0.73	0.73	0.69	0.71	0.40	0.39	0.35
K	0.18	0.16	0.18	0.46	0.13	0.14	0.14	0.14	0.13	0.14	0.13	0.14	0.15	0.14	0.13
F	0.09	0.11	0.10	0.09	0.08	0.09	0.08	0.09	0.07	0.09	0.12	0.08	0.18	0.30	0.29
Cl	0.00	0.00	0.00	0.00	0.00	0.00	0.01	0.00	0.00	0.00	0.00	0.00	0.01	0.01	0.01
OH*	1.91	1.89	1.90	1.91	1.92	1.91	1.91	1.91	1.93	1.91	1.88	1.92	1.81	1.69	1.70
Total	17.51	17.50	17.46	17.38	17.55	17.54	17.52	17.51	17.50	17.53	17.50	17.47	17.35	17.34	17.31
P (kbars)	5.0	4.5	4.3	5.1	6.9	6.9	6.8	7.1	6.6	6.9	5.9	6.7	2.9	1.4	1.2
ΔNNO	1.26	1.11	1.44	1.19	1.17	1.67	1.59	1.65	1.67	1.56	1.68	1.56	1.35	1.80	1.85
$\log fO_2$	-9.99	-9.52	-9.39	-9.90	-9.60	-9.05	-9.32	-9.07	-9.33	-9.17	-9.58	-9.35	-12.22	-12.70	-12.88
ΔFMQ	2.17	2.02	2.34	2.13	2.08	2.58	2.47	2.58	2.51	2.57	2.58	2.48	2.30	2.37	2.42
T (°C)	935	971	960	942	963	966	954	965	949	964	935	954	814	771	761

Table A3-amphibole (Conti.)

Sample number	QL-10	QL-10	QL-10	QL-10	QL-10	QL-10	QL-10	QL-10	QL-10	QL-10	QL-10	QL-10	QL-10	QL-10	JM11-36
Weight %															
SiO_2	49.37	48.49	48.98	48.99	48.76	49.15	49.13	48.80	49.37	48.48	49.90	49.37	49.69	49.76	48.18
TiO_2	1.07	1.07	0.91	1.10	1.13	0.91	1.07	1.03	0.99	0.87	0.87	0.82	0.86	0.85	0.97
Al_2O_3	5.43	6.06	5.54	5.76	5.85	5.62	5.45	5.92	5.49	5.56	5.13	5.12	5.21	5.07	6.21
FeO	12.05	12.57	12.52	12.46	12.54	12.52	12.01	12.57	11.69	12.04	12.00	11.91	11.78	11.78	14.03
MnO	0.34	0.38	0.40	0.38	0.37	0.33	0.37	0.39	0.36	0.36	0.42	0.38	0.35	0.41	0.46
MgO	15.43	14.61	14.87	14.75	15.21	14.87	15.10	14.83	15.27	15.29	15.50	15.59	15.45	15.43	13.98
CaO	11.89	11.82	11.80	12.00	11.80	11.86	11.68	11.78	11.93	12.04	11.79	12.00	11.56	11.83	11.69
Na_2O	1.32	1.36	1.41	1.32	1.57	1.27	1.41	1.44	1.22	1.36	1.33	1.33	1.42	1.34	1.45
K_2O	0.75	0.77	0.72	0.79	0.82	0.74	0.75	0.81	0.72	0.72	0.68	0.64	0.72	0.70	0.70
F	0.64	0.65	0.64	0.64	0.66	0.60	0.68	0.63	0.61	0.63	0.68	0.68	0.65	0.62	0.42
Cl	0.05	0.05	0.04	0.04	0.03	0.05	0.04	0.05	0.05	0.03	0.03	0.04	0.05	0.03	0.03
Total	98.34	97.83	97.83	98.23	98.73	97.91	97.69	98.24	97.70	97.39	98.32	97.87	97.74	97.82	98.12
No. of oxygens	23	23	23	23	23	23	23	23	23	23	23	23	23	23	23
Si	7.14	7.08	7.14	7.13	7.04	7.15	7.16	7.09	7.18	7.09	7.20	7.17	7.20	7.22	7.02
Al^{iv}	0.86	0.92	0.86	0.87	0.96	0.85	0.84	0.91	0.82	0.91	0.80	0.83	0.80	0.78	0.98
Al^{vi}	0.06	0.12	0.09	0.12	0.04	0.11	0.09	0.10	0.12	0.05	0.07	0.04	0.10	0.09	0.09
Ti	0.12	0.12	0.10	0.12	0.12	0.10	0.12	0.11	0.11	0.10	0.09	0.09	0.09	0.09	0.11
Cr	0.00	0.00	0.00	0.00	0.00	0.00	0.00	0.00	0.00	0.00	0.00	0.00	0.00	0.00	0.00
Fe^{3+}	0.38	0.34	0.35	0.25	0.43	0.35	0.33	0.36	0.30	0.37	0.40	0.38	0.39	0.32	0.49
Fe^{2+}	1.08	1.19	1.18	1.26	1.09	1.18	1.14	1.16	1.12	1.10	1.05	1.06	1.04	1.11	1.23
Mn	0.04	0.05	0.05	0.05	0.05	0.04	0.05	0.05	0.04	0.05	0.05	0.05	0.04	0.05	0.06
Mg	3.32	3.18	3.23	3.20	3.28	3.22	3.28	3.21	3.31	3.33	3.33	3.37	3.34	3.34	3.04
Ca	1.84	1.85	1.84	1.87	1.83	1.85	1.82	1.83	1.86	1.89	1.82	1.87	1.80	1.84	1.83
Na	0.37	0.38	0.40	0.37	0.44	0.36	0.40	0.41	0.34	0.39	0.37	0.37	0.40	0.38	0.41
K	0.14	0.14	0.13	0.15	0.15	0.14	0.14	0.15	0.13	0.14	0.12	0.12	0.13	0.13	0.13
F	0.29	0.30	0.29	0.29	0.30	0.28	0.31	0.29	0.28	0.29	0.31	0.31	0.30	0.29	0.19
Cl	0.01	0.01	0.01	0.01	0.01	0.01	0.01	0.01	0.01	0.01	0.01	0.01	0.01	0.01	0.01
OH*	1.70	1.69	1.70	1.69	1.69	1.71	1.68	1.70	1.71	1.70	1.69	1.68	1.69	1.71	1.80
Total	17.35	17.38	17.38	17.39	17.42	17.34	17.36	17.39	17.33	17.41	17.32	17.36	17.33	17.35	17.36
P (kbars)	1.4	2.0	1.5	1.7	1.7	1.6	1.4	1.8	1.5	1.6	1.1	1.2	1.2	1.1	2.1
ΔNNO	1.79	1.54	1.66	1.54	1.68	1.67	1.70	1.60	1.76	1.81	1.87	1.91	1.87	1.84	1.41
$\log fO_2$	-12.61	-12.61	-12.76	-12.74	-12.40	-12.79	-12.77	-12.61	-12.70	-12.35	-12.83	-12.60	-12.83	-12.85	-12.76
ΔFMQ	2.59	2.55	2.42	2.32	2.42	2.32	2.15	2.59	2.34	2.24	2.31	2.63	2.47	2.34	2.77
T (°C)	776	787	774	781	790	773	773	784	773	786	763	771	762	763	786

Table A3-amphibole (Conti.)

Sample number	JM11-36	JM11-36	JM11-36	JM11-36	JM11-36	JM11-36	JM11-36	JM11-36	JM11-36	JM11-36	JM11-36	JM11-36	JM11-36	JM11-36	JM11-36
Weight %															
SiO_2	48.11	49.11	48.74	49.21	49.30	49.12	48.20	47.67	49.12	48.79	48.56	47.62	48.75	47.79	48.45
TiO_2	1.12	0.98	1.00	0.92	0.94	1.00	1.01	1.28	0.91	1.06	1.07	1.16	0.95	0.96	0.95
Al_2O_3	5.93	5.79	6.02	5.73	5.71	5.82	6.40	6.76	5.69	5.86	6.25	6.25	5.62	6.00	6.53
FeO	14.02	13.53	13.74	13.55	13.24	13.60	14.22	14.07	13.34	13.52	13.90	13.99	13.36	13.75	14.04
MnO	0.45	0.49	0.43	0.38	0.47	0.40	0.44	0.47	0.47	0.38	0.44	0.39	0.41	0.50	0.47
MgO	14.14	14.23	14.14	14.42	14.43	14.13	13.81	13.63	14.51	13.84	13.66	13.82	14.62	14.11	13.95
CaO	11.64	11.42	11.51	11.54	11.58	11.56	11.61	11.61	11.54	11.53	11.63	11.57	11.63	11.41	11.73
Na_2O	1.45	1.30	1.33	1.24	1.29	1.39	1.42	1.54	1.36	1.32	1.38	1.43	1.34	1.52	1.41
K_2O	0.66	0.64	0.68	0.64	0.61	0.67	0.71	0.71	0.65	0.66	0.66	0.74	0.65	0.68	0.74
F	0.38	0.40	0.38	0.37	0.40	0.38	0.36	0.38	0.39	0.40	0.38	0.41	0.40	0.40	0.38
Cl	0.03	0.05	0.03	0.02	0.01	0.02	0.02	0.04	0.03	0.04	0.05	0.05	0.03	0.03	0.02
Total	97.93	97.93	98.00	98.01	97.98	98.09	98.20	98.15	98.01	97.39	97.98	97.43	97.75	97.13	98.67
No. of oxygens	23	23	23	23	23	23	23	23	23	23	23	23	23	23	23
Si	7.02	7.12	7.08	7.12	7.14	7.13	7.01	6.96	7.12	7.15	7.09	7.00	7.09	7.02	7.01
Al^{iv}	0.98	0.88	0.92	0.88	0.86	0.87	0.99	1.04	0.88	0.85	0.91	1.00	0.91	0.98	0.99
Al^{vi}	0.04	0.11	0.11	0.10	0.12	0.13	0.11	0.12	0.09	0.16	0.16	0.08	0.05	0.06	0.13
Ti	0.12	0.11	0.11	0.10	0.10	0.11	0.11	0.14	0.10	0.12	0.12	0.13	0.10	0.11	0.10
Cr	0.00	0.00	0.00	0.00	0.00	0.00	0.00	0.00	0.00	0.00	0.00	0.00	0.00	0.00	0.00
Fe^{3+}	0.53	0.51	0.51	0.53	0.46	0.40	0.50	0.45	0.50	0.34	0.37	0.48	0.53	0.57	0.48
Fe^{2+}	1.18	1.13	1.15	1.11	1.14	1.25	1.23	1.27	1.11	1.31	1.33	1.24	1.09	1.12	1.22
Mn	0.06	0.06	0.05	0.05	0.06	0.05	0.05	0.06	0.06	0.05	0.05	0.05	0.05	0.06	0.06
Mg	3.07	3.08	3.06	3.11	3.12	3.06	3.00	2.97	3.14	3.02	2.97	3.03	3.17	3.09	3.01
Ca	1.82	1.78	1.79	1.79	1.80	1.80	1.81	1.82	1.79	1.81	1.82	1.82	1.81	1.79	1.82
Na	0.41	0.37	0.37	0.35	0.36	0.39	0.40	0.44	0.38	0.37	0.39	0.41	0.38	0.43	0.40
K	0.12	0.12	0.13	0.12	0.11	0.12	0.13	0.13	0.12	0.12	0.12	0.14	0.12	0.13	0.14
F	0.17	0.18	0.18	0.17	0.18	0.17	0.17	0.17	0.18	0.18	0.17	0.19	0.18	0.18	0.17
Cl	0.01	0.01	0.01	0.00	0.00	0.00	0.01	0.01	0.01	0.01	0.01	0.01	0.01	0.01	0.00
OH*	1.82	1.80	1.82	1.83	1.81	1.82	1.83	1.82	1.81	1.81	1.81	1.79	1.81	1.81	1.82
Total	17.35	17.26	17.29	17.26	17.27	17.31	17.34	17.38	17.30	17.31	17.33	17.37	17.31	17.35	17.35
P (kbars)	1.8	1.7	1.9	1.6	1.6	1.7	2.2	2.5	1.6	1.8	2.1	2.1	1.6	1.9	2.3
ΔNNO	1.46	1.61	1.57	1.44	1.36	1.44	1.36	1.20	1.61	1.36	1.27	1.35	1.66	1.51	1.37
$\log fO_2$	-12.76	-13.03	-13.06	-13.14	-12.81	-13.14	-12.81	-12.67	-12.96	-13.23	-13.08	-12.73	-12.81	-12.71	-12.73
ΔFMQ	2.83	2.76	2.50	2.63	2.51	2.63	2.64	2.67	2.56	2.73	2.76	2.84	2.88	2.85	2.82
T (°C)	784	765	765	768	786	768	786	800	768	767	778	790	773	784	789

Table A3-magnetite and ilmenite (Conti.)

Sample number	WR-13-109	WR-13-109	WR-13-109	WR-13-109	WR-13-111	WR-13-111	WR-13-111	WR-13-111	WR-13-111	WR-13-111
Mineral	Magnetite	Ilmenite	Magnetite	Ilmenite	Magnetite	Ilmenite	Magnetite	Ilmenite	Magnetite	Ilmenite
Weight %										
SiO_2	0.08	0.09	0.08	2.10	0.11	0.03	0.09	0.05	0.02	0.05
TiO_2	11.48	47.70	9.67	47.98	9.67	43.79	7.67	50.24	7.66	47.68
Al_2O_3	2.37	0.05	0.41	0.54	5.14	0.05	4.90	0.03	2.61	0.03
FeO	76.10	40.19	78.04	32.54	76.42	34.97	77.84	35.55	70.87	36.32
MnO	2.48	9.05	2.90	12.89	2.18	9.61	2.28	12.25	1.99	9.71
MgO	0.05	0.06	0.01	0.07	0.26	0.29	0.04	0.06	0.16	0.31
CaO	0.02	0.03	0.03	2.07	0.06	0.02	0.02	0.07	0.03	0.02
Na_2O	0.00	0.00	0.03	0.00	0.00	0.01	0.00	0.00	0.00	0.04
K_2O	0.03	0.03	0.00	0.00	0.01	0.01	0.01	0.03	0.00	0.01
Cr_2O_3	0.44	0.20	0.00	0.03	0.02	0.02	0.05	0.00	0.08	0.06
Total	93.10	97.66	91.27	98.50	93.86	89.16	92.90	98.64	83.45	94.55
No. of oxygens	4	3	4	3	4	3	4	3	4	3
Si	0.00	0.00	0.00	0.05	0.00	0.00	0.00	0.00	0.00	0.00
Ti	0.33	0.92	0.29	0.91	0.27	0.93	0.22	0.97	0.25	0.95
Al	0.11	0.00	0.02	0.02	0.23	0.00	0.22	0.00	0.13	0.00
Fe^{3+}	1.21	0.14	1.40	0.06	1.22	0.14	1.33	0.06	1.37	0.08
Fe^{2+}	1.25	0.73	1.19	0.63	1.19	0.69	1.15	0.70	1.16	0.72
Mn	0.08	0.20	0.10	0.28	0.07	0.23	0.07	0.27	0.07	0.22
Mg	0.00	0.00	0.00	0.00	0.01	0.01	0.00	0.00	0.01	0.01
Ca	0.00	0.00	0.00	0.06	0.00	0.00	0.00	0.00	0.00	0.00
Na	0.00	0.00	0.00	0.00	0.00	0.00	0.00	0.00	0.00	0.00
K	0.00	0.00	0.00	0.00	0.00	0.00	0.00	0.00	0.00	0.00
Cr	0.01	0.00	0.00	0.00	0.00	0.00	0.00	0.00	0.00	0.00
Total:	3.00	2.00	3.00	2.00	3.00	2.00	3.00	2.00	3.00	2.00
Temperature	781.78		641.28		758.98		625.91		669.45	
fO_2		-14.68		-20.11		-14.99		-20.24		-18.28

Table A3-magnetite and ilmenite (Conti.)

Sample number	WR-13-15	WR-13-15	WR-13-15	WR-13-15	WR-13-15	WR-13-15	WR-13-15	WR-13-15	BPzk303	BPzk303
Mineral	Magnetite	Ilmenite	Magnetite	Ilmenite	Magnetite	Ilmenite	Magnetite	Ilmenite	Magnetite	Ilmenite
Weight %										
SiO_2	0.83	0.15	0.70	0.05	0.82	0.05	0.51	0.05	0.06	0.06
TiO_2	3.27	47.03	3.79	45.07	2.76	44.45	3.16	47.48	19.12	42.38
Al_2O_3	0.76	0.10	0.85	0.12	1.07	0.13	0.90	0.09	0.10	0.01
FeO	84.23	43.10	82.52	45.48	84.07	47.32	84.07	43.28	70.75	47.60
MnO	0.09	0.90	0.15	0.90	0.17	0.89	0.12	0.69	0.67	5.90
MgO	0.30	2.03	0.69	2.46	0.31	1.54	0.66	2.73	0.00	0.05
CaO	0.02	0.01	0.02	0.01	0.01	0.00	0.01	0.01	0.00	0.03
Na_2O	0.04	0.02	0.08	0.03	0.01	0.03	0.03	0.04	0.00	0.05
K_2O	0.02	0.02	0.03	0.03	0.03	0.02	0.01	0.03	0.00	0.00
Cr_2O_3	0.07	0.00	0.05	0.00	0.00	0.00	0.10	0.00	0.00	0.00
Total	89.69	93.60	88.87	94.38	89.26	94.67	89.58	94.66	90.70	96.08
No. of oxygens	4	3	4	3	4	3	4	3	4	3
Si	0.03	0.00	0.03	0.00	0.03	0.00	0.02	0.00	0.00	0.00
Ti	0.10	0.94	0.11	0.88	0.08	0.88	0.09	0.93	0.58	0.83
Al	0.04	0.00	0.04	0.00	0.05	0.00	0.04	0.00	0.00	0.00
Fe^{3+}	1.70	0.11	1.67	0.22	1.72	0.24	1.72	0.13	0.83	0.34
Fe^{2+}	1.11	0.84	1.09	0.77	1.09	0.80	1.07	0.81	1.56	0.70
Mn	0.00	0.02	0.00	0.02	0.01	0.02	0.00	0.02	0.02	0.13
Mg	0.02	0.08	0.04	0.10	0.02	0.06	0.04	0.11	0.00	0.00
Ca	0.00	0.00	0.00	0.00	0.00	0.00	0.00	0.00	0.00	0.00
Na	0.00	0.00	0.01	0.00	0.00	0.00	0.00	0.00	0.00	0.00
K	0.00	0.00	0.00	0.00	0.00	0.00	0.00	0.00	0.00	0.00
Cr	0.00	0.00	0.00	0.00	0.00	0.00	0.00	0.00	0.00	0.00
Total:	3.00	2.00	3.00	2.00	3.00	2.00	3.00	2.00	3.00	2.00
Temperature	630.38		708.46		694.93		637.23		1192.8	
fO_2		-17.94		-14.48		-14.45		-17.23		-7.13

Table A3-pyroxene (Conti.)

Sample number	WR-12-30	WR-12-30	WR-12-30	WR-12-30	WR-12-30	WR-12-30	WR-12-30	WR-12-30	WR-12-30	WR-12-30	WR-12-30	WR-12-30	WR-12-30	WR-12-30	WR-12-30
Final name:	diopside	augite	augite	augite	augite	augite	augite	augite	augite	augite	augite	augite	augite	augite	augite
Weight %															
SiO_2	51.19	52.86	52.97	52.00	52.79	53.00	52.99	52.94	53.04	53.10	53.18	52.80	53.30	53.58	53.80
TiO_2	0.14	0.17	0.19	0.31	0.30	0.20	0.30	0.20	0.19	0.34	0.31	0.32	0.32	0.30	0.29
Al_2O_3	0.39	0.37	0.42	0.40	0.77	0.48	0.83	0.48	0.45	0.81	0.93	0.92	0.85	0.83	0.92
Cr_2O_3	0.09	0.04	0.01	0.00	0.01	0.04	0.00	0.00	0.00	0.02	0.01	0.00	0.01	0.01	0.00
FeO	12.32	12.39	12.41	12.75	12.14	12.68	12.31	12.18	12.69	11.78	11.07	11.49	11.72	11.78	13.07
MnO	0.84	0.81	0.75	0.78	0.74	0.84	0.82	0.76	0.88	0.73	0.71	0.46	0.50	0.52	0.51
MgO	11.59	12.23	12.19	12.29	12.33	12.22	12.19	12.25	12.22	12.30	12.40	12.37	12.41	12.76	12.93
CaO	21.25	21.36	21.10	20.81	20.85	20.70	20.64	20.84	20.61	20.88	21.41	21.24	21.21	20.93	19.50
Na_2O	0.27	0.27	0.23	0.24	0.28	0.23	0.33	0.27	0.30	0.30	0.33	0.32	0.32	0.29	0.26
K_2O	0.01	0.00	0.00	0.02	0.00	0.00	0.00	0.00	0.00	0.01	0.00	0.00	0.00	0.00	0.00
Total	98.10	100.51	100.27	99.59	100.21	100.39	100.41	99.91	100.38	100.27	100.35	99.91	100.65	100.99	101.28
No. of oxygens	6	6	6	6	6	6	6	6	6	6	6	6	6	6	6
Si	1.98	1.99	2.00	1.98	1.99	2.00	2.00	2.01	2.00	2.00	2.00	1.99	2.00	2.00	2.01
Ti	0.00	0.00	0.01	0.01	0.01	0.01	0.01	0.01	0.01	0.01	0.01	0.01	0.01	0.01	0.01
Al	0.02	0.02	0.02	0.02	0.03	0.02	0.04	0.02	0.02	0.04	0.04	0.04	0.04	0.04	0.04
Cr	0.00	0.00	0.00	0.00	0.00	0.00	0.00	0.00	0.00	0.00	0.00	0.00	0.00	0.00	0.00
Fe^{3+}	0.03	0.01	-0.02	0.03	-0.02	-0.02	-0.02	-0.02	-0.01	-0.04	-0.03	-0.02	-0.03	-0.04	-0.05
Fe^{2+}	0.37	0.38	0.41	0.38	0.40	0.42	0.41	0.41	0.41	0.41	0.38	0.38	0.40	0.40	0.46
Mn	0.03	0.03	0.02	0.03	0.02	0.03	0.03	0.02	0.03	0.02	0.02	0.01	0.02	0.02	0.02
Mg	0.67	0.69	0.69	0.70	0.69	0.69	0.69	0.69	0.69	0.69	0.69	0.70	0.69	0.71	0.72
Ca	0.88	0.86	0.85	0.85	0.84	0.84	0.83	0.85	0.83	0.84	0.86	0.86	0.85	0.84	0.78
Na	0.02	0.02	0.02	0.02	0.02	0.02	0.02	0.02	0.02	0.02	0.02	0.02	0.02	0.02	0.02
K	0.00	0.00	0.00	0.00	0.00	0.00	0.00	0.00	0.00	0.00	0.00	0.00	0.00	0.00	0.00
Total	4.00	4.00	4.00	4.00	4.00	4.00	4.00	4.00	4.00	4.00	4.00	4.00	4.00	4.00	4.00
$Mg/(Mg+Fe^{2+})$	0.65	0.64	0.63	0.65	0.64	0.62	0.62	0.63	0.62	0.63	0.65	0.64	0.63	0.64	0.61
En	0.35	0.36	0.35	0.36	0.36	0.35	0.35	0.36	0.36	0.36	0.36	0.36	0.36	0.36	0.37
Fs	0.19	0.20	0.21	0.20	0.21	0.22	0.21	0.21	0.21	0.21	0.20	0.20	0.21	0.21	0.24
Wo	0.46	0.45	0.44	0.44	0.44	0.43	0.43	0.43	0.43	0.43	0.45	0.44	0.44	0.43	0.40

Table A3-pyroxene (Conti.)

Sample number	WR-12-30	WR-13-109	WR-13-109	WR-13-109	WR-13-109	QS-2	QS-9	QS-9	QS-9	QS-9	QS-9	QS-9	QS-9	QS-9
Final name:	augite	enstatite	enstatite	enstatite	enstatite	augite	diopside	diopside	diopside	diopside	augite	augite	diopside	diopside
Weight %														
SiO_2	53.56	54.03	54.05	53.30	53.94	50.63	51.61	51.16	50.74	51.13	50.38	51.84	51.63	52.06
TiO_2	0.32	0.21	0.21	0.28	0.22	0.07	0.10	0.13	0.15	0.12	0.09	0.08	0.28	0.27
Al_2O_3	0.79	1.00	1.30	1.64	1.02	0.83	0.77	0.99	0.95	0.91	0.82	0.84	1.29	1.38
Cr_2O_3	0.02	0.00	0.00	0.00	0.00	0.02	0.01	0.00	0.00	0.00	0.00	0.00	0.00	0.01
FeO	12.36	16.91	16.79	17.23	16.78	16.41	13.48	12.66	12.73	13.24	15.44	14.62	12.67	13.06
MnO	0.58	0.54	0.49	0.50	0.54	0.77	0.77	0.55	0.64	0.76	0.79	0.80	0.46	0.65
MgO	13.13	26.69	26.37	26.27	26.33	11.69	11.17	11.67	11.38	11.22	11.48	11.34	12.07	11.16
CaO	19.84	1.38	1.32	1.35	1.38	18.33	21.55	22.07	22.10	21.84	19.84	20.43	21.88	21.68
Na_2O	0.29	0.01	0.06	0.04	0.03	0.29	0.32	0.38	0.35	0.36	0.28	0.33	0.39	0.40
K_2O	0.00	0.00	0.01	0.00	0.00	0.01	0.00	0.01	0.01	0.00	0.01	0.00	0.01	0.00
Total	100.91	100.77	100.60	100.61	100.24	99.07	99.79	99.62	99.05	99.61	99.18	100.28	100.72	100.68
No. of oxygens	6	6	6	6	6	6	6	6	6	6	6	6	6	6
Si	2.00	1.94	1.95	1.92	1.95	1.95	1.97	1.94	1.94	1.95	1.94	1.97	1.94	1.96
Ti	0.01	0.01	0.01	0.01	0.01	0.00	0.00	0.00	0.00	0.00	0.00	0.00	0.01	0.01
Al	0.03	0.04	0.06	0.07	0.04	0.04	0.03	0.04	0.04	0.04	0.04	0.04	0.06	0.06
Cr	0.00	0.00	0.00	0.00	0.00	0.00	0.00	0.00	0.00	0.00	0.00	0.00	0.00	0.00
Fe^{3+}	-0.04	0.06	0.04	0.08	0.04	0.07	0.05	0.09	0.09	0.08	0.10	0.04	0.08	0.02
Fe^{2+}	0.42	0.45	0.46	0.44	0.46	0.46	0.38	0.31	0.32	0.35	0.40	0.42	0.32	0.39
Mn	0.02	0.02	0.01	0.02	0.02	0.03	0.02	0.02	0.02	0.02	0.03	0.03	0.01	0.02
Mg	0.73	1.43	1.42	1.41	1.42	0.67	0.64	0.66	0.65	0.64	0.66	0.64	0.68	0.63
Ca	0.79	0.05	0.05	0.05	0.05	0.76	0.88	0.90	0.91	0.89	0.82	0.83	0.88	0.88
Na	0.02	0.00	0.00	0.00	0.00	0.02	0.02	0.03	0.03	0.03	0.02	0.02	0.03	0.03
K	0.00	0.00	0.00	0.00	0.00	0.00	0.00	0.00	0.00	0.00	0.00	0.00	0.00	0.00
Total	4.00	4.00	4.00	4.00	4.00	4.00	4.00	4.00	4.00	4.00	4.00	4.00	4.00	4.00
$Mg/(Mg+Fe^{2+})$	0.63	0.76	0.75	0.76	0.75	0.60	0.62	0.68	0.67	0.65	0.62	0.60	0.68	0.62
En	0.38	0.74	0.73	0.74	0.73	0.36	0.33	0.35	0.35	0.34	0.35	0.34	0.36	0.33
Fs	0.22	0.23	0.24	0.23	0.24	0.24	0.20	0.17	0.17	0.18	0.21	0.22	0.17	0.21
Wo	0.41	0.03	0.03	0.03	0.03	0.40	0.46	0.48	0.48	0.48	0.44	0.44	0.47	0.46

Table A3-pyroxene (Conti.)

Sample number	QS-9	QS-9	QS-9	QS-9	QS-9	QS-9	QS-9	QS-9	QS-9	QS-9	QS-9	QS-9	QS-9	QS-9	QS-9
Final name:	diopside	diopside	diopside	diopside	diopside	diopside	ferro-silite	ferro-silite	ferro-silite	ferro-silite	ferro-silite	ferro-silite	ferro-silite	ferro-silite	ferro-silite
Weight %															
SiO_2	51.30	51.46	51.81	51.43	51.01	51.73	49.45	50.39	49.94	50.16	50.45	50.71	50.86	50.73	50.36
TiO_2	0.10	0.12	0.16	0.30	0.17	0.05	0.16	0.07	0.16	0.22	0.13	0.21	0.08	0.11	0.12
Al_2O_3	0.96	0.97	1.09	1.66	1.10	0.79	0.51	0.36	0.61	0.58	0.62	0.63	0.47	0.49	0.48
Cr_2O_3	0.00	0.00	0.01	0.03	0.00	0.01	0.00	0.00	0.01	0.01	0.01	0.00	0.00	0.03	0.04
FeO	12.53	12.66	12.72	12.26	13.35	13.82	32.00	31.68	32.11	31.55	31.64	31.26	31.59	31.70	31.12
MnO	0.52	0.55	0.69	0.48	0.76	0.78	2.07	2.05	1.99	1.78	1.88	1.77	1.89	1.82	2.03
MgO	11.22	11.38	11.27	11.55	11.22	10.97	14.49	14.70	14.23	14.80	14.79	15.05	15.00	14.85	14.72
CaO	22.31	22.34	21.95	21.79	21.57	21.36	1.06	1.09	1.09	1.04	1.10	1.10	0.81	1.00	0.86
Na_2O	0.39	0.34	0.39	0.36	0.36	0.31	0.04	0.04	0.04	0.04	0.03	0.02	0.00	0.03	0.00
K_2O	0.02	0.02	0.00	0.02	0.00	0.00	0.01	0.00	0.00	0.00	0.00	0.01	0.00	0.00	0.00
Total	99.35	99.84	100.10	99.88	99.57	99.88	99.82	100.39	100.19	100.18	100.67	100.78	100.69	100.78	99.75
No. of oxygens	6	6	6	6	6	6	6	6	6	6	6	6	6	6	6
Si	1.96	1.95	1.96	1.95	1.95	1.98	1.95	1.97	1.96	1.96	1.97	1.97	1.98	1.97	1.98
Ti	0.00	0.00	0.00	0.01	0.00	0.00	0.00	0.00	0.00	0.01	0.00	0.01	0.00	0.00	0.00
Al	0.04	0.04	0.05	0.07	0.05	0.04	0.02	0.02	0.03	0.03	0.03	0.03	0.02	0.02	0.02
Cr	0.00	0.00	0.00	0.00	0.00	0.00	0.00	0.00	0.00	0.00	0.00	0.00	0.00	0.00	0.00
Fe^{3+}	0.07	0.07	0.04	0.04	0.07	0.03	0.07	0.04	0.04	0.03	0.03	0.02	0.01	0.02	0.01
Fe^{2+}	0.33	0.33	0.36	0.35	0.35	0.41	0.98	1.00	1.02	1.00	1.00	1.00	1.02	1.01	1.02
Mn	0.02	0.02	0.02	0.02	0.02	0.03	0.07	0.07	0.07	0.06	0.06	0.06	0.06	0.06	0.07
Mg	0.64	0.64	0.64	0.65	0.64	0.62	0.85	0.86	0.83	0.86	0.86	0.87	0.87	0.86	0.86
Ca	0.91	0.91	0.89	0.88	0.88	0.87	0.04	0.05	0.05	0.04	0.05	0.05	0.03	0.04	0.04
Na	0.03	0.02	0.03	0.03	0.03	0.02	0.00	0.00	0.00	0.00	0.00	0.00	0.00	0.00	0.00
K	0.00	0.00	0.00	0.00	0.00	0.00	0.00	0.00	0.00	0.00	0.00	0.00	0.00	0.00	0.00
Total	4.00	4.00	4.00	4.00	4.00	4.00	4.00	4.00	4.00	4.00	4.00	4.00	4.00	4.00	4.00
$Mg/(Mg+Fe^{2+})$	0.66	0.66	0.64	0.65	0.64	0.61	0.46	0.46	0.45	0.46	0.46	0.47	0.46	0.46	0.46
En	0.34	0.34	0.34	0.35	0.34	0.33	0.45	0.45	0.44	0.45	0.45	0.46	0.45	0.45	0.45
Fs	0.18	0.18	0.19	0.19	0.19	0.21	0.52	0.52	0.54	0.52	0.52	0.52	0.53	0.53	0.53
Wo	0.48	0.48	0.47	0.47	0.47	0.46	0.02	0.02	0.02	0.02	0.02	0.02	0.02	0.02	0.02

Table A3-pyroxene (Conti.)

Sample number	QS-9	QS-9	QS-9	WR-13-122	WR-13-122	WR-13-122	WR-13-122	WR-13-122	WR-13-122	WR-13-122	WR-13-122	WR-13-122	WR-13-122	WR-13-122	WR-13-122
Final name:	ferro-silite	ferro-silite	pigeonite	augite	augite	augite	augite	diopside	augite	augite	augite	augite	augite	augite	diopside
Weight %															
SiO_2	50.45	50.37	50.89	53.78	52.64	52.93	51.77	52.59	51.53	51.57	51.49	50.94	52.09	51.40	50.02
TiO_2	0.09	0.13	0.20	0.22	0.32	0.34	0.39	0.42	0.45	0.40	0.43	0.40	0.47	0.39	0.57
Al_2O_3	0.48	0.64	0.81	1.06	1.67	1.49	2.01	1.83	2.27	2.28	2.07	1.74	1.80	1.93	3.27
Cr_2O_3	0.00	0.03	0.00	0.03	0.16	0.00	0.00	0.00	0.00	0.00	0.00	0.00	0.04	0.00	0.00
FeO	31.22	31.87	29.76	4.96	5.10	6.13	8.65	6.42	9.30	9.22	9.82	10.78	9.98	9.56	8.37
MnO	2.05	1.88	1.41	0.19	0.16	0.19	0.29	0.15	0.37	0.37	0.40	0.36	0.37	0.36	0.22
MgO	14.63	15.00	14.10	18.52	17.34	16.92	15.67	16.60	14.52	14.61	14.65	14.36	14.40	14.51	14.63
CaO	0.81	1.00	2.61	20.74	21.46	21.41	20.06	21.54	20.31	20.38	20.06	19.68	20.00	20.34	20.69
Na_2O	0.05	0.06	0.05	0.32	0.38	0.41	0.62	0.41	0.73	0.60	0.77	0.65	0.64	0.68	0.58
K_2O	0.00	0.00	0.00	0.01	0.01	0.01	0.01	0.00	0.00	0.00	0.00	0.00	0.01	0.01	0.00
Total	99.80	100.99	99.84	99.82	99.24	99.83	99.46	99.95	99.48	99.43	99.68	98.91	99.79	99.18	98.35
No. of oxygens	6	6	6	6	6	6	6	6	6	6	6	6	6	6	6
Si	1.98	1.96	2.00	1.96	1.93	1.94	1.92	1.93	1.92	1.92	1.91	1.92	1.94	1.92	1.88
Ti	0.00	0.00	0.01	0.01	0.01	0.01	0.01	0.01	0.01	0.01	0.01	0.01	0.01	0.01	0.02
Al	0.02	0.03	0.04	0.05	0.07	0.06	0.09	0.08	0.10	0.10	0.09	0.08	0.08	0.09	0.14
Cr	0.00	0.00	0.00	0.00	0.00	0.00	0.00	0.00	0.00	0.00	0.00	0.00	0.00	0.00	0.00
Fe^{3+}	0.01	0.06	-0.04	0.05	0.07	0.07	0.10	0.07	0.09	0.08	0.11	0.12	0.06	0.10	0.11
Fe^{2+}	1.02	0.98	1.01	0.10	0.09	0.12	0.17	0.12	0.20	0.21	0.19	0.22	0.25	0.20	0.15
Mn	0.07	0.06	0.05	0.01	0.01	0.01	0.01	0.00	0.01	0.01	0.01	0.01	0.01	0.01	0.01
Mg	0.86	0.87	0.82	1.00	0.95	0.92	0.87	0.91	0.81	0.81	0.81	0.81	0.80	0.81	0.82
Ca	0.03	0.04	0.11	0.81	0.84	0.84	0.80	0.85	0.81	0.81	0.80	0.79	0.80	0.81	0.83
Na	0.00	0.00	0.00	0.02	0.03	0.03	0.04	0.03	0.05	0.04	0.06	0.05	0.05	0.05	0.04
K	0.00	0.00	0.00	0.00	0.00	0.00	0.00	0.00	0.00	0.00	0.00	0.00	0.00	0.00	0.00
Total	4.00	4.00	4.00	4.00	4.00	4.00	4.00	4.00	4.00	4.00	4.00	4.00	4.00	4.00	4.00
$Mg/(Mg+Fe^{2+})$	0.46	0.47	0.45	0.91	0.92	0.89	0.84	0.88	0.80	0.80	0.81	0.78	0.76	0.80	0.84
En	0.45	0.46	0.42	0.53	0.50	0.49	0.47	0.48	0.44	0.44	0.45	0.44	0.43	0.44	0.45
Fs	0.53	0.52	0.52	0.05	0.05	0.06	0.09	0.07	0.11	0.11	0.11	0.12	0.14	0.11	0.08
Wo	0.02	0.02	0.06	0.42	0.45	0.45	0.44	0.45	0.45	0.44	0.44	0.44	0.43	0.45	0.46

Table A3-pyroxene (Conti.)

Sample number	WR-13-122	WR-13-122	WR-13-122
Final name:	diopside	diopside	diopside
Weight %			
SiO_2	53.63	52.32	52.34
TiO_2	0.28	0.28	0.31
Al_2O_3	1.12	1.41	1.28
Cr_2O_3	0.07	0.00	0.14
FeO	4.09	7.06	6.92
MnO	0.12	0.24	0.21
MgO	17.62	15.90	16.24
CaO	22.21	21.38	21.23
Na_2O	0.39	0.56	0.55
K_2O	0.01	0.00	0.01
Total	99.54	99.15	99.22
No. of oxygens	6	6	6
Si	1.96	1.94	1.94
Ti	0.01	0.01	0.01
Al	0.05	0.06	0.06
Cr	0.00	0.00	0.00
Fe^{3+}	0.05	0.09	0.09
Fe^{2+}	0.08	0.13	0.12
Mn	0.00	0.01	0.01
Mg	0.96	0.88	0.90
Ca	0.87	0.85	0.84
Na	0.03	0.04	0.04
K	0.00	0.00	0.00
Total	4.00	4.00	4.00
$Mg/(Mg+Fe^{2+})$	0.93	0.87	0.88
En	0.50	0.47	0.48
Fs	0.04	0.07	0.07
Wo	0.46	0.46	0.45

Table A3-plagioclase (Conti.)

Sample number	WR-13-109	WR-13-109	WR-13-109	WR-13-109	WR-13-109	WR-13-109	WR-13-109	WR-13-109	WR-13-109	WR-13-109	WR-13-111	WR-13-111	WR-13-111	WR-13-111	QS-2	QS-2	QS-9
Weight %																	
SiO_2	64.78	64.64	46.05	47.86	46.42	47.43	46.07	46.71	49.28	46.00	48.68	50.15	47.48	47.67	60.16	63.08	55.70
TiO_2	0.03	0.02	0.03	0.03	0.42	0.02	0.00	0.02	0.02	0.03	0.04	0.02	0.04	0.04	0.00	0.01	0.00
Al_2O_3	20.32	21.02	33.50	32.45	31.37	32.61	33.14	32.44	31.52	33.57	31.68	30.67	32.40	32.44	23.85	17.93	26.28
FeO	0.13	0.12	0.46	0.56	2.70	0.49	0.47	0.58	0.62	0.47	0.57	0.51	0.59	0.50	0.13	0.04	0.13
MnO	0.02	0.00	0.01	0.02	0.04	0.02	0.03	0.01	0.01	0.00	0.01	0.03	0.00	0.01	0.02	0.00	0.03
MgO	0.01	0.00	0.04	0.05	0.06	0.04	0.04	0.30	0.07	0.02	0.07	0.12	0.05	0.04	0.02	0.01	0.02
CaO	2.05	2.49	17.51	16.22	15.31	16.40	17.16	16.39	14.95	17.56	15.03	14.16	16.07	16.39	6.22	0.03	9.47
Na_2O	7.66	8.84	1.47	2.27	2.42	2.08	1.67	2.04	2.59	1.48	2.55	3.14	2.23	2.07	7.93	1.10	6.01
K_2O	3.11	1.38	0.02	0.03	0.02	0.03	0.03	0.13	0.47	0.02	0.08	0.10	0.04	0.05	0.18	15.04	0.20
Total	98.12	98.51	99.09	99.49	98.76	99.13	98.61	98.62	99.54	99.14	98.71	98.90	98.90	99.20	98.50	97.24	97.84
No. of oxygens	8	8	8	8	8	8	8	8	8	8	8	8	8	8	8	8	8
Si	2.64	2.62	1.86	1.92	1.88	1.91	1.87	1.89	1.98	1.86	1.97	2.03	1.92	1.92	2.44	2.59	2.28
Al	1.10	1.14	1.80	1.74	1.69	1.75	1.79	1.75	1.69	1.81	1.71	1.65	1.75	1.74	1.29	0.98	1.43
Ti	0.00	0.00	0.00	0.00	0.02	0.00	0.00	0.00	0.00	0.00	0.00	0.00	0.00	0.00	0.00	0.00	0.00
Fe	0.01	0.01	0.04	0.04	0.22	0.04	0.04	0.05	0.05	0.04	0.05	0.04	0.05	0.04	0.01	0.00	0.01
Mn	0.00	0.00	0.00	0.00	0.00	0.00	0.00	0.00	0.00	0.00	0.00	0.00	0.00	0.00	0.00	0.00	0.00
Mg	0.00	0.00	0.00	0.00	0.00	0.00	0.00	0.02	0.01	0.00	0.01	0.01	0.00	0.00	0.00	0.00	0.00
Ca	0.17	0.20	1.41	1.30	1.24	1.32	1.39	1.33	1.20	1.42	1.22	1.15	1.30	1.32	0.51	0.00	0.77
Na	1.25	1.44	0.24	0.37	0.39	0.34	0.27	0.33	0.42	0.24	0.41	0.51	0.36	0.33	1.29	0.18	0.98
K	0.51	0.22	0.00	0.01	0.00	0.00	0.01	0.02	0.08	0.00	0.01	0.02	0.01	0.01	0.03	2.47	0.03
An	8.69	10.86	85.45	77.88	75.82	79.53	83.43	79.06	70.97	85.42	74.11	68.62	77.99	79.49	27.73	0.09	43.25
Ab	64.94	77.10	14.35	21.80	23.97	20.17	16.24	19.68	24.59	14.40	25.15	30.44	21.65	20.08	70.70	6.83	54.90
Or	26.37	12.04	0.20	0.33	0.21	0.29	0.33	1.26	4.44	0.18	0.74	0.94	0.36	0.44	1.57	93.08	1.85

Table A3-plagioclase (Conti.)

Sample number	QS-9	QS-9	QS-9	QS-9	QS-9	QS-9	QS-9	QS-9	QS-9	QS-9	KMQ-12-2	KMQ-12-2	KMQ-12-2	RD-12-5	RD-12-5	RD-12-5	RD-12-5
Weight %																	
SiO_2	59.38	57.18	59.29	60.07	58.78	58.63	58.82	59.00	58.97	64.27	47.63	48.05	58.14	55.98	64.35	61.42	66.23
TiO_2	0.00	0.02	0.02	0.01	0.00	0.01	0.01	0.03	0.02	0.02	0.08	0.10	0.12	0.11	0.09	0.09	0.09
Al_2O_3	23.94	26.13	24.72	24.35	25.18	25.40	25.43	25.44	25.05	18.41	33.01	32.72	25.88	28.22	22.29	24.31	21.84
FeO	0.33	0.17	0.12	0.10	0.31	0.13	0.38	0.36	0.24	0.02	0.28	0.32	0.27	0.08	0.04	0.23	0.31
MnO	0.00	0.02	0.01	0.02	0.02	0.02	0.00	0.02	0.00	0.02	0.00	0.02	0.01	0.01	0.02	0.02	0.00
MgO	0.00	0.01	0.01	0.01	0.02	0.02	0.02	0.01	0.02	0.01	0.00	0.02	0.02	0.00	0.01	0.02	0.00
CaO	6.87	8.75	7.18	6.26	7.54	7.63	7.66	7.44	7.34	0.10	14.01	13.54	6.73	9.93	3.59	4.29	2.59
Na_2O	7.40	6.34	7.26	7.77	7.07	7.02	7.16	7.06	7.29	1.10	1.93	2.30	6.90	5.83	9.50	8.13	10.21
K_2O	0.37	0.34	0.41	0.22	0.30	0.33	0.26	0.26	0.28	14.93	0.03	0.06	0.05	0.14	0.35	0.54	0.48
Total	98.29	98.95	99.02	98.81	99.22	99.19	99.73	99.61	99.21	98.88	97.13	97.26	98.22	100.30	100.23	99.05	101.74
No. of oxygens	8	8	8	8	8	8	8	8	8	8	8	8	8	8	8	8	8
Si	2.42	2.31	2.40	2.43	2.37	2.36	2.36	2.37	2.38	2.60	1.96	1.98	2.37	2.23	2.57	2.48	2.60
Al	1.30	1.41	1.33	1.31	1.35	1.37	1.36	1.36	1.35	0.99	1.82	1.80	1.41	1.50	1.19	1.31	1.14
Ti	0.00	0.00	0.00	0.00	0.00	0.00	0.00	0.00	0.00	0.00	0.00	0.00	0.00	0.00	0.00	0.00	0.00
Fe	0.03	0.01	0.01	0.01	0.02	0.01	0.03	0.03	0.02	0.00	0.02	0.03	0.02	0.01	0.00	0.02	0.02
Mn	0.00	0.00	0.00	0.00	0.00	0.00	0.00	0.00	0.00	0.00	0.00	0.00	0.00	0.00	0.00	0.00	0.00
Mg	0.00	0.00	0.00	0.00	0.00	0.00	0.00	0.00	0.00	0.00	0.00	0.00	0.00	0.00	0.00	0.00	0.00
Ca	0.56	0.71	0.58	0.51	0.61	0.62	0.61	0.60	0.59	0.01	1.16	1.12	0.55	0.79	0.29	0.35	0.20
Na	1.20	1.03	1.17	1.26	1.14	1.13	1.15	1.13	1.18	0.18	0.32	0.38	1.12	0.93	1.52	1.31	1.61
K	0.06	0.05	0.07	0.03	0.05	0.05	0.04	0.04	0.05	2.42	0.00	0.01	0.01	0.02	0.06	0.09	0.07
An	30.66	39.57	31.89	28.16	33.83	34.17	34.05	33.70	32.65	0.30	78.19	74.16	32.65	45.39	15.42	19.84	10.81
Ab	66.06	57.35	64.49	69.91	63.44	62.87	63.66	63.96	64.85	6.85	21.49	25.23	66.88	53.30	81.62	75.21	85.23
Or	3.28	3.08	3.62	1.93	2.73	2.96	2.29	2.34	2.51	92.85	0.32	0.60	0.47	1.32	2.96	4.95	3.96

Table A3-plagioclase (Conti.)

Sample number	RD-12-5	RD-12-5	RD-12-5	RD-12-5	RD-12-5	RD-12-5	WR-12-30	WR-12-30	WR-12-30	WR-12-30	WR-12-30	WR-12-30	WR-12-30	WR-12-30	WR-12-30	WR-12-30	WR-12-30
Weight %																	
SiO_2	63.31	63.45	62.97	63.55	56.92	56.90	62.09	59.46	62.18	62.11	62.05	60.17	60.07	60.97	60.52	61.13	59.84
TiO_2	0.09	0.07	0.09	0.09	0.10	0.09	0.08	0.10	0.10	0.09	0.07	0.10	0.12	0.06	0.10	0.10	0.10
Al_2O_3	22.82	23.05	23.30	22.83	27.67	27.37	21.71	24.88	22.77	23.56	23.38	24.69	24.81	24.00	24.80	24.11	24.90
FeO	0.12	0.05	0.11	0.10	0.07	0.07	0.08	0.13	0.10	0.43	0.38	0.17	0.16	0.17	0.15	0.26	0.15
MnO	0.02	0.00	0.01	0.01	0.00	0.04	0.02	0.02	0.01	0.01	0.03	0.03	0.04	0.00	0.03	0.03	0.04
MgO	0.01	0.02	0.01	0.03	0.00	0.01	0.01	0.02	0.01	0.02	0.01	0.02	0.01	0.02	0.01	0.03	0.01
CaO	4.26	4.34	4.50	4.08	9.42	9.14	2.56	5.62	3.63	4.33	4.24	5.48	5.76	5.02	5.49	5.04	5.69
Na_2O	8.81	8.89	8.78	9.00	6.22	6.21	5.69	7.32	5.30	8.37	8.43	7.71	7.45	7.81	7.40	7.71	7.53
K_2O	0.66	0.55	0.61	0.50	0.18	0.17	4.21	0.26	2.41	0.34	0.35	0.37	0.32	0.37	0.38	0.53	0.39
Total	100.11	100.41	100.39	100.19	100.58	100.00	96.69	97.92	96.67	99.38	99.03	98.89	98.87	98.52	99.02	99.04	98.79
No. of oxygens	8	8	8	8	8	8	8	8	8	8	8	8	8	8	8	8	8
Si	2.53	2.53	2.51	2.54	2.26	2.28	2.58	2.43	2.58	2.50	2.51	2.44	2.43	2.48	2.45	2.47	2.43
Al	1.22	1.22	1.24	1.22	1.47	1.46	1.20	1.36	1.26	1.27	1.26	1.33	1.34	1.30	1.34	1.30	1.35
Ti	0.00	0.00	0.00	0.00	0.00	0.00	0.00	0.00	0.00	0.00	0.00	0.00	0.00	0.00	0.00	0.00	0.00
Fe	0.01	0.00	0.01	0.01	0.01	0.01	0.01	0.01	0.01	0.03	0.03	0.01	0.01	0.01	0.01	0.02	0.01
Mn	0.00	0.00	0.00	0.00	0.00	0.00	0.00	0.00	0.00	0.00	0.00	0.00	0.00	0.00	0.00	0.00	0.00
Mg	0.00	0.00	0.00	0.00	0.00	0.00	0.00	0.00	0.00	0.00	0.00	0.00	0.00	0.00	0.00	0.00	0.00
Ca	0.34	0.35	0.36	0.33	0.75	0.73	0.21	0.46	0.30	0.35	0.34	0.44	0.47	0.41	0.44	0.41	0.46
Na	1.41	1.42	1.40	1.44	0.99	0.99	0.94	1.20	0.88	1.35	1.36	1.25	1.21	1.27	1.20	1.25	1.22
K	0.11	0.09	0.10	0.08	0.03	0.03	0.70	0.04	0.40	0.05	0.06	0.06	0.05	0.06	0.06	0.09	0.06
An	18.36	18.69	19.32	17.68	42.41	41.74	11.46	27.04	19.06	19.91	19.44	25.34	27.02	23.48	26.10	23.41	26.45
Ab	75.95	76.58	75.41	78.02	56.01	56.72	50.89	70.46	55.67	76.95	77.34	71.26	69.95	73.04	70.33	71.66	69.96
Or	5.68	4.73	5.26	4.30	1.58	1.54	37.64	2.49	25.27	3.14	3.22	3.40	3.03	3.48	3.57	4.92	3.59

Table A3-plagioclase (Conti.)

Sample number	WR-12-30	WR-12-30	WR-12-30	WR-12-30	WR-12-30	WR-12-30	XB-12-3	XB-12-3	XB-12-3	XB-12-3	XB-12-3	XB-12-3	XB-12-3	XB-12-3	XB-12-3	XB-12-3	XB-12-3
Weight %																	
SiO_2	58.27	59.37	59.72	60.37	60.77	60.17	57.66	64.07	63.98	64.31	65.25	64.21	64.43	62.82	63.52	64.88	59.62
TiO_2	0.08	0.07	0.09	0.06	0.09	0.08	0.06	0.08	0.08	0.04	0.06	0.08	0.07	0.06	0.07	0.04	0.08
Al_2O_3	26.19	25.38	25.10	25.19	24.55	24.62	25.47	21.76	20.98	20.79	22.11	21.03	20.86	21.80	21.73	21.05	24.64
FeO	0.20	0.20	0.19	0.23	0.17	0.18	0.07	0.03	0.07	0.06	0.10	0.03	0.05	0.07	0.09	0.09	0.07
MnO	0.01	0.01	0.00	0.02	0.05	0.04	0.03	0.00	0.03	0.02	0.00	0.00	0.04	0.06	0.00	0.04	0.00
MgO	0.02	0.04	0.04	0.03	0.02	0.01	0.02	0.02	0.00	0.01	0.00	0.02	0.00	0.00	0.02	0.03	0.03
CaO	6.91	6.13	5.85	5.64	5.21	5.46	8.24	3.74	3.37	3.07	2.95	3.18	3.40	4.19	3.96	3.08	7.44
Na_2O	6.65	7.21	7.21	7.28	7.62	7.50	6.61	9.02	9.17	9.74	9.55	9.46	9.41	9.07	9.15	9.71	7.04
K_2O	0.28	0.36	0.40	0.43	0.47	0.40	0.11	0.11	0.21	0.18	0.29	0.17	0.23	0.15	0.20	0.23	0.17
Total	98.68	98.90	98.76	99.35	99.09	98.57	98.28	98.83	97.89	98.23	100.31	98.17	98.51	98.22	98.75	99.15	99.11
No. of oxygens	8	8	8	8	8	8	8	8	8	8	8	8	8	8	8	8	8
Si	2.36	2.40	2.42	2.43	2.46	2.44	2.35	2.59	2.61	2.62	2.60	2.62	2.62	2.56	2.57	2.62	2.41
Al	1.42	1.37	1.36	1.35	1.32	1.33	1.38	1.17	1.14	1.13	1.18	1.14	1.13	1.18	1.17	1.13	1.33
Ti	0.00	0.00	0.00	0.00	0.00	0.00	0.00	0.00	0.00	0.00	0.00	0.00	0.00	0.00	0.00	0.00	0.00
Fe	0.02	0.02	0.02	0.02	0.01	0.01	0.01	0.00	0.01	0.00	0.01	0.00	0.00	0.01	0.01	0.01	0.01
Mn	0.00	0.00	0.00	0.00	0.00	0.00	0.00	0.00	0.00	0.00	0.00	0.00	0.00	0.00	0.00	0.00	0.00
Mg	0.00	0.00	0.00	0.00	0.00	0.00	0.00	0.00	0.00	0.00	0.00	0.00	0.00	0.00	0.00	0.00	0.00
Ca	0.56	0.50	0.47	0.45	0.42	0.44	0.67	0.30	0.28	0.25	0.24	0.26	0.28	0.34	0.32	0.25	0.60
Na	1.08	1.17	1.17	1.17	1.23	1.22	1.08	1.46	1.50	1.59	1.52	1.54	1.53	1.48	1.48	1.57	1.14
K	0.04	0.06	0.06	0.07	0.08	0.07	0.02	0.02	0.03	0.03	0.05	0.03	0.04	0.02	0.03	0.04	0.03
An	33.30	28.80	27.76	26.77	24.33	25.67	38.01	17.00	15.23	13.40	13.04	14.17	15.00	18.51	17.48	13.41	34.05
Ab	64.04	67.79	68.47	69.11	71.23	70.53	60.98	82.01	82.88	85.00	84.42	84.34	83.02	80.15	80.76	84.58	64.44
Or	2.66	3.41	3.77	4.12	4.43	3.80	1.01	0.98	1.89	1.61	2.55	1.49	1.99	1.33	1.77	2.00	1.51

Table A3-plagioclase (Conti.)

Sample number	XB-12-3	XB-12-3	XB-12-3	XB-12-3	XB-12-3	XB-12-3	XB-12-3	XB-12-3	XB-12-3	XB-12-3	XB-12-3	XB-12-3	XB-12-3	XB-12-3	XB-12-3	WR-13-15	WR-13-15
Weight %																	
SiO_2	60.37	62.27	61.93	62.09	63.02	61.97	61.44	62.22	63.98	64.40	64.25	60.96	64.58	64.18	64.98	60.57	59.66
TiO_2	0.08	0.08	0.10	0.10	0.08	0.10	0.09	0.08	0.08	0.06	0.07	0.07	0.07	0.07	0.09	0.02	0.03
Al_2O_3	22.60	22.66	23.81	22.58	22.09	22.89	22.71	21.95	16.99	19.27	20.79	22.31	20.30	20.82	22.40	24.06	24.65
FeO	0.04	0.08	0.09	0.08	0.10	0.07	0.01	0.10	0.16	0.03	0.11	0.13	0.20	0.06	0.05	0.16	0.16
MnO	0.01	0.00	0.00	0.00	0.00	0.04	0.02	0.00	0.03	0.00	0.01	0.00	0.05	0.03	0.02	0.00	0.02
MgO	0.01	0.01	0.00	0.03	0.01	0.01	0.00	0.00	0.03	0.02	0.03	0.00	0.04	0.02	0.00	0.02	0.02
CaO	5.42	5.03	6.16	5.26	4.58	5.49	5.48	4.85	0.06	2.05	3.21	5.46	2.39	3.22	3.27	5.99	6.56
Na_2O	8.14	8.26	7.71	8.35	8.80	8.28	8.35	8.44	0.52	10.04	9.24	7.86	9.55	9.42	9.58	7.16	7.21
K_2O	0.17	0.17	0.21	0.21	0.25	0.29	0.25	0.41	15.47	0.16	0.24	0.29	0.16	0.15	0.21	0.74	0.63
Total	96.84	98.56	100.02	98.70	98.93	99.15	98.36	98.05	98.01	96.03	97.97	97.09	97.34	97.97	100.60	98.72	98.94
No. of oxygens	8	8	8	8	8	8	8	8	8	8	8	8	8	8	8	8	8
Si	2.49	2.53	2.48	2.52	2.55	2.50	2.50	2.54	2.63	2.68	2.62	2.51	2.65	2.62	2.58	2.45	2.41
Al	1.24	1.23	1.27	1.22	1.19	1.23	1.23	1.19	0.93	1.07	1.13	1.23	1.11	1.13	1.19	1.30	1.33
Ti	0.00	0.00	0.00	0.00	0.00	0.00	0.00	0.00	0.00	0.00	0.00	0.00	0.00	0.00	0.00	0.00	0.00
Fe	0.00	0.01	0.01	0.01	0.01	0.01	0.00	0.01	0.01	0.00	0.01	0.01	0.02	0.01	0.00	0.01	0.01
Mn	0.00	0.00	0.00	0.00	0.00	0.00	0.00	0.00	0.00	0.00	0.00	0.00	0.00	0.00	0.00	0.00	0.00
Mg	0.00	0.00	0.00	0.00	0.00	0.00	0.00	0.00	0.00	0.00	0.00	0.00	0.00	0.00	0.00	0.00	0.00
Ca	0.45	0.41	0.49	0.43	0.37	0.44	0.45	0.40	0.00	0.17	0.26	0.45	0.20	0.26	0.26	0.49	0.53
Na	1.34	1.34	1.23	1.35	1.42	1.34	1.36	1.38	0.09	1.67	1.51	1.30	1.57	1.54	1.52	1.16	1.17
K	0.03	0.03	0.03	0.03	0.04	0.05	0.04	0.07	2.54	0.03	0.04	0.05	0.03	0.02	0.03	0.12	0.10
An	24.58	22.98	28.01	23.49	20.20	24.27	24.16	21.51	0.17	9.13	14.48	25.09	10.96	14.40	14.32	27.50	29.49
Ab	73.84	75.47	70.11	74.59	77.62	73.20	73.62	74.88	3.23	89.46	83.35	72.24	87.56	84.25	83.89	65.74	64.83
Or	1.58	1.55	1.88	1.91	2.18	2.53	2.22	3.61	96.59	1.41	2.17	2.67	1.49	1.35	1.80	6.76	5.68

Table A3-plagioclase (Conti.)

Sample number	WR-13-15	WR-13-15	WR-13-15	WR-13-15	WR-13-15	WR-13-122	WR-13-122	WR-13-122	BPzk303	BPzk303	BPzk303	BPzk303	BPzk303	BPzk303	BPzk303	BPzk303	BPzk303
Weight %																	
SiO_2	61.04	61.55	75.18	75.23	62.06	66.66	61.64	62.16	61.08	64.81	64.41	64.27	58.14	64.77	64.20	65.04	64.83
TiO_2	0.01	0.00	0.20	0.23	0.01	0.13	0.11	0.11	0.14	0.09	0.11	0.10	0.12	0.08	0.09	0.08	0.08
Al_2O_3	23.39	23.23	13.84	13.39	22.59	17.27	20.83	20.58	22.20	21.93	21.50	22.08	26.58	21.88	22.23	21.53	18.34
FeO	0.20	0.16	0.33	0.28	0.12	0.90	0.31	0.29	0.34	0.02	0.05	0.07	0.44	0.06	0.13	0.05	0.06
MnO	0.01	0.00	0.01	0.00	0.01	0.01	0.00	0.02	0.00	0.01	0.02	0.03	0.03	0.03	0.02	0.03	0.00
MgO	0.03	0.02	0.02	0.03	0.01	0.05	0.01	0.02	0.03	0.00	0.00	0.01	0.26	0.00	0.02	0.01	0.00
CaO	5.53	5.20	1.14	1.50	4.46	0.69	2.15	2.08	4.26	2.97	2.82	3.17	0.60	2.98	0.95	2.53	0.19
Na_2O	7.56	7.18	4.25	4.39	7.76	4.63	4.97	5.32	8.90	9.87	9.58	9.47	6.62	9.82	9.74	9.82	4.11
K_2O	0.85	0.96	3.71	2.55	1.08	7.94	6.17	6.09	0.27	0.13	0.47	0.44	4.57	0.40	1.28	0.39	10.03
Total	98.61	98.30	98.68	97.60	98.10	98.28	96.19	96.67	97.21	99.84	98.95	99.64	97.37	100.02	98.66	99.47	97.63
No. of oxygens	8	8	8	8	8	8	8	8	8	8	8	8	8	8	8	8	8
Si	2.48	2.50	3.05	3.08	2.53	2.71	2.56	2.57	2.51	2.60	2.60	2.58	2.39	2.59	2.60	2.62	2.66
Al	1.27	1.26	0.75	0.73	1.23	0.94	1.15	1.14	1.22	1.17	1.16	1.18	1.46	1.17	1.20	1.15	1.00
Ti	0.00	0.00	0.01	0.01	0.00	0.01	0.00	0.00	0.01	0.00	0.00	0.00	0.00	0.00	0.00	0.00	0.00
Fe	0.02	0.01	0.03	0.02	0.01	0.07	0.03	0.02	0.03	0.00	0.00	0.01	0.04	0.00	0.01	0.00	0.00
Mn	0.00	0.00	0.00	0.00	0.00	0.00	0.00	0.00	0.00	0.00	0.00	0.00	0.00	0.00	0.00	0.00	0.00
Mg	0.00	0.00	0.00	0.00	0.00	0.00	0.00	0.00	0.00	0.00	0.00	0.00	0.02	0.00	0.00	0.00	0.00
Ca	0.45	0.42	0.09	0.12	0.36	0.06	0.18	0.17	0.35	0.24	0.23	0.25	0.05	0.24	0.08	0.20	0.02
Na	1.23	1.17	0.69	0.72	1.27	0.75	0.83	0.88	1.46	1.58	1.55	1.52	1.09	1.57	1.58	1.58	0.67
K	0.14	0.16	0.60	0.42	0.18	1.29	1.03	1.01	0.04	0.02	0.08	0.07	0.75	0.06	0.21	0.06	1.64
An	24.75	24.22	6.69	9.75	20.15	2.66	8.80	8.35	18.85	12.93	12.31	13.79	2.62	12.72	4.11	11.03	0.66
Ab	67.68	66.88	49.82	57.09	70.11	35.85	40.69	42.73	78.76	85.92	83.62	82.36	57.61	83.85	84.75	85.60	28.87
Or	7.56	8.90	43.49	33.16	9.75	61.49	50.51	48.92	2.39	1.16	4.07	3.85	39.77	3.43	11.14	3.37	70.47

Table A3-plagioclase (Cont.)

Sample number	BPzk303	BPzk303
Weight %		
SiO_2	50.57	62.85
TiO_2	0.13	0.07
Al_2O_3	29.34	22.97
FeO	2.63	0.05
MnO	0.05	0.05
MgO	1.41	0.02
CaO	0.78	4.45
Na_2O	1.78	8.89
K_2O	8.52	0.42
Total	95.21	99.76
No. of oxygens	8	8
Si	2.12	2.52
Al	1.64	1.23
Ti	0.01	0.00
Fe	0.22	0.00
Mn	0.00	0.00
Mg	0.12	0.00
Ca	0.07	0.36
Na	0.30	1.43
K	1.43	0.07
An	3.64	19.29
Ab	16.65	77.08
Or	79.71	3.62

Table A4 LA-HR-ICPMS trace element data of zircons from Cenozoic Gangdese igneous rocks.

Sample number	QS-11	QS-11	QS-11	NM11-01	NM11-01	NM11-01	NM11-01	NM11-01	WR-12-11	WR-12-11	WR-12-11	WR-12-11	WR-12-11
Age (Ma)	53	52-55	52-55	54	47-55	47-55	52	52	54-63	54-63	54-63	54-63	54-63
ppm													
CaO	635.3	240.7	712.4	bdl	75.6	1283.0	515.8	104.6	bdl	252.1	126.3	46.4	124.7
Sc	581	1158	1148	1457	1579	1260	2102	1844	887	976	1252	1276	1210
TiO_2	8.14	16.29	11.02	51.39	72.30	63.05	45.64	53.49	6.53	14.58	7.40	6.52	10.77
Ti	4.88	9.76	6.60	30.80	43.33	37.79	27.35	32.06	3.91	8.74	4.43	3.91	6.45
V	0.58	0.34	1.11	0.82	1.91	1.27	0.61	0.55	0.10	0.19	0.09	0.01	0.03
Cr	1.34	7.32	3.41	1.15	1.86	bdl	2.81	5.25	5.30	2.87	3.39	5.03	2.28
MnO	2.38	2.59	1.69	bdl	0.48	2.52	5.14	0.13	bdl	7.84	1.17	0.32	0.39
Co	bdl	0.01	bdl	bdl	0.03	bdl	0.07	0.02	bdl	0.03	0.02	0.12	0.04
Ni	0.55	1.46	0.88	bdl	3.21	0.18	1.53	0.19	bdl	2.09	0.26	bdl	bdl
Cu	0.48	1.03	0.37	1.41	0.54	0.76	2.31	0.81	0.86	1.09	1.52	0.69	0.39
Zn	bdl	1.49	0.98	0.14	0.02	bdl	bdl	1.71	1.45	0.36	0.72	1.85	bdl
Ga	0.26	0.10	0.14	0.20	0.33	0.42	0.15	0.15	0.09	0.16	0.04	0.22	0.04
Ge	bdl	bdl	0.55	0.08	0.85	bdl	0.33	0.59	0.67	bdl	0.60	0.70	0.58
Ge	0.15	0.63	0.22	0.12	0.04	0.19	1.14	0.63	0.04	0.47	0.19	0.50	0.37
Rb	0.06	0.15	0.31	bdl	0.71	1.08	0.72	1.26	0.38	1.46	0.63	0.57	0.45
Sr	2.00	1.14	1.19	1.55	1.88	1.99	2.11	1.28	0.80	1.78	0.88	0.89	0.99
Y	2145	711	984	1048	2282	2671	1194	2205	2218	1678	1858	1650	1151
Zr	482096	482410	481239	474170	472752	476396	475606	476948	494959	484780	486371	494469	485410
Nb	2.50	4.50	3.81	5.28	5.65	3.90	5.43	6.01	5.86	4.04	9.82	7.88	2.47
Mo	6.69	6.41	6.08	11.12	10.82	11.23	10.21	7.03	4.24	5.01	5.34	5.88	5.27
Ba	0.13	0.25	0.41	bdl	0.29	0.02	bdl	0.08	0.39	5.89	1.23	0.17	0.47
La	1.46	3.81	1.54	0.07	0.15	1.01	3.16	0.14	0.04	0.96	0.11	0.12	0.09
Ce	31.05	28.14	23.69	32.05	40.65	49.34	38.96	36.08	17.32	21.71	19.55	20.64	10.00
Pr	0.75	0.81	0.22	0.16	0.42	0.91	0.54	0.51	0.09	0.34	0.09	0.08	0.12
Nd	5.44	2.22	3.33	1.64	4.41	7.14	3.74	8.05	1.99	3.46	1.01	1.20	2.50
Sm	4.46	3.52	4.61	3.85	8.84	10.90	10.30	26.04	6.97	6.13	2.92	4.36	5.45
Eu	0.79	0.53	0.87	1.57	3.93	2.67	1.92	5.14	0.43	1.51	0.51	0.75	1.39
Gd	37.87	14.21	20.19	27.02	63.74	85.64	30.22	64.76	35.18	31.14	26.18	26.33	23.61
Tb	12.60	3.78	5.89	6.94	13.88	16.22	5.96	13.98	16.88	12.02	10.11	11.17	7.74
Dy	118.0	83.5	113.3	51.8	121.7	130.8	108.6	326.1	241.9	177.1	169.3	169.6	117.7
Ho	38.41	39.13	59.12	39.00	107.10	86.74	74.14	181.60	78.03	68.85	77.49	66.81	44.05
Er	305	196	262	254	617	599	255	720	339	291	367	256	211
Tm	78.56	32.19	43.31	41.70	82.66	97.10	41.28	77.45	86.71	61.22	71.80	57.33	38.90
Yb	674	427	474	305	530	571	347	792	1079	829	569	619	483
Lu	81.6	89.4	108.8	64.7	118.0	106.9	123.2	267.0	141.6	142.5	136.2	110.8	85.8
Hf	12655	14084	14584	23604	22873	17333	20447	16916	8147	8887	10696	9846	10492
U	598	381	384	92	191	268	145	301	1260	402	653	538	169
Th	456	257	347	167	490	725	237	749	359	219	301	228	122
Ta	1.25	0.89	0.67	0.72	0.87	1.03	0.50	0.51	1.83	0.90	2.49	1.58	0.35
W	0.23	0.17	0.09	0.08	0.33	0.18	0.12	0.28	0.20	0.30	0.05	0.17	0.02
Pb	1.60	1.50	1.94	0.53	2.13	1.97	1.66	4.06	2.45	1.43	2.24	1.76	0.96
Ce^{4+}/Ce^{3+}	9.42	7.63	11.26	58.35	28.37	11.79	8.15	19.10	38.53	7.30	38.66	34.53	11.57
T°C	682	739	706	851	889	873	838	855	665	729	674	665	704
Eu_N/Eu_N*	0.19	0.23	0.27	0.47	0.51	0.27	0.33	0.38	0.08	0.33	0.18	0.22	0.37
∑REE	1390	924	1121	829	1713	1766	1044	2519	2045	1647	1450	1344	1032

Table A4 (Cont.)

Sample number	KMQ-12-2	KMQ-12-2	KMQ-12-2	KMQ-12-2	KMQ-12-2	ZD-2	ZD-2	ZD-2	RD-12-5	RD-12-5	RD-12-5	RD-12-5	RD-12-5
Age (Ma)	49-52	52	51	49-52	52	52-61	48	52-61	64-73	65	69	65	73
ppm													
CaO	bdl	29.8	89.3	53.2	53.6	627.1	317.8	881.0	3216.0	114.8	34.6	170.1	44.8
Sc	932	968	1082	1021	1010	998	987	1225	995	1311	990	1326	1023
TiO_2	35.53	31.49	33.61	42.28	27.79	10.69	11.48	24.38	16.64	12.81	21.15	11.20	11.21
Ti	21.29	18.87	20.14	25.34	16.66	6.41	6.88	14.61	9.97	7.68	12.68	6.71	6.72
V	0.95	0.35	3.11	2.65	0.78	0.44	0.20	0.63	0.40	0.33	0.31	0.08	0.13
Cr	2.46	5.69	4.79	1.70	1.94	7.57	0.34	1.13	3.04	3.23	1.77	1.69	2.55
MnO	bdl	0.07	0.71	bdl	0.22	2.94	0.06	2.23	23.02	1.98	bdl	0.34	0.99
Co	bdl	0.05	0.03	bdl	0.07	0.08	0.17	0.11	0.04	0.03	bdl	bdl	bdl
Ni	bdl	bdl	bdl	0.20	0.17	2.17	bdl	bdl	0.84	bdl	0.96	bdl	1.32
Cu	0.15	0.20	0.66	0.17	0.49	0.44	0.76	1.53	0.39	0.53	0.45	bdl	0.29
Zn	0.94	0.94	bdl	1.83	bdl	bdl	0.28	0.86	0.61	1.18	0.79	1.69	bdl
Ga	0.36	0.15	0.36	0.59	0.33	0.19	0.10	0.06	0.52	0.35	0.33	0.20	0.16
Ge	0.36	0.47	0.85	0.96	0.97	bdl	0.69	bdl	0.34	0.64	0.12	bdl	0.34
Ge	0.44	0.16	0.39	0.40	0.37	0.39	0.45	0.65	0.01	0.21	0.12	0.12	0.10
Rb	0.30	0.41	1.21	0.55	0.63	0.35	0.30	1.01	0.86	0.38	0.32	0.74	0.29
Sr	1.29	1.08	1.42	1.29	1.15	1.95	2.75	1.81	5.34	1.07	0.97	1.38	1.03
Y	3245	2003	5203	3899	3762	1141	912	1621	2337	2546	1731	3326	1914
Zr	484345	485706	479743	483949	483087	483825	485087	481275	481543	483461	487725	481462	481131
Nb	3.84	2.36	4.38	3.78	3.48	3.36	3.17	2.45	5.93	8.23	3.20	8.00	5.00
Mo	6.98	5.74	6.88	6.39	6.05	7.46	8.52	8.48	5.98	5.66	5.72	5.62	5.43
Ba	0.41	0.11	0.19	0.33	0.19	0.38	0.02	0.13	1.02	0.25	0.32	bdl	0.18
La	0.04	0.03	0.11	0.08	0.11	1.59	0.26	0.27	3.76	0.13	0.02	0.08	0.06
Ce	23.33	13.38	41.30	25.54	19.87	31.28	30.40	21.40	50.14	44.72	23.70	31.49	26.89
Pr	0.52	0.29	0.66	0.69	0.58	0.55	0.36	0.51	1.43	0.16	0.11	0.13	0.13
Nd	8.57	5.62	8.84	11.71	9.19	3.00	1.49	5.26	7.75	2.52	2.08	1.92	1.62
Sm	19.66	12.27	20.43	27.21	19.98	2.56	1.91	5.60	5.99	6.09	4.07	7.07	3.89
Eu	2.61	1.83	2.64	4.33	2.40	1.08	0.56	2.46	2.08	2.00	2.17	2.43	1.58
Gd	109.20	61.98	157.30	126.70	101.60	22.41	14.00	39.15	42.72	40.19	28.62	52.11	25.68
Tb	25.27	15.92	36.46	32.25	28.65	6.21	3.94	10.45	13.14	17.00	10.36	20.83	9.69
Dy	274.2	201.1	424.4	329.8	382.6	69.4	43.9	103.0	136.2	238.8	120.2	282.6	126.4
Ho	108.30	70.32	166.20	124.60	144.40	29.47	20.61	55.10	55.35	89.23	46.73	109.90	49.06
Er	545	344	884	531	532	194	200	309	342	411	261	534	266
Tm	91.37	54.68	145.70	94.33	87.04	46.77	41.67	62.78	75.86	95.29	62.36	122.60	64.04
Yb	680	485	1024	745	730	429	345	483	662	1041	625	1366	666
Lu	92.0	76.0	156.1	107.6	139.4	77.5	52.2	87.6	109.6	187.0	107.8	247.8	111.0
Hf	9223	9434	10793	8839	9939	11703	11201	13758	9692	9061	7380	10942	7989
U	320	163	664	293	308	390	209	172	507	478	168	673	302
Th	352	188	982	365	337	375	222	221	1015	390	198	407	163
Ta	0.51	0.47	0.80	0.66	0.72	0.96	1.22	0.43	1.36	1.98	0.62	2.11	1.35
W	0.30	0.13	0.41	0.23	0.09	0.14	0.15	0.04	0.08	0.24	0.20	bdl	0.31
Pb	1.55	0.69	3.80	1.51	1.68	2.32	0.75	1.11	4.51	2.31	1.18	2.13	0.91
Ce^{4+}/Ce^{3+}	21.46	19.93	26.72	14.34	12.36	11.58	33.99	11.33	6.04	53.22	66.75	51.13	53.28
T°C	812	800	807	830	788	703	709	775	741	718	762	707	707
Eu_N/Eu_N*	0.17	0.20	0.14	0.23	0.16	0.44	0.33	0.51	0.40	0.39	0.61	0.39	0.48
∑REE	1980	1342	3068	2160	2198	914	757	1185	1508	2175	1294	2779	1353

Table A4 (Cont.)

Sample number	XB-12-3	XB-12-3	XB-12-3	CB-3	CB-3	JM11-36	JM11-36	JM11-36	JM11-36	JM11-36	PG11-06	PG11-06	PG11-06
Age (Ma)	22-26	23	22	27	26-29	17	17	17	16	16	17	15	14
ppm													
CaO	125.8	45.5	113.3	185.8	71.5	185.5	174.7	226.7	235.8	361.7	142.1	127.9	275.8
Sc	1020	1172	1017	948	951	955	908	1006	938	795	830	983	901
TiO_2	8.45	4.71	5.71	11.94	8.34	5.97	6.04	4.20	5.34	3.63	2.77	3.17	8.19
Ti	5.07	2.82	3.42	7.16	5.00	3.58	3.62	2.52	3.20	2.17	1.66	1.90	4.91
V	0.10	0.38	0.21	0.23	0.11	0.25	0.08	1.34	0.01	0.11	0.09	0.12	0.16
Cr	3.83	3.10	3.05	1.93	14.96	bdl	bdl	bdl	bdl	0.56	1.57	1.03	0.42
MnO	0.73	0.20	bdl	1.48	1.09	bdl	0.85	0.06	0.52	0.38	bdl	0.42	0.02
Co	bdl	0.01	0.01	0.02	bdl	bdl	bdl	0.01	0.05	bdl	bdl	0.10	0.04
Ni	0.15	bdl	bdl	1.79	bdl	bdl	0.22	0.30	bdl	0.16	bdl	1.15	0.44
Cu	0.42	0.93	0.98	0.37	0.60	0.35	0.26	0.72	0.28	0.24	0.43	0.39	0.45
Zn	0.58	bdl	0.67	1.00	0.96	bdl	0.62	0.36	0.28	bdl	0.51	0.28	bdl
Ga	0.14	0.48	0.40	0.47	0.60	0.41	0.62	0.28	0.28	0.28	0.35	0.17	0.62
Ge	0.36	0.71	0.46	bdl	bdl	bdl	0.26	0.08	0.78	0.81	0.69	0.24	0.44
Ge	0.12	0.43	0.13	0.54	0.35	0.17	0.23	0.14	0.30	0.29	0.22	0.31	0.24
Rb	0.05	0.28	0.07	0.17	0.53	0.18	0.99	0.36	0.04	0.01	0.02	0.20	0.34
Sr	0.85	1.28	0.78	1.49	0.92	0.94	0.91	0.90	0.77	0.58	0.62	0.61	1.05
Y	799	1593	1266	548	554	960	525	879	270	570	495	299	637
Zr	484193	482284	484896	486791	467284	483090	482563	482421	484161	484557	485745	485368	482041
Nb	10.22	11.57	11.35	2.86	2.56	4.59	3.44	2.71	1.94	2.27	2.37	1.93	3.28
Mo	5.70	6.17	4.38	5.16	5.03	6.41	5.26	5.75	5.81	5.07	4.85	4.47	5.35
Ba	0.28	0.15	0.03	1.48	0.14	0.37	0.68	0.34	0.07	0.02	0.13	0.06	0.02
La	0.06	0.14	0.18	0.68	0.04	0.13	0.07	0.26	0.08	0.08	0.08	0.13	0.49
Ce	11.27	66.85	48.37	28.42	22.94	29.51	59.54	26.38	20.76	33.65	25.57	16.87	74.19
Pr	0.08	0.22	0.23	0.28	0.10	0.11	0.11	0.08	0.01	0.04	0.06	0.04	0.20
Nd	0.43	3.07	1.17	2.16	1.23	1.14	1.90	0.96	0.69	0.64	0.98	0.90	2.62
Sm	1.70	6.15	3.15	2.67	3.14	2.30	4.22	1.99	1.65	1.28	1.94	1.66	5.18
Eu	0.29	1.65	0.74	1.07	0.83	0.97	1.02	1.14	0.64	0.58	0.96	0.68	1.80
Gd	12.51	31.79	19.93	12.93	13.04	15.09	18.20	12.56	6.25	9.10	9.69	5.99	21.91
Tb	4.49	9.09	6.23	3.78	3.83	5.32	5.07	4.65	2.00	3.21	3.39	1.86	5.98
Dy	64.0	103.5	75.1	43.7	41.6	65.4	58.8	61.8	26.6	32.8	34.4	29.1	62.6
Ho	24.00	42.18	29.05	15.94	15.74	28.90	20.07	26.58	11.60	13.19	14.22	11.61	22.92
Er	127	231	167	80	84	157	89	154	56	77	57	48	110
Tm	30.02	53.81	47.34	18.34	18.59	40.54	19.36	41.79	12.64	28.20	17.12	11.08	22.43
Yb	299	553	522	206	200	450	226	524	158	315	198	171	243
Lu	41.7	94.3	88.8	36.6	37.7	87.3	44.0	120.3	39.9	60.1	40.1	50.7	48.1
Hf	11464	11125	9634	9334	9538	12682	12159	12491	12811	10964	10858	11540	12877
U	1553	2146	2454	451	366	977	1730	1864	829	1712	684	673	1651
Th	256	1088	686	282	238	481	1392	528	222	502	505	324	1587
Ta	3.25	2.33	3.81	0.75	0.53	1.13	0.98	0.48	0.41	0.59	0.45	0.32	0.82
W	0.19	0.51	0.16	0.37	bdl	0.12	0.24	0.24	0.26	0.08	0.20	0.17	0.20
Pb	0.72	2.17	1.62	0.84	0.74	0.80	2.03	1.01	0.52	0.76	0.97	0.65	2.25
Ce^{4+}/Ce^{3+}	39.93	64.16	61.53	18.62	66.04	60.91	111.05	49.04	103.34	132.49	80.96	53.00	54.40
T°C	685	641	655	712	683	658	659	633	650	623	604	613	682
Eu_N/Eu_N*	0.19	0.36	0.29	0.56	0.40	0.50	0.36	0.70	0.61	0.52	0.68	0.66	0.52
∑REE	616	1197	1009	453	443	884	548	977	337	574	403	349	621

Table A4 (Cont.)

Sample number	PG11-06	PG11-06	PZ11-03	PZ11-03	PZ11-03	PZ11-03	PZ11-03	PZ11-03	PZ11-03	PZ11-03	PZ11-03	JR11-06	JR11-06
Age (Ma)	14	18	17	18	17	18	19	18	17	17	17	16	16
ppm													
CaO	197.9	69.5	43.6	71.8	78.0	101.9	101.4	154.5	67.7	96.8	64.5	144.9	145.9
Sc	980	868	1187	1250	960	955	1098	938	921	900	919	845	1055
TiO_2	5.77	5.65	8.53	14.59	16.03	7.74	26.09	17.14	15.26	8.27	12.24	7.45	4.51
Ti	3.46	3.39	5.11	8.74	9.61	4.64	15.64	10.27	9.15	4.96	7.34	4.47	2.70
V	0.06	0.08	bdl	0.13	0.05	bdl	0.12	0.16	0.19	0.05	0.06	0.08	0.09
Cr	bdl	0.20	1.50	3.72	2.66	2.13	0.32	4.45	1.63	3.27	0.89	0.07	1.15
MnO	0.26	0.15	0.12	0.01	0.26	0.05	0.49	bdl	bdl	0.45	bdl	0.01	0.25
Co	0.00	0.05	bdl	bdl	bdl	bdl	bdl	0.02	bdl	0.25	0.03	bdl	0.04
Ni	bdl	0.38	bdl	0.70	bdl	1.53	1.57	bdl	bdl	bdl	0.05	bdl	2.28
Cu	bdl	0.50	0.49	0.65	0.10	0.24	0.40	0.12	0.50	0.11	bdl	0.34	0.37
Zn	0.09	bdl	0.73	0.08	bdl	bdl	0.80	bdl	0.49	bdl	0.69	0.30	1.80
Ga	0.46	0.10	0.18	0.14	0.12	bdl	0.15	0.20	0.18	0.04	0.07	0.33	0.24
Ge	0.33	0.83	0.18	0.39	bdl	0.53	0.37	bdl	bdl	0.33	0.31	bdl	bdl
Ge	0.32	0.11	bdl	0.13	0.34	0.25	0.11	0.31	0.39	bdl	bdl	0.07	0.35
Rb	0.36	0.38	0.77	0.66	0.22	0.14	0.60	bdl	bdl	0.27	0.38	0.17	0.07
Sr	0.80	0.62	1.09	0.89	1.05	0.83	1.52	0.86	0.74	2.08	0.69	0.83	0.71
Y	496	386	1677	1899	598	319	1062	1217	717	332	740	1135	583
Zr	484221	486452	484303	484358	487601	485992	487801	486387	487380	498572	489287	486288	486240
Nb	2.58	2.96	4.25	4.65	1.67	1.78	2.30	3.59	2.20	1.44	1.60	3.10	1.98
Mo	4.79	5.19	5.91	6.61	5.40	6.27	6.58	5.68	5.99	5.98	4.88	5.48	5.15
Ba	0.29	0.21	0.17	0.17	0.36	0.21	1.43	0.16	0.07	1.11	0.15	0.15	0.36
La	0.11	0.02	0.02	0.03	0.06	0.04	0.02	0.02	0.00	0.00	0.01	0.03	0.03
Ce	38.93	11.88	10.07	21.03	11.06	4.50	16.03	12.69	14.93	5.37	9.17	21.32	22.34
Pr	0.08	0.08	0.04	0.12	0.08	0.03	0.14	0.05	0.12	0.03	0.04	0.07	0.06
Nd	1.52	1.22	1.10	2.17	1.47	0.26	2.48	1.67	2.37	0.47	1.43	1.63	1.47
Sm	3.02	2.75	3.72	6.49	3.31	1.10	4.67	3.65	4.70	1.42	3.17	3.37	3.57
Eu	1.13	1.31	2.35	4.50	1.74	0.65	2.97	2.54	2.49	0.85	2.02	1.73	1.12
Gd	12.45	11.22	23.74	41.99	15.06	6.56	25.74	28.53	22.16	7.63	15.66	22.33	14.71
Tb	4.00	3.58	8.92	13.97	4.58	1.93	7.82	9.17	6.03	2.49	5.72	7.73	4.30
Dy	46.6	39.4	125.4	160.8	52.2	24.0	87.6	98.4	64.4	28.5	65.1	83.6	55.4
Ho	15.83	12.09	52.80	63.41	18.95	9.09	33.50	33.13	20.86	9.89	24.07	28.88	20.51
Er	77	54	258	302	85	51	168	175	104	47	103	142	93
Tm	18.73	11.49	53.37	59.67	18.58	10.91	34.93	38.15	21.66	10.91	22.37	33.25	19.97
Yb	228	137	541	612	195	110	348	383	204	111	236	327	237
Lu	49.5	22.3	98.8	101.8	39.5	21.0	66.4	64.2	35.5	21.3	43.0	56.7	49.2
Hf	11323	10460	11119	10531	9301	11669	8088	9570	9432	9643	7303	9886	10421
U	1303	600	464	433	119	104	146	402	175	123	109	440	376
Th	959	335	107	206	73	23	118	125	121	38	71	147	170
Ta	0.55	0.69	0.66	0.74	0.26	0.25	0.37	0.68	0.47	0.24	0.14	0.71	0.29
W	0.14	0.17	0.25	0.13	0.19	0.14	0.19	0.20	0.25	0.24	0.14	0.23	0.23
Pb	1.46	0.75	0.15	0.32	0.16	0.11	0.21	0.13	0.21	0.36	0.27	0.32	0.35
Ce^{4+}/Ce^{3+}	85.36	49.37	57.65	57.64	32.32	35.91	54.91	59.28	82.37	34.55	53.16	81.76	87.90
T°C	655	654	685	729	737	678	782	743	733	683	714	675	638
Eu_N/Eu_N*	0.56	0.72	0.77	0.83	0.75	0.74	0.83	0.76	0.74	0.79	0.87	0.61	0.47
∑REE	496	308	1178	1390	447	240	798	849	504	247	531	730	522

Table A4 (Cont.)

Sample number	JR11-06	JR11-06	PG11-03	PG11-03	PG11-03	PG11-03	PG11-03	PG11-03	JR-2	JR-2	JR-2	JR-5	JR-5
Age (Ma)	17	16	16	15	15	16	16	16	14-17	15	14	16	16
ppm													
CaO	144.8	402.9	56.1	212.3	141.0	79.8	90.6	107.5	68.1	189.0	bdl	228.8	154.4
Sc	894	864	684	701	1039	1260	1293	1119	1009	1093	944	1460	1058
TiO_2	8.07	8.25	4.74	4.67	6.66	10.60	9.69	7.17	9.42	7.35	6.60	2.99	6.65
Ti	4.83	4.95	2.84	2.80	3.99	6.35	5.81	4.30	5.65	4.40	3.96	1.79	3.99
V	0.16	0.22	0.13	0.10	0.06	0.41	0.11	0.06	0.05	0.04	0.17	0.11	0.78
Cr	6.66	4.43	3.42	1.66	1.67	2.04	2.55	3.21	bdl	0.71	3.64	1.64	3.23
MnO	0.42	1.11	bdl	0.07	0.45	0.16	0.30	0.06	0.71	bdl	0.01	bdl	bdl
Co	0.08	0.01	bdl	0.02	0.01	0.00	0.01	bdl	bdl	0.03	bdl	bdl	0.02
Ni	0.10	1.18	0.52	bdl	bdl	bdl	1.04	bdl	bdl	2.14	0.06	bdl	0.72
Cu	0.13	0.56	0.16	0.28	0.18	0.10	0.88	0.25	0.50	0.65	0.67	0.18	0.05
Zn	1.69	0.23	0.06	bdl	0.33	0.38	0.33	1.21	0.48	1.31	bdl	bdl	bdl
Ga	0.57	1.00	0.25	0.33	0.31	0.66	0.26	0.22	0.10	0.03	0.09	0.09	0.55
Ge	1.52	0.34	0.51	0.53	0.13	0.81	bdl	0.19	0.03	0.43	0.07	bdl	bdl
Ge	bdl	0.32	0.17	0.21	bdl	0.38	0.42	0.05	0.53	0.58	0.27	0.39	0.36
Rb	bdl	bdl	0.06	0.16	0.13	0.09	bdl	bdl	bdl	0.17	bdl	0.21	0.93
Sr	0.79	1.30	0.56	0.77	0.93	1.16	0.79	1.04	0.88	1.04	0.75	1.35	0.92
Y	1070	1584	369	592	327	930	420	477	555	694	944	745	1955
Zr	485929	484572	490973	486050	483146	479035	482672	481587	487746	485842	483593	482565	492944
Nb	3.37	6.35	1.70	2.42	2.78	4.88	3.75	2.74	1.74	2.35	2.44	2.35	3.42
Mo	5.68	6.58	4.34	6.67	5.95	6.82	4.95	6.77	5.19	6.36	5.52	8.91	5.24
Ba	0.10	0.48	0.09	0.08	0.25	bdl	0.28	0.23	bdl	0.10	0.37	0.54	2.99
La	0.06	0.57	0.06	0.39	0.17	0.10	0.27	0.04	0.04	0.10	0.01	0.05	0.01
Ce	43.68	120.60	18.56	40.80	43.16	72.87	45.28	37.41	12.68	12.33	15.70	33.45	51.73
Pr	0.10	0.30	0.07	0.25	0.11	0.33	0.10	0.10	0.01	0.07	0.07	0.09	0.18
Nd	2.01	4.64	1.31	1.43	1.07	4.59	1.50	0.96	1.03	0.73	1.02	0.76	4.73
Sm	4.21	9.95	1.92	1.96	2.52	10.16	3.89	2.05	2.10	2.19	3.61	1.18	10.45
Eu	2.11	3.87	0.66	0.64	0.97	2.96	1.23	0.92	1.18	1.38	1.75	1.06	4.39
Gd	28.38	52.80	6.54	11.09	10.49	35.31	11.41	11.57	12.26	13.60	19.90	16.27	46.37
Tb	8.75	15.53	2.49	3.35	2.51	6.47	3.29	2.29	3.62	4.53	6.51	3.64	16.72
Dy	83.3	156.4	32.2	32.4	31.4	84.9	50.5	32.2	39.0	52.1	75.6	29.9	166.5
Ho	25.32	49.04	9.92	12.08	12.61	39.84	23.01	14.47	15.17	20.05	28.48	14.07	48.48
Er	109	226	49	81	58	174	83	83	78	106	135	103	193
Tm	26.15	49.42	13.58	23.60	12.32	34.82	16.52	16.68	18.86	23.04	28.63	25.47	54.63
Yb	289	442	204	236	151	278	201	197	185	247	278	206	473
Lu	43.8	64.7	39.7	38.5	34.0	67.9	55.6	44.2	33.3	50.4	51.2	40.3	69.7
Hf	9909	9039	8379	10064	13344	16107	13662	15300	9251	10690	9338	13960	7134
U	671	1237	645	827	852	973	764	592	138	425	201	475	916
Th	443	1392	285	747	867	1802	818	632	53	190	92	296	508
Ta	0.97	1.27	0.29	0.64	0.50	1.06	0.63	0.38	0.31	0.28	0.33	0.15	0.68
W	0.24	0.22	0.28	0.02	0.19	0.16	0.07	0.19	0.11	0.05	0.30	0.05	0.19
Pb	0.90	2.12	0.51	0.88	1.63	2.96	1.64	1.11	0.12	0.34	0.03	0.56	1.19
Ce^{4+}/Ce^{3+}	102.65	64.07	63.86	47.13	77.31	68.48	64.40	141.86	79.04	34.79	89.38	135.91	123.75
T°C	681	683	641	640	666	703	695	672	693	674	666	609	666
Eu_N/Eu_N*	0.59	0.52	0.57	0.42	0.58	0.48	0.57	0.58	0.71	0.77	0.63	0.74	0.61
∑REE	666	1196	380	484	360	813	496	442	402	533	646	476	1140

See Table 3-1 for age sources

Zircon temperature is estimated from equations of Watson and Harrison (2005)

Zircon Ce^{4+}/Ce^{3+} and Eu_N/Eu_N*ratios are calculated from equations of Ballard et al. (2002)

bdl: below the detection limit

Fig. A1 Cathodoluminescence images of representative zircons from Cenozoic igneous rocks in the Gangdese belt.

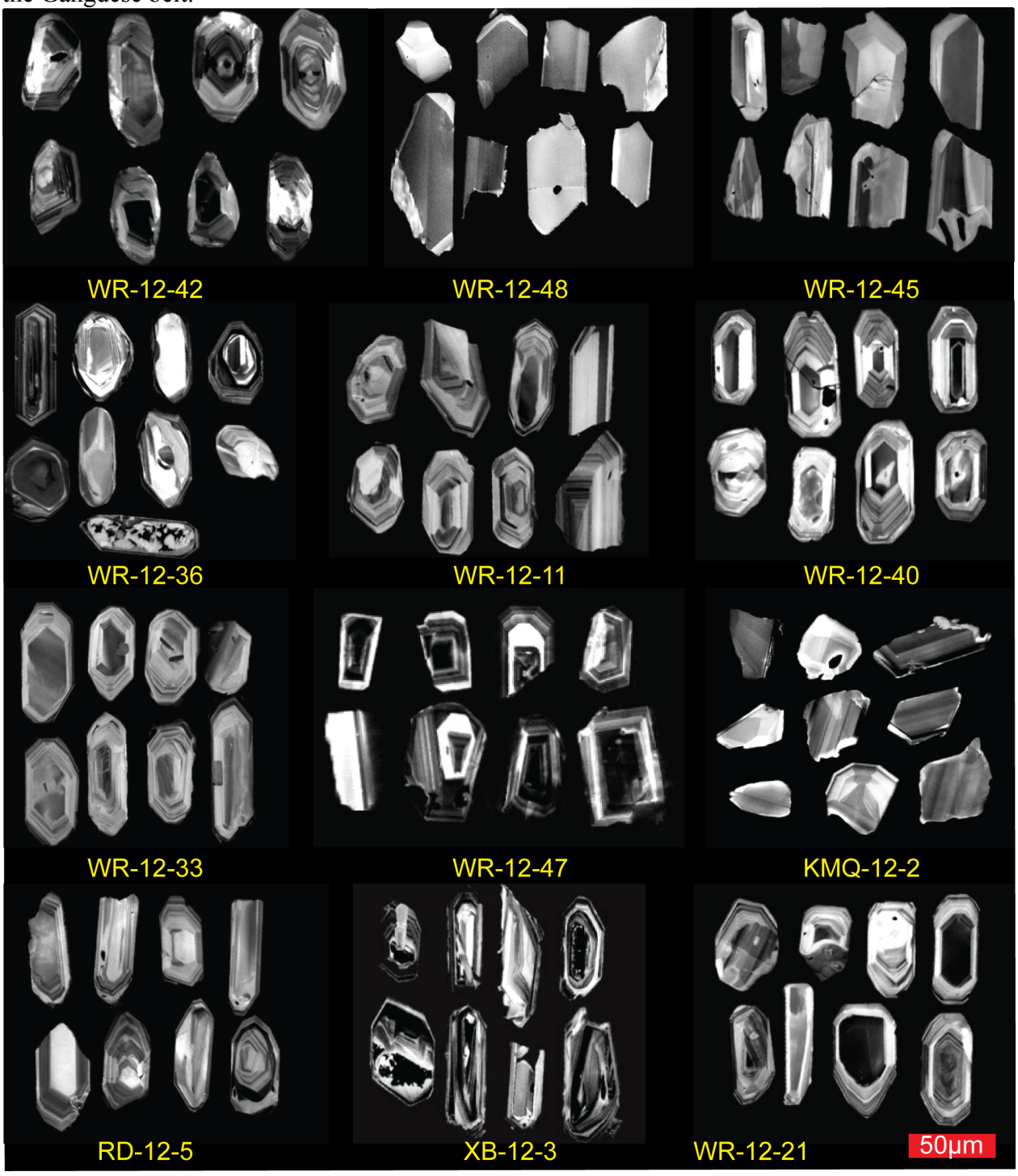

References

Ahmadian, J., Haschke, M., McDonald, I., Regelous, M., RezaGhorbani, M., Emami, M.H., and Murata, M., 2009, High magmatic flux during Alpine–Himalayan collision: Constraints from the Kal-e-Kafi complex, central Iran: Geological Society of American Bulletin, v. 121, p. 857–868.

Aitchison, J.C., Ali, J.R., and Davis, A.M., 2007, When and where did India and Asia collide: Journal of Geophysical Research, v. 112, p. B05423, doi: 10.1029/2006JB004706.

Ali, J.R., and Aitchison, J.C., 2005, Greater India: Earth-Science Reviews, v. 72, p. 169–188.

Allégre, C.J., Courtillot, V., Taponnier, P., Hirn, A., Mattauer, M., Coulon, C., Jaeger, J. J., Achache, J., Schärer, U., Marcoux, J., Burg, J. P., Girardeau, J., Armijo, R., Gaiety, C., Göpel, C., Li, T., Xiao, X., Chang, C., Li, G., Lin, B., T, J., Wang, N., Chen, G., Han, T., Wang, X., Den, W., Sheng, H., Gao, Y., Zhou, J., Qiu, H., Bao, P., Wang, S., Wang, B., Zhou, Y., and Xu, R., 1984, Structure and evolution of the Himalayan-Tibet orogenic belt: Nature, v. 307, p.17–22.

Aminzadeh, B., Shahabpour, J., and Maghami, M., 2011, Variation of Rhenium contents in molybdenites from the Sar Cheshmeh porphyry Cu-Mo deposit in Iran: Resource Geology, v. 61, p. 290–295.

Andersen, D.J., and Lindsley, D.H., 1985, New (and final!) models for the Ti-magnetite/ilmenite geothermometer and oxygen barometer: Abstract AGU 1985 Spring Meeting Eos Transactions, v. 46, p. 416.

Anderson, J.L., Barth, A., Wooden, J.L., and Mazdab, F., 2008, Thermometers and thermobarometers in granitic systems: Reviews in Mineralogy and Geochemistry, v. 69, p. 121–142.

Andersen, D.J., Lindsley, D.H., and Davidson, P.M., 1993, QUILF: A Pascal program to assess equilibria among Fe-Mg-Mn-Ti oxides, pyroxenes, olivine, and quartz: Computers and Geosciences, v. 19, p. 1333–1350.

Armijo, R., Tapponnier, P., Mercier, J.L., and Han, T.L., 1986, Quaternary extension in southern Tibet: Field observations and tectonic implications: Journal of Geophysical Research v, 9, p. 13,803–13,872.

Arculus, R., and Powell, R., 1986, Source component imixing in the regions of arc magma generation: Journal of Geophysical Research, v. 91, p. 5913–5926.

Ashton, K.E., Heaman, L.H., Lewry, J.F., Hartlaub, R.P., and Shi, R., 1999, Age and origin of the Jan Lake Complex: a glimpse at the buried Archean craton of the Trans-Hudson Orogen: Canadian Journal of Earth Sciences, v. 36, p. 185–208.

Audétat, A., and Pettke, T., 2006, Evolution of a porphyry-Cu mineralized magma system at Santa Rita, New Mexico (USA): Journal of Petrology, v. 47, p. 2021–2046.

Ayati, F., Yavuz, F., Asadi, H., Richards, J.P., and Jourdan, F., 2013, Petrology and geochemistry of calc-alkaline volcanic and subvolcanic rocks, Dalli porphyry copper-gold deposit, Markazi Province, Iran: International Geology Review, v. 55, p. 158–184.

Baxter, A.T., Aitchison, J.C., and Zyabrev, S.V., 2009, Radiolarian age constraints on Mesotethyan ocean evolution, and their implications for development of the Bangong-Nujiang suture, Tibet: Journal of the Geological Society, v.166, p. 689–694.

Bacon, C.R., and Hirschmann, M.M., 1988, Mg/Mn partitioning as a test for equilibrium between coexisting Fe–Ti oxides: American Mineralogist, v. 73, p. 57–61.

Ballard, J.R., Palin, J.M, and Campbell, I.H., 2002, Relative oxidation states of magmas inferred from Ce(IV)/Ce(III) in zircon: Application to porphyry copper deposits of northern Chile: Contributions to Mineralogy Petrology, v. 144, p. 347–364.

Baker, D.R. and Eggler, D.H., 1983, Fractionation paths of Atka (Aleutians) high-alumina basalts: constraints from phase relations: Journal of Volcanology and Geothermal Research, v.18, p. 387–404.

Banerjee, P., Bürgmann., Nagarajan, B., and Apel, 2008, Intraplate deformation of the Indian subcontinent: Geophysical Research Letters, v. 35, L18301, doi: 10.1029/2008GL035468.

Barker, S.J., Wilson, C.J.N., Baker, J.A., Millet, M.A., Rotella, M.D., Wright, I.C., and Wysoczanski, J.W., 2013, Geochemistry and petrogenesis of silicic magmas in the intra-oceanic Kermadec arc: Journal of Petrology, v. 54, p. 351–391.

BGMRXAR (Bureau of Geology Mineral Resources of Xizang Autonomous Region), 1993, Regional Geology of Xizang (Tibet) Autonomous Region: Geological Publishing House, Beijing, 450 p. (in Chinese with English abstract)

Black, L.P., Kamo, S.L., Allen, C.M., Davis, D., Aleinikoff, J.N., Valley, J.W., Mundil, R., Campbell, I.H., Korsch, R.J., Williams, I.S., and Foudoulis, C., 2004, Improved $^{206}Pb/^{238}U$ microprobe geochronology by the monitoring of a trace-element-related matrix effect; SHRIMP, ID-TIMS, ELA-ICP-MS and oxygen isotope documentation for a series of zircon standards: Chemical Geology, v. 205, p. 115–140.

Blisniuk, P.M., Hacker, B.R., Glodny, J., Ratschbacher, L., Bi, S.W., Wu, Z.H., McWilliams, M.O., and Calvert, A., 2001, Normal faulting in central Tibet since at least 13.5 Myr ago: Nature, v. 412, p. 628–632.

Blevin, P.L., 2004, Redox and compositional parameters for interpreting the granitoid metallogeny of Eastern Australia: Implications for gold-rich ore system: Resource Geology, v. 54, p. 241–252.

Bornhorst, T.J., and Rose, W.I., 1986, Partitioning of gold in young calc-alkaline volcanic rocks from Guatemala: Journal of Geology, v. 94, p. 412–418.

Botcharnikov, R.E., Linnen, R.L., Holtz, W.M., Jugo, P.J., and Berndt, J., 2011, High gold concentrations in sulphide-bearing magma under oxidizing conditions: Nature Geoscience, v. 4, p. 112–115.

Brett, R., and Sato, M., 1984, Intrinsic oxygen fugacity measurements on seven chondrites, a pallasite, and a tektite and the redox state of meteorite parent bodies: Geochimica et Cosmochimica Acta, v. 48, p. 111–120.

Buddington, A.F., and Lindsley, D.H., 1964, Iron–titanium oxide minerals and synthetic equivalents: Journal of Petrology, v. 5, p. 310–357.

Burg, J.P., and Chen, G.M., 1984, Tectonics and structural formation of southern Tibet, China: Nature, v. 11, p. 219–223.

Burnham, C.W., 1979, Magmas and hydrothermal fluids, in Barnes, H.L., ed., Geochemistry of hydrothermal ore deposits, 2nd edition: New York, John Wiley and Sons, p. 71–136.

Burnham, A.D. and Berry, A.J., 2012, An experimental study of trace element partitioning between zircon and melt as a function of oxygen fugacity: Geochimica et Cosmochimica Acta, v. 95, p. 196–212.

Candela, P.A., 1986, The evolution of aqueous vapor from silicate melts: Effect on

oxygen fugacity: Geochimica et Cosmochimica Acta, v. 50, p. 1205–1211.

Candela, P.A., 1992, Controls on ore metal ratios in granite-related ore systems: An experimental and computational approach: Transactions of the Royal Society of Edinburgh, Earth Sciences, v. 83, p. 317–326.

Capitanio, F.A., Morra, G., Goes, S., Weinberg, R.F., and Moresi, L., 2010, India-Asia convergence driven by the subduction of the Greater Indian continent: Nature Geoscience, v. 3, p. 136–139.

Carmichael, I.S.E., 1991, The redox states of basic and silicic magmas: a reflection of their source regions?: Contribution to Mineralogy and Petrology, v. 106, p. 129–141.

Carroll, M.R., and Rutherford, M.J., 1985, Sulfide and sulfate saturation in hydrous silicate melts: Journal of Geophysical Research, v. 90, Supplement, p. C601–C612.

Chan, G.H.N., Waters, D.J., Searle, M.P., Aitchison, J.C., Horstwood, M.S.A., Crowley, Q., Lo, C.H., and Chan, J.S.L., 2009, Probing the basement of southern Tibet: evidence from crustal entrained in a Miocene ultrapotassic dyke: Journal of the Geological society, London, v. 166, p. 45–52.

Chazot, G., Lowry, D., Menzies, M., and Mattey, D., 1997, Oxygen isotope compositions of hydrous and water-poor mantle peridotite: Geochimica et Cosmochimica Acta, v. 61, p. 161–169.

Chen, T., 2006, Geochemistry of the Qushui intrusive of Gangdese in Tibet and its implications for magma mixing: Unpublished Master thesis (in Chinese), China University of Geosciences, Beijing, 59 p.

Chen, L., Qin, K.Z., Li, G.M., Li, J.X., Xiao, B., Jiang, H.Z., Zhao, J.X., Fan, X., and Jiang, S.Y., 2012, Geological and skarn mineral characteristics of Nuri Cu-W-Mo deposit in southern Gangdese, Tibet: Mineral Deposits, v. 31, p. 417–437 (in Chinese with English abstract).

Chen, L., Qin, K.Z., Li, J.X., Xiao, B., Li, G.M., Zhao, J.X., and Fan, X., 2011, Fluid Inclusion and hydrogen, oxygen, sulfur isotopes of Nuri Cu-W-Mo deposit in the southern Gangdese, Tibet: Resource Geology, v. 62, p. 42–62.

Chen, T., 2006, Geochemistry of the Qushui intrusive of Gangdese in Tibet and its implications for magma mixing: Unpublished Master thesis (in Chinese), China University of Geosciences, Beijing, 59 p.

Chiaradia, M., Merino, D., and Spikings, R., 2009, Rapid transition to long-lived deep crustal magmatic maturation and the formation of giant porphyry-related mineralization (Yanacocha, Peru): Earth and Planetary Science Letters, v. 288, p. 505–515.

Chiaradia, M., Ulianov, A., Kouzmanov, K., and Beate, B., 2012, Why large porphyry Cu deposits like high Sr/Y magmas?: Scientific Reports, v. 2, 685; doi : 10.1038/srep00685.

Chiaradia, M., 2014, Copper enrichment in arc magmas controlled by overriding plate thickness: Nature Geoscience, v. 7, p. 43–46.

Chou, I.M., 1978, Calibration of oxygen buffers at elevated P and T using the hydrogen fugacity sensor: American Mineralogist, v. 63, p. 690–703.

Chu, M.F., Chung, S.L., Song, B., Liu, D.Y., O'Reilly, S.Y., Pearson, N.J., Ji, J.Q., and Wen, D.J., 2006, Zircon U-Pb and Hf isotope constraints on the Mesozoic tectonics and crustal evolution of southern Tibet: Geology, v. 34, p. 745–748.

Chung, S.L., Chu, M.F., Zhang, Y.Q., Xie, Y.W., Lo, C.H., Lee. T.Y., Lan, C.Y., Li, X.H., Zhang, Q., and Wang, Y.Z., 2005, Tibetan tectonic evolution inferred from spatial and temporal variations in post-collisional magmatism: Earth-Science Reviews, v. 68, p. 173–196.

Chung, S.L., Liu, D., Ji, J.Q., Chu, M.F., Lee, H.Y., Wen, D.J., Lo, C.H., Lee, T.Y., Qian, Q., and Zhang, Q., 2003, Adakites from continental collision zones: melting of thickened lower crust beneath southern Tibet: Geology, v. 31, p. 1021–1024.

Clayton, R.N., and Mayeda, T.K., 1963, The use of bromine penta-fluoride in the extraction of oxygen from oxide and silicates for isotope analysis: Geochimica et Cosmochimica Acta, v. 27, p. 43–52.

Cloos, M., and Housh, T.B., 2008, Collisional delamination: Implications for porphyry-type Cu–Au ore formation in New Guinea: Arizona Geological Society Digest, v. 22, p. 277–293.

Cogan, M.J., Nelson, K.D., Kidd, W.S.F., Wu, C.D., and Project INDEPTH Team, 1998, Shallow structure of the Yadong-Gulu rift, southern Tibet, from refraction analysis of Project INDEPTH common midpoint data: Tectonics, v. 17, p. 46–61.

Cooke, D.R., Hollings, P., and Walshe, J.L., 2005, Giant porphyry deposits:

characteristics, distribution, and tectonic controls: Economic Geology, v. 100, p. 801–818.

Coulon, C., Maluski, H., Bollinger, C., and Wang, S., 1986, Mesozoic and Cenozoic volcanic rocks from central and southern Tibet: $^{39}Ar/^{40}Ar$ dating, petrological characteristics and geodynamical significance: Earth and Planetary Science Letters, v. 79, p. 281–302.

Copley, A., Avouac, J.P., and Wernicke, B.P., 2012, Evidence for mechanical coupling and strong Indian lower crust beneath southern Tibet: Nature, v. 472, p. 79–81.

Corfu, 2013, A century of U-Pb geochronology: the long quest towards concordance: GSA bulletin, v. 125, p. 33–47.

Creaser, R.A., Papanastassiou, D.A., and Wasserburg, G.J., 1991, Negative thermal ion mass spectrometry of osmium, rhenium and iridium: Geochimica Cosmochimica Acta, v. 55, p. 397– 404.

Creaser, R.A., Erdmer, P., Stevens, R.A., and Grant, S.L., 1997, Tectonic affinity of Nisutlin and Anvil assemblage strata from the Teslin tectonic zone, northern Canadian Cordillera: Constraints from neodymium isotope and geochemical evidence: Tectonics, v. 16, p. 107–121.

Creaser, R.A., Grutter, H., Carlson, J. and Crawford, B., 2004, Macrocrystal phlogopite Rb–Sr dates for the Ekati property kimberlites, Slave Province, Canada: evidence for multiple intrusive episodes in the Paleocene and Eocene: Lithos, v. 76, p. 399–414.

Davidson, J., Turner, S., Handley, H., Macpherson, C., and Dosseto, A., 2007, Amphibole “sponge” in arc crust?: Geology, v. 35, p. 787–790.

Davies, J.H., and Stevenson, D.J., 1992, Physical model of source region of subduction zone volcanics: Journal of Geophysical Research, v. 97, p. 2037–2070.

de Sigoyer, J., Chavagnac, V., Blichert-Toft, J., Villa, I.M., Luais, B., Guillot, S., Cosca, M., and Mascle, G., 2000, Dating the Indian continental subduction and collision thickening in the northwest Himalaya: Multichronology of the Tso Morari eclogites: Geology, v. 28, p. 487–490.

DePaolo, D., 1981, Trace element and isotopic effects of combined wallrock assimilation and fractionation: Earth and Planetary Science Letters, v. 53, p. 189–202.

DeCelles, P.G., Gehrels, G.E., Najman, Y., Martin, A.J., Carter, A., and Garzanti, E.,

2004, Detrital geochronology and geochemistry of Cretaceous–early Miocene strata of Nepal: implications for timing and diachroneity of initial Himalayan orogenesis: Earth and Planetary Science Letters, v. 227, p. 313–330.

DeCelles, P.G., Gehrels, G.E., Quade, J., LaReau, B., Spurlin, M., 2000, Tectonic implication of U–Pb zircon ages of the Himalayan orogenic belt in Nepal: Science, v. 288, p. 497–499.

Deng, W.M., Huang, X., and Zhong, D., 1998, Alkali-rich porphyry and its relation with intraplate deformation of north part of Jinsha River belt in western Yunnan, China: Science in China (Series D), v. 41, p. 297–305.

Defant, M.J., and Drummond, M.S., 1990, Derivation of some modern arc magmas by melting of young subducted lithosphere: Nature, v. 347, p. 662–665.

Dewey, J.F., Shackelton, R.M., Chang, C., and Sun, Y., 1988, The tectonic evolution of the Tibetan Plateau: Philosophical Transactions of the Royal Society London, v. 327, p. 379–413.

de Sigoyer, J., Chavagnac, V., Blichert-Toft, J., Villa, I.M., Luais, B., Guillot, S., Cosca, M., and Mascle, 2000, Dating the Indian continental subduction and collision thickening in the northwest Himalaya: Multichronology of the Tso Morari eclogites: Geology, v. 28, p. 487–490.

Dickin, A.P., 2005, Radiogenic isotope geology (2nd edition): Cambridge University Press, 492 p.

Dilles, J.H., 1987, Petrology of the Yerington batholith, Nevada: Evidence for evolution of porphyry copper ore fluids: Economic Geology, v. 82, p. 1750–1789.

Ding, L., Kapp. P., Zhong, D., and Deng, W., 2003, Cenozoic volcanism in Tibet: Evidence for a transition from oceanic to continental subduction: Journal of Petrology, v. 44, p. 1833–1865.

Dong, G.C., 2002, Linzizong volcanic rocks and implications for probing India-Eurasia collision process in Linzhou Volcanic Basin, Tibet: Unpublished Ph.D. Thesis (in Chinese), China University of Geosciences, 150 p.

Dong, G.C., Mo, X.X., Zhu, D.C., Wang, L.L., Chen, T., and Li, B., 2006a, Magma mixing in middle part of Gangdese magma belt: Evidences from granitoid complex: Acta Petrologica Sinica, v.22, p. 835–844 (in Chinese with English abstract).

Dong, G.C., Mo, X.X., Zhao, Z.D., Zhu, D.C., Song, Y.T., and Wang, L., 2006b. Gabbros from southern Gangdese: Implication for mass exchange between mantle and crust: Acta Petrologica Sinica, v. 24, p. 203–210 (in Chinese with English abstract).

Droop, G.T.R., 1987. A general equation for estimating Fe^{3+} concentrations in ferromagnesian silicates and oxides from microprobe analyses, using stoichiometric criteria: Mineralogical Magazine, v. 51, p. 431–435.

Du, A.D., Wu, S.Q., Sun, D.Z., Wang, S.X, Qu, W.J., Markey, R., Stein, H., Morgan, J., and Malinovskiy, D., 2004, Preparation and certification of Re-Os dating reference materials: molybdenite HLP and JDC: Geostandard and Geoanalytical Research, v. 28, p. 41–52.

Du, D.H., Yang, Z.M., Li, Q.Y., Liu, Y.F., Ge, S., and Wang, H.Y., 2012, Determination of Eocene porphyritic monzogranite intrusions in Tinggong ore district of Tibet and its geological significance: Mineral Deposits, v. 31, p. 745–757 (in Chinese with English abstract).

England, P., and Houseman, G., 1989, Extension during active convergence, with application to the Tibetan Plateau, Journal of Geophysics Research, v. 94, p.17561–17579.

Enkelemann, E., Weislogel, A., Ratchbacher, L., Eide, E., Renno, A., and Wooden, J., 2007, How was the Triassic Songpan-Ganzi basin filled? A provenance study: Tectonics, v. 26, TC4007.

Eiler, J.M., 2001, Oxygen isotope variations of basaltic lavas and upper mantle rocks, in Valley, J.W., Cole, D.R., eds., Stable isotope geochemistry, Reviews in Mineralogy and Geochemistry, v. 43, p. 319–364.

Eugster, H.P., and Wones, D.R., 1962, Stability relations of the ferroginous biotite, annite: Journal of Petrology, v. 3, p. 82–125.

Feldl, N., and Bilham, R., 2006, Great Himalayan earthquakes and the Tibetan plateau: Nature, v. 444, p. 165–170.

France-Lanord, C., Sheppard, S.M.F., and Le Fort, P., 1988, Hydrogen and oxygen isotope variations in the High Himalaya peraluminous Manaslu leucogranite: Evidence for heterogeneous sedimentary source: Geochemica et Cosmochimica Acta: v. 52, p. 513–526.

Frey, F.A., Chappell, B.W., and Roy, S.D., 1978, Fractionation of rare-earth elements in the Tuolumne Intrusive Series, Sierra Nevada batholith, California: Geology, v. 6, p. 239–242.

Gao, Y.F., Hou, Z.Q., Kamber, B., Wei, R.H., Meng, X.J., and Zhao, R.S., 2007, Adakite-like porphyries from the southern Tibetan continental collision zones: evidence for slab melt metasomatism: Contributions to Mineralogy and Petrology, v. 153, p. 105–120.

Gao, Y.F, Wei, R.H, Hou, Z.Q, Tian, S.H, and Zhao, R.S., 2008, Eocene high-MgO volcanism in southern Tibet: New constraints for mantle source characteristics and deep process: Lithos, v. 105, p. 63–72.

Gao, Y.F., Yang, Z.S., Santosh, M., Hou, Z.Q., Wei, R.H., and Tian, S.H., 2010, Adakitic rocks from slab melt-modified mantle sources in the continental collision zone of southern Tibet: Lithos, v. 119, p. 651–663.

Ge, L.S., Li, H.G., Wang, K.Q., Zou, Y.L., Wang, Z.H., Zhang, X.J., Yuan, S.S., and Xing, J.B., 2006, Geochemical characteristics of the W-Mo-Bi polymetallic deposit in the snow-capped Jaggang mountain, Xainza Country, Tibet: Mineral Deposits, v. 25, p. 345–348 (in Chinese with English abstract).

Ghiorso, M.S., and Sack, R.O., 1991, Fe–Ti oxide geothermometry: thermodynamic formulation and the estimation of intensive variables in silicic magmas. Contribution to Mineralogy and Petrology, v. 108, p. 485–510.

Ghiorso, M.S., and Evans, B.W., 2008, Thermodynamics of rhombohedral oxide solid solutions and a revision of the Fe–Ti two-oxide geothermometer and oxygenbarometer: American Journal of Science, v. 308, p. 957–1039.

Gill, J.B., 1981, Orogenic andesites and plate tectonics: New York, Springer-Verlag, 390 p.

Goldstein, S.L., O'Nions, R.K., and Hamilton, P.J., 1984, A Sm-Nd isotopic study of atmospheric dusts and particulates from major river systems: Earth and Planetary Science Letters, v. 70, p. 221–236.

Gramlich, J.W., Murphy, T.J., Garner, E.L., and Shields, W.R., 1973, Absolute isotopic abundance ratio and atomic weight of a reference sample of rhenium: Journal of Research of National Bureau of Standards, v. 77A, p. 691–698.

Green, T.H., and Pearson, N.J., 1985, Experimental determination of REE partition coefficients between amphibole and basaltic to andesitic liquids at high pressure: Geochimica et Cosmochimica Acta, v. 49, p. v. 1465–1468.

Grove, T.L., Elkins-Tanton, L.T., Parman, S.W., Müntener, O., and Gaetani, G.A., 2003, Fractional crystallization and mantle melting controls on calc-alkaline differentiation trends: Contribution to Mineralogy and Petrology, v. 145, p. 515–533.

Guo, Z.F., Wilson, M., and Liu, J.Q., 2007, Post-collisional adakites in south Tibet: products of partial melting of subduction-modified lower crust: Lithos: v. 96, p. 205–224.

Guo, Z.F., Wilson, M., Zhang, M.L., Cheng, Z.H., and Zhang, L.H., 2013, Post-collisional, K-rich mafic magmatism in south Tibet: constraints on Indian slab-to-wedge transport processes and plateau uplift: Contribution to Mineralogy and Petrolgy, v. 165, p. 1311–1340.

Hamlyn, P.R., Keays, R.R., Cameron, W.E., Crawford, A.J., and Waldron, H.M., 1985, Precious metals in magnesian low-Ti lavas: Implications for metallogenesis and sulfur saturation in primary magmas: Geochimica et Cosmochimica Acta, v, 49, p. 1797–1811.

Harris, N.B.W., Pearce, J.A., and Tindle, A.G., 1986, Geochemical characteristics of collisional-zone magmatism. In: Coward, M.P., Reis, A.C., eds., Collision tectonics: Geological Society, London, Special Publications, v. 19, p. 67–81.

Harrison, T.M., Yin, A., Grove, M., and Lovera, O.M., 2000, The Zedong window: A record of superposed Tertiary convergence in southeastern Tibet, Journal of Geophysical Research: v. 105, p. 19211–19230.

Hanson, G.N., 1980, Rare earth elements in petrogenetic studies of igneous systems: Annual Review of Earth Planetary Sciences, v. 8, p. 371–406.

Harrison, T.M., Yin, A., Grove, M., and Lovera, O.M., 2000, The Zedong window: A record of superposed Tertiary convergence in southeastern Tibet: Journal of Geophysical Research, v. 105, p. 19211–19230.

Haschke, M., Ahmadian, J., Murata, M., and McDonald, I., 2010, Copper mineralization prevented by arc-root delamination during Alpine–Himalayan collision in central Iran: Economic Geology, v. 105, p. 855–865.

He, S.D., Kapp, P., DeCelles, P.G., Gehrels, G.E., and Heizler, M., 2007, Cretaceous-Tertiary geology of the Gangdese arc in the Linzhou area, southern Tibet: Tectonophysics, v. 433, p. 15-37.

Hébert, R., Guilmette, C., Dostal, J., Bezard, R., Lesage, G., Bédard, É., and Wang, C.S., 2014, Miocene post-collisional shoshonites and their crustal xenoliths, Yarlung Zangbo Suture Zone southern Tibet: Geodynamic implications: Gondwana Research, v. 25, p. 1263–1271.

Hedenquist, J.W., and Lowenstern, J.B., 1994. The role of magmas in the formation of hydrothermal ore deposits: Nature, v. 370, p. 519–527.

Hetzel, R., Dunkl, I., Haider, V., Strobl, M., von Eynatten, H., Ding, L., and Frei, D., 2011, Peneplain formation in southern Tibet predates the India-Asia collision and plateau uplift: Geology, v. 39, p.983-986.

Hezarkhani, A., 2006, Hydrothermal evolution of the Sar-Cheshmah porphyry Cu-Mo deposit, Iran: Evidence from fluid inclusions: Journal of Asian Earth Sciences, v. 28, p. 409–422.

Hidalgo, P.J., Vogel, T.A., Rooney, T., Currier, R., and Layer, P.W., 2011, Origin of silicic volcanism in the Panamanian arc: evidence for a two-stage process at El Valle volcano: Contributions to Mineralogy and Petrology, v. 162, p. 1115–1138.

Hildreth, W., and Moorbath, S., 1988, Crustal contributions to arc magmatism in the Andes of central Chile: Contributions to Mineralogy and Petrology, v. 98, p. 455–489.

Hollister, L.S., Grissom, G.C., Peters, E.K., Stowell, H.H., and Sisson, V.B., 1987, Confirmation of the empirical correlation of Al in hornblende with pressure of solidification of calc-alkaline plutons: American Mineralogist, v. 72, p. 231–239.

Holzheid, A., and Lodders, K., 2001, Solubility of copper in silicate melts as function of oxygen and sulfur fugacities, temperature, and silicate composition: Geochimica et Cosmochimica Acta, v. 65, p. 1933–1951.

Hoskin, P.W.O., and Schaltegger, U., 2003, The composition of zircon and igneous and metamorphic petrogenesis, in Hanchar, J.M., and Hoskin, P.W.O. eds., Zircon: Reviews in Mineralogy and Geochemistry, v. 53, p. 27–62.

Hou, Z.Q., Zhang, H.R., Pan, X.F., and Yang, Z.M., 2011, Porphyry Cu (-Mo-Au) deposits related to melting of thickened mafic lower crust: Examples from the eastern

Tethyan metallogenic domain: Ore Geology Review, v. 39, p. 21–45.

Hou, Z.Q., Yang, Z.M., Qu, X.M., Meng, X.J., Li, Z.Q., Beaudoin, G., Rui, Z.Y., Gao, Y.F., and Zaw, K., 2009, The Miocene Gangdese porphyry copper belt generated during post-collisional extension in the Tibetan Orogen: Ore Geology Reviews, v. 36, p. 25–31.

Hou, Z.Q., Gao, Y.F., Qu, X.M., Rui, Z.Y., and Mo, X.X., 2004, Origin of adakitic intrusives generated during mid-Miocene east-west extension in southern Tibet: Earth and Planetary Science Letters, v. 220, p. 139–155.

Hu, D.G., Wu, Z.H., Jiang, W., Shi, Y.R., Ye, P.S., and Liu, Q.S., 2005, SHRIMP zircon U–Pb age and Nd isotopic study on the Nyainqêntanglha Group in Tibet: Science in China (Series D: Earth Sciences), v. 48, p. 1377–1386.

Hu, M.Y., He, H.L., Zhan, X.C., Fan, X.T., Wang, G., and Jia, Z.R., 2008, Matrix normalization fro in-situ multi-element quantitative of zircon in Laser Ablation-Inductively Coupled Plasma Mass Spectrometry: Chinese Journal of Analytical Chemistry, v. 36, p. 947–983. (in Chinese with English abstract)

Hu, P., Nie, F.J., Jiang, S.H., Liu, Y., and Zhang, W.Y., 2006, Zircon SHRIMP U-Pb age of Songtuoga intrusion in Mayum gold deposit district, Xizang (Tibet) and its geological significances: Gelogical Review, v. 52, p. 276–282 (in Chinese with English abstract).

Huang, G.C., Wu, F.T., Roecker, S.W., and Sheehan, A.F., 2009, Lithospheric structure of the central Himalaya from 3-D tomographic imaging: Tectonophysics, v. 475, p. 524–543.

Huang, K., Zheng, Y., Zhang, S., Li, W., Sun, Q., Li, Q., Liang, W., Fu, Q., and Hou, Z., 2012, LA-ICP-MS zircon U-Pb dating of two types of porphyry in the Yaguila mining area, Tibet: Acta Petrologica et Mineralogica, v. 31, p. 348–360 (in Chinese with English abstract).

Huebner, J.S., 1971, Buffering techniques for hydrostatic systems at elevated pressure in G. C. Ulmer, ed., Research Techniques for High Pressure and High Temperature: New York, Springer-Verlag, p. 123–177.

Huebner, J.S., and Sato, M., 1970, The oxygen fugacity-temperature relationships of manganese oxide and nickel oxide buffers: American Mineralogist, v. 55, p. 934–952.

Idrus, A., Kolb, J., and Meyer, F.M., 2007, Chemical composition of rock-forming minerals in copper-gold-bearing tonalite porphyries at the Batu Hijau deposit, Sumbawa island, Indonesia: Implications for crystallization conditions and fluorine–chlorine fugacity: Resource Geology, v. 57, p.102–113.

Imer, A., Richards, J.P., and Creaser, R., 2012, Age and tectonomagmatic setting of the Eocene Çöpler–Kabataş magmatic complex and porphyry-epithermal Au deposits, East Central Anatolia, Turkey: Mineralium Deposita, v. 48, p. 557–583.

Inger, S., and Harris, N., 1993, Geochemical constraints on leucogranite magmatism in the Langtang valley, Nepal Himalaya: Journal of Petrology, v. 34, p. 345–368.

Irvine, T.N., and Baragar, W.R.A., 1971, A guide to the chemical classification of the common volcanic rocks: Canadian Journal of Earth Sciences, v. 8, p. 523–548.

Jamieson, R.A., Unsworth, M.J., Harris, N.B,W., Rosenberg, C.L., and Schulmann, 2011, Crustal melting and the flow of mountains: Elements, v. 7, p. 253–260.

Jamieson, R.A., and Beaumont, C., 2013, On the origin of orogens: GSA Bulletin, v. 125, p. 1671–1702.

Ji, W.Q., Wu, F.Y., Chung, S.L., Li, J.X., and Liu, C,Z., 2009, Zircon U-Pb geochronology and Hf isotopic constraints on petrogenesis of the Gangdese batholith, southern Tibet: Chemical Geology, v. 262, p. 229–245.

Ji, W.Q., Wu, F.Y., Liu, C.Z., and Chung, S.L., 2012, Early Eocene crustal thickening in southern Tibet: New age and geochemical constraints from the Gangdese batholith: Journal of Asian Earth Sciences, v. 53, p. 82–95.

Johnson, M.C., and Rutherford, M.J., 1989, Experimental calibration of the aluminum-in-hornblende geobarometer with application to Long Valley caldera (California) volcanic rocks: Geology, v. 17, p. 837–841.

Jugo, P., 2009, Sulfur content at sufide saturation in oxidized magmas: Geology, v. 37, p. 415–418.

Jugo, P., Luth, R., and Richards, J., 2005a, An experimental study of the sulfur content in basaltic melts saturated with immiscible sulfide or sulfate liquids at 1300 °C and 1.0 GPa: Journal of Petrology, v. 46, p. 783–798.

Jugo, P., Luth, R., and Richards, J., 2005b, Experimental data on the speciation of sulfur

as a function of oxygen fugacity in basaltic melts: Geochimica et Cosmochimica Acta, v. 69, p. 497–503.

Kapp, P., Yin, A., Harrison, T.M., and Ding, L., 2005, Cretaceous–Tertiary shortening, basin development, and volcanism in central Tibet: Geological Society of America Bulletin, v. 117, p. 865–878, doi: 10.1130/ B25595.1.

Kapp, P., DeCelles, P.G., Leier, A.L., Fabijanic, J.M., He, S., Pullen, A., Gehrels, G.E., and Ding, L., 2007, The Gangdese retroarc thrust belt revealed: GSA Today, v. 17, p. 4–10.

Kay, S.M., and Mpodozis, C., 2001, Central Andean ore deposits linked to evolving shallow subduction systems and thickening crust: GSA Today, v. 11, p. 4–9.

Khan, T., Khan, M.A., Jan, M.Q., and Naseem, M., 1996, Back-arc basin assemblages in Kohistan, Northern Pakistan: Geodinamica Acta, v. 9, p. 30–40.

Kind, R., and Yuan, X., 2010, Seismic images of the biggest crash on earth: Science, v. 329, p. 1479–1480.

King, J., Harris, N., Argles, T., Parrish, R., Charlier, B., Sherlock, S., and Zhang, H.F., 2007, First field evidence for southward ductile flow of Asian crust beneath southern Tibet: Geology, v. 35, p. 727–730.

Kumar, P., Yuan, X., Kind, R., Ni, J., 2006, Imaging the colliding Indian and Asian lithospheric plates beneath Tibet: Journal of Geophysical Research, v.111, B6: doi: 10.1029/2005JB003930.

Kyser, T. K., 1986, Stable isotope variations in the mantle: Mineralogical Society of America, Reviews in Mineralogy, v. 16, p. 141–164.

Le Maitre, R.W., ed., 1989, A classification of igneous rocks and glossary of terms: Oxford, Blackwell Scientific Publications, 193 p.

Lee, C.T., Luffi, P., Chin, E., Bouchet, R., Dasgupta., Morton, D.M., Roux, V.L., Yin, Q.Z., and Jin, D., 2012, Copper systematics in arc magmas and implications for crust–mantle differentiation: Science, v. 336, p. 64–68.

Lee, H.Y., Chung, S.L., Ji, J.Q., Qian, Q., Gallet, S., Lo, C.H., Lee, T.Y., and Zhang, Q., 2011, Geochemical and Sr-Nd isotopic constraints on the genesis of the Cenozoic Linzizong volcanic successions, southern Tibet: Journal of Asian Earth Sciences, v. 53, p. 96–114.

Lee, T.Y., and Lawver, L.A., 1995, Cenozoic plate reconstruction of Southeast Asia: Tectonophysics, v. 251, p. 85–138.

Lepage, L.D., 2003, ILMAT: an Excel worksheet for ilmenite–magnetite geothermometry and geobarometry: Computers and Geosciences, v. 29, p. 673–678.

Li, C., van der Hilst, R.D., Meltzer, A.S., and Engdahl, E.R., 2008, Subduction of the Indian lithophere beneath the Tibetan plateau and Burma: Earth and Planetary Science Letters, v. 274, p. 157–168.

Li, J.X., Qin, K.Z., Li, G.M., Xiao, B., Chen, L., and Zhao, J.X., 2011, Post-collsional ore-bearing adakitic porphyries from Gangdese porphyry copper belt, southern Tibet: Melting of thickened juvenile arc lower crust: Lithos, v. 126, p. 264–277.

Li, J.Z., Zhang, Y.Y., and Luo, H.Y., 1992, A research on petrological characters and genesis of the Cenozoic volcanic rocks in the Yangying village geothermal field, Dangxiong, Tibet, China: Geoscience, v. 6, p. 96–109. (in Chinese with English abstract)

Li, L.Q., Pan, L.C., and Zhang, G.F., 2010, Non-contamination powdering procedures for geochemical samples: Geological Survey and Research, v. 33, p. 238–240.

Liang, H.Y., Campbell, I.H., Allen C., Sun, W.D., Liu, C.Q., Yu, H.X., Xie, Y.W., and Zhang, Y.Q., 2006, Zircon Ce^{4+}/Ce^{3+} ratios and ages for Yulong ore-bearing porphyries in eastern Tibet: Mineralium Deposita, v. 41, p. 152–159.

Liang, X.F., Sandvol, E., Chen, Y.J., Hearn, T., Ni, J., Klemperer, S., Shen, Y., and Tilmann, F., 2012, A complex Tibetan upper mantle: A fragemented Indian slab and no south-verging subduction of Eurasian lithosphere: Earth and Planetary Sciences Letters, v. 333–334, p. 101–111.

Liu, C.Z., Wu, F.Y., Chung, S.L., and Zhao, Z.D., 2012, Fragments of hot and metasomatized mantle lithosphere in Middle Miocene ultrapotassic lavas, southern Tibet: Geology, v. 39, p. 923–926.

Liu, D., Zhao, Z.D., Zhu, D.C., Niu, Y.L., and Harrison, T.M., 2014, Zircon xenocrysts in Tibetan ultrapotassic magmas: Imaging the deep crust through time: Geology, v. 42, p. 43–46.

Liu, S., Hu, R.Z., Feng, C.X., Zou, H.B., Li, C., Chi, G.X., Peng, J.T., Zhong, H., Qi, L., Qi, Y.Q., and Wang, T., 2008, Cenozoic high Sr/Y volcanic rocks in the Qiangtang

terrane, northern Tibet: geochemical and isotopic evidence for the origin of delaminated lower continental melts: Geological Magazine, v. 145, p. 463–474.

Loucks, R.R., 2013, Distinctive composition and genesis of copper ore-forming arc magmas: Mineralogical Magazine, v. 77, p. 1642.

Luck, J.M., and Allègre, C.J., 1983, ^{187}Re–^{187}Os systematics in meteorites and Cosmochemical consequence: Nature, v. 302, p. 130–132.

Lu, Y.J., Kerrich, R., Kemp, A.I.S., McCuaig, T.C., Hou, Z.Q., Hart, C.J.R., Bagas, L.,Yang, Z.M., Cliff, J., Belousova, E.A., Jourdan, F., and Evans, N.J., 2013, Intracontinental Eocene-Oligocene porphyry Cu mineral systems of Yunnan, western Yangtze Craton, China: Compositional characteristics, sources, and implications for continental collision metallogeny: Economic Geology, v. 108, p. 1541–1576

Ludwig, 2008, User's manual for Isoplot 3.7: A geochronological toolkit for Microsoft Excel: Berkeley Geochronology Center, Special Publication 4, 76 p.

Martin, H., Adakitic magmas: modern analogues of Archaean granitoids: Lithos, v. 46, p. 411–429.

Mattey, D.P., Lowry, D., Macpherson, C.G., and Chazot, G., 1994a, Oxygen isotope compositions of mantle minerals by laser fluorination analysis: homogeneity in peridotite, heterogeneity in eclogites: Mineralogical Magazine, v. 58A, p. 573–574.

Mattey, D., Lowry, D., and Macpherson, C., 1994b, Oxygen isotope composition of mantle peridotite: Earth and Planetary Science Letters, v. 128, p. 231–241.

Mechie, J., and Kind, R., 2013, A model of the crust and mantle structure down to 700 km depth beneath the Lhasa to Golmud transect across the Tibetan plateau as derived from seismological data: Tectonophysics, doi:10.1016/j.tecto.2013.04.030 (in press)

Meng, J., Wang, C., Zhao, X., Coe, R., Li, Y.L., and Finn, D., 2012, India-Asia collision was at 24° N and 50 Ma: Paleomagnetic proof from southern Asia: Scientific Reports, 2, 925; doi: 10.1038/srep00925.

Meng, X., Hou, Z., Gao, Y., Huang, W., Qu, X., and Qu, W., 2003, Re-Os dating for molybdenite from Qulong porphyry copper deposit in Gangdese metallogenic belt, Xizang and its metallogenic significance, v. 49, p. 660–666 (in Chinese with English abstract).

Meisel, T., Walker, R.J., Irving, A.J., and Lorand, J.P., 2001, Osmium isotopic

compositions of mantle xenoliths: A global perspective: Geochimica et Cosmochimica Acta, v. 65, p. 1311–1323.

Metcalfe, I., 2009, Late Palaeozoic and Mesozoic tectonic and palaeogeographical evolution of SE Asia, in Buffetaut, E., et al., eds., Late Palaeozoic and Mesozoic ecosystems in SE Asia: Geological Society of London Special Publication 315, p. 7–23, doi:10.1144/ SP315.2.

McInnes, B.I.A., Evans, N.J., Fu, F.Q., Garwin, S., Belousova, E., Griffin, W.L., Bertens, A., Sukarna, D., Permanadewi, S., Andrew, R.L., and Deckart, K., 2003, Thermal history analysis of selected Chilean, Indonesian and Iranian porphyry Cu-Mo-Au deposits; in Porter, T.M. (Ed.), Super porphyry copper and gold deposits: A global perspective, PGC Publishing, Adelaide, v.1, p. 27–42.

Middlemost, 1994, Naming materials in the magma / igneous rock system: Earth Science Reviews, v. 37, p. 215–224.

Mitsuishi, M., Wallis, S.R., Aoya, M., Lee, J., and Wang, Y., 2012, E-W extension at 19 Ma in the Kung Co area, S, Tibet: Evidence for contemporaneous E-W and N-S extension in the Himalayan orogen: Earth and Planetary Science Letters, v. 325–326, p. 10–20.

Moore, G.M., and Carmichael, I.S.E., 1998, The hydrous phase equilibria (to 3 kbar) of an andesite and basaltic andesite from western Mexico: Constraints on water content and conditions of phenocryst growth: Contributions to Mineralogy and Petrology, v. 130, p. 304–319.

Mo, X.X., Niu, Y.L., Dong, G.C., Zhao, Z.D., Hou, Z.Q., Zhou, S., and Ke, S., 2008, Contribution of syncollisional felsic magmatism to continental crust growth: A case study of the Paleogene Linzizong volcanic succession in southern Tibet: Chemical Geology, v. 250, p. 49–67.

Mo, X.X., Hou, Z.Q., Niu, Y.L., Dong, G.C., Zhao, Z.D. and Yang, Z.M., 2007, Mantle contributions to crustal thickening during continental collision: Evidence from Cenozoic igneous rocks in southern Tibet: Lithos, v. 96, p. 225–242.

Mo, X.X., Dong, G.C., Zhao, Z.D., Guo, T.Y., Wang, L.L., and Chen, T., 2005, Timing of magma mixing in the Gangdise magmatic belt during the India-Asia collision: Zircons SHRIMP U-Pb dating: Acta Geologica Sinica, v. 79, p. 66–76.

Moore, G.M., and Carmichael, I.S.E., 1998, The hydrous phase equilibria (to 3 kbar) of an andesite and basaltic andesite from western Mexico: Constraints on water content and conditions of phenocryst growth: Contributions to Mineralogy and Petrology, v. 130, p. 304–319.

Mungall, J.F., 2002, Roasting the mantle: slab melting and the genesis of major Au and Au-rich deposits: Geology, v. 30, p. 915–918.

Müntener, O., Kelemen, P.B., and Grove, T.L., 2001, The role of H_2O during crystallization of primitive arc magmas under uppermost mantle conditions and genesis of igneous pyroxenites: An experimental study: Contributions to Mineralogy and Petrology, v. 141, p. 643–658.

Muñoz, M., Charrier, R., Fanning, C.M., Maksaev, V. and Deckart, K., 2012, Zircon trace element and O–Hf isotope analyses of mineralized intrusions from El Teniente ore deposit, Chilean Andes: Constraints on the source and magmatic evolution of porphyry Cu–Mo related magmas: Journal of Petrology, v. 53, p. 1091–1122.

Naney, M.T., 1983, Phase equilibria of rock-forming ferromagnesian silicates in granitic systems: American Journal of Science, v. 283, p. 993–1033.

Pan, G.T., Ding, J., Yao, D., and Wang, L., 2004, The Guide Book of 1:1,500,000 Geologic map of the Qinghai-Xizang (Tibet) Plateau and adjacent Areas: Chengdu Cartographic Publishing House, 44 p. (in Chinese).

Pearce, J.A., 1982, Trace element characteristics of lavas from destructive plate boundaries, in Thorp, R.S., eds., Andesites: Orogenic Andesites and Related Rocks, John Wiley and Sons, New York, 724 p.

Pearce, N.J.G., Perkins, W.T., Westgate, J.A., Gorton, M.P., Jackson, S.E., Neal, C.R., and Chenery, S.P., 1997, A compilation of new and published major and trace element data for NIST SRM 610 and NIST SRM 612 glass reference materials: Geostandards Newsletter, v. 21, p. 115–144.

Perfit, M.R., Gust, D.A., Bence, A.E., Arculus, R.J., and Taylor, S.R., 1984, Chemical characteristics of island arc basalts: implication for mantle sources: Chemical Geology, v. 30, p. 227–256.

Pichavant, M., Martel, C., Bourdier, J.L., and Scaillet, B., 2002, Physical conditions,

structure, and dynamics of a zoned magma chamber: Mount Peleè (Martinique, Lesser Antilles Arc): Journal of Geophysical Research, v. 107, B5, 2093. doi:10.1029/2001JB000315.

Powell, R., and Powell, M., 1977, Geothermometry and oxygen barometry using coexisting iron-titanium oxides: a reappraisal: Mineralogical Magazine, v. 41, p. 257–263.

Pollard, P.J., Taylor, R.G., and Peters, L., 2005, Ages of intrusion, alteration, and mineralization at the Grasberg Cu–Au deposit, Papua, Indonesia: Economic Geology, v. 100, p. 1005–1020.

Qu, X., Hou, Z., and Li, Y., 2004, Melt components derived from a subducted slab in late orogenic ore-bearing porphyries in the Gangdese copper belt, southern Tibetan Plateau: Lithos, v. 74, p. 131–148.

Qu, X., Hou, Z., Khin Zaw, and Li, Y., 2007, Characteristics and genesis of Gangdese porphyry copper deposits in the southern Tibetan Plateau: preliminary geochemical and geochronological results: Ore Geology Reviews, v. 31, p. 205–223.

Rickwood, P.C., 1989, Boundary lines within petrologic diagrams which use oxides of major and minor elements: Lithos, v. 22, p. 247–263.

Rowley, D.B., 1996, Age of initiation of collision between India and Asia: a review of stratigraphic data: Earth and Planetary Science Letters, v. 145, p. 1–13.

Royden, L.H., Burchfiel, B.C., King, R.W., Wang, E., Chen, Z.L., Shen, F., and Liu, Y.P., 1997, Surface Deformation and lower crustal flow in eastern Tibet: Science, v. 276, p. 788–790.

Rhodes, J.M. and Vollinger, M.J., 2005, Ferric/ferrous ratios in 1984 Mauna Loa lavas: a contribution to understanding the oxidation state of Hawaiian magmas: Contributions to Mineralogy and Petrology, v. 149, 666–674.

Replumaz, A., Negredo, A.M., Villaseñor, A., and Guillot, S., 2010, Indian continental subduction and slab breakoff during Tertiary collision: Terra Nova, v. 22, p. 290–296.

Ridolfi, F., Renzulli, A., and Puerini, M., 2010, Stability and chemical equilibrium of amphibole in calc-alkaline magmas: An overview, new thermobarometric formulations and application to subduction-related volcanoes: Contributions to Mineralogy and Petrology, v. 160, p. 45–66.

Richards, J.P., McCulloch, M.T., Chappell, B.W., and Kerrich, R., 1991, Sources of metals in the Porgera gold deposit, Papua New Guinea: Evidence from alteration, isotope, and noble metal geochemistry: Geochimica et Cosmochimica Acta, v. 55, p. 565–580.

Richards, J.P., 1995, Alkalic-type epithermal gold deposits—a review: Mineralogical Association of Canada Short Course Series, v. 23, p. 367–400.

Richards, J.P., 2003, Tectono-magmatic precursors for porphyry Cu-(Mo-Au) deposit formation: Economic Geology, v. 98, p. 1515−1533.

Richards, J.P., 2009, Postsubduction porphyry Cu–Au and epithermal Au deposits: products of remelting of subduction-modified lithosphere. Geology, v.37, p. 247–250.

Richards, J.P., 2011, Magmatic to hydrothermal metal fluxes in convergent and collided margins: Ore Geology Reviews, v. 40, p. 1–26.

Richards, J.P., and Mumin, H., 2013, Lithospheric fertilization and mineralization by arc magmas: Genetic links and secular differences between porphyry copper ± molybdenum ± gold and magmatic-hydrothermal iron oxide copper-gold deposits: Society of Economic Geologists, Special Publications, v. 17, p. 277–299.

Rickwood, P.C., 1989, Boundary lines within petrologic diagrams which use oxides of major and minor elements: Lithos, v. 22, p. 247–263.

Rohrlach, B., and Loucks, R., 2005, Multi-million-year cyclic ramp-up of volatiles in a lower crustal magma reservoir trapped below the Tampakan Cu-Au deposit by Mio-Pliocene crustal compression in the southern Philippinel; in Porter, T.M. (ed.), Super Porphyry Copper & Gold Deposits: A Global Perspective: PGC Publishing, Adelaide, v. 2, p. 369–407.

Rohrmann, A., Kapp, P., Carrapa, B., Reiners, P.W., Guynn, J., Ding, L., and Heizler, M., 2012, Thermochronologic evidence for plateau formation in central Tibet by 45 Ma: Geology, v. 40, p. 187–190.

Rolland, Y., and Pêcher, A., and Picard, C., 2000, Middle Cretaceous back-arc formation and arc evolution along the Asian margin: the Shyok Suture Zone in northern Ladakh (NW Himalaya): Tectonophysics, v. 325, p. 147–173.

Rollinson, H., 1993, Using geochemical data: evaluation, presentation, interpretation: Pearson Education Limited, Harlow, England, 352 p.

Rowley, D.B., 1996, Age of initiation of collision between India and Asia: a review of stratigraphic data: Earth and Planetary Science Letters, v. 145, p. 1–13

Rooney, T.O., Franceschi, P., and Hall, C.M., 2011, Water-saturated magmas in the Panama Canal region: A precursor to adakite-like magma generation?: Contributions to Mineralogy and Petrology, v. 161, p. 373–388.

Sauerzapf, U., Lattard, D., Burchard, M., and Engelmann, R., 2008, The titanomagnetite–ilmenite equilibrium: new experimental data and thermo-oxybarometric application to the crystallisation of basic to intermediate rocks: Journal of Petrology, v. 49, p. 1161–1185.

Scaillet, B., and Evans, B.W., 1999, The 15 June 1991 eruption of Mount Pinatubo; I, Phase equilibria and pre-eruption P–T–fO_2–fH_2 conditions of the dacite magmas: Journal of Petrology, v. 40, p. 381–411.

Schmidt, M.W., 1992, Amphibole composition in tonalite as a function of pressure; an experimental calibration of the Al-in hornblende barometer: Contribution to Mineralogy and Petrology, v. 110, p. 304–310.

Schmidberger, S.S., Heaman, L.M., Simonetti, A., Creaser, C.A., and Whiteford, S., 2007, Lu-Hf, in-situ Sr and Pb isotope and trace element systematics for mantle eclogites from the Diavik diamond mine: Evidence for Paleoproterozoic subduction beneath the Slave craton, Canada: Earth and Planetary Science Letters, v. 254, p. 55–68.

Sengör, A.M.C., Altmer, D., Cin, A., Ustaömer, T., and Hsü, K.J., 1988, Origin and assembly of the Tethyside orogenic collage at the expense of Gondwana Land, in Audley-Charles, M.G and Hallam, A., ed., Gondwana and Tethys: Geological Society, London, Special Publications, v. 37, p. 119–181.

Shafiei, B., Haschke, M., and Shahabpour, J., 2009, Recycling of orogenic arc crust triggers porphyry Cu mineralization in Kerman Cenozoic arc rocks, southeastern Iran: Mineralium Deposita, v. 44, 265–283.

Shokoohi Razi, A., Levin, V., Roecker, S.W., and Huang G.D., 2014, Crustal and uppermost mantle structure beneath western Tibet using seismic traveltime tomography: Geochemistry, Geophysics, Geosystems, DOI 10.1002/2013GC005143

Shirey, S.B., and Walker, R.J., 1998, The Re-Os isotope system in cosmochemistry and high temperature geochemistry: Annual Reviews of Earth and Planetary Sciences: v. 26, p. 423–500.

Sillitoe, R.H., 2010, Porphyry copper system: Economic Geology, v. 105, p. 3−41.

Simonetti, A., Heaman, L.M., Hartlaub, R.P., Creaser, R.A., MacHattie, T.G., and Böhm, C., 2005, U-Pb zircon dating by laser ablation-MC-ICP-MS using a new multiple ion counting Faraday collector array: Journal of Analytical Atomic Spectrometry, v. 20, p. 677–686.

Simmons, A.T., Tosdal, R.M., Wooden, J.L., Mattos, B., Concha, O., McCracken, S., and Beale, T., 2013, Punctuated magmatism associated with porphyry Cu-Mo formation in the Paleocene to Eocene of southern Peru: Economic Geology, v. 108, p. 625–639.

Sisson, T.W., and Grove, T.L., 1993, Temperature and H_2O contents of low-MgO high-alumina basalts: Contribution to Mineralogy and Petrology, v. 113, p. 167–184.

Spencer, K.J., and Lindsley, D.H., 1981, A solution model for coexisting iron-titanium oxides: American Mineralogist, v. 66, p. 1189–1201.

Spooner, E.T.C., 1993, Magmatic sulphide/volatile interaction as a mechanism for producing chalcophile element enriched, Archean Au-quartz, epithermal Au-Ag and Au skarn hydrothermal ore fluids: Ore Geology Reviews, v. 7, p. 359–379.

Stern, R.A., and Ickert, R.B., 2010, Zircon oxygen isotopes by SIMS: Performance evaluation of the Canadian IMS1280: Geochimica et Cosmochimica Acta, v. 74, A993.

Sun, S.S., and McDonough, W.F., 1989, Chemical and isotopic systematics of oceanic basalts: Implications for mantle composition and processes. Geological Society of London Special Publication, v. 42: p. 313–345.

Tafti, R., 2011, Metallogeny, geochronology and tectonic setting of the Gangdese belt, southern Tibet, China: Unpublished Ph.D. thesis, University of British Columbia, Canada, 451 p.

Tanaka, T., Togashi, S., Kamioka, H., Amakawa, H., Kagami, H., Hamamoto, T., Yuhara, M., Orihashi, Y., Yoneda, S., Shimizu, H., Kunimaru, T., Takahashi, K., Yanagi, T., Nakano, T., Fujimaki, H., Shinjo, R., Asahara, Y., Tanimizu, M., and

Dragusanu, C., 2000, JNdi-1; a neodymium isotopic reference in consistency with LaJolla neodymium: Chemical Geology, v. 168, p. 279–281.

Taylor, S.R., and McLennan, S.M., 1985, The Continental Crust: its Composition and Evolution. Oxford: Blackwell Scientific, 328 p.

Tera, F., and Wasserburg, G.J., 1972, U-Th-Pb systematics in three Apollo 14 basalts and the problem of initial Pb in lunar rocks: Earth and Planetary Science Letters, v. 14, p. 281–304.

Tindle, A.G. and Webb, P.C., 1994, PROBE-AMPH a spreadsheet program to classify microprobe-derived amphibole analyses: Computers and Geosciences, v. 20, p. 1201–1228.

Tomkins, A.G., Weinberg, R.F., and McFarlane, C.R.M., 2009, Preferential magma extraction from K- and metal-enriched source regions in the crust: Mineralium Deposita, v. 44, p. 171–181.

Toummite, A., Ikenne, M., and Beraaouz, E.H., 2012, Geothermobarometry of Askaoun pluton in Ouzellarh-Sirwa promontory (Central Anti-Atlas; Morocco): Open Journal of Geology, v. 2, p. 136–147.

Trail, D., Watson, E.B., and Tailby, N.D., 2011, The oxidation state of Hadean magmas and implications for early Earth's atmosphere: Nature, v. 480, p. 79–82.

Treloar, P.J., Petterson, M.G., Jan, M.Q., and Sullivan, M.A., 1996, A re-evaluation of the stratigraphy and evolution of the Kohistan Arc sequence, Pakistan Himalaya: Implications for magmatic and tectonic arc-building processes: Journal of the Geological Society, v. 153, p. 681–693.

Turner, S., Arnaud, N., Liu, J., Rogers, N., Hawkesworth, C., Harris, N., and Kelley, S., 1996, Post-collision, shoshonitic volcanism on the Tibetan Plateau: Implications for convective thinning of the lithosphere and the source of ocean island basalts: Journal of Petrology, v. 37, p. 45–71.

Unsworth, M.J., Jones, A.G., Wei, W., Marquis, G., Gokarn, S.G., Spratt, J.E., 2005, Crustal rheology of the Himalaya and Southern Tibet inferred from magnetotelluric data: Nature, v. 438, p. 78–81.

Unterschutz, J.L.E., Creaser, R.A., Erdmer, P., Thompson R.I., and Daughtry, K.L., 2002, North American margin origin of Quesnel terrane strata in the southern

Canadian Cordillera: Inferences from geochemical and Nd isotopic characteristics of Triassic metasedimentary rocks: Geological Society of America Bulletin, v. 114, p. 462–475.

Valley, J.W., Kinny, P.D., Schulze, D.J., Spicuzza, M.J., 1998, Zircon megacrysts from kimberlite: oxygen isotope variability among mantle melts: Contributions to Mineralogy and Petrology, v. 133, p. 1–11.

Valley, J.W., Lackey, J.S., Cavosie, A.J., Clechenko, C.C., Spicuzza, M.J., Basei, M.A.S., Bindeman, I.N., Ferreira, V.P., Sial, A.N., King, E.M., Peck, W.H., Sinha, A.K., and Wei, C.S., 2005, 4.4 billion years of crustal maturation: oxygen isotope ratios of magmatic zircon: Contributions to Mineralogy and Petrology, v. 150, p. 561–580.

Van der Voo, R., Spakman, W., and Bijwaard, H., 1999, Tethyan subducted slabs under India: Earth and Planetary Sciences Letters, v. 171, p. 7–20.

Van der Beek, P., Melle, J.V., Guillot, S., Pêcher, A., Reiners, P.W., Nicolescu, S., and Latif, M., 2009, Eocene Tibetan plateau remnants preserved in the northwest Himalaya: Nature Geoscience, v. 2, p. 364–368.

van Hinsbergen, D.J.J., Lippert, P.C., Dupont-Nivet, G., McQuarrie, N., Doubrovine, P.V., Spakman, W., and Torsvik, T.H., 2012, Greater India basin hypothesis and a two-stage Cenozoic collision between India and Asia: Proceedings of the National Academy of Science of the United States of America, v. 20, p. 7659–7664.

Venezky, D.Y., and Rutherford, M.J., 1999, Petrology and Fe–Ti oxide reequilibration of the 1991 Mount Unzen mixed magma: Journal of Volcanology and Geothermal Research, v. 89, p. 213–230.

Völkening, J., Walczyk, T., and Heumann, K.G., 1991, Osmium isotope ratio determinations by negative thermal ion mass spectrometry: International Journal of Mass Spectrometry and Ion Processes, v. 105, p. 147–159.

Wang, B.D., Xu, J.F., Chen, J.L., Zhang, X.G., Wang, L.Q., and Xia, B.B., 2010, Petrogenesis and geochronology of the ore-bearing porphyritic rocks in Tangbula porphyry molybdenum-copper deposit in the eastern segment of the Gangdese metallogenic belt: Acta Petrologica Sinica, 26, v. 26, 1820–1830 (in Chinese with English abstract).

Wang, F.Y., Liu, S.A., Li, S.G., and He, Y.S., 2013, Contrasting zircon Hf-O isotopes and trace elements between ore-bearing and ore-barren adakitic rocks in central-eastern China: Implications for genetic relation to Cu–Au mineralization: Lithos, v. 156–159, p. 97–111.

Wang, R., Richards, J.P., Hou, Z.Q., and Yang, Z.M., 2014a, Extent of underthrusting of the Indian plate beneath Tibet controlled of Miocene porphyry Cu-Mo±Au deposits: Mineralium Deposita, v. 49, p. 165–173, DOI: 10.1007/s00126-013-0507-y

Wang, R., Richards, J.P., Hou, Z.Q., Yang, Z.M., and DuFrane, S.A., 2014b, Increased magmatic water content–the key to Oligo-Miocene porphyry Cu-Mo±Au formation in the eastern Gangdese belt, Tibet: Economic Geology, in press.

Wang, R., Richards, J.P., Hou, Z.Q., Yang, Z.M., Gou, Z.B., and DuFrane, S.A., 2014c, Increasing magmatic oxidation state from Paleocene to Miocene in the eastern Tibetan Gangdese belt: Implication for collision-related porphyry Cu–Mo±Au mineralization: Economic Geology, in press.

Wang, S.F., Wang, C., Phillips, R.J., Murphy, M.A., Fang, X.M., and Yue, Y.H., 2012a, Displacement along the Karakoram fault, NW Himalaya, estimated from LA-ICP-MS U-Pb dating of offset geologic markers: Earth and Planetary Sciences Letters, v. 337–338, p. 156–163.

Wang, Z.H, Liu, Y.L., Liu, H.F., Guo, L.S., Zhang, J.S., and Xu, K.F., 2012, Geochronology and geochemistry of the Bangpu Mo-Cu porphyry ore deposit, Tibet: Ore Geology Review, v. 46, p. 95–105.

Watson, E.B., and Harrison, T.M., 2005, Zircon thermometer reveals minimum melting conditions on earliest Earth: Science, v. 308, p. 841–844.

Wen, D.R., 2007, The Gangdese batholith, Southern Tibet: Ages, geochemical characteristics and petrogenesis: Unpublished Ph.D. thesis, National Taiwan University, 120 p.

Weill, D.F., Drake, M.J., 1973, Europium anomaly in plagioclase feldspar: Experiment results and seimiquantitative model: Science, v. 180, p. 1059–1060.

White, L.T., Ahmad, T., Ireland, T.R., Lister, G.S., and Forster, M.A., 2011, Deconvolving episodic age spectra from zircons of the Ladakh batholith, northwest Indian Himalaya: Chemical Geology, v. 289, p. 179–196.

Widow, E., Hoernle, K.A., Shirey, S.B., and Schmincke, H.U., Os isotope systematics in the Canary Islands and Madeira: Lithospheric contamination and mantle plume signatures: Journal of Petrology, v. 40, p. 279–296.

Williams, I.S., 1998, U-Th-Pb geochronology by ion microprobe. In McKibben, M. A., Shanks III, W. C., and Ridley, W. I. (eds.): Applications of micro-analytical techniques to understanding mineralizing processes: Reviews in Economic Geology, v. 7, P. 1–35.

Williams, H.M., 2000, Magmatic and tectonic evolution of Southern Tibet and the Himalaya: Ph.D. thesis, The Open University, 329 p.

Wilkinson, J.J., 2013, Triggers for the formation of porphyry ore deposits in magmatic arcs: Nature Geoscience, v. 6, p. 915–925.

Wu, S., Zheng, Y.Y., Sun, X., Liu, S.A., Geng, R.R., You, Z.M., Ouyang, H.T., Lei, D., and Zhao, Z.Y., 2014, Origin of the Miocene porphyries and their mafic microgranular enclaves from Dabu porphyry Cu-Mo deposit, southern Tibet: implications for magma mixing/mingling and mineralization: International Geology Review: v, 56, p. 571–595.

Xia, B.B., Xia, B., Wang, B.D., Li, J.F., Zhang, X.G., and Wang, Y.C., 2010, Formation of the Tangbula porphyry Mo-Cu deposit evidence from SHRIMP Zircon U-Pb dating of Tangbula ore-bearing porphyries: Geotectonic et Metallogenia, v. 34, p. 291–297.

Xiao, B., 2011, Highly oxidized magmatic-hydrothermal ore-forming process at the Qulong giant porphyry Cu-Mo deposit, Gangdese, Tibet: Unpublished Ph.D. thesis (in Chinese), Institute of Geology and Geophysics, Chinese Academy of Sciences, Beijing, 275 p.

Xu, W.C., Zhang, H.F., Guo, L., and Yuan, H.L., 2010, Miocene high Sr/Y magmatism, south Tibet: Product of partial melting of subducted Indian continental crust and its tectonic implication: Lithos, v. 114, p. 293–306.

Yang, Z.M., Hou, Z.Q., White, N.C., Chang, Z.S., Li, Z.Q., and Song, Y.C., 2009, Geology of the post-collisional porphyry copper-molybdenum deposit at Qulong, Tibet: Ore Geology Reviews, v. 36, p. 133–159.

Yang, Z.M., 2008, The Qulong giant porphyry copper deposit in Tibet: Magmatism and mineralization: Unpublished Ph.D. thesis (in Chinese), Institute of Geology Chinese Academy of Geological Sciences, Beijing, 144 p. (in Chinese with English abstract).

Yang, Z.M., Hou, Z.Q., Jiang, Y.F., Zhang, H.R., and Song, Y.C., 2011, Sr-Nd-Pb and zircon Hf isotopic constraints on petrogenesis of the late Jurassic granitic porphyry at Qulong, Tibet: Acta Petrologica Sinica, v. 27, p. 2003–2010. (in Chinese with English abstract)

Yin, A., and Harrison, T.M., 2000, Geologic evolution of the Himalayan-Tibetan orogen: Annual Review of Earth and Planetary Sciences, v. 28, p. 211–280.

Ying, L.J., Wang, C.S., Tang, J.X., Wang, D.H., Qu, W.J., and Li, C., 2014, Re-Os systematics of sulfides (chalcopyrite, bornite, pyrite and pyrrhotite) from the Jima Cu-Mo deposit of Tibet, China: Journal of Asian Earth Sciences, v. 79, p. 497–506.

Yu, F., Hou, Z.F., Zhao, Z.D., Zheng, Y.C., Li, Q.Y., and Duan, L.F., 2013, Geochemistry and origin of Yare complex in western Tibet: constraints from Zircon U-Pb and Hf-O isotopes: 2013's National Symposium on Petrology and Geodynamics Abstract, p. 521–522.

Zajacz, Z., Candela, P.A., Piccoli, P.M., Wälle, M., and Sanchez-Valle, C., 2012, Gold and copper in volatile saturated mafic to intermediate magmas: Solubilities, partitioning, and implications for ore deposit formation: Geochimica et Cosmochimica Acta, v. 91, p. 140–159.

Zajacz, Z., Candela, P.A., Piccoli, P.M., Sanchez-Valle, C., and Wälle, M., 2013, Solubility and partitioning behavior of Au, Cu, Ag and reduced S in magmas: Geochimica et Cosmochimica Acta, v. 112, p. 288–304.

Zhang, G.Y., Zheng, Y.Y., Gong, F.Z., Gao, S.B., Qu, W.J., Pang, Y.C., Shi, Y.R., and Yan, S.Y., 2008, Geochronologic constraints on magmatic intrusions and mineralization of the Jiru porphyry copper deposit, Tibet, associated with continent-continent collisional process: Acta Petrologica Sinica, v. 24, p. 473–479.

Zhang, K.J., Xia, B.D., Wang, G.M., Li, Y.T., and Ye, H.F., 2004, Early Cretaceous stratigraphy, depositional environments, sandstone provenance, and tectonic setting of central Tibet, western China: Geological Society of America Bulletin, v. 116, p. 1202–1222.

Zhang, K, Zhang, Y, Li, B, and Zhong, L, 2007, Nd isotopes of siliciclastic rock from Tibet, western China: constraints on provenance and pre-Cenozoic tectonic evolution: Earth and Planetary Science Letter, v. 256, p. 604–616.

Zhang, S., Zheng, Y., Huang, K., Li, W., Sun, Q., Li, Q., Fu, Q., and Liang, W., 2012, Re-Os dating of molybdenite from Nuri Cu-W-Mo deposit and its geological significance: Mineral deposits, v. 31, p. 337–346 (in Chinese with English abstract).

Zhang, P., Shen, Z., Wang, M., Gan, W.J., Bürgmann, R., Molnar, P., Wang, Q., Niu, Z., Sun, J., Wu, J., Sun, H., and You, X., 2004, Continuous deformation of the Tibetan plateau from global positioning system data: Geology, v. 32, p. 809–812.

Zhao, J.X., Qin, K.Z., Li, G.M., Li, J.X., Xiao, B., and Chen, L., 2011a, Geochemistry and petrogenesis of granitoids at Sharang Eocene porphyry Mo deposit in the main-stage of India-Asia continental collision, northern Gangdese, Tibet: Resource Geology, v. 62, p. 84–98.

Zhao, J., Yuan, X., Liu, H., Kumar, P., Pei, S., Kind, R., Zhang, Z., Teng, J, Ding, L., Gao, X., Xu, Q., and Wang, W., 2010, The boundary between the Indian and Asian tectonic plates below Tibet: Proceedings of the National Academy of Science of the United States of America, v. 107, p. 11229–11233.

Zhao, Z.D., Zhu, D.C., Dong, G.C., Mo, X.X., DePaolo, D., Jia, L.L., Hu, Z.C., and Yuan, H.L., 2011b, The ~54 Ma gabbro–granite intrusive in southern Dangxung area, Tibet: Petrogenesis and implications: Acta Petrologica Sinica, v. 27, p. 3513–3524.

Zheng, Y.C., Hou, Z.Q., Li, Q.Y., Sun, Q.Z., Liang, W., Fu, Q., Li, W., and Huang, K.X., 2012a, Origin of late Oligocene adakitic intrusives in the southeastern Lhasa terrane: Evidence from in situ zircon U-Pb dating, Hf-O isotopes: Lithos, v. 148, p. 296–311.

Zheng, Y.C., Hou, Z.Q., Li, W., Liang, W., Huang, K.X., Li, Q.Y., Sun, Q.Z., Fu, Q., and Zhang, S., 2012b, Petrogenesis and geological implications of the Oligocene Chongmuda-Mingze adakite-like intrusions and their mafic enclaves, southern Tibet: Journal of Geology, v. 120, p. 647–669.

Zheng, Y.Y., Duo, J., Cheng, S.B., Gao, S.B., and Dai, F.H., 2007, Progress in porphyry copper exploration from the Gangdise belt, Tibet, China: Frontier of Earth Science in China, v. 1, p. 226–232.

Zheng, Y.Y., Sun, X., Gao, S.B., Zhao, Z.D., Zhang, G.Y., Wu, S., You, Z.M., and Li, J.D., 2014, Multiple mineralization events at the Jiru porphyry copper deposit, southern Tibet: Implications for Eocene and Miocene magma sources and resource potential: Journal of Asian Earth Sciences, v. 79, p. 842–857.

Zhou, L.M., Hou, Z.Q., Zheng, Y.C., and Li, W., 2011, Study on accessory minerals in Yaja granite, northern Tibet: Indicator of the magma source: Acta Petrologica Sinia, 27, p. 2786–2794 (in Chinese with English abstract).

Zhou, S., Mo, X.X., Zhao, Z.D., Qiu, R.Z., Zhang, S.Q., and Guo, T.Y., 2004, ^{40}Ar–^{39}Ar geochronology of Yangying post-collisional volcanic rock south Tibet and its geological significance: Progress in Natural Sciences, v. 12, p. 1411–1488. (in Chinese with English abstract)

Zhou, S., Mo, X.X., Zhao, Z.D., Qiu, R.Z., Niu, Y.L., Guo, T.Y., and Zhang, S.G., 2009, $^{40}Ar/_{39}Ar$ geochronology of post-collisional volcanism in the middle Gangdese belt, southern Tibet: Journal of Asian Earth Sciences, v. 37, p. 246–258.

Zhu, D.C., Mo, X.X., Niu, Y.L., Zhao, Z.D., Wang, L.Q., Liu, Y.S., and Wu, F.Y., 2009, Geochemical investigation of Early Cretaceous igneous rocks along an east-west traverse throughout the central Lhasa Terrane, Tibet: Chemical Geology, v. 268, p. 298–312.

Zhu, D.C., Mo, X.X., Zhao, Z.D., Niu, Y.L., Wang, L.Q., Chu, Q.H., Pan, G.T., Xu, J.F., and Zhou, C.Y., 2010, Presence of Permian extension- and arc-type magmatism in southern Tibet: Petrogeographic implications: Geological Society of America Bulletin, v. 122, p. 979–993.

Zhu, D.C., Zhao, Z.D., Niu, Y.L., Mo, X.X., Chung, S.L., Hou, Z.Q., Wang, L.Q., and Wu, F.Y., 2011, The Lhasa terrane: Record of a microcontinent and its histories of drift and growth: Earth and Planetary Science Letters, v. 301, p. 241–255.

Zhu, D.C., Zhao, Z.D., Niu, Y.L., Dilek, Y., Hou, Z.Q. and Mo, X.X., 2013, The origin and pre-Cenozoic evolution of the Tibetan Plateau: Gondwana Research, v. 23, p. 1429–1454.

Zimmer, M.M., Plank, T., Hauri, E.H., Yogodzinski, G.M., Stelling, P., Larsen, J., Singer, B., Jicha, B., Mandeville, C., and Nye, C.J., 2010, The role of water in generating the calc-alkaline trend: New volatile data for Aleutian magmas and a new Tholeiitic Index: Journal of Petrology, v. 51, p. 2411–2444.